

**Suche nach Neuer Physik  
in Elektron-Tau Endzuständen in  
Proton-Antiproton Kollisionen  
bei 1.96 TeV**

DISSERTATION  
zur  
Erlangung der Doktorwürde  
der Fakultät für Mathematik und Physik  
der Albert-Ludwigs-Universität in Freiburg i.Br.

vorgelegt von  
Carsten Nöding  
geb. in Rotenburg an der Fulda

April 2006



# Contents

<b>Introduction</b>	<b>vii</b>
<b>1 Theoretical Aspects</b>	<b>1</b>
1.1 Standard Model . . . . .	1
1.1.1 Electroweak Interaction . . . . .	2
1.1.2 Strong Interaction . . . . .	4
1.1.3 Higgs Sector . . . . .	5
1.1.4 Problems of the Standard Model . . . . .	7
1.2 Supersymmetry . . . . .	9
1.2.1 R-Parity . . . . .	10
1.2.2 Minimal Supersymmetric Standard Model (MSSM) . . . . .	10
1.2.3 Constrained MSSM . . . . .	14
1.2.4 Supersymmetry Breaking . . . . .	14
1.2.5 SUSY Mass Spectrum . . . . .	16
1.2.6 Higgs Sector in the MSSM . . . . .	17
1.2.7 Search for Supersymmetry . . . . .	20
<b>2 Experimental Apparatus</b>	<b>23</b>
2.1 Units and Coordinate System . . . . .	23
2.2 Fermilab Accelerator Chain . . . . .	24
2.3 DØ Detector . . . . .	26
2.3.1 Tracking System . . . . .	26
2.3.2 Preshower Detectors . . . . .	29
2.3.3 Calorimeter System . . . . .	30
2.3.4 Muon Spectrometer . . . . .	32
2.3.5 Luminosity Monitor . . . . .	34
2.3.6 Forward Proton Detector . . . . .	35
2.3.7 Trigger and Data Acquisition . . . . .	35
<b>3 Phenomenology of <math>p\bar{p}</math> Collisions</b>	<b>41</b>
3.1 General Properties of $p\bar{p}$ Collisions . . . . .	41
3.2 Parton Distribution Functions (PDF) . . . . .	42
3.3 Factorization and Renormalization Scale . . . . .	43
3.4 Cross Section . . . . .	44
3.5 Higher Order QCD corrections . . . . .	44
3.6 Event Simulation . . . . .	45
3.6.1 Monte Carlo Generation . . . . .	45
3.6.2 Detector Simulation . . . . .	47

<b>4 Event Reconstruction and Object Identification</b>	<b>49</b>
4.1 Track Reconstruction . . . . .	49
4.2 Primary Vertex . . . . .	50
4.3 Electron Reconstruction and Identification . . . . .	50
4.3.1 Electron Likelihood . . . . .	53
4.4 Tau Reconstruction and Identification . . . . .	54
4.4.1 Reconstruction Algorithm . . . . .	56
4.4.2 Classification of Tau Candidates . . . . .	57
4.4.3 Neural Network . . . . .	58
4.5 Jet Reconstruction and Identification . . . . .	67
4.6 Missing Transverse Energy ( $\cancel{E}_T$ ) . . . . .	68
<b>5 Data Sample and Monte Carlo Simulation</b>	<b>71</b>
5.1 Data Sample . . . . .	71
5.1.1 Data Quality Criteria . . . . .	71
5.1.2 Trigger Selection . . . . .	72
5.2 Integrated luminosity . . . . .	72
5.3 Standard Model Monte Carlo Samples . . . . .	73
5.4 Background from QCD Jet Production . . . . .	75
5.5 Monte Carlo Efficiency and Resolution Corrections . . . . .	77
5.5.1 Trigger Efficiency . . . . .	78
5.5.2 Electron Efficiency and Resolution Corrections . . . . .	80
5.5.3 Tau Efficiency and Resolution Corrections . . . . .	84
5.5.4 $p_T(Z)$ Reweighting . . . . .	85
5.5.5 Track Smearing . . . . .	85
5.5.6 $\cancel{E}_T$ Smearing . . . . .	86
<b>6 Search for Associated Chargino/Neutralino Production in <math>e + \tau_h</math> Final States</b>	<b>89</b>
6.1 Trilepton Signature at the Tevatron . . . . .	89
6.1.1 Production of Supersymmetric Particles . . . . .	89
6.1.2 Decay of Supersymmetric Particles . . . . .	90
6.1.3 Signal Topology . . . . .	93
6.1.4 Standard Model Background . . . . .	94
6.2 Signal Monte Carlo . . . . .	96
6.3 Reference Signal: $Z/\gamma^* \rightarrow \tau\tau \rightarrow e + \tau_h$ . . . . .	97
6.3.1 Event Selection . . . . .	97
6.3.2 Results . . . . .	101
6.4 Trilepton Event Selection and Data/Monte Carlo Comparison . .	102
6.5 Systematic Uncertainties . . . . .	111
6.6 Results . . . . .	113
6.6.1 Flavor Composition of the Signal Final State . . . . .	116
6.6.2 Combination with Additional Trilepton Analyses . . . . .	117
6.6.3 Further Prospects . . . . .	120
6.7 Outlook: Sensitivity for the SUSY Parameter Space with Large Values of $\tan\beta$ . . . . .	122

<b>7 Search for MSSM Higgs Bosons in <math>e + \tau_h</math> Final States</b>	<b>127</b>
7.1 MSSM Higgs Boson Signature at the Tevatron . . . . .	127
7.1.1 Neutral Higgs Boson Production . . . . .	128
7.1.2 Neutral Higgs Boson Decay . . . . .	129
7.1.3 Higgs Width . . . . .	133
7.1.4 Signal Topology . . . . .	133
7.1.5 Standard Model Background . . . . .	134
7.2 Signal Monte Carlo . . . . .	135
7.3 Event Selection and Data/Monte Carlo Comparison . . . . .	136
7.4 Systematic Uncertainties . . . . .	145
7.5 Results . . . . .	148
7.5.1 The $e + \tau_h$ Result . . . . .	148
7.5.2 Combination with Additional MSSM Higgs Analyses . . .	153
7.6 Outlook . . . . .	161
<b>8 Summary and Conclusion</b>	<b>163</b>
<b>List of Tables</b>	<b>II</b>
<b>List of Figures</b>	<b>VI</b>
<b>Bibliography</b>	<b>VII</b>
<b>Acknowledgements</b>	<b>XIV</b>

*Contents*

---

# Introduction

During the last decades, particle physicists have studied the tiniest building blocks of matter – the quarks and the leptons – and the forces between them in great detail. From these experiments, a theoretical framework has been built that describes the observed results with high precision. The achievement of this theory, which is referred to as the Standard Model of elementary particle physics, was the elaboration of a unified description of the strong, weak and electromagnetic forces in the framework of quantum gauge-field theories. Moreover, the Standard Model combines the weak and electromagnetic forces in a single electroweak gauge theory. The fourth force which is realized in nature, gravity, is too weak to be observable in laboratory experiments carried out in high-energy particle physics and is not part of the Standard Model.

Although the Standard Model has proven highly successful in correlating a huge amount of experimental results, a key ingredient is as yet untested: the origin of electroweak symmetry breaking. Currently, the only viable ansatz that is compatible with observation is the Higgs mechanism. It predicts the existence of a scalar particle, called the Higgs boson, and the couplings to the fundamental Standard Model particles, however not its mass. An upper limit on the mass of the Higgs boson of  $\sim 1$  TeV can be inferred from unitarity arguments. One of the key tasks of particle physics in the next years will be to verify the existence of this particle.

The introduction of an elementary scalar particle in a quantum field theory is highly problematic. The Higgs boson mass is subject to large quantum corrections, which makes it difficult to understand how its mass can be less than a TeV as required by theory. In addition, the Standard Model does not provide an answer to fundamental questions like the values of free parameters of the model, the pending integration of gravity or the evolution of the coupling constants of the fundamental forces at large energy regimes. Hence there are strong reasons to believe that the Standard Model is only a low-energy approximation to a more fundamental theory.

One of the best studied candidates for an extension of the Standard Model is supersymmetry, which predicts the existence of a supersymmetric partner for each fundamental particle that differs only in spin. To allow different masses for Standard Model particles and their corresponding supersymmetric partners, supersymmetry must be broken. The mechanism behind supersymmetry breaking is currently unknown, however, various hypotheses exist. Supersymmetric models do not only solve the problem of the large quantum corrections to the Higgs boson mass, but they also allow the unification of the coupling constants

## *Introduction*

---

at a common scale. In addition, certain supersymmetric models provide a suitable candidate for cold dark matter, which represents a large fraction of mass in our universe.

Searches for supersymmetric particles have been performed by the four LEP<sup>1</sup> experiments (ALEPH, DELPHI, L3, OPAL) up to the kinematic limit. Since no evidence for supersymmetric particles has been found, lower limits on their masses have been derived. The search for supersymmetry is now continuing at the Tevatron collider, located at the Fermi National Accelerator Laboratory in Batavia, Illinois. Two dedicated detector systems, CDF and DØ, are installed at the Tevatron to analyze proton-antiproton collisions at a center-of-mass energy of 1.96 TeV. A particular promising discovery channel for supersymmetry within the Tevatron energy range is the trilepton channel. In this channel, the lighter supersymmetric partners of the Higgs and gauge bosons, the charginos and neutralinos, decay into final states with leptons or hadrons and missing energy. Using the leptonic final states, the signal can be separated from the large Standard Model background. Supersymmetry requires an extension of the Standard Model Higgs sector, leading to more than one neutral Higgs boson. Enhanced couplings result in sizable cross sections for Higgs boson production, and the decay into a tau pair becomes an important Higgs boson discovery channel.

Within the present thesis, a search for new physics predicted by constrained supersymmetric models is performed in final states consisting of an electron and a tau using data collected with the DØ detector from April 2002 to July 2004. The first analysis searches for the associated production of the lightest chargino and the second lightest neutralino in final states with an electron, a hadronically decaying tau, an additional lepton and missing transverse energy:  $e + \tau_h + \ell + \cancel{E}_T$ . The second analysis searches for neutral supersymmetric Higgs bosons in the decay mode  $\phi \rightarrow \tau\tau \rightarrow e + \tau_h + \cancel{E}_T$ . To improve the sensitivity, the results are interpreted in combination with other channels.

---

<sup>1</sup>Large Electron Positron Collider, CERN (Geneva)

# 1 Theoretical Aspects

The first part of the following chapter gives an overview of the Standard Model (SM) of particle physics [1], which is the accepted theory of particles and their forces. The Standard Model is built from many theoretical and experimental studies done in the last forty years, and it is in excellent agreement with almost all current data. However, there are many hints that there exists a more fundamental theory. The second part describes such a more profound theory, called supersymmetry (SUSY), which is the theoretical framework for this analysis.

## 1.1 Standard Model

The Standard Model sums up our current understanding of fundamental particles and the forces between them. The fundamental particles are divided into two groups according to their spin  $s$ : fermions (with  $s = \frac{1}{2}$ ) and bosons (with  $s = 1$ ).

An overview of the fundamental fermions is given in Table 1.1. Fermions are divided into two elementary categories: leptons and quarks. Leptons participate only in the electroweak interactions, whereas quarks participate in both strong and electroweak interactions. The entire collection of fermions is divided into three generations. The first generation contains the up- and down quark ( $u, d$ ), the electron ( $e$ ) and the electron-neutrino ( $\nu_e$ ). The second generation contains the charm- and the strange-quark ( $c, s$ ), muon ( $\mu$ ) and muon-neutrino ( $\nu_\mu$ ) while the third generation consists of the bottom- and top-quark ( $b, t$ ), tau ( $\tau$ ) and tau-neutrino ( $\nu_\tau$ ). For each fermion exists an antiparticle with identical mass but inverse additive quantum numbers. The quarks and charged leptons of the second and third family are unstable and decay weakly into fermions of lower families.

The interactions between particles are mediated by gauge bosons. An overview of the different gauge bosons is given in Table 1.2. There are four different interactions known: electromagnetic, weak, strong and gravitational. The first three are described by local gauge symmetries, while gravity is described by general relativity outside the framework of gauge theories. However gravitation is irrelevant at the current accessible energy scale due to the small masses of Standard Model particles and the tiny interaction strength.

The Standard Model unifies the Glashow-Weinberg-Salam model (GSW) of electroweak interaction [1] and the strong force of Quantum Chromodynamics [2]. It is a gauge theory which is based on  $SU(3)_C \times SU(2)_L \times U(1)_Y$  symmetry.

Leptons			Quarks		
Name	Symbol	Mass	Name	Symbol	Mass
electron neutrino	$\nu_e$	< 3 eV	up	$u$	1.5 to 4 MeV
muon neutrino	$\nu_\mu$	< 0.2 MeV	down	$d$	4 to 8 MeV
tau neutrino	$\nu_\tau$	< 18.2 MeV	strange	$s$	80 to 130 MeV
electron	$e$	511.0 keV	charm	$c$	1.15 to 1.35 GeV
muon	$\mu$	105.7 MeV	bottom	$b$	4.6 to 4.9 GeV
tau	$\tau$	1.777 GeV	top	$t$	174.3 $\pm$ 5.1 GeV

Table 1.1: Overview of the Standard Model fermions and their masses (from Ref. [3]). Throughout this thesis, the so-called *natural units* are used. The fundamental constants  $\hbar$  and  $c$  are set to 1, and all quantities (e.g. masses) have the dimension of a power of energy.

The subgroup  $SU(2)_L \times U(1)_Y$  represents the unification of the electromagnetic and the weak interaction. Electromagnetism acts on all charged particles, and the underlying theory is Quantum Electrodynamics (QED). The corresponding gauge boson is the massless  $\gamma$ . The weak interaction affects, in contrast to the electromagnetic and strong interaction, all Standard Model particles. The gauge bosons are the  $W^\pm$  and  $Z$ . Section 1.1.1 gives a more detailed introduction to the electroweak interaction.  $SU(3)_C$  is the gauge group of the strong interaction. The strong interaction is responsible for the quark-gluon interactions. The underlying theory is called Quantum Chromodynamics (QCD), and a further discussion follows in Section 1.1.2.

### 1.1.1 Electroweak Interaction

The electromagnetic and the weak interactions are combined to one theory, called electroweak theory. It is based on the  $SU(2)_L \times U(1)_Y$  gauge group generated by the hypercharge  $Y$  and the weak isospin  $\vec{T}$ . The electroweak theory is a non-abelian local gauge theory, meaning that the group generators do not commute and leading to interactions between the gauge bosons. The index  $L$  denotes that the  $SU(2)$  part (with the corresponding gauge fields) acts only on the left-handed part of the fermion fields, while the  $U(1)$  part acts on both right- and left-handed components.

Requiring the Lagrangian  $\mathcal{L}_{EW}$  to be locally invariant under  $SU(2)_L \times U(1)_Y$

Name	Field	Interaction	Charge [e]	Mass [GeV]
Photon $\gamma$	$A_\mu$	electromagnetic	$< 5 \times 10^{-30}$	$< 6 \times 10^{-26}$
Z Boson $Z$	$Z_\mu$	electroweak	0	$91.1876 \pm 0.0021$
W Bosons $W^\pm$	$W_\mu^\pm$	weak	$\pm 1$	$80.425 \pm 0.038$
Gluon $g$	$G_\mu^a$	strong	0	0

Table 1.2: Standard Model gauge bosons and their properties [3].

transformations, four gauge fields have to be introduced: one ( $B_\mu$ ) to compensate for the local phase transformation of the  $U(1)_Y$  group and three more ( $W_\mu^a$ ,  $a = 1, 2, 3$ ) related to the transformations of  $SU(2)_L$ . The locally invariant Lagrangian is:

$$\begin{aligned}\mathcal{L}_{EW} &= i\bar{L}\gamma^\mu\partial_\mu L + i\bar{R}\gamma^\mu\partial_\mu R - \frac{1}{4}B^{\mu\nu}B_{\mu\nu} - \frac{1}{4}\vec{W}^{\mu\nu}\vec{W}_{\mu\nu} \\ &+ \bar{L}\gamma^\mu g'\frac{Y_L}{2}B_\mu L + \bar{R}\gamma^\mu g'\frac{Y_R}{2}B_\mu R + \bar{L}\gamma^\mu g\frac{1}{2}\bar{\tau}\vec{W}_\mu L\end{aligned}\quad (1.1)$$

with the field tensors  $B_{\mu\nu} = \partial_\mu B_\nu - \partial_\nu B_\mu$  and  $\vec{W}_{\mu\nu} = \partial_\mu \vec{W}_\nu - \partial_\nu \vec{W}_\mu + ig\vec{W}_\mu \times \vec{W}_\nu$ .  $g$  is the coupling constant for  $SU(2)_L$ , and  $g'$  is the coupling constant for  $U(1)_Y$ . They describe the coupling strength of the gauge fields to the weak isospin respectively to the weak hypercharge.  $\tau_i$  ( $i = 1, 2, 3$ ) are the three linear independent generators of the  $SU(2)$  gauge group, the weak hypercharge  $Y$  is the generator of  $U(1)$ . The  $L$  and  $R$  terms denote (considering only the leptons of the first generation) the left-handed weak isospin doublet

$$L \equiv \begin{pmatrix} \nu_e \\ e \end{pmatrix}_L \quad (1.2)$$

with  $Y = -\frac{1}{2}$ , and a right-handed weak isospin singlet

$$R \equiv e_R \quad (1.3)$$

with  $Y = -1$  (see also Table 1.3). The quarks are organized identically to the leptons. The eigenstates of the down-type quarks in weak interactions  $d'$ ,  $s'$ ,  $b'$  are not identical to the mass eigenstates of  $d$ ,  $s$ ,  $b$ . The transformation is done by the Cabibbo-Kobayashi-Maskawa (CKM) matrix [4].

The terms in the first line in Eqn. 1.1 describe the kinetic energy of the fermions and gauge fields, while the second line describes the interactions between the fermions and gauge fields. The last term on the first line contains self-interactions of the  $SU(2)_Y$  gauge fields  $W_\mu^a$ , a feature common to non-abelian groups.  $B_\mu$  cannot be identified with the  $\gamma$ , since the first term on the second line would describe a coupling of the neutral neutrino to the photon. Therefore the gauge field  $B_\mu$  and  $W_\mu^a$  cannot be identified with the experimentally observed gauge bosons  $\gamma$  and  $W^\pm$ ,  $Z$ . To describe the gauge boson fields realized in nature the following combinations have to be constructed:

$$W_\mu^\pm = \frac{1}{\sqrt{2}}(W_\mu^1 \mp iW_\mu^2) \quad (1.4)$$

$$Z^\mu = -B^\mu \sin \theta_W + W_3^\mu \cos \theta_W \quad (1.5)$$

$$A^\mu = B^\mu \cos \theta_W + W_3^\mu \sin \theta_W. \quad (1.6)$$

$\theta_W$  is the weak mixing angle, which is determined by the two coupling constants  $g$  and  $g'$ :

$$\cos \theta_W = \frac{g}{\sqrt{g^2 + g'^2}}. \quad (1.7)$$

	1. Generation	2. Generation	3. Generation	$ \vec{T} $	$T_3$	$Y$	$Q/e$
Leptons	$\nu_e$	$\nu_\mu$	$\nu_\tau$	$\frac{1}{2}$	$\frac{1}{2}$	$-\frac{1}{2}$	0
	$e_L$	$\mu_L$	$\tau_L$	$\frac{1}{2}$	$-\frac{1}{2}$	$-\frac{1}{2}$	-1
	$e_R$	$\mu_R$	$\tau_R$	0	0	-1	-1
Quarks	$u_L$	$c_L$	$t_L$	$\frac{1}{2}$	$\frac{1}{2}$	$\frac{1}{6}$	$2/3$
	$d'_L$	$s'_L$	$b'_L$	$\frac{1}{2}$	$-\frac{1}{2}$	$\frac{1}{6}$	$-1/3$
	$u_R$	$c_R$	$t_R$	0	0	$\frac{2}{3}$	$2/3$
	$d'_R$	$s'_R$	$b'_R$	0	0	$-\frac{1}{3}$	$-1/3$

Table 1.3: Weak Isospin, hypercharge and electric charge of the fermions. The indices  $L(R)$  denote left(right)-handed fermions. The weak hypercharge  $Y$  is defined by  $Q/e = T_3 + Y$ . The prime indicates that the weak eigenstates of the quarks are not their mass eigenstates. The quark mixing is described by the Cabibbo-Kobayashi-Maskawa (CKM) matrix [4].

The coupling constants are related to the electric charge by

$$e = g' \cos \theta_W = g \sin \theta_W. \quad (1.8)$$

Table 1.2 gives an overview of the gauge bosons.

The electroweak Lagrangian (Eqn. 1.1) does not contain any mass terms for the fermion and gauge fields. Mass terms will be introduced by the Higgs mechanism through spontaneous symmetry breaking in Section 1.1.3.

### 1.1.2 Strong Interaction

Quantum Chromodynamics (QCD) is the gauge field theory which describes the strong interactions of quarks and gluons. It is based on the  $SU(3)_C$  gauge group. The index  $C$  denotes the fact that quarks and gluons have an additional internal degree of freedom called *color*. Like the electroweak theory, QCD is a non-abelian theory. The QCD Lagrangian at tree level can be constructed by adding up the following three terms:

$$\mathcal{L}_{QCD} = \mathcal{L}_{quark} + \mathcal{L}_{int} + \mathcal{L}_{glue}. \quad (1.9)$$

$\mathcal{L}_{quark}$  describes the propagation of the free quarks and yields the Dirac equation for spin 1/2 particle for each quark with a given flavor and color. Since the Dirac equation is not invariant under local gauge transformations, gauge invariance is restored in the same way as it is restored in QED or in the electroweak theory: a 'compensating' spin-1 field is introduced that interacts with the quark fields. There is one separate spin-1 field for each of the eight degrees of freedom determining the gauge transformations, leading to eight gluons. This results in a quark-gluon interaction term  $\mathcal{L}_{glue}$  which needs to be added to the QCD Lagrangian:

$$\mathcal{L}_{int}(x) = g_s \sum_{q=u,d,s,\dots} \bar{\psi}_{qi}(x) \frac{(\lambda^a)_k^i}{2} \gamma^\mu \psi_q^k(x) A_\mu^a(x). \quad (1.10)$$

$A_\mu^a$  (with  $a = 1\dots8$ ) denotes the gluon fields,  $g_s$  is the dimensionless coupling analogous to  $e$  in  $\mathcal{L}_{QED}$  and  $\lambda^a$  are the generators of the SU(3) group. The indices  $i$  and  $k$  denote the quark color. In contrast to the electromagnetic interaction, where the photon field is electrically neutral, the gluon fields also carry color charge. Hence the color state of a quark changes after emission or absorption of a gluon. The color charge leads to gluon self-interactions, where gluons couple to other gluons. The color of the gluon can be identified with a superposition of quark and antiquark colors.

The last term  $\mathcal{L}_{glue}$  describes the propagation of the gluon fields:

$$\mathcal{L}_{glue}(x) = -\frac{1}{4}G_{\mu\nu}^a(x)G^{a\mu\nu}(x) \quad (1.11)$$

where

$$G_{\mu\nu}^a = \partial_\mu A_\nu^a - \partial_\nu A_\mu^a + g_s f^{abc} A_\mu^b A_\nu^c. \quad (1.12)$$

$G_{\mu\nu}^a$  is the gluon field-strength tensor, the  $f_{abc}$  ( $a, b, c = 1\dots8$ ) are the structure constants of SU(3). Local gauge invariance of  $\mathcal{L}_{glue}$  implies that gluons are massless.  $G_{\mu\nu}^a$  is more complicated than its QED analog  $B_{\mu\nu}$  since it allows three- and four-gluon vertices (gluon self-interactions).

The QCD Lagrangian at tree level is given by:

$$\mathcal{L}_{QCD} = \sum_{q=u,d,s,\dots} \bar{\psi}_q(iD_\mu\gamma^\mu - m_q)\psi_q - \frac{1}{4}G_a^{\mu\nu}G_{a\mu\nu} \quad (1.13)$$

using the covariant derivative

$$D_\mu = \partial_\mu - ig_s \frac{\lambda^a}{2} \cdot A_\mu^a. \quad (1.14)$$

### 1.1.3 Higgs Sector

The presence of mass terms in the Lagrangian would break the  $SU(3)_C \times SU(2)_L \times U(1)_Y$  symmetry and therefore destroy gauge symmetry. However, experiments have shown that only gluons and the photon are massless, while all other particles are massive<sup>1</sup>. A solution to this problem is provided by the Higgs mechanism, which exploits the principle of spontaneous symmetry breaking in the electroweak interaction.

A spontaneous breaking in the  $SU(2)_L \times U(1)_Y$  symmetry is facilitated by introducing one complex scalar field with two components:

$$\Phi = \begin{pmatrix} \phi^+ \\ \phi^0 \end{pmatrix} = \frac{1}{\sqrt{2}} \begin{pmatrix} \phi_1^+ + i\phi_2^+ \\ \phi_1^0 + i\phi_2^0 \end{pmatrix}. \quad (1.15)$$

The following Lagrangian is added to  $\mathcal{L}_{EW}$  (see Eqn. 1.1):

$$\mathcal{L}_{Higgs} = |D_\mu\Phi|^2 - V(\phi) \quad (1.16)$$

$$\text{with : } D_\mu = \partial_\mu - \frac{1}{2}ig\vec{\tau}\vec{W}_\mu - \frac{1}{2}ig'YB_\mu. \quad (1.17)$$

---

<sup>1</sup>Oscillations experiments indicate that the neutrinos must have mass [5].

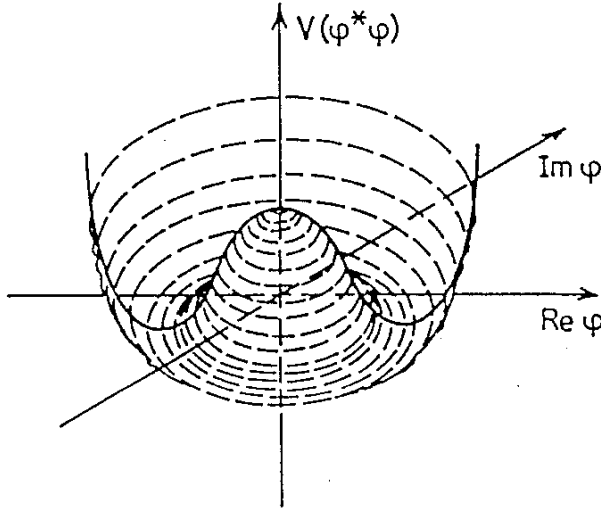


Figure 1.1: The Higgs potential in the case of a single complex scalar field  $\phi$ :  $\text{Re}(\phi) = \phi_1$ ,  $\text{Im}(\phi) = \phi_2$ .

The corresponding Higgs potential has the form:

$$V = -\mu^2|\Phi|^2 + \lambda|\Phi|^4. \quad (1.18)$$

For  $\mu^2 > 0$  the Higgs potential has a continuous minimum and a typical shape described as a Mexican hat. A graphical two-dimensional representation is given in Figure 1.1. The vacuum state corresponds to a certain choice within the minimum, and the U(1) symmetry of the Higgs potential is not preserved for the chosen minimum. In other words, the vacuum state has a lower symmetry than the potential itself. This phenomenon is referred to as “Spontaneous Symmetry Breaking.” The vacuum expectation value of the Higgs field is chosen to be:

$$\langle \Phi \rangle = \begin{pmatrix} 0 \\ v \end{pmatrix}, \quad v^2 = \mu^2/2\lambda. \quad (1.19)$$

The  $\phi^+$  component of the Higgs field is zero to ensure the conservation of the electromagnetic charge. The Higgs particle is interpreted as a space-time dependant “radial” fluctuation  $h(x)$  of the field  $\Phi$  near the vacuum configuration:

$$\Phi = \frac{1}{\sqrt{2}} \begin{pmatrix} 0 \\ v + h(x) \end{pmatrix}. \quad (1.20)$$

The Lagrangian, expressed in terms of the vacuum expectation value  $v$  and the physical state  $h$ , effectively describes a scalar particle with a mass  $m_h = \sqrt{2\lambda}v$ :

$$\mathcal{L} = \frac{1}{2}\partial_\mu\partial^\mu h - \lambda v^2 h^2 - \lambda v h^3 - \frac{\lambda}{4}h^4. \quad (1.21)$$

The scalar particle described by the Lagrangian is referred to as the Standard Model Higgs boson. It is the only remaining neutral physical state after

	All fermions	$WW$	$ZZ$
$H$	$-\frac{ig}{2m_W} m_f$	$ig m_W g^{\mu\nu}$	$\frac{ig}{2 \cos \Theta_W} m_Z g^{\mu\nu}$

Table 1.4: Couplings of the Standard Model Higgs boson to fermions and massive gauge bosons [16].

electroweak symmetry breaking, representing one of the four components introduced in Eqn. 1.15. The other three components manifest themselves as the longitudinally polarized components of the weak vector bosons. For the masses of the weak vector bosons follows:

$$\cos \theta_W = \frac{M_W}{M_Z}. \quad (1.22)$$

The Higgs boson is neutral and couples to fermions proportional to their masses and to massive gauge bosons. The couplings are summarized in Table 1.4. It is the only particle in the Standard Model that has not been discovered yet, however, a lower limit on the Standard Model Higgs boson mass has been set by the LEP experiments. Direct searches in electron-positron collisions up to a center-of-mass energy of  $\sqrt{s} \leq 209$  GeV have excluded a Higgs boson mass of  $m_H = 114.1$  GeV and lower at 95 % CL [6].

#### 1.1.4 Problems of the Standard Model

Despite of the success of the Standard Model in describing all observed low-energy data using very few parameters, it is still unsatisfactory since it builds on many assumptions and leaves fundamental questions unanswered. There is no explanation for the existence of three generations of leptons and quarks, why the absolute values of electron charge and proton charge are identical or why leptons and quarks are fundamental particles. A few more of the remaining puzzles of the Standard Model are:

- Gravity Problem

Gravity is the only remaining interaction that is not incorporated in the Standard Model. Due to its weakness at the low energy scales, it can be safely neglected in particle physics. However, gravitational effects must be taken into account at the latest when the energy is at the order of the Planck scale, given by  $M_P = \frac{1}{\sqrt{8\pi G_N}} \approx 2.4 \times 10^{18}$  GeV. Gravity is described by the Einstein formalism outside the framework of gauge theories, and adding it to the Standard Model gauge theories destroys their renormalizability. In addition, the gravitational force cannot be derived from the principle of local gauge invariance [7].

- Fine Tuning Problem (Mass Hierarchy Problem)

The Standard Model does not offer an explanation why the electroweak scale and the Planck scale differ by seventeen orders of magnitude

$(M_P/M_W \sim 10^{17})$ . This is known as the *mass hierarchy problem*, and it is directly related to the *fine tuning problem*.

Electroweak precision measurements indicate that the value of the Higgs boson mass is of the order  $\mathcal{O}(100)$  GeV. Assuming that the Standard Model is valid up to an energy scale  $\Lambda$ , the squared Higgs mass receives quadratically divergent quantum loop correction at the order of  $\mathcal{O}(\Lambda^2)$  from Standard Model particles. The problem arises when radiative corrections to masses of scalar particles are calculated, with the Higgs boson being the only elementary scalar particle in the Standard Model. For 1-loop corrections, the mass corrections are of the form

$$\delta m_s^2 \sim \mathcal{O}\left(\frac{\alpha}{2\pi}\right) \Lambda^2 \quad (1.23)$$

due to contributions from fermion and gauge boson loops (see Figure 1.2) and from quartic scalar couplings. Assuming that the Standard Model is valid up to the Planck scale,  $\Lambda$  would be at the order of the Planck Mass  $M_P$ . Hence the mass corrections to the Higgs boson mass would be enormous, thus destroying the stability of the weak scale.

This problem can be solved by fine-tuning the bare Higgs boson mass so that it contains a large negative term, which almost exactly cancels the 1-loop corrections. However this requires a precise fine tuning with an accuracy of  $10^{-34}$  to the squared Higgs mass. In addition, there are still 2-loop (and higher order) corrections that also have to be accurately canceled. Such a series of cancellation might be technically feasible, but lacks any explanation.

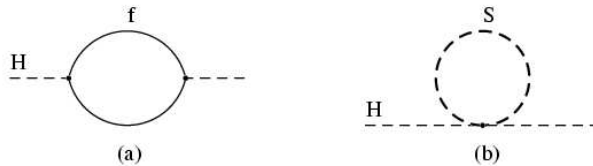


Figure 1.2: Radiative corrections to the squared Higgs boson mass from fermions (a) and bosons (b).

- Unification of Coupling Constants

The Standard Model has three different gauge groups postulated from phenomenological considerations. They are associated with three different coupling constants, which are arbitrary. Embedding the Standard Model into a higher symmetry group, which is broken at low energy scales into the known Standard Model symmetry groups, leads to a more fundamental and predictive theory. One of the implications of such a Grand Unified Theory (GUT) consists in the unification of the electroweak and strong couplings at GUT scale ( $M_{GUT} \approx 10^{16}$  GeV). Extrapolation of the current measurements of the couplings strengths towards higher energies

hints to a unification of the coupling constants; however, all three do not unify at the same energy scale (see Figure 1.3).

## 1.2 Supersymmetry

Out of the variety of extensions to the Standard Model which are presently discussed, supersymmetry (SUSY) is one of the most popular models. It unites the two different groups of particles in the Standard Model, fermions and bosons, into a common representation. Supersymmetry is necessary in String Theory, by many seen as the best candidate of a theory of everything (TOE). In addition local supersymmetry gives rise to supergravity, which unites general relativity with the quantum field theory of the Standard Model and therefore describing all four interactions seen in nature. The minimal supersymmetric extension to the Standard Model (MSSM), discussed below, leads to the unification of all three gauge couplings (see Figure 1.3). The most compelling argument for Supersymmetry is that it solves the problem with quadratic divergences (*mass hierarchy problem*) in the Standard Model which are discussed in 1.1.4. Supersymmetry also includes a candidate for Cold Dark Matter.

Supersymmetry postulates a symmetry between fermions and bosons. The theory requires the invariance of the Lagrangian under a global supersymmetry transformation, hence for each fermionic degree of freedom a bosonic degree of freedom has to exist and vice versa. Since there are no candidate pairs of Standard Model particles with equal quantum numbers, except for the spin, supersymmetry requires a new partner for each Standard Model field: scalar *sfermions* as partners of the Standard Model fermions, fermionic *gauginos* as partners for the Standard Model gauge bosons and fermionic *higgsinos* as partners for the Standard Model Higgs bosons. As discussed in Section 1.1.3 the Standard Model requires only one Higgs doublet, supersymmetry, however, requires at least two Higgs doublets in order to give mass to both up and down quarks and to cancel gauge anomalies connected to the hypercharge  $Y$ . The

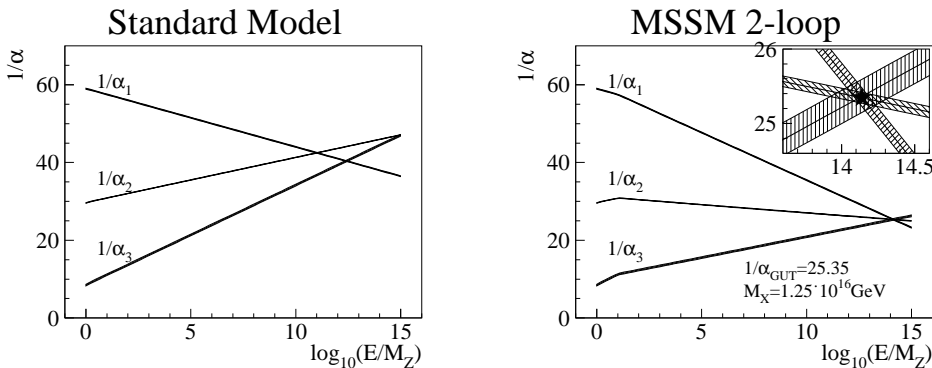


Figure 1.3: Scale dependence of the couplings in the SM (left) and in a MSSM scenario (right).

consequences of two Higgs doublets are discussed in Section 1.2.6.

Since no supersymmetric partners of the Standard Model particles have been found yet, SUSY has to be broken to allow a heavier mass for the supersymmetric particles when compared to their Standard Model partner. To maintain the above discussed advantages of a supersymmetric theory, the masses of the SUSY particles are expected to be in the range  $\mathcal{O}(100 \text{ GeV} - 1 \text{ TeV})$  and SUSY has to be broken “softly.” More details on supersymmetry breaking follow in Sections 1.2.2 and 1.2.4.

### 1.2.1 R-Parity

R-parity is defined as a multiplicative quantum number using the baryon number  $B$ , the lepton number  $L$  and the spin  $S$  of the particle:

$$R \equiv (-1)^{3B+L+2S}. \quad (1.24)$$

Using this definition all Standard Model particles have R-parity +1, while all SUSY particles have R-parity -1. The conservation of R-parity forbids lepton and baryon number violating terms in the superpotential (see discussion in Section 1.2.2 and equation 1.28) and leads to the following implications:

- Supersymmetric particles are always produced in pairs.
- There exists a lightest supersymmetric particle (LSP) which is stable.

The LSP must be neutral with respect to electromagnetic and strong interactions, since there are stringent cosmological bounds on stable light charged or colored particles. It is only weakly interacting and therefore difficult to detect. This makes the LSP an ideal candidate for Cold Dark Matter.

SUSY searches are performed in both R-parity conserving (RPC) and R-parity violating (RPV) models, since R-parity violation is not ruled out experimentally. This analysis, however, focuses on RPC scenarios.

### 1.2.2 Minimal Supersymmetric Standard Model (MSSM)

#### Particle Content of the MSSM

The minimal supersymmetric Standard Model (MSSM) has the smallest possible field content necessary to give rise to all fields of the Standard Model. An overview is given in Table 1.5, where the Standard Model particles and their respective supersymmetric partners are listed. The supersymmetric partners of quarks and leptons are called *squarks* and *sleptons*. The index  $L$  or  $R$  denote that the corresponding Standard Model particle is either left-handed or right-handed. The Higgs boson gains a fermionic partner called *Higgsino*. The gauge fields get fermionic partners. The supersymmetric partners of the

gluinos, the  $W^\pm$  and  $Z$  and the  $\gamma$  are called *gluinos*, *winos*, and *photino* (or *bino*). The common name for partners of the gauge fields is *gauginos*. Neutral higgsinos and gauginos mix to *neutralino* mass eigenstates, charged gauginos and higgsinos mix to *chargino* mass eigenstates.

### MSSM Lagrangian

Supersymmetry is based on the concept of superfields being the generator of the supersymmetric multiplets [7]. A superfield is a function on superspace, which is an extension of ordinary space-time by the inclusion of additional fermionic coordinates. There are two different kinds of superfields:

- **chiral superfields**  $\Psi = (\tilde{\psi}, \psi)$ : chiral (or scalar) superfields represent the matter fields. They contain the fermions and Higgs bosons with the resp. supersymmetric partner. A chiral superfield consists of a spin 0 field  $\tilde{\psi}$  (Higgs resp. sfermion field) and the corresponding spin  $\frac{1}{2}$  field  $\psi$  (Higgsino resp. fermion field).
- **vector superfields**  $\hat{V} = (V, \tilde{V})$ : vector superfields represent vector gauge fields and their supersymmetric partner. A vector superfield contains the spin 1 gauge field  $V$  and the corresponding spin  $\frac{1}{2}$  gaugino field  $\tilde{V}$ .

An overview of the superfields is given in Table 1.6.

The Lagrangian of the MSSM can be divided into three parts:

$$\mathcal{L}_{MSSM} = \mathcal{L}_{kin-gauge} + \mathcal{L}_W + \mathcal{L}_{soft}. \quad (1.25)$$

$\mathcal{L}_{kin-gauge}$  contains terms which are determined by the Standard Model, hence it is constructed in analogon to the Standard Model Lagrangian. This includes

R-parity: +1			R-parity: -1		
Spin	Name	Symbol	Spin	Name	Symbol
$\frac{1}{2}$	quark	$q$	0	squark	$\tilde{q}_R, \tilde{q}_L$
$\frac{1}{2}$	lepton	$l$	0	slepton	$\tilde{l}_R, \tilde{l}_L$
$\frac{1}{2}$	neutrino	$\nu$	0	sneutrino	$\tilde{\nu}$
1	gluon	$g$	$\frac{1}{2}$	gluino	$\tilde{g}$
1	photon	$\gamma$	$\frac{1}{2}$	photino	$\tilde{\gamma}$
1	W, Z boson	$W^\pm, Z$	$\frac{1}{2}$	wino, zino	$\tilde{W}^\pm, \tilde{Z}$
0	Higgs	$H^\pm, H^0$	$\frac{1}{2}$	Higgsino	$\tilde{H}_1^0, \tilde{H}_2^+$
		$h, A$			$\tilde{H}_1^-, \tilde{H}_2^0$
			$4 \times \tilde{\chi}^0$ and $2 \times \tilde{\chi}^\pm$		

Table 1.5: Overview of the SUSY particles.

the kinetic terms for scalar and fermion fields, gauge interactions and the self-interactions of the gauge fields:

$$\begin{aligned}
 \mathcal{L}_{kin-gauge} = & \sum_i \left[ (D_\mu \tilde{\psi}_i^*)(D^\mu \tilde{\psi}_i) + i \bar{\psi}_i \gamma_\mu D^\mu \psi_i \right] \\
 & + \sum_j \left[ -\frac{1}{4} F_{\mu\nu}^j F_j^{\mu\nu} + \frac{i}{2} \bar{V}_j \gamma_\mu D^\mu V_j \right] \\
 & - \sqrt{2} \sum_{i,j} g_j \left[ \tilde{\psi}_i^* T_j \bar{\psi}_i \tilde{V}_j + \text{h.c.} \right] \\
 & - \frac{1}{2} \sum_j \left[ \sum_i g_j \tilde{\psi}_i^* T_j \tilde{\psi}_i \right]^2.
 \end{aligned} \tag{1.26}$$

$D_\mu$  is the covariant derivative, while  $F_{\mu\nu}^i$  are the field strength tensors of the vector fields.  $g_j$  and  $T_j$  are coupling strength and generator of the corresponding symmetry group. The index  $i$  represents the chiral superfields, the index  $j$  the vector superfields. The first two lines correspond to the Lagrangian of the electroweak and strong interaction of the Standard Model. The third line describes the interaction of the chiral superfields with the fermionic partners of the gauge fields; the fourth line the interaction between the four scalars.

$\mathcal{L}_W$  contains all additional terms, which leave the Lagrangian supersymmetric and gauge invariant. It also contains the self-interaction of the chiral superfields.  $\mathcal{L}_W$  is described using the super potential  $W$  and has the form:

$$\mathcal{L}_W = - \sum_i \left| \frac{\partial W}{\partial \Psi_i} \right|^2 - \frac{1}{2} \sum_{i,j} \left[ \frac{\partial^2 W}{\partial \Psi_i \partial \Psi_j} \psi_i \psi_j + \text{h.c.} \right]. \tag{1.27}$$

The superpotential is a gauge invariant function of the chiral superfields  $\Psi_i$  and can be split up in a R-parity conserving (RPC) and a R-parity violating (RPV) term:

$$W = W_{RPC} + W_{RPV}. \tag{1.28}$$

Chiral superfield $\Psi$		Spin 0 ( $\tilde{\psi}$ )	Spin $\frac{1}{2}$ ( $\psi$ )	$SU(3)_C$	$SU(2)_L$	Y
Leptons	$L$	$(\tilde{\nu} \tilde{l}_L)$	$(\nu e_L)$	singlet	doublet	$-\frac{1}{2}$
	$E$	$\tilde{e}_R^*$	$e_R^\dagger$	singlet	singlet	1
Quarks	$Q$	$(\tilde{u}_L \tilde{d}_L)$	$(\tilde{u}_L \tilde{d}_L)$	triplet	doublet	$\frac{1}{6}$
	$U$	$\tilde{u}_R^*$	$u_R^\dagger$	triplet	singlet	$-\frac{2}{3}$
	$D$	$\tilde{d}_R^*$	$d_R^\dagger$	triplet	singlet	$\frac{1}{3}$
Higgs	$H_1$	$(H_1^0 H_1^-)$	$(\tilde{H}_1^0 \tilde{H}_1^-)$	singlet	doublet	$-\frac{1}{2}$
	$H_2$	$(H_2^+ H_2^0)$	$(\tilde{H}_2^+ \tilde{H}_2^0)$	singlet	doublet	$+\frac{1}{2}$
Vector superfield $\tilde{V}$		Spin 1 ( $V$ )	Spin $\frac{1}{2}$ ( $\tilde{V}$ )	$SU(3)_C$	$SU(2)_L$	Y
$U(1)_Y$	$\hat{B}$	$B$	$\tilde{B}$	singlet	singlet	0
$SU(2)_L$	$\hat{W}$	$W^a$	$\tilde{W}^a$	singlet	triplet	0
$SU(3)_C$	$\hat{G}$	$g$	$\tilde{g}$	octet	singlet	0

Table 1.6: The superfields in the MSSM with the resp. quantum numbers.

Assuming R-parity conservation the second term is set to zero:  $W_{RPV} = 0$ . The R-parity conserving term can be parametrized as<sup>2</sup>:

$$W_{RPC} = \epsilon_{ij} \left[ U \frac{\mathbf{m}_u}{v_2} Q^i H_2^j - D \frac{\mathbf{m}_d}{v_1} Q^i H_1^j - E \frac{\mathbf{m}_e}{v_1} L^i H_1^j + \mu H_1^i H_2^j \right]. \quad (1.29)$$

$\mathbf{m}_x$  can be understood as mass matrices in generation space,  $i$  and  $j$  are the indices of the weak doublets and  $v_x$  are the vacuum expectation values of the Higgs doublets.

The MSSM is regarded as an effective low-energy theory. Supersymmetry breaking occurs at a high scale and is parametrized by soft-symmetry breaking mass terms for scalar members of the chiral multiplets and for gaugino members of the vector multiplets. These terms are called “soft” mass terms because they are small enough not to re-introduce the problem of quadratic divergences. The corresponding Lagrangian  $\mathcal{L}_{soft}$ , which contains all terms that break supersymmetry, can be written as:

$$\begin{aligned} \mathcal{L}_{soft} = & - \frac{1}{2} \sum_v M_v \tilde{V}_v \tilde{V}_v + \text{h.c.} \\ & - \sum_c \mathbf{m}_c^2 |\tilde{\psi}_c|^2 + \text{h.c.} \\ & - m_{12}^2 (\epsilon_{kl} H_1^k H_2^l + \text{h.c.}) \\ & - \epsilon_{kl} (\mathbf{a}_d H_1^k \tilde{q}_L^l \tilde{d}_R^* + \mathbf{a}_u H_2^k \tilde{q}_L^l \tilde{u}_R^* + \mathbf{a}_e H_1^k \tilde{l}_L^l \tilde{e}_R^*) + \text{h.c.}. \end{aligned} \quad (1.30)$$

SUSY-breaking terms are additional Majorana masses for gauginos ( $M_v$ ), additional scalar masses ( $\mathbf{m}_c$ ) and additional bi- and trilinear couplings of the scalars. The indices  $v$  resp.  $c$  correspond to the different vector resp. chiral superfields, the indices  $i, j$  for the entries in the weak isospin doublet.  $\tilde{q}_l$  and  $\tilde{l}_L$  are the weak squark and slepton doublets,  $\mathbf{a}_x$  are complex  $3 \times 3$  matrices which parametrize the couplings between three scalars.

A closer look at the origin of the SUSY-breaking terms is presented in Section 1.2.4. As a consequence of these terms, the mass degeneracy between the Standard Model particles and their supersymmetric partners is lifted and the SUSY particles become heavy.

### Phenomenological Constraints

The SUSY-breaking terms contain more than 100 additional free parameters. This number can be reduced by a set of assumptions, which are motivated by experimental evidence: supersymmetry should observe the measured amount of CP violation and the results concerning the Kaon mixing (GIM mechanism) as well as the limits on FCNC and on the electric dipole moments of the neutron and the electron. This can be obtained most easily if the soft supersymmetry breaking parameters are real, the mass matrices are diagonal and the trilinear couplings are proportional to the Yukawa couplings [8].

---

<sup>2</sup> $\epsilon_{ij} = -\epsilon_{ji}$  and  $\epsilon_{12} = 1$

### 1.2.3 Constrained MSSM

The MSSM has many appealing characteristics and several experimentally testable predictions; however, it suffers from a large number of unknown parameters. This makes it impossible to pin down a unique theory. Using the above mentioned assumptions and embedding supersymmetry in a GUT framework results in large simplification.

Regarding the MSSM as a low-energy effective theory of a more fundamental theory at a large energy scale – as implied by the apparent unification of the coupling constants in Figure 1.3 – leads to simplifications of the soft supersymmetry breaking terms, which comply with the phenomenological constraints mentioned above. The resulting model is called the *constrained MSSM* (*cMSSM*). It is based on the MSSM, but the number of unknown parameter is reduced from 124 in the case of the MSSM to 23 (including the 18 Standard Model parameters) in case of the cMSSM. The cMSSM is based on the following assumptions at the GUT scale:

- Gaugino mass unification:  $M_i = m_{1/2}$ ,  $i = 1, 2, 3$
- Scalar mass unification:  $\tilde{M}_{Q,u,d,L,e}^2 = m_0^2$
- Common tri-linear coupling:  $A_f = A_0$ ,  $f = u, d, e$

leaving the following additional degrees of freedom:

- Ratio of the vacuum expectation values of the Higgs fields:  $\tan \beta$
- Higgs mass parameter:  $\mu$ .

The SUSY breaking parameters at the electroweak scale are calculated using renormalization group equations. As an example, Figure 1.4 shows the running of the masses with the energy  $Q$  from the GUT scale to the electroweak scale.

### 1.2.4 Supersymmetry Breaking

The MSSM leaves the question of the origin of the supersymmetry breaking terms unanswered. There are several theories for the origin of supersymmetry breaking being discussed at present, the two most popular theories being *gravity-mediated* and *gauge-mediated* supersymmetry breaking. The underlying assumption common to all supersymmetry breaking theories is that SUSY is dynamically broken in a “hidden sector,” which is distinct from the “visible sector” of the MSSM fields. A third sector, called “messenger sector,” is employed to transmit SUSY breaking from the hidden to the visible sector.

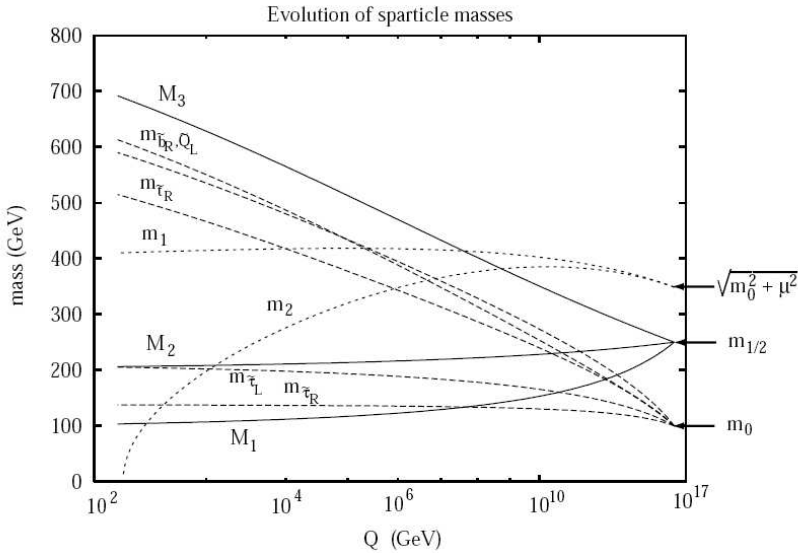


Figure 1.4: An example of the running of the soft-supersymmetry breaking parameters with  $Q$  (from Ref. [12]).

### Gravity-Mediated Supersymmetry Breaking

Gravity-mediated SUSY breaking models (SUGRA models) assume that the dynamical or spontaneous local supersymmetry breaking occurs in a hidden sector at energy scale  $\sqrt{F}$  (usually  $\sqrt{F} \gg M_W$ ), giving rise to a gravitino of mass  $m_{3/2} = \frac{F}{\sqrt{3}M_P}$ . The breaking is transmitted to the visible sector through gravity-like interactions, utilizing the fact that gravity couples to all massive fields in the hidden and visible sector. The resulting low-energy theory consists of the unbroken MSSM together with all possible soft supersymmetry breaking terms. Assuming that the couplings of all gauginos and scalars to the hidden sector superfield are equal at  $M_{GUT}$  results in a minimal Supergravity (mSUGRA) model. In this model, the SUSY degrees of freedom are reduced to four continuous and one discrete parameter, commonly chosen as:

$$m_0, m_{1/2}, A_0, \tan \beta \text{ and } \text{sign}(\mu). \quad (1.31)$$

The masses of all supersymmetric particles at electroweak scale can be calculated from these parameters using renormalization group equations. Over most of the model space,  $\mu^2$  is large (gaugino region) with the approximate relation:

$$2m_{\tilde{\chi}_1^0} \approx m_{\tilde{\chi}_2^0} \approx m_{\tilde{\chi}^\pm}. \quad (1.32)$$

mSUGRA yields to a promising SUSY breaking scenario, and the presented thesis is performed within this framework.

### Gauge-Mediated Supersymmetry Breaking

Supersymmetry breaking can also be transmitted to the MSSM sector by gauge interactions [13]. The structure of such models involves a hidden sector where

SUSY is broken, a messenger sector consisting of particles with  $SU(3) \times SU(2) \times U(1)$  quantum numbers, and the (visible) fields of the MSSM. A supersymmetry breaking spectrum in the messenger sector is generated by the direct coupling of the messengers to the hidden sector. The breaking is transmitted to the MSSM via the virtual exchange of the messengers. In GMSB models, the gravitino is the lightest SUSY particle (LSP) with a mass typically in the eV to keV range. The phenomenology is therefore determined by the next-to-lightest SUSY particle (NLSP), which can be either a neutralino or a slepton.

### 1.2.5 SUSY Mass Spectrum

As is the case for the Standard Model, the particle fields of the SUSY Lagrangian are gauge eigenstates, not mass eigenstates. The mass eigenstates are obtained by diagonalizing the mass-squared matrix. Using the phenomenological constraints (see Section 1.2.2), the sfermion mass matrices for the first generation are (using the abbreviations:  $s_W^2 \equiv \sin^2 \theta_W$  and  $Z_\beta^2 \equiv M_Z^2 \cos 2\beta$ ):

$$M_{\tilde{u},LR}^2 = \begin{pmatrix} m_Q^2 + m_u^2 + (\frac{1}{2} - \frac{2}{3}s_W^2)Z_\beta^2 & m_u(A_u - \mu \cot \beta) \\ m_u(A_u - \mu \cot \beta) & m_U^2 + m_u^2 + \frac{2}{3}s_W^2 Z_\beta^2 \end{pmatrix}, \quad (1.33)$$

$$M_{\tilde{d},LR}^2 = \begin{pmatrix} m_Q^2 + m_d^2 + (-\frac{1}{2} - \frac{1}{3}s_W^2)Z_\beta^2 & m_d(A_d - \mu \tan \beta) \\ m_d(A_d - \mu \tan \beta) & m_D^2 + m_d^2 - \frac{1}{3}s_W^2 Z_\beta^2 \end{pmatrix}, \quad (1.34)$$

$$M_{\tilde{e},LR}^2 = \begin{pmatrix} m_L^2 + m_e^2 - (\frac{1}{2} - s_W^2)Z_\beta^2 & m_e(A_e - \mu \tan \beta) \\ m_e(A_e - \mu \tan \beta) & m_E^2 + m_e^2 - s_W^2 Z_\beta^2 \end{pmatrix}, \quad (1.35)$$

$$M_{\tilde{\nu}}^2 = m_L^2 + \frac{1}{2}s_W^2 Z_\beta^2. \quad (1.36)$$

The parameters  $m_L$ ,  $m_E$  etc. are the explicit mass terms in the soft SUSY-breaking Lagrangian  $\mathcal{L}_{soft}$ . The remaining terms are a consequence of the coupling to a Higgs field in  $\mathcal{L}_{SUSY}$  or  $\mathcal{L}_{soft}$ . The off-diagonal terms in each mass matrix are proportional to the mass of the corresponding Standard Model partner, hence they introduce a mixing between the two sfermion chirality states. The effect can be neglected for the first two generations due to the small mass of the Standard Model partner. For the third generation however, the mixing can have a significant impact on the resulting mass terms. This is of importance for the trilepton analysis, and a more detailed discussion of the mixing effects follows in Chapter 6.

The neutral higgsinos and the fermion partners of the neutral  $B$  and  $W^3$  gauge bosons mix to *neutralino* mass eigenstates. Using the abbreviations  $s_\beta \equiv \sin \beta$ ,  $c_\beta \equiv \cos \beta$ ,  $s_W \equiv \sin \theta_W$  and  $c_W \equiv \cos \theta_W$ , the mass matrix is given by (in the basis  $\tilde{B}$ ,  $\tilde{W}^3$ ,  $\tilde{H}_1^0$ ,  $\tilde{H}_2^0$ ):

$$M_{\tilde{\chi}^0} = \begin{pmatrix} M_1 & 0 & -c_\beta s_W M_Z & +s_\beta s_W M_Z \\ 0 & M_2 & +c_\beta c_W M_Z & -s_\beta c_W M_Z \\ -c_\beta s_W M_Z & +c_\beta c_W M_Z & 0 & -\mu \\ +s_\beta s_W M_Z & -s_\beta c_W M_Z & -\mu & 0 \end{pmatrix}. \quad (1.37)$$

The charged higgsinos and the charged gauginos mix to *chargino* mass eigenstates. The chargino mass matrix is given by (in the basis  $\tilde{W}^+$ ,  $\tilde{H}_2^+$ ,  $\tilde{W}^-$ ,  $\tilde{H}_1^-$ ):

$$M_{\tilde{\chi}^\pm} = \begin{pmatrix} 0 & X^T \\ X & 0 \end{pmatrix} \quad \text{with } X = \begin{pmatrix} M_2 & \sqrt{2}s_\beta M_W \\ \sqrt{2}c_\beta M_W & \mu \end{pmatrix}. \quad (1.38)$$

The chargino masses follow by diagonalizing:

$$\begin{aligned} m_{\tilde{\chi}_{1,2}^\pm}^2 &= \frac{1}{2} [ |M_2|^2 + |\mu|^2 + 2 M_W^2 \\ &\mp \sqrt{(|M_2|^2 + |\mu|^2 + 2 M_W^2)^2 - 4 |\mu M_2 - M_W^2 \sin 2\beta|^2} ] . \end{aligned} \quad (1.39)$$

### 1.2.6 Higgs Sector in the MSSM

The Higgs sector in the MSSM is based on two Higgs doublets. This is necessary to generate the masses of the up- and down-type fermions within the MSSM and to avoid gauge anomalies [14]. The first Higgs doublet carries hypercharge +1 and couples to up-type fermions, while the second Higgs doublet carries hypercharge -1 and couples to down-type fermions:

$$H_1 = \begin{pmatrix} H_1^0 \\ H_1^- \end{pmatrix}, \quad H_2 = \begin{pmatrix} H_2^+ \\ H_2^0 \end{pmatrix}. \quad (1.40)$$

The vacuum expectation values of the Higgs doublets are:

$$\langle H_1 \rangle = \begin{pmatrix} v_1 \\ 0 \end{pmatrix}, \quad \langle H_2 \rangle = \begin{pmatrix} 0 \\ v_2 \end{pmatrix}. \quad (1.41)$$

Before symmetry breaking, the two complex Higgs doublets have 8 degrees of freedom. Three of these are absorbed to give the W and Z bosons their masses, leaving 5 physical degrees of freedom. These are:

- two charged Higgs bosons:  $H^\pm$ ,
- one CP-odd neutral (pseudoscalar) Higgs boson:  $A$ ,
- two CP-even neutral (scalar) Higgs bosons:  $h, H$  ( $h$  denotes the lighter of the two).

Most of the experimental investigations are interpreted assuming CP conservation in the Higgs sector. In such scenarios the three neutral Higgs bosons are CP eigenstates as described above. However, CP violation in the Higgs sector cannot be excluded a priori [15]. Scenarios with CP violation are theoretically appealing since they provide one of the ingredients needed to explain the observed cosmic matter-antimatter asymmetry (the observed size of CP violation in the Standard Model is not sufficient). Substantial CP-violating effects can be

MSSM Higgs	$d\bar{d}, s\bar{s}, b\bar{b}, e^+e^-, \mu^+\mu^-, \tau^+\tau^-$	$u\bar{u}, c\bar{c}, t\bar{t}$	$ZZ, WW$
$h$	$-\frac{\sin \alpha}{\cos \beta}$	$\frac{\cos \alpha}{\sin \beta}$	$\sin(\beta - \alpha)$
$H$	$\frac{\cos \alpha}{\cos \beta}$	$\frac{\sin \alpha}{\sin \beta}$	$\cos(\beta - \alpha)$
$A$	$-ig \tan \beta$	$-ig \cot \beta$	0

Table 1.7: MSSM correction factors to Higgs boson couplings with respect to the Standard Model couplings to fermions and massive gauge bosons at leading order (from Ref. [16]).

induced in the MSSM by radiative corrections, especially from third-generation squarks. In CP-violating scenarios, the three neutral Higgs mass eigenstates are mixtures of CP-even and CP-odd fields, hence their production and decay properties may be widely different compared to CP conserving scenarios. For this analysis, CP conservation in the Higgs sector is assumed.

The ratio of the vacuum expectation values of the two Higgs doublets,  $\tan \beta$ , is given by:

$$\tan \beta = \frac{v_2}{v_1}. \quad (1.42)$$

The Higgs mass spectrum is determined by only two parameters, commonly chosen to be the mass of the pseudoscalar Higgs boson  $m_A$  and  $\tan \beta$ . At leading order the masses of the remaining Higgs bosons are given by:

$$m_{H,h}^2 = \frac{1}{2} \left[ (m_A^2 + m_Z^2) \pm \sqrt{(m_A^2 + m_Z^2)^2 - 4m_A^2 m_Z^2 \cos^2 2\beta} \right], \quad (1.43)$$

$$m_{H^\pm}^2 = m_A^2 + m_W^2. \quad (1.44)$$

The couplings for the neutral Higgs bosons to fermions and massive gauge bosons at tree level are obtained from the Standard Model Higgs couplings (see Table 1.4) multiplied with the correction factors shown in Table 1.7. The mixing angle  $\alpha$  ( $-\frac{\pi}{2} < \alpha < 0$ ) is required to diagonalize the Higgs mass matrix and is given by:

$$\cos 2\alpha = -\cos 2\beta \cdot \frac{m_A^2 - m_Z^2}{m_H^2 - m_h^2}. \quad (1.45)$$

The tree level formulas for the Higgs boson masses and couplings are subject to large radiative corrections, which are dominated by the exchange of virtual top and bottom quarks and squarks in the loop diagrams. The upper limit on the mass of the lightest Higgs boson  $m_h$ , which is bound to  $m_h \leq M_Z$  at leading order, is shifted towards  $m_h \leq 135$  GeV for  $m_t = 175$  GeV and  $M_{SUSY} = 1$  TeV by including calculations up to the 2-loop level [17].  $M_{SUSY}$  stands for the energy scale of the supersymmetry breaking; it is assumed to be a common mass parameter for all sfermions at the electroweak scale.

For high values of  $\tan \beta$ , the  $A$  and  $H$  are degenerated regarding their mass and couplings. Requiring  $\tan \beta > 10$ , the couplings to down-type quarks and leptons

	$m_{SUSY}$ [GeV]	$\mu$ [GeV]	$M_2$ [GeV]	$X_t$ [GeV]	$m_{\tilde{g}}$ [GeV]
$m_h^{max}$	1000	$\pm 200$	200	2000	800
no-mixing	2000	$\pm 200$	200	0	800

Table 1.8: Values of the SUSY parameters for the benchmark scenarios that are used in this analysis (from Ref. [17]).

are strongly enhanced, while those to up-type quarks and massive gauge bosons are suppressed. Hence, the leading decay modes of  $A/H$  are  $b\bar{b}$  ( $\sim 90\%$ ) and  $\tau^+\tau^-$  (8-10%). The enhanced coupling to  $b$  quarks for high  $\tan\beta$  is important for the production of  $A/H$ : the dominating production channel is the associated  $bbH/A$  production. A more detailed discussion of the phenomenology follows in Chapter 7.

### Benchmark Scenarios

Due to the large number of free parameters in the MSSM, different benchmark scenarios suitable for the MSSM Higgs boson search have been proposed for interpretation of the results [17]. As discussed above, the masses and couplings of the neutral MSSM Higgs bosons depend, in addition to  $\tan\beta$  and  $m_A$ , on the SUSY parameters through radiative corrections. In a constrained model, were unification of SU(2) and U(1) gaugino masses is assumed, the most relevant parameters are the trilinear coupling in the stop sector ( $A_t$ ), the Higgs mass parameter ( $\mu$ ), the gaugino mass term ( $M_2$ ), the gluino mass ( $m_{\tilde{g}}$ ) and a common scalar mass ( $M_{SUSY}$ ). Instead of  $A_t$ , the stop mixing parameter  $X_t := A_t - \mu \cot\beta$  is usually used. The two important benchmark scenarios, which were also used in the LEP II Higgs boson searches [18], are:

- *$m_h$ -max scenario*: the parameters are chosen such that the maximum possible Higgs boson mass as a function of  $\tan\beta$  is obtained. For fixed  $M_2$ ,  $\mu$ ,  $m_{SUSY}$  and  $m_g$  this is achieved by adjusting  $X_t$ . This model provides the largest parameter space and therefore the most conservative exclusion bounds.
- *no-mixing scenario*: this scenario is associated with vanishing mixing in the  $\tilde{t}$  sector (by setting  $X_t = 0$ ) and with a higher SUSY mass scale as compared to the  $m_h$ -max scenario, resulting in a relatively restricted MSSM parameter space. This scenario typically gives a small mass for the lightest Higgs boson  $h$ .

The values of the SUSY parameters for the two benchmark scenarios are listed in Table 1.8. Both scenarios are examined with positive and negative sign of the Higgs mass parameter  $\mu$ .

### 1.2.7 Search for Supersymmetry

So far no evidence for supersymmetry has been found experimentally. SUSY searches have been performed as direct searches in  $e^+e^-$  collisions at LEP and in  $p\bar{p}$  collisions at DØ and CDF, but additional constraints on supersymmetry exist from indirect searches (e.g. anomalous magnetic moment of the muon [24]) and cosmology. The following subsections present a brief overview of some results, which are of interest for this thesis.

#### Direct searches for MSSM particles

The search for supersymmetric particles at LEP II by the four LEP collaborations (ALEPH, DELPHI, L3 and OPAL) has resulted in stringent mass limits, which are then interpreted within a specific SUSY model in order to constrain the parameter space of the model. Figure 1.5a shows the part of the  $m_{\tilde{l}_R} - m_{\tilde{\chi}_1^0}$  plane which is excluded by direct searches of the LEP experiments. The following mass limits have been established for large  $\tilde{l}$ -LSP mass differences [25]:  $m_{\tilde{e}_R} > 99$  GeV,  $m_{\tilde{\mu}_R} > 94$  GeV and  $m_{\tilde{\tau}_R} > 86$  GeV. Figure 1.5b shows the lower limit on the mass of the lightest chargino ( $\tilde{\chi}_1^+$ ) as a function of the sneutrino mass ( $m_{\tilde{\nu}}$ ). For large slepton/sneutrino masses, chargino masses are excluded nearly up to the kinematic production threshold of 104 GeV at LEP II [26]. Limits on  $\tilde{\chi}_1^+$  by DØ [22] and CDF [23] using Run I data are not competitive.

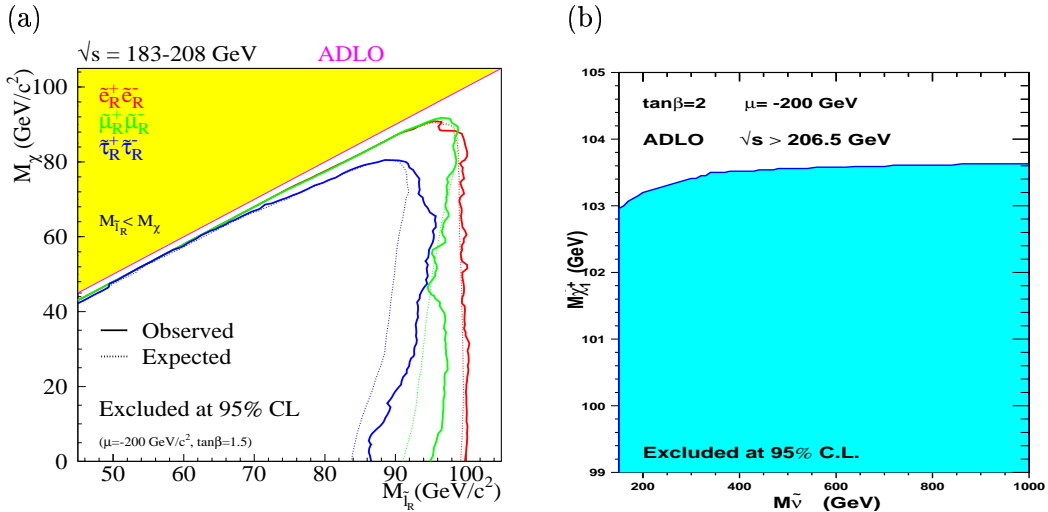


Figure 1.5: LEP combined lower limits in a constraint MSSM (a) on the slepton masses as a function of the mass of the lightest neutralino and (b) on the chargino mass as a function of the sneutrino mass.

#### Search for MSSM Higgs bosons

The four LEP collaborations have searched for neutral Higgs bosons within the MSSM framework. Since no excess of events has been observed, absolute limits

are set on the masses of neutral Higgs bosons, leading to lower mass limits on  $m_h$  and  $m_A$  for low values of  $\tan \beta$  [18]. The Tevatron experiments CDF and DØ have searched for neutral Higgs bosons in recent Run II data. These searches are complementary to the LEP search, providing sensitivity in the large  $\tan \beta$  region. CDF has performed an analysis using  $\mathcal{L} = 310 \text{ pb}^{-1}$ , searching for neutral Higgs bosons decaying into tau pairs [19]. DØ has performed a search for neutral Higgs bosons produced in association with bottom quarks using  $\mathcal{L} = 260 \text{ pb}^{-1}$  [20]. Both results agree with Standard Model expectations, and upper limits on the production cross section have been set.

A detailed discussion of these results and a comparison to the present analysis follows in Chapter 7.

*1 Theoretical Aspects*

---

## 2 Experimental Apparatus

Fermi National Accelerator Laboratory (FNAL) [28] near Chicago is home of the Tevatron collider [27]. Protons and antiprotons are accelerated and collide at a center-of-mass energy of  $\sqrt{s} = 1.96$  TeV. Until the startup of the LHC [29] at CERN [30] (Geneva) in 2007, where proton-proton collision at a center-of-mass energy of 14 TeV will be studied using dedicated experiments, Tevatron remains the world's highest energy particle accelerator. The two multi-purpose experiments CDF [31] and DØ [32] are located along the Tevatron ring and analyze the  $p\bar{p}$  collisions.

The first data taking period (Run I) from 1992 to 1996 ended successfully with the discovery of the top quark. During Run I, each experiment collected an integrated luminosity of about  $\mathcal{L} = 120 \text{ pb}^{-1}$  at a center-of-mass energy of 1.8 TeV. The second period of data taking (Run II) started in 2001, after an extensive upgrade of both the accelerator and the two experiments. Since then, each experiment has collected data corresponding to  $\mathcal{L} \approx 1 \text{ fb}^{-1}$ . By the end of Run II, an integrated luminosity of  $8 \text{ fb}^{-1}$  is expected for each experiment.

This analysis is based on data collected from April 2002 to June 2004 by the DØ detector. The following chapter describes the basic units and the coordinate system that are used throughout this thesis, the accelerator chain used for Run II and the DØ detector, whose data has been analyzed.

### 2.1 Units and Coordinate System

The total number of times a given process occurs ( $N$ ) is proportional to the cross-section of the process ( $\sigma$ ) and the integrated luminosity ( $\mathcal{L}$ ):

$$N = \sigma \cdot \mathcal{L}. \quad (2.1)$$

The integrated luminosity is the integral over time of the instantaneous luminosity  $L$ :  $\mathcal{L} = \int L dt$ . Since the cross-section of a process is fixed for a given center-of-mass energy and particle beam type, the goal of the accelerator is to maximize the integrated luminosity delivered to the experiments. The cross-section has the dimension of an area and is usually expressed in *barn*:

$$1 \text{ barn} = 1 \text{ b} = 10^{-24} \text{ cm}^2. \quad (2.2)$$

Typical cross-sections for interesting physical processes at the Tevatron are of the order of pico-barns (pb), thus the integrated luminosity is often expressed

## 2 Experimental Apparatus

---

in inverse pico-barns,  $\text{pb}^{-1}$ . Assuming that two bunches containing  $n_1$  and  $n_2$  particles collide with the frequency  $f$ , the luminosity is approximately given by:

$$L = f \frac{n_1 \cdot n_2}{4\pi\sigma_x\sigma_y}. \quad (2.3)$$

$\sigma_x$  and  $\sigma_y$  characterize the Gaussian transverse beam profiles in the horizontal and vertical directions. Using the luminosity, the event rate  $R = \frac{dN}{dt}$  is given by  $R = \sigma L$ .

Throughout this analysis, standard spherical coordinates are used to describe the positions of particles:  $r$ ,  $\phi$  (azimuthal) and  $\theta$ . The system is centered at the interaction region, at the center of the detector. The  $z$  direction is defined along the beam-line, the  $y$ -axis is pointing upward. Instead of the polar angle  $\theta$ , the pseudo-rapidity  $\eta$  is usually used to describe the position of particles. The pseudo-rapidity is defined as:

$$\eta = -\ln(\tan \frac{\theta}{2}). \quad (2.4)$$

The pseudo-rapidity is an approximation for the true rapidity  $y$  for finite angles in the massless limit ( $\frac{m}{E} \approx 0$ ):

$$\eta = \frac{1}{2} \ln \frac{2 \cos^2 \frac{\theta}{2}}{2 \sin^2 \frac{\theta}{2}} = \frac{1}{2} \ln \frac{E(1 - \cot \theta)}{E(1 - \cos \theta)} \approx \frac{1}{2} \ln [(E + p_z)(E - p_z)] = y. \quad (2.5)$$

The number of particles, which result from high-energy particle collisions, is roughly constant as a function of  $\eta$ , assuming identical beam energies and particle types. The position of a particle can be described either with respect to the vertex position using *physics*- $\eta$  ( $\eta_{phys}$ ) or with respect to the center of the detector using *detector*- $\eta$  ( $\eta_{det}$ ). The vertex position is the interaction point where the two beams collide. The separation of objects is usually measured in terms of  $\Delta\mathcal{R}$ :

$$\Delta\mathcal{R} = \sqrt{(\Delta\phi)^2 + (\Delta\eta)^2}. \quad (2.6)$$

## 2.2 Fermilab Accelerator Chain

The Fermilab accelerator chain consists of numerous stages of acceleration and storage to prepare protons and antiprotons for injection into the last stage, the Tevatron. A schematic overview of the whole accelerator chain is shown in Figure 2.1.

In the first stage, protons are accelerated as  $H^-$  ions to 0.75 MeV using a *Cockcroft-Walton* accelerator. A linear accelerator (*LINAC*) accelerates the hydrogen ions to 400 MeV, after which they pass through a carbon foil to strip off the electrons, leaving only the protons. A circular synchrotron, called *Booster*, is used to group the protons into bunches and to accelerate them to 8 GeV. In the next step, proton bunches are transferred to the *Main Injector*, where

they are accelerated to 150 GeV. Antiprotons are produced in a hadronic reaction by shooting proton bunches from the Main Injector at a nickel/copper target. Only 15 antiprotons are collected from every million protons on target, making this the limiting factor for increasing the luminosity at the Tevatron. The bunch structure of the antiprotons, remnant from the Main Injector proton bunches, is removed in the *Debuncher*. In addition, the antiprotons are also stochastically cooled and their energies made uniform. The *Accumulator* is used to store the antiprotons. A crucial part in increasing the antiproton rate has the *Recycler*, a storage ring which is located in the Main Injector tunnel directly above the Main Injector beamline. The Recycler ring provides more antiprotons for the Tevatron by acting as a post-accumulator and receptacle for recycled antiprotons from the previous collider store. When a sufficient number of antiprotons is available in the Accumulator (typically about  $150 - 200 \times 10^{10}$  antiprotons), 36 bunches of protons from the Main Injector are loaded into the Tevatron at 150 GeV. Four bunches of antiprotons at a time are transferred to the Main Injector, where they are accelerated to 150 GeV and injected into the Tevatron synchrotron. After 36 bunches of antiprotons have been injected into the Tevatron, both proton and antiproton bunches are accelerated to the

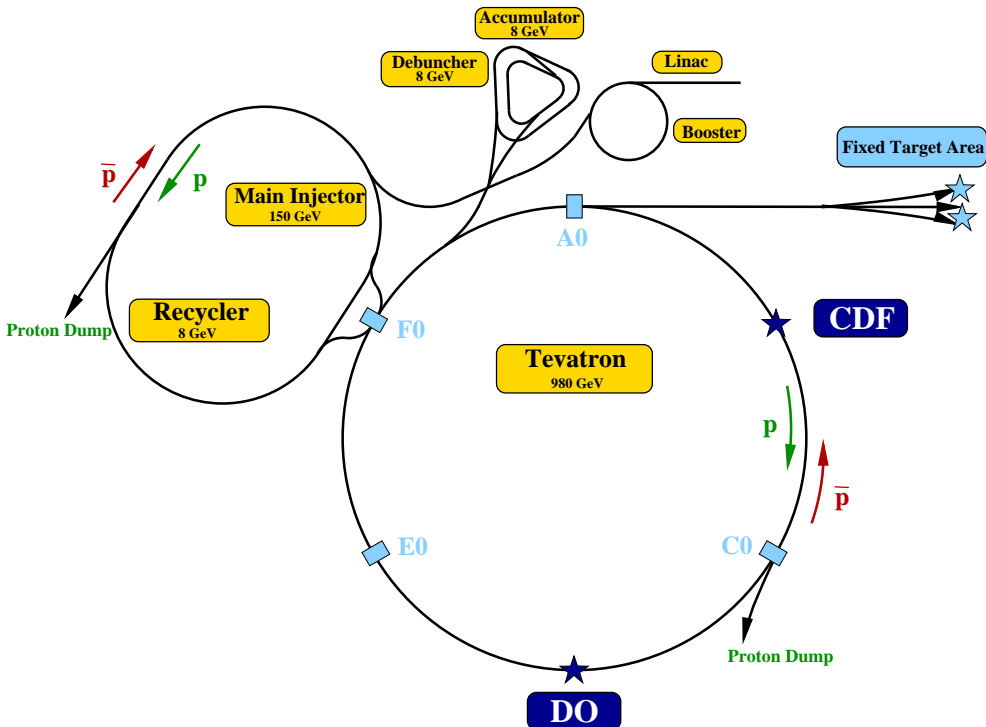


Figure 2.1: Schematic view of the Fermilab accelerator chain, showing the different acceleration stages and the two multi-purpose experiments DØ and CDF. The Tevatron is the last stage of a chain of accelerators and has a circumference of 6.3 km.

maximum beam energy of 980 GeV.

In the Tevatron, protons and antiprotons are arranged into three *super bunches* separated by 2.6  $\mu$ s. Each super bunch is composed of 12 bunches, separated by 396 ns. The length of each bunch is about 60 cm, which corresponds to 2 ns. The beam half-life is about 9-10 hours, and collisions are recorded for typically about 20 hours. The beams are collided at two interaction points where the multi-purpose experiments CDF and D $\emptyset$  are located, resulting in p $\bar{p}$  collisions at a center-of-mass energy of 1.96 TeV. Eventually the beams are dumped intentionally because of decreased beam currents and focus, which results in an exponentially decreasing luminosity.

### 2.3 D $\emptyset$ Detector

The D $\emptyset$  detector is a multi purpose detector that uses dedicated subsystems to identify and precisely measure photons, electrons, muons, neutrinos (in the form of missing transverse energy) and jets of quarks and gluons. The setup follows the classical collider detector design, where the subdetectors are arranged cylindrically around the interaction point. The detector has been significantly upgraded for Run II of the Tevatron collider. This upgrade was necessary to fully take advantage of the improvements done to the accelerator system. During Run I, the Tevatron operated using six bunches of each proton and antiprotons, with 3500 ns spacing between bunch crossings and a center-of-mass energy of 1.8 TeV.

Figure 2.2 shows a side view of the upgraded D $\emptyset$  detector. The detector consists of three major subsystems, which will be described briefly in the following Chapters: the central tracking system, the calorimeter system, and the muon spectrometer. In addition, a brief introduction to the trigger and data acquisition system is given. A complete description of the original Run I detector can be found in Ref. [36]. The upgraded Run II detector is described in detail in Ref. [37].

#### 2.3.1 Tracking System

The purpose of the tracking system is to measure the trajectories of charged particles produced in a collision and to determine the primary interaction vertex. A charged particle with momentum  $p$  in a solenoidal magnetic field of strength  $B$  along the  $z$  direction will travel on a helix with radius  $r$  given by:

$$r[m] = \frac{p_T[\text{GeV}]}{0.3 \cdot B[\text{T}]}. \quad (2.7)$$

The D $\emptyset$  tracking system consists of the silicon microstrip tracker (SMT) and the central fiber tracker (CFT) surrounded by a superconducting, 2 Tesla solenoidal magnet. Its performance is of vital importance for the two analyses presented

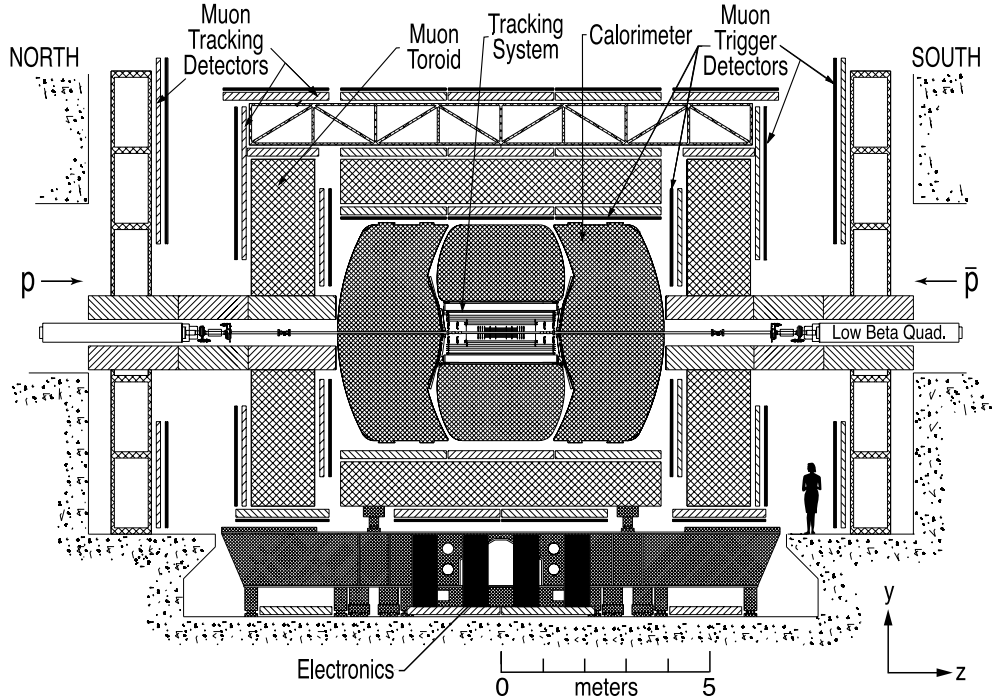


Figure 2.2: Diagram of the upgraded DØ detector (from Ref. [36]). The side view is taken from inside the Tevatron ring.

in this thesis, since both the electron and tau reconstruction rely heavily on it (see discussion in Chapter 4). A schematic view of the central tracking system is shown in Figure 2.3.

### Silicon Microstrip Tracker (SMT)

The SMT is the innermost tracking detector, starting at a radius of 2.7 cm. The design was driven to cover the length of the interaction region ( $\sigma \approx 25$  cm) and to provide both tracking and vertexing over nearly the full  $\eta$  coverage of the calorimeter and muon systems. Figure 2.4 provides an isometric view of the SMT.

In the central region ( $|z| < 53$  cm), the detector consists of six barrel modules; each barrel being capped at high  $|z|$  with a disk of twelve double-sided wedge detectors (*F-disk*). Each barrel module consists of four silicon readout layers. Layer 1 and 2 are equipped with 12 double-sided silicon readout modules (called *ladder*), layer 3 and 4 with 24 modules. Forward of each disk/barrel assembly is a unit consisting of three F-disks. Two large-diameter disks (*H-disks*) provide tracking in the far forward regions at high  $|\eta|$  (110 cm and 120 cm from the detector center).

The barrel detectors primarily measure the  $r - \phi$  coordinate, while the disk

## 2 Experimental Apparatus

---

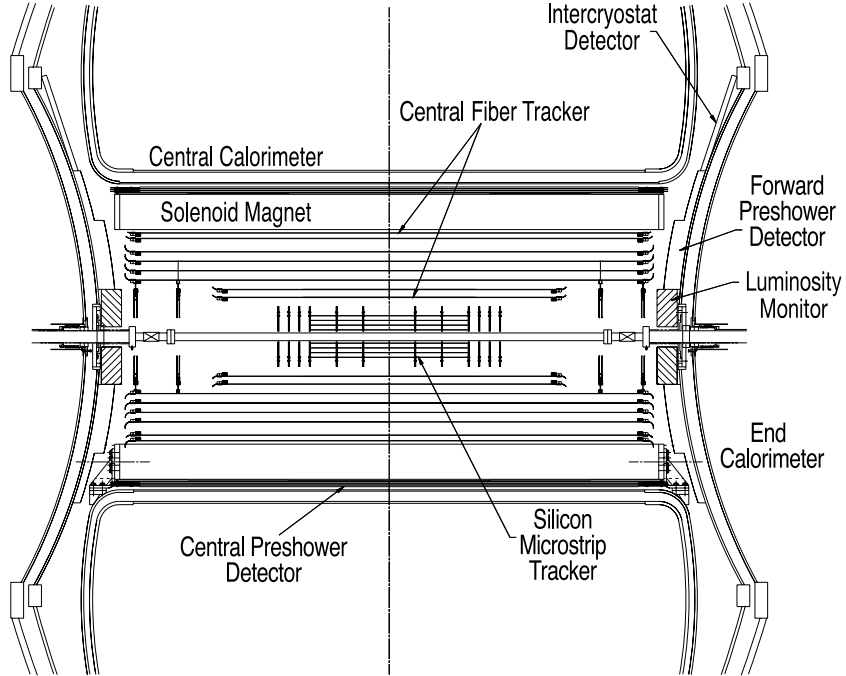


Figure 2.3: The central tracking system (from Ref. [37]).

detectors measure  $r - z$  as well as  $r - \phi$ . Hence vertices for high- $\eta$  particles are reconstructed in three dimensions by the disks, and vertices of small- $\eta$  particles are measured in the barrels and the central fiber tracker.

### Central Fiber Tracker (CFT)

The CFT (Figure 2.3) surrounds the SMT and provides tracking up to  $|\eta_{det}| < 1.6$ . It consists of scintillating fibers mounted on eight concentric support cylinders, occupying the radial space from 20 to 52 cm from the center of the beam pipe. The scintillating fibers are  $835\text{ }\mu\text{m}$  in diameter and either 1.66 m (two innermost cylinders) or 2.52 m (outer six cylinders) long. The fibers are optically connected to clear fiber waveguides, which carry the scintillation light to visible light photon counters (VLP Cs) for read out. Each cylinder supports one doublet layer of fibers oriented along the beam direction ( $z$ ) and a second doublet layer at a stereo angle of  $+3^\circ$  ( $u$ ) or  $-3^\circ$  ( $v$ ). From the smallest cylinder outward, the fiber orientation is  $zu-zv$  in alternating mode.

The CFT has a total of 76,800 readout channels. Signals from doublet layers along the beam direction are used to form a fast hardware trigger based upon the number of track candidates above a specific  $p_T$ -threshold. More details on the trigger system follow in Section 2.3.7.

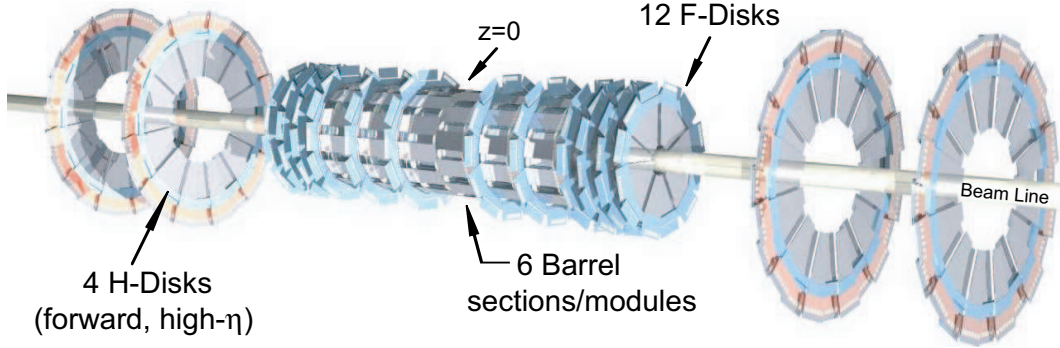


Figure 2.4: Schematic 3D view of the silicon microstrip detector (SMT), showing the disk/barrel design (from Ref. [37])

### Solenoid Magnet

The solenoid magnet surrounds the CFT at a radius of 60 cm and has a length of 2.7 m. It provides a uniform magnetic field of 2 T inside the tracking volume and consists of two concentric coils of superconducting Cu:NbTi cable. The magnet is operated with a current of 4.7 kA at a temperature of 10 K and has a stored energy of 5 MJ. The superconducting solenoid coil plus cryostat wall has a thickness of about 1 electromagnetic interaction length ( $X_0$ ) at  $\eta_{det} = 0$ .

#### 2.3.2 Preshower Detectors

The preshower detectors operate as calorimeters as well as tracking detectors, enhancing the spatial matching resolution between tracks and electromagnetic showers. They can be used to correct the electromagnetic energy measurement of the calorimeter system for losses in the solenoid and upstream material, such as cables and supports. Preshower information is also used in the trigger system due to the fast energy and position measurements.

The central preshower detector (CPS) covers the region  $|\eta_{det}| < 1.3$  and is located between the solenoid and the central calorimeter. The forward preshower detectors (FPS) cover  $1.5 < |\eta_{det}| < 2.5$  and are attached to the faces of the end calorimeters. Both detectors are made from triangular strips of scintillator, which are arranged in a way that there is no dead space between the strips. The CPS consists of three concentric cylindrical layers of scintillator strips. The three layers are arranged in an axial- $u$ - $v$  geometry, with a  $u$  resp.  $v$  stereo angle of  $+24^\circ$  resp.  $-24^\circ$ . The combined electromagnetic radiation length of the solenoid and the CPS is about  $2X_0$ .

Each of the two FPS detectors (north and south) is made of two double layers of scintillator strips, which are separated by a  $2X_0$ -thick lead-stainless steel absorber. The layers in front of the absorber are referred to as the minimum ionizing particle (MIP) layers, while the layers behind the absorber are called

## 2 Experimental Apparatus

---

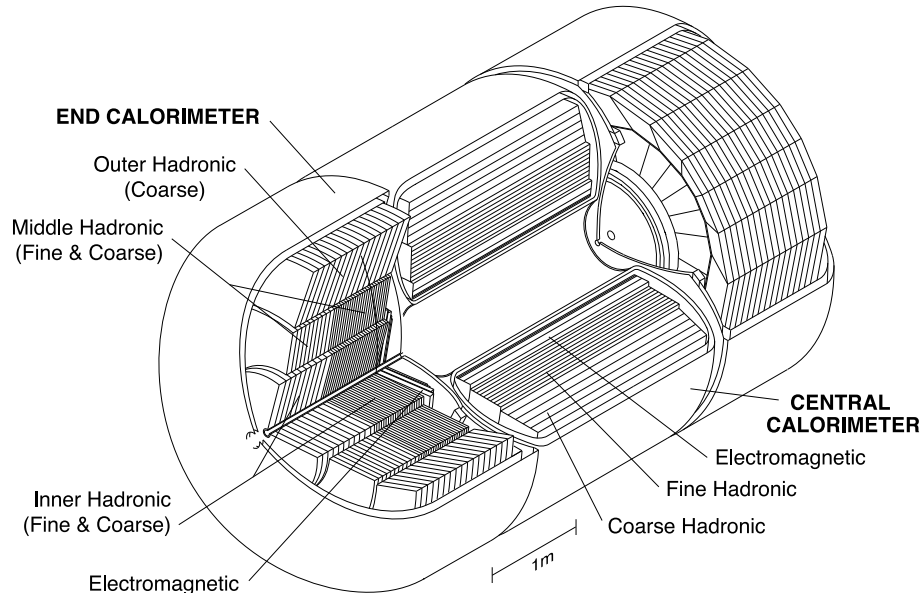


Figure 2.5: Isometric view of the central and two end calorimeters (from Ref. [37]).

shower layers. All charged particles passing through the detector will produce a hit in the MIP layer, allowing measurement of the location (in  $\eta$ ,  $\phi$  and  $z$ ) of the track. Electrons most likely start showering in the absorber, leading to a cluster of energy in the shower layer that is matched to the signal in the MIP layer. Photons will not generally interact in the MIP layer, but produce a shower signal in the shower layer. Muons and hadrons are less likely to shower in the absorber, hence producing a second hit signal in the shower layer.

For the data used in this analysis the preshower detectors were not fully included in both online triggering and offline reconstruction, hence their information is not used.

### 2.3.3 Calorimeter System

The calorimeter system provides the energy measurement for electrons, photons and hadrons in the form of jets. By measuring electromagnetic and hadronic shower characteristics like longitudinal profile, width and isolation it assists in the identification of electron, photons, jets and muons. The full coverage in  $\phi$  allows to establish the transverse energy balance in an event.

The DØ calorimeter system consists of three uranium/liquid-argon calorimeters and the intercryostat detector, which are described briefly in the following. A good performance of the calorimeter system is essential for this analysis, which relies on an efficient reconstruction of electrons and hadronic tau decays.

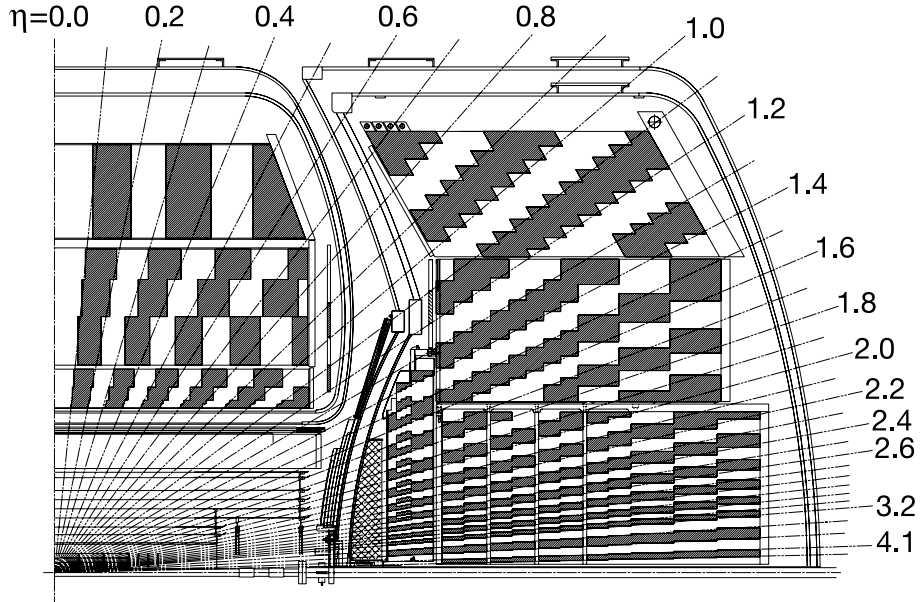


Figure 2.6: Schematic view of a portion of the  $D\emptyset$  calorimeter showing the transverse and longitudinal segmentation pattern (from Ref. [37]).

### Liquid Argon Calorimeter

The calorimeters are shown in Figure 2.5. The central calorimeter (CC) covers  $|\eta_{det}| \lesssim 1.1$ , and the two end calorimeters ECN (north) and ECS (south) extend the coverage up to  $|\eta_{det}| \lesssim 4$ . Each calorimeter contains an electromagnetic section closest to the interaction region followed by fine and coarse hadronic sections. Liquid argon is used as the active medium for all of the calorimeters, and each is located within a cryostat that keeps the temperature of the liquid argon at approximately 80 K. Calorimeter cells are the basic building blocks of the pseudo-projective towers shown in Figure 2.6, with each tower subdivided in depth. The towers in both electromagnetic and hadronic modules are  $\Delta\eta_{det} \times \Delta\phi = 0.1 \times 0.1$ . Cell boundaries in the central region lead to small non-sensitive regions in each layer, which are called  $\phi$ -cracks.

The electromagnetic section (EM) of the central calorimeter has four cylindrical floors (EM1-4) representing  $2 + 2 + 7 + 10$  radiation lengths at  $\eta_{det} = 0$ . The granularity of the cells in the third electromagnetic layer (EM3), where the maximal energy deposition of the electromagnetic shower is expected, is doubled in both  $\eta$  and  $\phi$  ( $0.05 \times 0.05$  in  $\eta$ - $\phi$ ). This allows a precise measurement of the location and size of the shower.

## 2 Experimental Apparatus

---

The hadronic section in the central calorimeter corresponds to a thickness of about 7 hadronic interaction lengths and is divided into four cylindrical floors (FH1-3 and CH). The innermost layer (FH1) is included in the identification of electromagnetic objects since it allows to sample the energy deposition in the tail of the electromagnetic shower.

The electromagnetic section in the end calorimeters is built in the same way as in the central part. The four floors represent  $0.3 + 2.6 + 8 + 9$  radiations lengths. The cell granularity corresponds to the one in the central calorimeter for  $|\eta_{det}| < 2.6$ . The cell size increases with increasing  $\eta$  up to a maximum value of  $0.4 \times 0.4$  for  $|\eta_{det}| \approx 4.0$  to avoid very small cells.

The hadronic section in the end calorimeters is arranged into three modules. The two inner hadronic modules are cylindrical, consisting each of a fine hadronic and a coarse hadronic portion (see Figure 2.5). The *Inner Hadronic* consists of four fine hadronic and one coarse hadronic layer. The thickness is  $4 \times 1.1 + 4.1$  hadronic interaction lengths. The *Middle Hadronic* consists of four fine hadronic and one coarse hadronic layer and has a thickness of  $4 \times 0.9 + 4.4$  hadronic interaction lengths. The *Outer Hadronic* modules have a maximum thickness of 6 hadronic interaction lengths.

The calorimeter system has approximately 47,000 readout channels. The signals from the calorimeter cells are amplified and shaped in the preamplifiers, located on the cryostats, before being sent to the signal shaping and analog storage circuits, where the signals are shaped and sampled at the peak. Baseline subtraction is performed in order to remove low frequency noise or pile-up present in the signal. Analog sums of the signal provide prompt inputs to the trigger system, while the signal is meanwhile kept in an analog buffer awaiting trigger decision. More details on the trigger system follow in Section 2.3.7.

### Intercryostat Region

The calorimeter system provides incomplete coverage in the region  $0.8 < |\eta_{det}| < 1.4$ , as can be seen in Figure 2.6. The gap between the central and endcap cryostat is needed for the supply lines and cabling of the tracking system. There is a substantial amount of unsampled material in this region, degrading the energy resolution. This is addressed by additional layers of sampling within this region. Single-cell structures without absorber, called *massless gaps*, are located inside the CC and EC cryostat walls. In addition, the intercryostat detector (ICD) provides scintillator sampling in the region  $1.1 < |\eta_{det}| < 1.4$ , where no electromagnetic calorimeter is instrumented. The ICD consists of a series of scintillating tiles, each tile covering an area of  $\Delta\eta \times \Delta\phi = 0.3 \times 0.3$ .

#### 2.3.4 Muon Spectrometer

For triggering and precise measurements of muons, DØ uses a dedicated muon spectrometer. Muons, in contrast to other charged particles and hadrons, pass

through the calorimeter leaving a MIP signal and are detected in the muon system that surrounds the calorimeter. Hence a muon signature consists of a signal in the muon system and a matching track from the tracking system in order to get a precise momentum measurement.

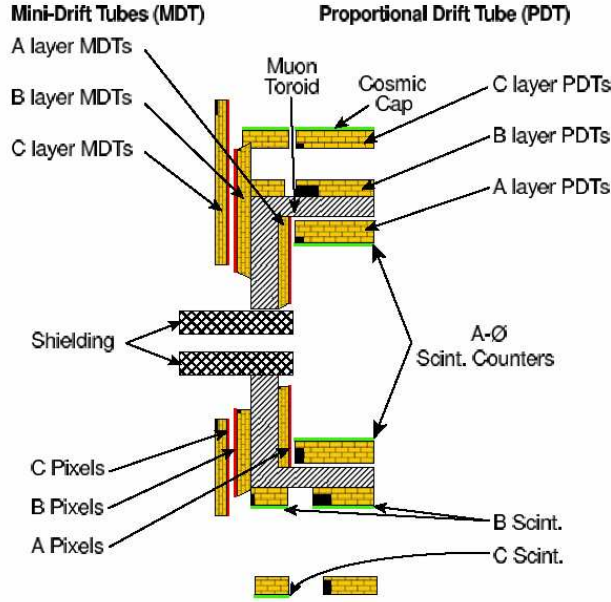


Figure 2.7: Schematic side view of the muon system with proportional drift tubes (PDTs), mini drift tubes (MDTs), scintillation counters, toroid magnet and shielding (from Ref. [37]).

The muon spectrometer is the outermost part of the  $D\bar{\Omega}$  detector (see Figure 2.2). It is located on both sides of an iron toroid magnet which surrounds the calorimeters at a distance of  $3.18 \text{ m} < r < 4.27 \text{ m}$  to the beam pipe in the central part and in a distance of  $4.54 \text{ m} < |z| < 6.10 \text{ m}$  from the interaction region in the forward parts. The toroid creates an internal field of 1.8 T to allow momentum measurement in the muon system.

Figure 2.7 shows a schematic view of the  $D\bar{\Omega}$  muon spectrometer. The system consists of a central part ( $|\eta_{det}| \leq 1$ ) and a forward angle muon system, which extends the coverage up to  $|\eta_{det}| \leq 2$ . Each part uses fast scintillation counters for triggering and timing measurements and drift tubes for precise position measurements, a rough momentum estimate and also for triggering.

The central region uses proportional drift tubes (PDTs) as drift chambers. Three layers of PDTs are located inside (layer A) and outside (layer B and C) of the central toroid magnet. The drift tubes are made of rectangular extruded aluminum tubes of 10.1 cm across and a maximum length of 5.79 m. Each drift tube contains an anode wire at the center, parallel to the toroidal field lines (operated at 4.7 kV) and cathode pads located above and below the wire (operated at 2.3 kV), to provide hit information along the wire. The gas mixture

## 2 Experimental Apparatus

---

consists of 84 % argon, 8 % methane and 8 % CF<sub>4</sub>. The PDTs are arranged to chambers of 3-4 decks of drift tubes with 24 tubes each. The central muon system is only partially instrumented at the bottom region ( $4.25 < \phi < 5.15$ ) to make room for support structures.

The forward region uses mini drift tubes (MDTs) for muon track reconstruction, due to their short electron drift time (< 132 ns), high segmentation and radiation hardness. The MDTs are arranged in three layers, as in the case of the PDTs. A layer consists of 3-4 planes of tubes, each tube comprises eight  $1 \times 1 \text{ cm}^2$  cells with a maximum length of 5.83 m. The tubes are mounted along the magnetic field lines and operated at 3.2 kV. The MDT system uses a CF<sub>4</sub>-CH<sub>4</sub> (90 %-10 %) gas mixture.

Shielding structures isolate the muon detectors from backgrounds generated near the beam pipe and accelerator elements. The scintillation counters in both central and forward regions are positioned alongside the PDTs and MDTs.

### 2.3.5 Luminosity Monitor

The primary purpose of the luminosity monitor is to make an accurate determination of the Tevatron luminosity at the DØ interaction region by measuring the rate of inelastic  $p\bar{p}$  collisions. In addition, the luminosity monitor identifies beam crossings with multiple  $p\bar{p}$  interactions, makes a fast measurement of the  $z$ -coordinate of the interaction vertex and measures beam halo rates. Each luminosity monitor detector consists of two arrays of 24 plastic scintillation counters with photomultiplier readout and is placed in front of the end calorimeters at  $z = \pm 140 \text{ cm}$ , covering  $2.7 < |\eta_{det}| < 4.4$  (see Figure 2.8).

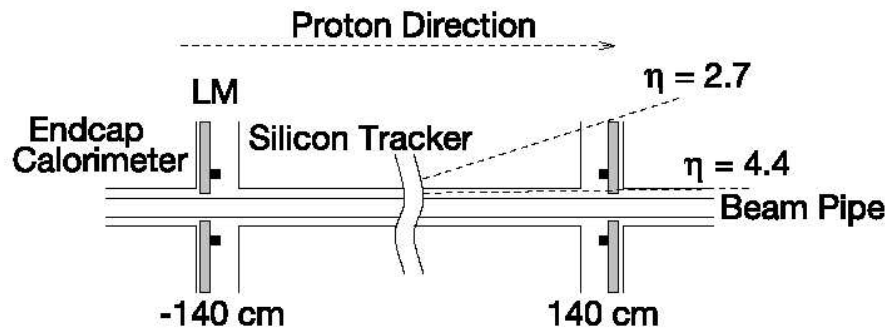


Figure 2.8: Schematic drawing showing the location of the luminosity monitor detectors (from Ref. [37])

### 2.3.6 Forward Proton Detector

The forward proton detector measures protons and antiprotons scattered at small angles that are missed by the main  $D\bar{\emptyset}$  detector. It consists of a series of momentum spectrometers that make use of the accelerator magnets in conjunction with position detectors along the beam line. Special stainless steel containers (*Roman pots*) house the position detectors, allowing them to function outside the accelerator's ultra-high vacuum and to be moved away from the beam during unstable beam conditions. The forward proton detector consists of 18 Roman pots arranged in six steel chambers located at various distances from the  $D\bar{\emptyset}$  interaction point.

### 2.3.7 Trigger and Data Acquisition

As discussed before, most of the  $p\bar{p}$  interactions are soft collisions and therefore only of minor interest. In order to select the interesting physics events and in order to reduce the data flow from approximately 2 MHz to a recordable rate of 50 Hz,  $D\bar{\emptyset}$  uses a sophisticated trigger system. Three distinct levels form the trigger system, and each succeeding level examines fewer events but in greater detail and with more complexity.

A schematic overview of the  $D\bar{\emptyset}$  trigger and data acquisition system is shown in Figure 2.9. The triggers are configured by a list of individual triggers (*trigger list*), which are defined by a set of requirements at each trigger level. The following sections provide a brief overview of the tasks and structure of each different trigger level, with emphasis on the components that are of interest for this analysis. A block diagram of the  $D\bar{\emptyset}$  trigger system is shown in Figure 2.10.

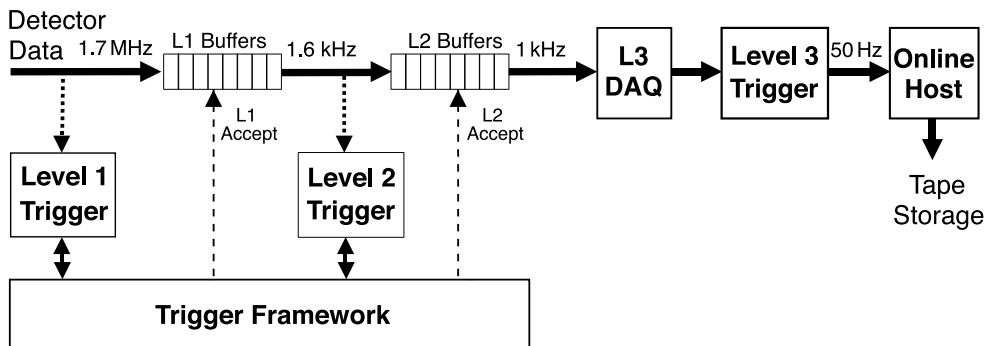


Figure 2.9: Overview of the  $D\bar{\emptyset}$  trigger and data acquisition system (from Ref. [37]).

### **Level 1 Trigger**

The first trigger stage (Level 1 or L1) is implemented in custom-designed hardware to provide dead-time less trigger decisions and to examine every event for interesting signatures. A L1 trigger decision is made within  $4.2 \mu\text{s}$ , resulting in a reduction of the data flow from 1.7 MHz down to 1.6 kHz. The Level 1 trigger uses input data from the following detector systems (see Figure 2.10): calorimeter system (L1CAL), central/forward preshower detectors and central fiber tracker (central track trigger, L1CTT), muon system (L1MUO) and the forward proton detector (L1FPD). Both the L1CTT and the L1CAL are important for this analysis, hence a brief discussion follows.

The L1CAL looks for local energy depositions, which exceed programmable thresholds on transverse energy deposits. It receives fast analog signals from the calorimeter system, which are converted to  $E_T$  on input. The summed transverse energy deposition within the electromagnetic or all layers of  $\Delta\eta \times \Delta\phi = 0.2 \times 0.2$  calorimeter towers are the basic trigger objects. In total there are 1280 electromagnetic and 1280 hadronic trigger towers: 40 slices in  $\eta$  (covering  $|\eta| < 4$ ) and 32 slices in  $\phi$  (covering the full azimuth). Electromagnetic objects are identified by using the EM layers only, while jets are identified by using the total transverse energy. The trigger coverage has been increased during the first two years of Run II data taking from  $|\eta_{det}| < 0.8$  to  $|\eta_{det}| < 3.2$ . The vast majority of the data for this analysis has been taken with full coverage.

The L1CTT reconstructs the trajectories of charged particles with  $p_T > 1.5 \text{ GeV}$  using discriminator data provided by the central fiber tracker and the central/forward preshower detectors. For fast processing, the hit information of the three scintillator-based detectors is compared to predefined track patterns in a  $\phi$  sector of  $4.5^\circ$ . To balance the available hardware resources, the predefined track patterns are grouped into four  $p_T$  bins:  $1.5 \text{ GeV} < p_T < 3 \text{ GeV}$ ,  $3 \text{ GeV} < p_T < 5 \text{ GeV}$ ,  $5 \text{ GeV} < p_T < 10 \text{ GeV}$ ,  $10 \text{ GeV} < p_T$ . In addition to finding tracks, the L1CTT also identifies CPS clusters, matches tracks to clusters and reports the overall occupancy of the CFT. A list of seed tracks is provided for L1MUO, and various track and cluster information is sent to subsystems in the second trigger level. The CFT part of the L1CTT has been included into data taking starting with trigger version 12 in Summer 2003. The CPS information has been included in trigger version 13 (Summer 2004), which is not part of this analysis.

### **Level 2 Trigger**

The second trigger level (Level 2 or L2) collects data from both front-end electronics and the L1 trigger processors in order to perform a more detailed analysis. L2 can combine data across detectors to form higher quality physics objects than Level 1 and to examine event-wide correlations in all L2 physics objects. The system handles a maximum input rate of 10 kHz and has an accept rate of 1 kHz at a maximum dead-time of 5 % and a maximal latency of  $100 \mu\text{s}$ .

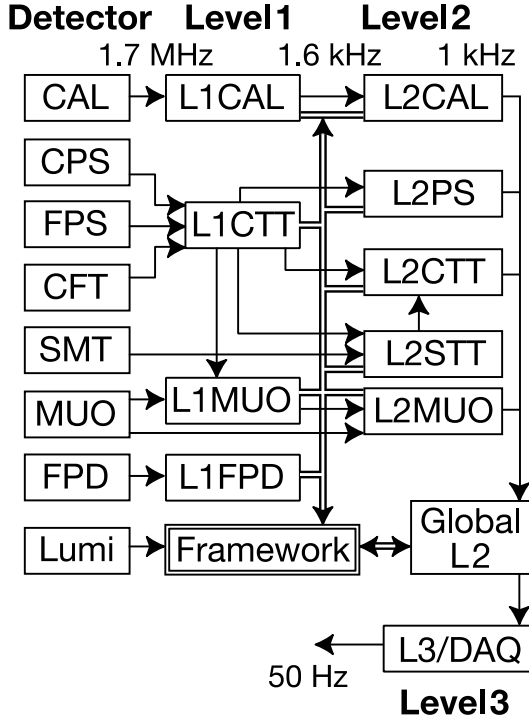


Figure 2.10: Block diagram of the  $D\emptyset$  trigger system (from Ref. [37]) The arrows indicate the flow of trigger-related data.

The L2 trigger includes preprocessors for each detector subsystem and a global processor for integration of the data (see Figure 2.10). The preprocessor subsystems include tracking (L2CTT, L2STT), calorimeter (L2CAL), preshower (L2PS) and muon systems (L2MUO). All subsystems work in parallel, and the final L2 trigger decision is made in the L2Global stage based on physics objects reconstructed in the preprocessors. L2Global examines correlations across all detector systems, and it imposes cuts on the physics objects according to configuration information from the trigger list. Preprocessing is performed either with serial CPU-based cards or with CPU cards plus highly parallelized DSP or programmable logic-based cards.

The L2CAL preprocessor identifies jets and electrons/photons and calculates the energy imbalance in the event ( $\cancel{E}_T$ ) using the 2560 calorimeter trigger towers. Algorithms calculate the total energy, isolation and the electromagnetic fraction of specific tower combinations.

The L2CTT preprocessor combines inputs from the L1CTT and the L2STT. It refines the  $p_T$  measurement and determines the azimuthal angle using additional hit and tracking information provided by the Level 1 readout. The L2STT reconstructs particles found in the L1CTT with increased precision by utilizing the finer spatial resolution of the silicon microstrip tracker, allowing to measure the impact parameter of tracks precisely enough to tag the decays of long-lived

## 2 Experimental Apparatus

---

particles like  $B$  hadrons.

### Level 3 Trigger

The entire DØ detector is read out for events passing the Level 1 and Level 2 trigger, including the L1 and L2 systems themselves. Each event is fully reconstructed at Level 3, with algorithms running on a CPU farm that resemble those for offline event processing as closely as possible, given restrictions due to available processing power. This allows Level 3 to make a final trigger decision within 200 ms and to reduce the maximum input rate of 1 kHz to 50 Hz. Its decisions are based on complete physics objects as well as on the relationships between such objects, e.g. angular separation of physics objects or their invariant mass. Candidate physics objects (or relations between them) are generated by object-specific software algorithms (*filter tools*). *Reference sets* of programmable algorithm parameters are input to the filter tools via the trigger list. These reference sets define the physics objects precisely.

The L3 jet tools implement a simple cone algorithm, which relies on the high-precision calorimeter readout and primary vertex position. The L3 electron tools are based on a simple  $\Delta\mathcal{R} < 0.25$  jet cone, with specific requirements on the minimum electromagnetic fraction and the transverse shower shape. For further reduction of background, a match to the preshower detector signal can be required.

The L3 tracking is based on CFT and SMT information. Track finding is performed using specific tracking algorithms for the CFT and the SMT. A global (CFT+SMT) high-momentum track finder starts from axial CFT seed propagated towards the SMT by a linear fit in  $r - \phi$ . The primary interaction vertex is determined in the vertexing tool using CFT tracks. L3 tracks are used in the electron and muon filters to increase efficiency and background rejection at low values of  $E_T$ .

### Data Acquisition System

The data acquisition system consists of the *L3DAQ* and the *online host system*. The task of L3DAQ is to transport detector component data stored in readout crates to the processing nodes of the L3 trigger filtering farm. The online host system receives event data from the L3 farm nodes and distributes that data to logging and monitoring tasks. The raw data is written to files and transported to the mass storage system, consisting of disk and tape storage. Corresponding meta data is generated and stored in a database.

The raw data is reconstructed with the software DØRECO [38], which provides two output formats: the *data summary tier (DST)* and the *thumbnail (TMB)*. The size of the DST corresponds to approximately 150 kb per event, while the TMB size is approximately 20 kb per event. The DST contains all information necessary to perform any physics analysis, including limited re-reconstruction

of high-level physics objects. The TMB can be used directly to perform many physics analyses, the size reduction is achieved by dropping part of the information and by compression.

## *2 Experimental Apparatus*

---

# 3 Phenomenology of $p\bar{p}$ Collisions

The following chapter gives a brief overview of the terminology common to hadron collider physics and describes processes that are of interest for this analysis. A short description of the event simulation closes this chapter.

## 3.1 General Properties of $p\bar{p}$ Collisions

Protons and antiprotons are composite particles, made of quarks and gluons (so-called *partons*) – hence they are *hadrons*. The quarks or antiquarks which impart quantum numbers to hadrons are called *valence quarks*. In the case of the proton (antiproton), these are two  $u$  ( $\bar{u}$ ) quarks and one  $d$  ( $\bar{d}$ ) quark. Apart from these valence quarks, hadrons may contain an indefinite number of virtual quarks, antiquarks and gluons which do not contribute to their quantum numbers. Such virtual quarks are called *sea quarks*.

The quarks and gluons are the fundamental degrees of freedom to participate in the strong interactions at high energies. Therefore a collision of protons and antiprotons at high energies has to be regarded as an interaction of the partons. The longitudinal parton momentum inside an accelerated proton is not precisely known, while the transverse momentum has to be zero. In addition, partons which do not participate in the hard scattering carry a significant amount of the energy of hadrons and form the underlying event (see below). Their longitudinal momentum is not measurable. As a consequence, the final state objects after a collision are characterized using transverse momentum ( $p_T$ ) and transverse energy ( $E_T$ ), making use of transverse momentum/energy conservation.

In the hard-scattering interactions of quarks and gluons at a hadron collider, the effective center-of-mass energy of the interaction ( $\sqrt{\hat{s}}$ ) is smaller than the center-of-mass energy of the machine ( $\sqrt{s}$ ) and given by

$$\sqrt{\hat{s}} = \sqrt{x_a x_b s} \quad (3.1)$$

with  $x_a$  and  $x_b$  being the fractions of the proton/antiproton momentum carried by the two colliding partons called  $a$  and  $b$ .

The majority of interactions in a proton-antiproton collision are uninteresting, being the result of large-distance collisions between the incoming partons. The momentum transfer in these interactions is small, resulting in low transverse momenta of the secondary particles (“soft collisions”). Interesting physics events are characterized by large momentum transfers, leading to final state particles with large  $p_T$  (“hard scattering”). Despite of the hard scattering various other processes might happen:

- *Initial State Radiation (ISR)*: Emission of e.g. a gluon or photon from the incoming partons, which results in significant corrections to the cross section and to the event topology by increasing the amount of final state particles.
- *Final State Radiation (FSR)*: Emission of e.g. a gluon or photon from outgoing partons, having the same consequences as described for ISR.
- *Beam-beam remnants*: The parton, which participates in the hard scattering, carries only a fraction of the energy of the hadron, while the rest is carried by the so-called hadron remnant. The fragmentation of the remnant leads to additional final state particles.

The term *underlying event* is used to describe everything but the direct products of the hard scattering process and the final state radiation of the hard scattered partons. It receives contributions from the beam remnants plus initial and final state radiation.

Due to the large inelastic scattering cross section of  $\sigma_{inel} \approx 70$  mb at the Tevatron center-of-mass energy (see Figure 3.2), a typical bunch crossing is characterized by multiple soft interactions. These kind of events are called *minimum bias* events.

The term *pile-up* refers to irreducible background stemming from the previous bunch crossing. In the case where detectors are not fast enough to resolve individual interactions, the current bunch crossing is overlayed by signals from the previous bunch crossing. For the DØ detector, pile-up is e.g. relevant in the calorimeter system: the shaping time of the calorimeter readout electronics is longer than the bunch crossing time of 396 ns, hence the signal from an earlier bunch crossing may contribute to the energy of the jet under consideration.

## 3.2 Parton Distribution Functions (PDF)

In order to simulate proton-antiproton collisions, the parton distribution functions (PDFs)  $f_i(x, Q^2)$  of the constituents have to be known. The quantity  $f_i(x, Q^2)dx$  is the probability that a parton of type  $i$  carries a momentum fraction between  $x$  and  $x + dx$  of the momentum of the hadron, and it depends on the 4-momentum exchanged in the interaction ( $Q^2$ ). At large  $Q^2$ , the interacting particle sees the short-distance structure of the protons, and therefore has access to the sea quarks. Hence the parton distribution functions are shifted to small  $x$  values. For small  $Q^2$ , the valence quarks dominate and the PDFs peak at large  $x$  values. Figure 3.1 shows a parameterization of the PDFs of valence and sea quarks provided by the CTEQ group [39] for  $Q^2 = 10^4$  GeV $^2$ , which is a typical value at the Tevatron. Although gluons are only dominating at very small  $x$  values, electron-proton scattering experiments have revealed that they carry half of the total proton momentum. The other half is carried by the valence and sea quarks.

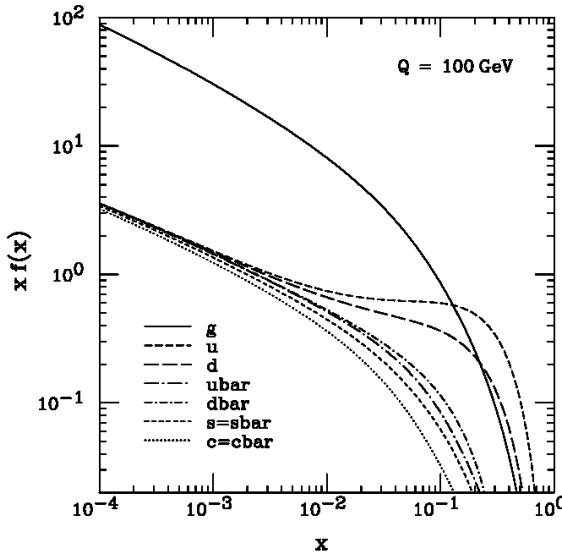


Figure 3.1: Parton distribution function of the proton as calculated for  $Q^2 = 10^4$  GeV using CTEQ6 provided by the CTEQ group [39].

The parton distribution functions are parameterizations based on results from various experiments. Quark and gluon PDFs are mainly based on results from deep inelastic scattering (DIS) of electrons, muons and neutrinos with nucleons. Recent experiments which performed precise DIS measurements are ZEUS [33] and H1 [34], both located at DESY [35] in Hamburg. Gluon PDFs are also inferred indirectly from measurements of inclusive and differential jet production cross sections at hadron collider experiments (CDF, DØ).

### 3.3 Factorization and Renormalization Scale

Cross sections for processes that involve strong interactions are factorized into a short-distance (hard) part and a long-distance (soft) part. The short-distance part depends on the particular process and is calculable with perturbative QCD (pQCD). The long-distance part cannot be calculated with pQCD, however it is universal and therefore experimentally measurable. The *factorization scale*  $\mu_f$  is introduced to separate the two regimes. It characterizes the boundary between short- and long-distance physics and is usually at the order  $Q$  of the hard interaction.

The factorization is applicable at all orders of the perturbation expansion. With increasing order of the calculation, the dependence of the cross section on the choice of  $\mu_f$  decreases. The variation of the cross section with the factorization scale gives an estimate of the magnitude of higher-order corrections. The complete perturbation expansion is independent of the choice of  $\mu_f$ . Renormalization of the QCD expansion introduces an arbitrary scale  $\mu_R$ , at which the coupling constant of the strong interaction is evaluated. The renormalization scale  $\mu_R$  is usually chosen to be equal to the factorization scale  $\mu_f$ .

### 3.4 Cross Section

The cross section of a generic hard-scattering interaction at leading order is given by the sum over different parton combinations:

$$\frac{d\sigma}{dQ^2} = \sum_{a,b} \int dx_a \int dx_b f_a(x_a, Q^2) f_b(x_b, Q^2) \frac{\hat{\sigma}_{ab}(x_a, x_b)}{dQ^2} \quad (3.2)$$

where  $\hat{\sigma}_{ab}$  is the cross section of the elementary interaction between two partons, and the  $f_a(x_a, Q^2)$  and  $f_b(x_b, Q^2)$  are parton distribution functions for the two partons. Various cross sections for selected processes at the Tevatron are shown in Figure 3.2. It is obvious that sophisticated analyses are necessary to select interesting processes, like the production of SUSY particles, because the corresponding cross sections are orders of magnitude lower than the di-jet cross section or the inelastic scattering cross section.

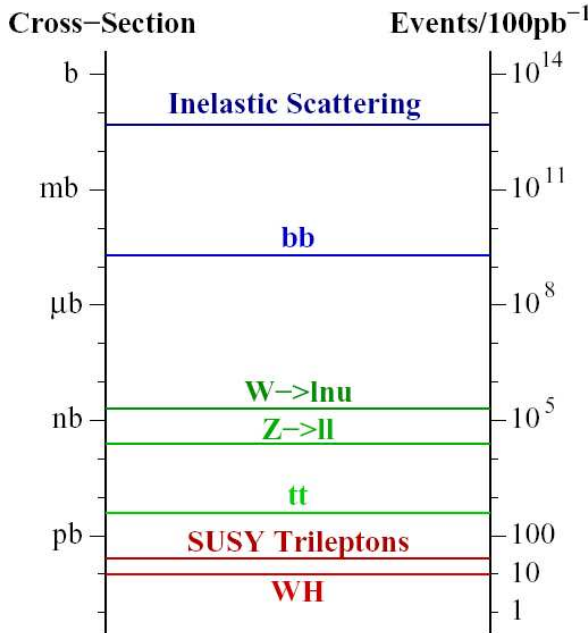


Figure 3.2: Cross sections (left axis) and number of expected events for an integrated luminosity of  $100 \text{ pb}^{-1}$  (right axis) for selected processes at the Tevatron. Precise values with errors for all processes that are relevant for this thesis are given in Table 5.4.

### 3.5 Higher Order QCD corrections

Higher order contributions to the leading order cross section consist of virtual corrections (e.g. emission and absorption of a gluon) and emission of real particles (e.g. emission of a gluon which can be detected as a jet). These QCD

corrections can lead to considerable corrections to the total cross section. For hadron colliders, cross section calculations for most processes of interest are available at next-to-leading order (NLO), where corrections up to  $\alpha_s^2$  beyond the leading order cross section are taken into account.

Higher order corrections also affect kinematic variables and angular distributions in the final state. In most cases it is sufficient to simulate the event topology at leading order and use approximations for higher order effects. The total cross section is corrected using the *K-factor*, which is defined as the ratio of higher order and leading order cross section:

$$K_{(N)NLO} \equiv \frac{\sigma_{(N)NLO}}{\sigma_{LO}}. \quad (3.3)$$

Cross sections of Standard Model processes need to be known with high accuracy, especially for searches for non-Standard Model physics where Drell-Yan,  $Z(+jet)$ ,  $W(+jet)$  and di-boson production are major backgrounds. In addition, accurate predictions of signal cross sections are needed for interpretation of upper cross section limits in terms of model parameters.

## 3.6 Event Simulation

The simulation of proton-antiproton collisions and the identification of the collision products is a complex task, which makes a direct comparison of the experimental results with theoretical predictions very complicated. A detailed and precise event simulation is necessary to address this problem.

The generation of simulated events consists of two steps: Monte Carlo generation and detector simulation. Both steps are briefly discussed here, since explicit predictions for experimental quantities and the process under study are derived from event simulations. In the following, the simulated events will be referred to as *Monte Carlo events*.

### 3.6.1 Monte Carlo Generation

Most of the signal and background events that are used in this analysis are generated using the PYTHIA [40] event generator in version 6.202. PYTHIA is a multi-purpose high-energy particle collision simulator capable of simulating  $e^+e^-$ ,  $pp$ ,  $p\bar{p}$  and  $ep$  collisions.

PYTHIA simulates all Standard Model processes that result from the  $p\bar{p}$  collision. In addition, it also allows the simulation of processes that are expected from new physics like supersymmetry. For most of these processes, leading order matrix elements are used. These leading order calculations of the hard subprocess are supplemented by parton showering. In addition, PYTHIA performs the hadronization of colored partons into colorless hadrons. Both the modeling of initial/final state radiation and the fragmentation/hadronization

process are discussed below. PYTHIA allows the use of different parton distributions functions. For this analysis, all Monte Carlo samples were produced using CTEQ4-6.

The simulation of leptonic and hadronic tau decays is of significant importance for this thesis. The software package TAUOLA [41] is used for the simulation of tau decay, which includes spin effects [42].

### **Modeling of ISR and FSR**

In every process that contains colored and/or charged objects in the initial or final state, initial and/or final state radiation may result in large corrections to the overall event topology and the cross section (see Section 3.1). This is taken into account by PYTHIA using the *parton shower method*. This method approximates the effects from ISR and/or FSR in a probabilistic approach by an evolution in a series of branchings of a mother parton into two daughter partons. The momentum fractions of the two daughter partons are  $z$  and  $1 - z$ . The branching is described by the Altarelli-Parisi splitting functions  $P(z)$  [43]. Starting from the energy scale of the hard interaction  $Q_{max}^2$ , the evolution of the branchings is either performed forwards (for FSR) or backwards (for ISR). The shower evolution is cut off at some lower scale  $Q_0 \approx 1$  GeV. The parton shower method gives a good description of the radiation of collinear and soft partons, but has limited predictive power for the emission of hard and wide-angle partons. Nevertheless this method is a reasonable approach for the physics processes that are important in this thesis.

### **Fragmentation/Hadronization**

As stated in Section 3.3, perturbative QCD is only valid at short distances, while the perturbation theory breaks down at long distances. In the confinement regime, the colored partons are transformed into colorless hadrons. This process is called fragmentation or hadronization.

The fragmentation of partons into hadrons cannot be calculated and is described in analogy to the description of the partonic structure of the proton: fragmentation functions  $d_q^i(z, E)$  give the probability that a quark produces a hadron  $i$  with a fraction  $z$  of the quark energy  $E$ . These fragmentation functions have been measured at LEP [44]. The most successful theoretical approach in describing fragmentation is the *string fragmentation* [45]. In this model, the confinement is represented by a string with a certain energy density between the partons that are moving apart. Quark-antiquark pairs are created along the string in such a way that the string breaks up into hadrons. The resulting products are stable and unstable hadrons. The decay of unstable hadrons is simulated using decay matrix elements or results of measurements.

PYTHIA uses the Lund string fragmentation model [46] implemented in the program JETSET.

### **3.6.2 Detector Simulation**

The particles produced by the Monte Carlo generator are passed through the detector simulation, which is handled by the programs DØGSTAR [47] and DØSIM [48]. In the present thesis, software version p14 is used.

DØGSTAR simulates the interaction of particles with the detector material. It is based on GEANT [49], a software program that describes the passage of elementary particles through matter. This step is the most time consuming in the whole event simulation, since the software has to model all particle interactions in detail.

In the next step, DØSIM modifies the simulated events to account for various detector-related effects. It adds minimum bias events, pile-up from previous bunch crossings and includes the simulation of noise from the detector and electronic readout. The output of DØSIM is in the same format as the data recorded by the data acquisition system. It contains additional Monte Carlo information which makes it possible to correlate the detector data with generator output.

The output of the detector simulation is reconstructed with the reconstruction software DØRECO [38]. Again program version p14 is used. This is the same reconstruction software used for the reconstruction of data events.



## 4 Event Reconstruction and Object Identification

The task of the event reconstruction and object identification is to translate the stream of readout signals from the detector (so-called *raw data*) into basic physics objects and to provide an accurate estimate of the kinematics of the interaction. Algorithms have been developed to identify tracks, electrons, muons, taus, jets and neutrinos (in the form of missing transverse energy  $\cancel{E}_T$ ) as precisely as possible. The raw energy of these physics objects is calibrated and corrected in order to reconstruct the event kinematics.

The following chapter describes the reconstruction of the physics objects which are relevant for this analysis. The event signature consists of an electron, a hadronically decaying tau and missing transverse energy, hence these physics objects are described in detail. Additional information is needed from tracks, jets and the primary vertex, which will also be discussed. Strategies on how to separate these physics objects from the background are also presented.

### 4.1 Track Reconstruction

The trajectory of a charged particle (called *track*) is reconstructed using hit information in the tracking system, which consists of the SMT and the CFT (see Section 2.3.1). Both detectors are used for tracking in  $|\eta_{det}| \leq 1.6$ , while only the SMT can be used in the remaining region up to  $|\eta_{det}| \leq 3.0$ . The track reconstruction relies on two algorithms: the *Alternative Algorithm* (AA) and the *Histogram Track Finder* (HTF).

The AA [50] uses a road-following method to reconstruct tracks. Starting from any combination of three hits in the SMT barrels or disks, the algorithm extrapolates the sequence of hits moving outwards to the next SMT or CFT layer. If a hit is found within the search window, an  $\chi^2$  test is performed. The found hit is associated with the track candidate if the  $\chi^2$  value is below a certain threshold. A “miss” is recorded when no hit is found in the layer. The construction of track candidates ends when the last CFT layer is reached or when three misses are recorded.

The HTF [51] method relies on a histogramming method. The trajectory of a charged particle moving perpendicular to a homogeneous magnetic field can be characterized by  $\rho$ , the radius of the curvature,  $d_0$ , the distance of closest approach (DCA) with respect to  $(0, 0)$ , and  $\Phi$ , the direction of the track at

the point of closest approach to  $(0, 0)$ . For track candidates with small impact parameters, every pair of hits in  $x$  and  $y$  that belongs to the same track corresponds to a single point in the  $\rho - \phi$  plane. Filling each pair of hits into the 2-dimensional  $\rho - \phi$  histogram, a peak in the histogram would correspond to a track candidate.

A final list of tracks is generated by merging the output of both algorithms and removing duplicates. The final track list is sorted by the number of hits, fewest misses and lowest  $\chi^2$  value.

The transverse momentum of a track is calculated from the curvature of the trajectory in the magnetic field. The track momentum resolution degrades with increasing momentum ( $\frac{\sigma_{p_T}}{p_T} \sim p_T$ ), while the energy resolution of the calorimeter improves with increasing energy ( $\frac{\sigma_{E_T}}{E_T} \sim \frac{1}{\sqrt{E_T}}$ ). Hence, the calorimeter gives a more accurate measurement of the electron kinematics for the electrons in the interesting  $p_T$  range of this analysis. In addition, the  $p_T$  measurement for electron tracks suffers from the radiation of *bremsstrahlung*, due to the small electron mass. This effect can be neglected for heavier charged particles.

## 4.2 Primary Vertex

The vertex of the hard scattering process is called *primary vertex*. The measurement of its position is crucial for an accurate estimate of the transverse momentum of the physics objects, especially for the missing transverse energy. Due to additional softer minimum-bias interactions, a second hard scattering process in the same bunch crossing and misreconstruction, it is possible to have more than one candidate vertex.

Primary vertex candidates are determined using reconstructed tracks (see Section 4.1). At least three tracks with SMT hits have to point to the same vertex. The exact vertex position is determined by a fit that uses the associated tracks. The  $z$  position has to be within the SMT acceptance region ( $|z_0| < 60$  cm). The primary vertex of a hard collision is picked among the vertex candidates based on track multiplicity and the transverse momentum of the associated tracks, since minimum bias interactions will result in tracks with smaller transverse momentum.

## 4.3 Electron Reconstruction and Identification

The identification of electromagnetic objects like electrons and photons is initially based on the reconstruction of electromagnetic showers in the calorimeter system. The longitudinal shower profile is sampled in the four electromagnetic layers  $EM1$ ,  $EM2$ ,  $EM3$  and  $EM4$ , and the first fine-hadronic layer is used additionally to sample the tail of the shower. The shower maximum is expected to be in  $EM3$ , hence this layer has a higher granularity (see discussion in 2.3).

Since photons do not leave signals in the tracking system, a track associated to the energy deposition in the calorimeter provides a tool to distinguish electrons from photons.

The electron reconstruction software uses cell towers in the first five calorimeter layers in a cone of  $\Delta\mathcal{R} < 0.4$  to form the initial calorimeter clusters. This is done by the *simple cone algorithm*. The simple cone algorithm defines a list of seed towers, which is initialized with the highest  $E_T$  tower. The distance  $\Delta\mathcal{R}$  between unassigned towers and the seed is calculated, and the unassigned tower is added to the seed if the distance is smaller than the specified cone size. If the unassigned tower cannot be matched to the seed, it is added to the list of seed towers. After all entries in the list of seed towers are processed, the list of seeds contains the found clusters.

Since the reconstructed electromagnetic clusters are dominated by background from hadronic jets, further requirements are imposed on the cluster. These requirements utilize that jets are characterized by broad showers with a large fraction of energy deposited in the hadronic calorimeter. The electromagnetic clusters are assigned an ID of 10 if they have  $E_T > 1.5$  GeV and an electromagnetic fraction (EMfrac) above 0.9. The electromagnetic fraction is the ratio of the cluster energy deposited in the four EM layers compared to the total cluster energy. If the cluster has a track loosely matched to it, the ID is set to  $\pm 11$ , depending on the sign of the track (electrons get ID = +11, positrons get ID = -11). In addition, it is required that the isolation of the cluster (iso) is less than 0.2. The isolation variable is defined as:

$$\text{iso} = \frac{E_{\text{tot}}(0.4) - E_{\text{EM}}(0.2)}{E_{\text{EM}}(0.2)}, \quad (4.1)$$

where  $E_{\text{tot}}(\Delta\mathcal{R})$  and  $E_{\text{EM}}(\Delta\mathcal{R})$  denote the total energy and electromagnetic energy within a cone of radius  $\Delta\mathcal{R}$ . Electromagnetic clusters which fulfill these requirements are called *EM candidates*. The energy of the EM candidate corresponds to the sum of the energy deposition in all five layers. A calibration is performed, which has been derived by a data-Monte Carlo comparison of the invariant di-electron mass and its resolution in  $Z \rightarrow ee$  and  $J/\Psi \rightarrow ee$  events [52].

Requiring that a track is matched to the electromagnetic cluster is a powerful discriminant between electrons and photons. There are two different ways of how to match a track to a calorimeter cluster, which are both used in this thesis. The first one is referred to as *spatial track match*, while the second one is called *track match with  $E/p$* .

### Spatial Track Match

The track algorithm searches in a window of  $\Delta\mathcal{R} < 0.1$  around the calorimeter cluster center for candidate tracks. The  $\phi$  and  $\eta$  position of the candidate tracks are extrapolated into the calorimeter for this calculation. The spatial

track match uses the difference of the  $z$  position and the azimuthal angle  $\phi$  of track and cluster axis to calculate the  $\chi^2$ :

$$\chi^2 = \left( \frac{\Delta z}{\sigma_z} \right)^2 + \left( \frac{\Delta \phi}{\sigma_\phi} \right)^2. \quad (4.2)$$

The  $\sigma_z$  and  $\sigma_\phi$  are the root mean squares of the experimental distributions of the associated quantities. The track with the largest  $\chi^2$  probability is selected as the electron track.

### Track Match with E/p

The track match with E/p method uses the same approach. The track algorithm searches in a window of  $\Delta\mathcal{R} < 0.1$  around the calorimeter cluster center for candidate tracks. Since the track momentum is expected to match the measurement of the transverse energy in the calorimeter, the  $\chi^2$  has an additional term using the ratio of the track momentum ( $p_T$ ) and transverse energy of the calorimeter cluster ( $E_T$ ):

$$\chi^2 = \left( \frac{\Delta z}{\sigma_z} \right)^2 + \left( \frac{\Delta \phi}{\sigma_\phi} \right)^2 + \left( \frac{\frac{E_T}{p_T} - 1}{\sigma_{\frac{E_T}{p_T}}} \right)^2. \quad (4.3)$$

As before,  $\sigma_z$ ,  $\sigma_\phi$  and  $\sigma_{\frac{E_T}{p_T}}$  are the root mean squares of the experimental distributions of the associated quantities. The performance of the track match with E/p suffers from the worse momentum resolution in the tracking system and especially from *bremstrahlung*, which results in long tails in the  $E_T/p_T$  distribution and hence inefficiencies.

### H-Matrix

An important calorimeter variable for electron identification is the *H-Matrix* (*HMx8*), which makes use of the distinct shower profile of an electron or a photon when compared to the profile of a jet. To obtain the best discrimination against hadrons, both the longitudinal and transverse shower shapes are used and correlations between energy deposits in the calorimeter cells are taken into account. This is done using a covariance matrix. In the present analysis, the matrix is 8-dimensional, using the energy fractions of the four EM layers, the total EM energy, the vertex  $z$ -position and the transverse shower width in  $z$  and  $\phi$ . The covariance matrix is defined as:

$$M_{ij} = 1/N \sum_{n=1}^N (x_i^n - \bar{x}_i)(x_j^n - \bar{x}_j) \quad i, j = 1 \dots 8, \quad (4.4)$$

where  $x_i^n$  is the value of the variable  $i$  for the particle  $n$ . The inverse of the 8x8 covariance matrix is called H-Matrix:  $H = M^{-1}$ . The  $\chi^2$  is defined as [55]:

$$\text{HMx8 } \chi^2 = \sum_{ij}^n (x_i - \mu_i) H_{ij} (x_j - \mu_j) \quad (4.5)$$

with the observed values  $x_i$  and the means  $\mu_i$  for the shower shape observables, which are derived from Monte Carlo electrons. By applying a cut on HMx8, an electromagnetic shower can be distinguished from a hadronic shower.

### 4.3.1 Electron Likelihood

Requiring an electron candidate with a matched track, especially when using the track match with E/p, is well suited for suppressing QCD backgrounds. However, instrumental or “fake electron” backgrounds from QCD multijet events still pose a serious problem, due to the overwhelming rate of this background. The main background sources for high  $p_T$  electrons are photons and jets, which are dominated by a leading  $\pi^0$  which decays into two photons. In either case, there can be a track associated to the electromagnetic cluster due to photon conversion to an electron-positron pair or a low energy charged hadron close to the photon or  $\pi^0$ . Hence, the two main background sources for electrons are:

- Photon conversions;
- Hadronic overlaps.

Further components of fake electron backgrounds include:

- Charged pions that undergo charge exchange in the early layers of the calorimeter;
- Fluctuations of QCD shower shapes.

Studies of the fake electron background composition in Monte Carlo QCD events, requiring an EM candidate with a tight track match and  $p_T > 15$  GeV, show that the QCD background for electrons is mainly made of neutral pions [53, 54].

In order to efficiently select real electrons while suppressing fakes resulting from misidentification, an *electron likelihood* has been developed [82]. The likelihood function combines information from various quantities measured in the calorimeter and in the tracking system to form a single likelihood variable:

- Electromagnetic fraction (EMfrac): neutral pions are produced in association with other charged hadrons. Hence the electromagnetic fraction of the calorimeter cluster is worse due to significant hadronic energy stemming from the surrounding hadrons.
- Shower shape H-Matrix  $\chi^2$ : this variable is the most important calorimeter variable, since it uses the distinct shower profile of an electron (or a photon) to distinguish these objects from jets (see discussion above).

- $E_T/p_T$ : the calorimeter quantities of photon conversions are nearly identical to that of an electron, though they might be slightly wider than an electron shower. However photon conversions are marked by the presence of a second track close to the electron track and a large values of  $E_T/p_T$ .
- $\chi^2$  probability of the spatial match: neutral pions have to overlap a track from charged hadrons in order to fake an electron, hence their track matching can be poor.
- Number of tracks with  $p_T > 0.5$  GeV in a  $\Delta R < 0.05$  cone around and including the electron track: this variable is meant to suppress fake electrons from photon conversions where one would expect more than one track very close to the electron.
- $p_T$  sum of all tracks with  $p_T > 0.5$  GeV in a  $\Delta R < 0.4$  cone around, but excluding, the electron track: this variable is meant to discriminate against  $\pi^0$  produced in association with charged hadrons. Additional tracks that are present around isolated electrons will tend to have extremely low  $p_T$ , whereas tracks from jets are likely to have large  $p_T$ .
- Distance of closest approach (DCA): measures the shortest distance of the selected track to the line parallel to the  $z$ -axis, which passes through the primary vertex.

Figure 4.1 shows the distribution of various quantities which are used for the calculation of the electron likelihood. As a signal sample, a Monte Carlo  $Z/\gamma^* \rightarrow ee$  sample with  $15 \text{ GeV} < M(e,e) < 60 \text{ GeV}$  is used. The background sample is derived from data, requiring two electrons with the same charge and an invariant mass in the same mass range as in the Monte Carlo sample. In both signal and background sample, only events with two electrons that pass the EM candidate requirements and have a spatial track match are retained. In addition, the two electrons in the signal sample are required to have opposite charge. The resulting electron likelihood distribution is shown in Figure 4.2.

## 4.4 Tau Reconstruction and Identification

The tau lepton has a mass of  $1777 \text{ MeV}/c^2$  and is therefore the heaviest lepton in the Standard Model (see Table 1.1). Unlike electrons or muons, taus decay within the detector and must be reconstructed from their decay products. Due to its large mass, the tau does not only decay leptonically into electron or muon, but also hadronically into quark pairs, which hadronize into resonances like  $\pi$ ,  $K$ ,  $\rho$ ,  $K^*$  or  $a_1$ . Table 4.1 provides a detailed overview of the most relevant tau decay channels and their corresponding branching ratios. The leptonic branching ratio sums up to 35 %, while the semi-hadronic branching ratio (usually referred to as the hadronic decay mode) sums up to 65 %. One distinguishes the *1-prong* decay, resulting in one charged particle (plus zero or

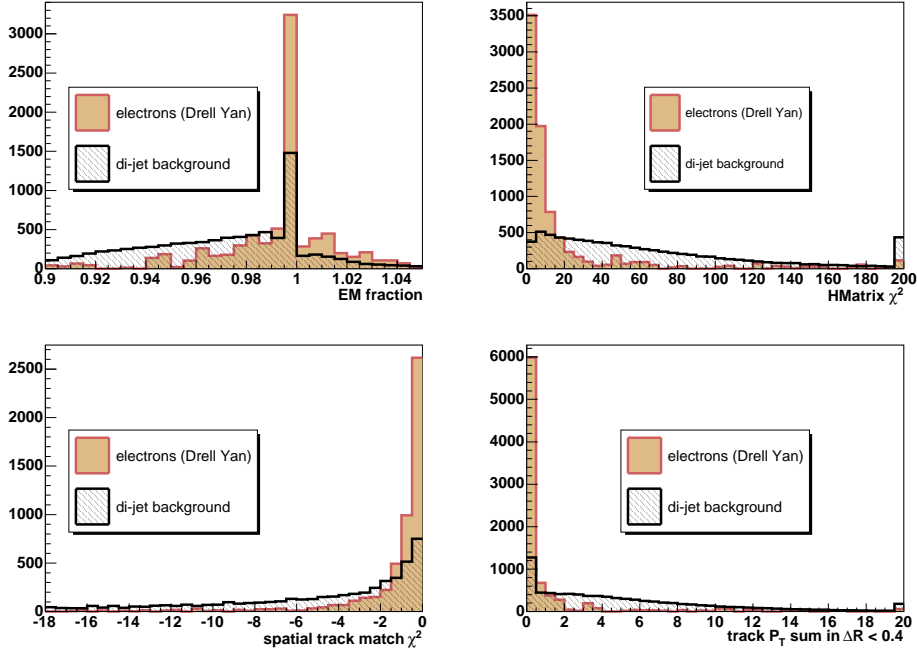


Figure 4.1: Distribution of various input quantities for the electron likelihood for electrons (shaded) and jets (hatched). The plots are taken from Ref. [78].

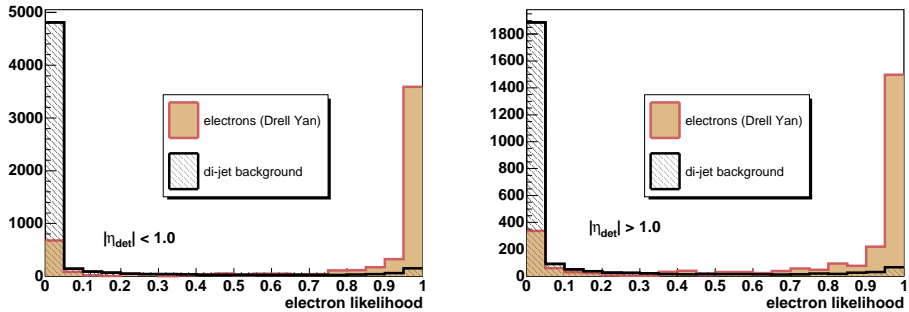


Figure 4.2: Distribution of the resulting electron likelihood for electrons (shaded) and jets (hatched) for  $|\eta_{det}| < 1.0$  and  $|\eta_{det}| > 1.0$ . The plots are taken from Ref. [78].

more  $\pi^0$ ), and the 3-prong decay, resulting in three charged particles (plus zero or more  $\pi^0$ ).

The tau decay length corresponds to  $c\tau = 87 \mu m$ , which is about 4 times smaller than the decay length of the  $b$  quark. Identification of taus based on separation of its decay (secondary) vertex from the production (primary) vertex is more difficult than for  $b$  quarks, hence the leptonic tau decay can not be distinguished from direct decay into either electron or muon.

	Decay Channel	Branching Ratio
leptonic decay (1-prong)	$\tau^- \rightarrow \mu^- \bar{\nu}_\mu \nu_\tau$	17.37 %
	$\tau^- \rightarrow e^- \bar{\nu}_e \nu_\tau$	17.83 %
hadronic decay with 1 charged particle (1-prong)	$\tau^- \rightarrow \pi^- \nu_\tau$	11.09 %
	$\tau^- \rightarrow \pi^- \pi^0 \nu_\tau$	25.40 %
	$\tau^- \rightarrow \pi^- 2\pi^0 \nu_\tau$	9.13 %
	$\tau^- \rightarrow \pi^- 3\pi^0 \nu_\tau$	1.08 %
hadronic decay with 3 charged particles (3-prong)	$\tau^- \rightarrow \pi^- \pi^+ \pi^- \nu_\tau$	9.49 %
	$\tau^- \rightarrow \pi^- \pi^+ \pi^- \pi^0 \nu_\tau$	4.32 %

Table 4.1: Overview of the most common tau decay channels and their branching ratios (from Ref. [3]).

#### 4.4.1 Reconstruction Algorithm

The hadronic decay products of tau leptons appear as narrow isolated jets with low track and  $\pi^0$  multiplicity. To reconstruct these decay products, the reconstruction algorithm performs three steps. In the first step, the tau calorimeter cluster is built. In the second step, the candidate  $\pi^0$  decay products are resolved. The final tau candidate is formed in the third step, by matching tracks to the calorimeter cluster ([59], [60]).

In the following, all three reconstruction steps are summarized in more detail.

#### Calorimeter Cluster

The tau reconstruction identifies calorimeter clusters for tau candidates using two algorithms: one seeded using calorimeter energy clusters and the other using high  $p_T$ -tracks [59].

The calorimeter seeded algorithm uses a simple cone algorithm with a cone size of  $\Delta R = 0.3$ . Starting point is a calorimeter tower with at least  $E_T > 1.0$  GeV. The final calorimeter cluster must satisfy  $E_T > 4.0$  GeV.

The track seeded algorithm uses all tracks above  $p_T > 5$  GeV as seeds. If the calorimeter energy in a  $\Delta R = 0.3$  cone around the track exceeds 2 GeV, the cluster is added to the list of tau candidates.

An *isolation cone* is constructed around the centroid of the calorimeter cluster of the tau candidate. The cone has a size of  $\Delta R = 0.5$ , and its  $E_T$  is used later for the tau identification purposes to ensure that the calorimeter cluster is isolated.

## EM Subclusters

The fine segmentation of the calorimeter system allows the reconstruction of  $\pi^0$  clusters distinct from charged pions. A nearest-neighbor algorithm is used for cells in the EM3 layer of the electromagnetic calorimeter, since this layer has the finest granularity and is at the shower maximum of electromagnetic showers. The cell with the highest  $E_T$  is used as a seed, and the neighbor with the highest  $E_T$  is added to the cluster. These two cells and all their neighbors sharing a common boundary are combined to an EM3 subcluster. The energy of cells in the other EM layers overlapping with the cluster are then added to this object. All unused cells are used to search for more subclusters. The transverse energy of an EM subcluster has to exceed 0.8 GeV. The minimum requirement on the EM subcluster  $E_T$  is of importance for the classification of the tau candidates, which is discussed in Section 4.4.2.

## Track Matching

The aim of the track matching algorithm is to differentiate between tracks from tau decays and those from the underlying event or QCD background. Up to three tracks are associated to the tau candidate.

The track matching algorithm starts by sorting all tracks in a  $\Delta R = 0.5$  cone around the centroid of the calorimeter cluster in decreasing  $p_T$ . The ordered track list is traversed in an attempt to associate tracks with the calorimeter cluster. Only tracks with  $p_T > 1.5$  GeV are considered. After the first track is found, up to two more tracks are considered, if they originate within 2 cm in  $z$  of the the first track at the point of closest approach. A second track is added, if the invariant mass of the first and the second track is less than 1.1 GeV. A third track is added, if the invariant mass of all three tracks is less than 1.7 GeV and the sum of their charges is either +1 or -1. Tau candidates with only two matched tracks and a total charge of zero are discarded.

### 4.4.2 Classification of Tau Candidates

In the reconstruction, a tau candidate is unambiguously assigned to a certain category, depending on the number of tracks and the calorimeter subclusters. This classification is done to identify specific discrimination variables for each category, which allow an optimal identification of hadronic tau decays and an efficient rejection of backgrounds. There are three categories in total, which are referred to as *tau types*:

- type 1: a single track with a calorimeter cluster but no associated electromagnetic subclusters ( $\pi^\pm$ -like);
- type 2: a single track with a calorimeter cluster and at least one associated electromagnetic subcluster ( $\rho$ -like);

- type 3: 2 or 3 tracks consistent with the tau mass.

Neglecting type misclassification, a 1-prong tau decay will be classified as either tau type 1 (if no electromagnetic clusters have been associated with the tau candidate) or as tau type 2 (if at least one electromagnetic cluster has been associated with the tau candidate). Significant amount of electromagnetic energy in hadronic tau decays is expected from the  $\pi^0$ , which appear in nearly 40 % of the tau decays, corresponding to roughly 60 % of the hadronic decay modes (see Table 4.1). A 3-prong tau decay will be categorized as tau type 3.

### Type Misclassification

Detector peculiarities and misreconstruction of tracks as well as electromagnetic clusters can lead to type misclassification, where e.g. a tau decaying into a charged pion and a tau neutrino is wrongly classified as a tau of type 2. Figure 4.3 visualizes the effects of type misclassification, which have been studied using  $Z \rightarrow \tau\tau$  Monte Carlo events.

The main sources of type misidentification are early hadronic showers that can cause a true type 1 decay to be classified as “type 2,” and lost electromagnetic subclusters (especially in the inter-cryostat region) that often result in classification of a true type 2 decay as “type 1.” Of lesser importance are effects of tracking inefficiency and attaching a track from the underlying event to the tau candidate. Due to photon conversions, a non-negligible fraction of true type 2 decays has more than one track matched to it and is therefore classified as “type 3.”

No attempt is made at the reconstruction stage to separate electrons from taus. Indeed, it is expected that electrons will be reconstructed with very high efficiency as tau type 2, except in the inter-cryostat region where they will pass as tau type 1 due to lack of electromagnetic calorimeter. Hence in both analyses presented in this thesis a significant increase from Standard Model processes which have an electron in the final state is expected, and the issue will be addressed during the discussion of the analyses in Chapter 6 and 7.

#### 4.4.3 Neural Network

The classification of the tau candidates allows to select certain variables for each type which are suitable to identify hadronic tau decays and reject background from QCD jets. However, for each individual tau type these variables are naturally correlated, making it difficult to efficiently select tau candidates using simple square cuts. Correlations are best taken into account by using a multivariate analysis technique, like e.g. the likelihood discriminant for electrons in Section 4.3.1.

For the identification of hadronic tau decays, a set of neural networks has been developed to make efficiently use of discriminating tau variables [57]. Three

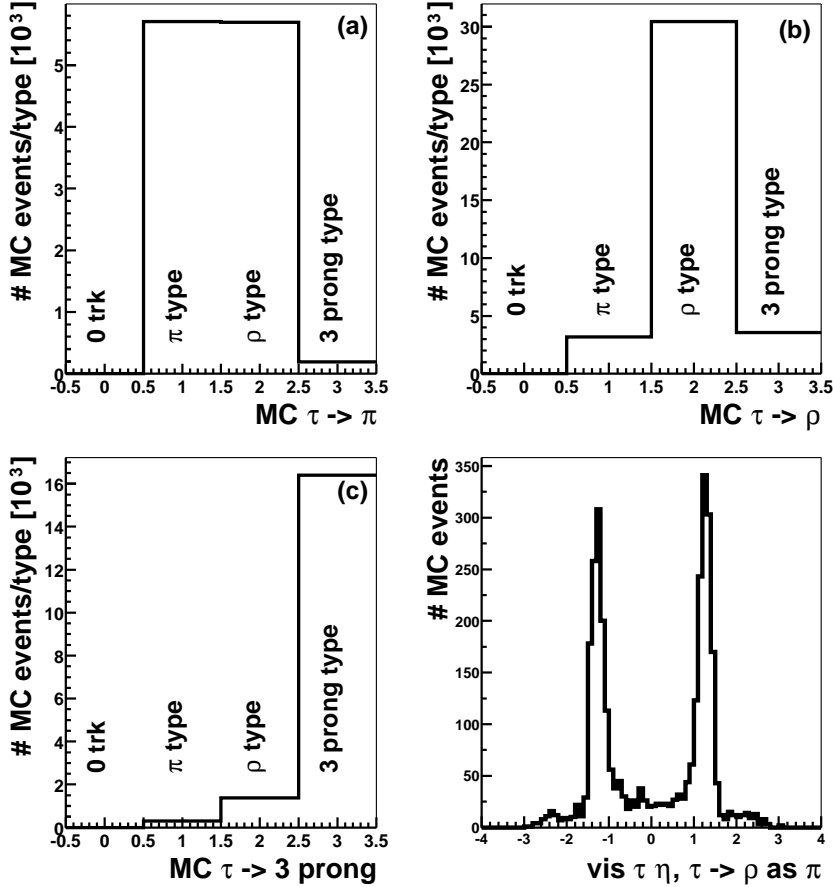


Figure 4.3: Histogram (a) shows the reconstructed tau types for a generated type 1. Early hadronic showers lead to a misclassification as “type 2.” Histogram (b) shows the reconstructed tau types for a generated type 2. Photon conversions lead to additional track(s), and hence to a classification as “type 3.” Misidentified “type 1” taus are located in the ICR, which is not covered by an EM calorimeter. The lower right plot shows the  $\eta$  distribution of these misidentified taus. Histogram (c) shows the reconstructed tau types for a generated type 3 (from Ref. [59]).

neural networks – one for each tau type – have been designed in order to identify taus, based on the track and calorimeter signature they leave in the detector. A detailed discussion of the neural network structure, the neural network training and the chosen discriminating variables follows.

The chosen neural network package is part of the ROOT example applications [58] and uses a vanilla back propagation method, which suits especially for particle physics classification tasks. The selected layout is identical for all three tau types and uses a configuration consisting of a single input layer, a single hidden layer and a single output layer. The input layer has one node for each input variable, resulting in five input nodes for tau type 1 and six input nodes for tau type 2 and 3. The hidden layer consists of several nodes, the number being equivalent to the number of input nodes. The output layer con-

sists of a single node. There is no connection between any two nodes of a given layer, nor is there any direct connection between input nodes and the output.

Each hidden node  $h_j$  represents a neuron that performs a linear combination of input signals:

$$h_j = \sum_{i=1}^{n_i} W_{ij}x_i \quad (4.6)$$

where  $x_i$  is the i-th input and  $W_{ij}$  is a weighting factor. It generates an output in a normalized sigmoid form:

$$s(h_j + B_j) = \frac{1}{1 + \exp(-(h_j + B_j))}. \quad (4.7)$$

The bias  $B_j$  is added in order to improve the response of the sigmoid function. The output is a linear combination of the hidden node outputs, on which a sigmoid function is also applied.

For  $n_i$  inputs and  $n_h$  hidden nodes, there are all together  $n_h(n_i + 1)$  free parameters for the weights and  $n_h + 1$  free parameters for the biases. Given a set of signal and a set of background events for training, the program determines the weights and biases by iterative function minimization for optimal signal-background discrimination. The weights and biases are corrected in proportion to the error they have generated (desired output value - computed valued) and to the derivative of the sigmoid function  $s(s-1)$ . This leads to a more important correction if the output of a given neuron does not peak near to 0 or 1.

According to the convention, 1 (0) represents the desired signal (background) output. Each neural network is trained with a reasonably high number of epochs (500-1000). As a signal training sample, a Monte Carlo sample of single tau leptons uniformly distributed in  $\eta$  and transverse energy overlaid with a minimum bias event are chosen. As the background training sample, a data sample of jets which recoil against a non-isolated muon are used. The tau candidate used for the training is required to have a visible  $E_T$  above 10 GeV and  $|\eta_{phys}| < 3.0$ , otherwise the event is discarded.

## Discriminating Variables

The neural networks use input variables, which fill directly the values of the input node. The input variables were chosen to minimize the dependence on the tau energy and to exploit the narrow width of the energy deposition in the calorimeter, the low track multiplicity and the low tau mass. Table 4.2 presents an overview of the input variables that are used for each tau type. The variables are explained in the following:

- profile =  $\frac{E_{T_1} + E_{T_2}}{E_T}$ :  $E_{T_1}$  and  $E_{T_2}$  are the transverse energies of the two most energetic calorimeter towers;
- iso =  $\frac{E_T(\Delta R < 0.5) - E_T(\Delta R < 0.3)}{E_T(\Delta R < 0.3)}$ : calorimeter isolation parameter used for all tau types;

- $E_{T,iso}^\tau$ : transverse energy of the tau cluster in the isolation cone defined as  $\Delta\mathcal{R} < 0.5$ ;
- $\text{ettr} = \sum p_T^{trk}$ : sum of all tracks within a  $\Delta\mathcal{R} < 0.5$  cone that are not associated with the tau;
- $\text{ettsum} = \sum p_T^{\tau trk}$ : sum of all tracks that are associated with the tau;
- $\text{EM12isof} = \frac{E^{EM1} + E^{EM2}}{E}$ : ratio of the tau energy deposition in the first two layers of the electromagnetic calorimeter (EM1 and EM2) and the total tau energy deposition. The energy is calculated in a  $\Delta\mathcal{R} < 0.5$  cone;
- $p_T^{\tau trk1}$ : transverse momentum of the highest  $p_T$  track associated with the tau;
- $e1e2 = \sqrt{\text{ettsum} \cdot E_T^{\text{EM}}}$ : product of the  $p_T$  sum of all tau tracks (see definition above) and the transverse energy deposited in the EM layer of the calorimeter;
- $\delta\alpha = \sqrt{(\Delta\phi/\sin\theta)^2 + (\Delta\eta)^2}$ : the differences are calculated between the sum of the tau tracks and the sum of the electromagnetic clusters, while  $\theta$  is the azimuthal angle of the calorimeter cluster centroid. In the small angle approximation, the tau mass is given by  $e1e2 \cdot \delta\alpha$ .

The neural networks either use directly these variables or a combination of them, as indicated in Table 4.2. Figure 4.4 shows the distribution of each input variable that is used for tau type 1. As a signal, a hadronically decaying tau in  $Z \rightarrow \tau\tau$  Monte Carlo is used. The QCD background is derived from data by selecting events with a like-sign electron and tau candidate, where the shower profile of the electron corresponds to a QCD jet. This is achieved by inversion of the HMx8 variable (see Section 4.3.1). As a further requirement, both objects have to be well-separated ( $\Delta\mathcal{R} > 0.5$ ). The resulting neural network output for signal and background sample is presented in Figure 4.5. The distributions of the input variables for tau type 2 are shown in Figure 4.6. The resulting neural network output is presented in Figure 4.7. The corresponding plots for tau type 3 are shown in Figure 4.8 and Figure 4.9. In Figure 4.10 the background rejection is shown as a function of the signal efficiency for all three tau types.

Variable	Tau type 1	Tau type 2	Tau type 3
profile	yes	yes	yes
iso	yes	yes	yes
ettr/ettsum	yes	yes	yes
EM12isof	yes	no	no
$p_T^{\tau trk1}/E_{T,iso}^\tau$	no	yes	yes
$p_T^{\tau trk}/E_T^\tau$	yes	no	no
e1e2/ $E_T^\tau$	no	yes	yes
$\delta\alpha/\pi$	no	yes	yes

Table 4.2: Input variables for the three neural networks, corresponding to the three different tau types (yes/no=variable is/is not used). The variables are explained in the text.

#### 4.4 Tau Reconstruction and Identification

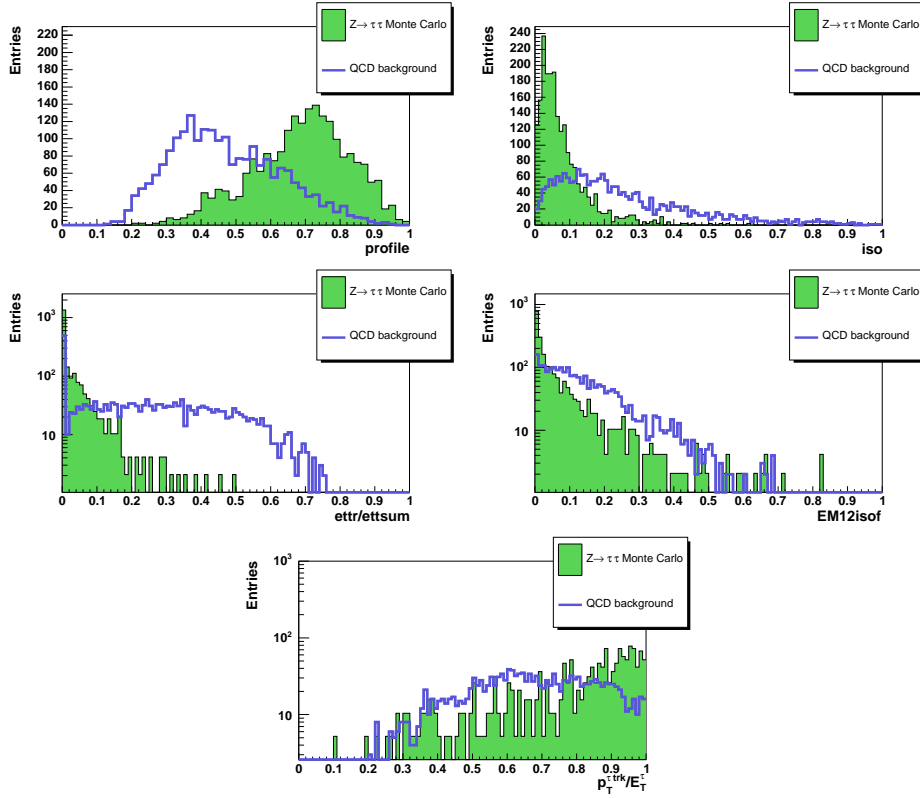


Figure 4.4: Neural network input variables for tau type 1: `profile`, `iso`, `ettr/ettsum`, `EM12isof`,  $p_T^{\text{trk}}/E_T$ . The green histogram represents hadronic decays of taus in  $Z \rightarrow \tau\tau$  Monte Carlo, the empty histogram a QCD sample that is derived using data. All input variables have to be in the range between 0 and 1, larger values are set to 1.

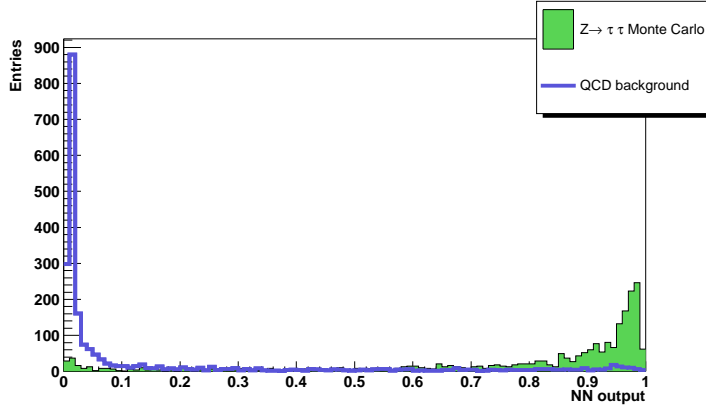


Figure 4.5: Resulting neural network output variable for tau type 1. The green histogram represents hadronic decays of  $\tau$ s in  $Z \rightarrow \tau\tau$  Monte Carlo, the empty histogram a QCD sample. According to the chosen convention, the  $Z \rightarrow \tau\tau$  signal Monte Carlo leads to a peak at 1, while the background peaks at 0.

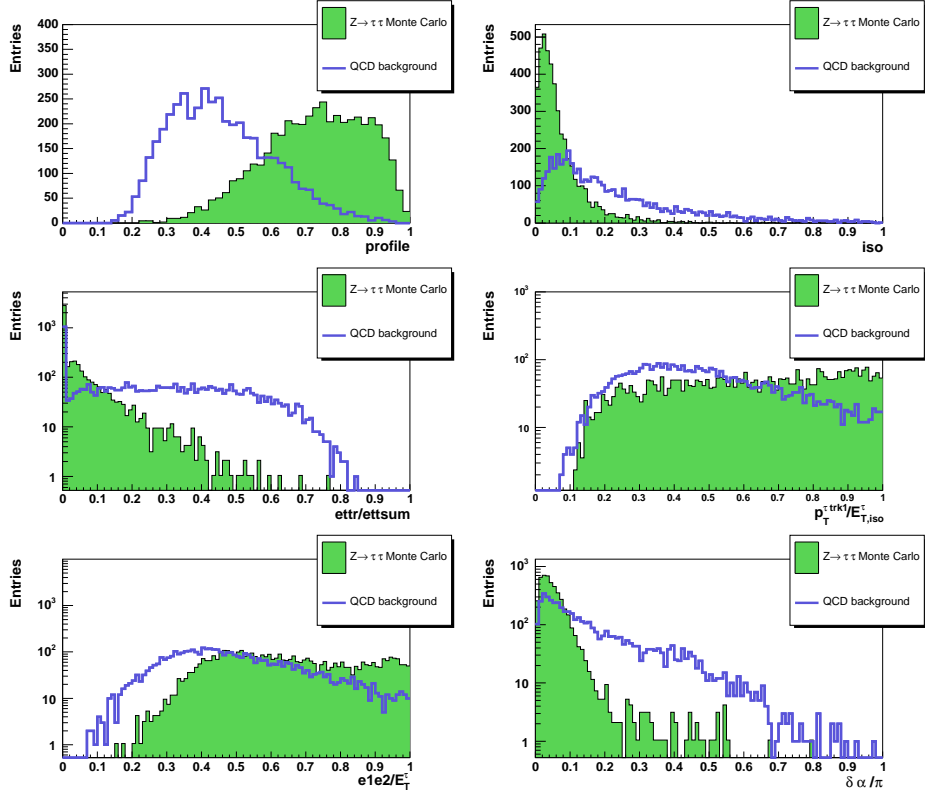


Figure 4.6: Neural network input variables for tau type 2: `profile`, `iso`, `ettr/etsum`,  $p_T^{\tau trk}/E_{T,\text{iso}}^{\tau}$ ,  $e1e2/E_T^{\tau}$ ,  $\delta\alpha/\pi$ . The green histogram represents hadronic decays of taus in  $Z \rightarrow \tau\tau$  Monte Carlo, the empty histogram a QCD sample that is derived using data. All input variables have to be in the range between 0 and 1, larger values are set to 1.

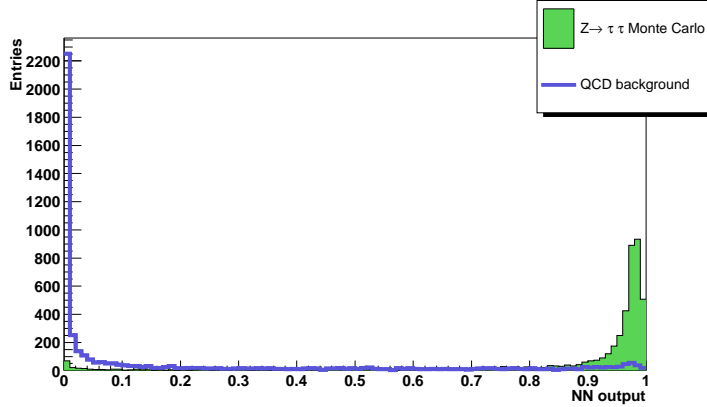


Figure 4.7: Neural network output variable for tau type 2. The green histogram represents hadronic decays of taus in  $Z \rightarrow \tau\tau$  Monte Carlo, the empty histogram a QCD sample. According to the chosen convention, the  $Z \rightarrow \tau\tau$  signal Monte Carlo leads to a peak at 1, while the background peaks at 0.

#### 4.4 Tau Reconstruction and Identification

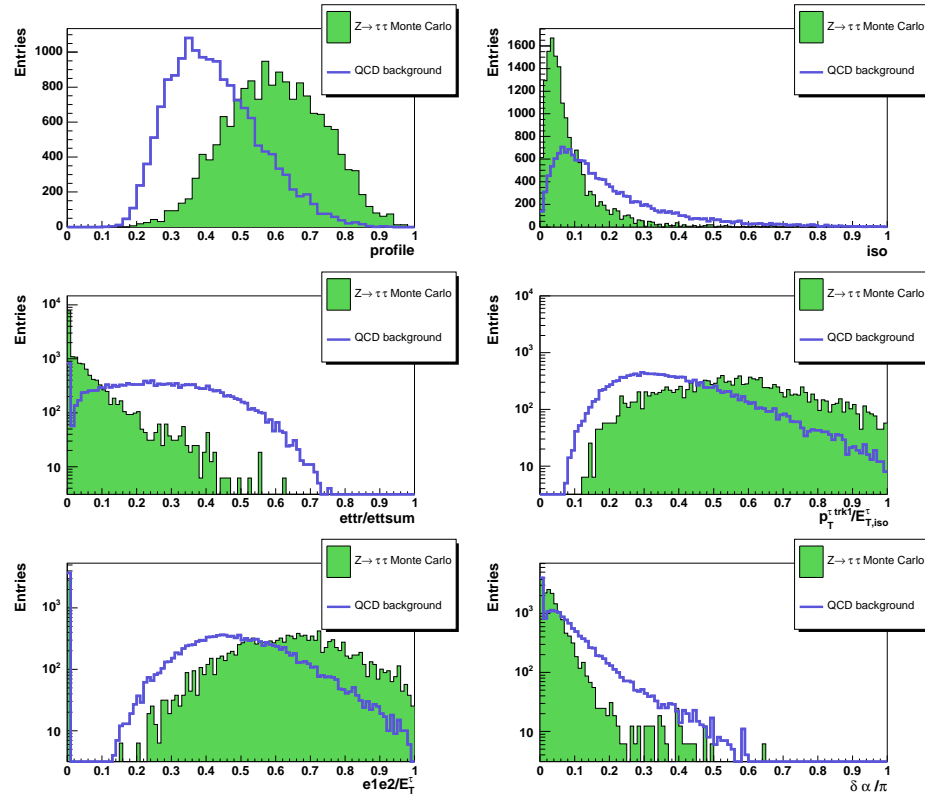


Figure 4.8: Neural network input variables for tau type 3: `profile`, `iso`, `ettr/ettsum`,  $p_T^{\text{trk}}/E_T^{\text{iso}}$ ,  $e1e2/E_T^{\text{iso}}$ ,  $\delta\alpha/\pi$ . The green histogram represents hadronic decays of taus in  $Z \rightarrow \tau\tau$  Monte Carlo, the empty histogram a QCD sample that is derived using data. All input variables have to be in the range between 0 and 1, larger values are set to 1.

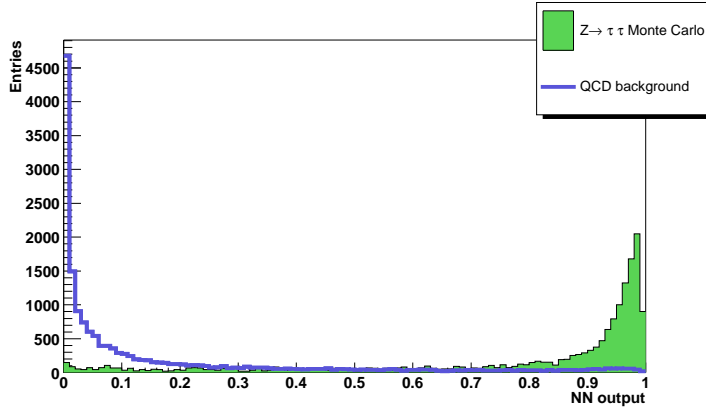


Figure 4.9: Neural network output variable for tau type 3. The green histogram represents hadronic decays of taus in  $Z \rightarrow \tau\tau$  Monte Carlo, the empty histogram a QCD sample. According to the chosen convention, the  $Z \rightarrow \tau\tau$  signal Monte Carlo leads to a peak at 1, while the background peaks at 0.

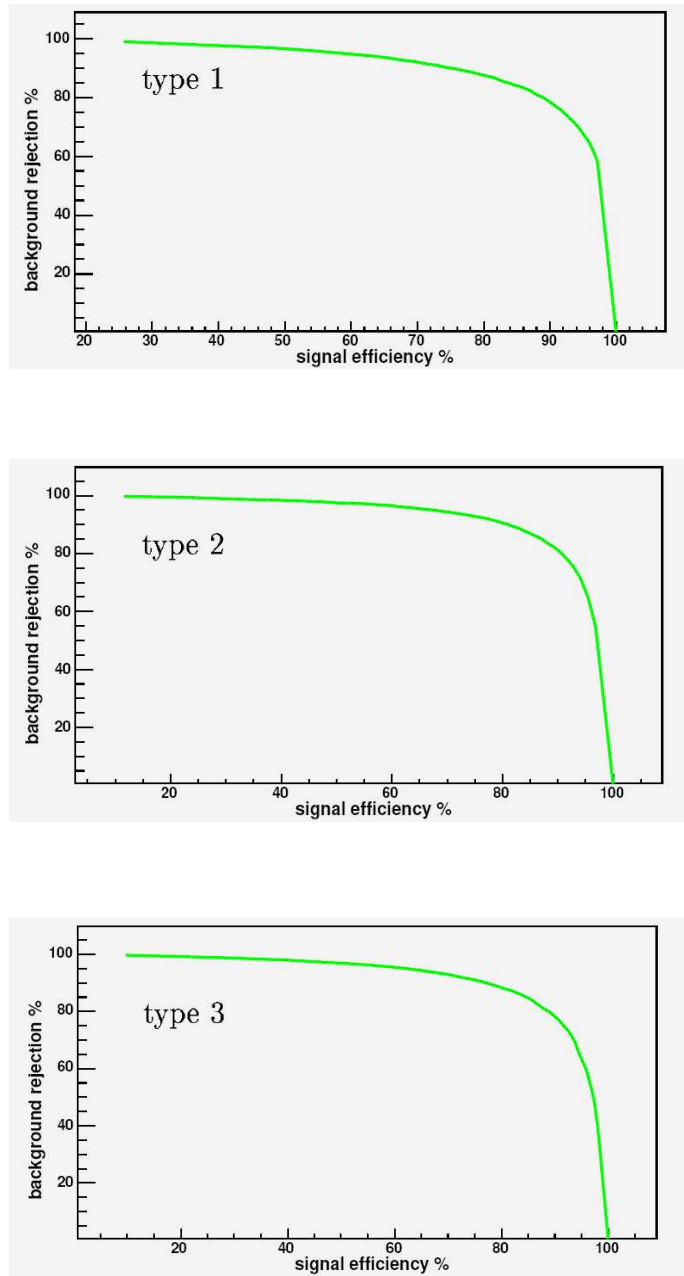


Figure 4.10: Background rejection versus tau efficiency for tau type 1, 2 and 3 (from Ref. [57]).

## 4.5 Jet Reconstruction and Identification

Collimated streams of hadrons are observed as jets in the detector, since individual quarks and gluons cannot be detected directly due to color confinement.

The jet algorithm uses the simple cone algorithm to build preclusters, which serve as seeds for the *Run II Cone Algorithm*. The Run II Cone Algorithm proceeds in three steps called clustering, addition of midpoints and merging/splitting. A detailed description can be found in [56]. In the following, jets with a low fraction of the jet energy deposited in the electromagnetic layers of the calorimeter (EM fraction  $< 0.9$ ) are called *hadronic jets*, while jets with a higher EM fraction (EM fraction  $> 0.9$ ) are called *electromagnetic jets*.

This analysis uses  $\Delta R = 0.5$  cone jets, which have to fulfill the following identification requirements [61]:

- $HOTf < 10$ : The ratio of the energy of the highest to the next-to-highest calorimeter tower is used to remove jets clustered from *hot cells*. Hot cells/towers are usually related to detector problems like hardware failure or abnormal electronic noise. The energy of a hot cell is typically large ( $> 1$  GeV).
- $N90 > 1$ : The number of calorimeter towers containing 90 % of the energy of the jet is used to remove jets that are clustered from a single hot tower.
- $0.05 < EM\ fraction < 0.9$ : The fraction of the jet energy deposited in the electromagnetic layers of the calorimeter is used to remove isolated electromagnetic particles.

Calorimeter noise, stemming from either the calorimeter cells or the calorimeter electronics in the readout chain, can be misidentified as jets. These jets are the main background source after application of the jet identification criteria, and they are suppressed by applying the following quality requirements [62]:

- The calorimeter noise from the cells is dominated by the coarse hadronic layers (CHF). To remove jets which predominantly deposit their energy in the coarse hadronic layers, the energy fraction in the coarse hadronic layers (CHF) has to be smaller than 0.4.
- To remove jets originating from noise in the calorimeter readout, the L1 trigger readout chain is utilized. To confirm the presence of real jets, the ratio of the jet energy measured by the L1 system to the jet energy measured by the precision readout must be larger than 0.4. This is referred to as L1 confirmation.

A jet that satisfies both the identification criteria and the quality requirements is regarded as a *good jet*. This analysis uses only good jets with a corrected transverse energy (see below) of  $E_T > 15$  GeV.

### Jet Energy Scale Correction

Although the calorimeter effectively absorbs the hadronic energy of the jet, there are several mechanisms which can cause the energy of the cells clustered into a jet to deviate from the energy of the initial parton(s). The most important are:

- *Calorimeter Response (R)*: The measured jet energy can be distorted due to a varying response to different particles, a non-linear response as a function of the particle energy, uninstrumented regions of the detector and dead material.
- *Energy Offset (O)*: Energy contribution to the measured jet from the underlying event, multiple interactions, energy pile-up, electronics noise and noise from the uranium absorber can result in an offset to the jet energy.
- *Showering Corrections (S)*: Due to shower leakage outside the jet cone ( $\Delta R < 0.5$ ), a fraction of the jet energy is not accounted for.

In contrast to electromagnetic jets, which are corrected using the electromagnetic scale, hadronic jets are calibrated using the jet energy scale (JES) [63]. The JES corrections attempt to correct the reconstructed jet energy ( $E^{reco}$ ) back to the particle level energy ( $E^{corr}$ ), using the following equation:

$$E^{corr} = \frac{E^{reco} - O}{R \times S}. \quad (4.8)$$

The main contribution to the JES corrections stems from the calorimeter response R. It is derived from studying  $\gamma + jet$  events, where the high energetic photon recoils against the jet. The conservation of transverse momentum allows the correction of the jet energy using the electromagnetic scale, which is independently calibrated using  $Z \rightarrow ee$  events. The energy offset O is determined from energy densities in events which are triggered when a minimum activity in the luminosity monitor is reported (so-called minimum-bias triggered events). The showering corrections S are determined from measured energy profiles of jets.

The JES correction factors are derived separately for Monte Carlo and data since the calorimeter response is not modelled perfectly in the Monte Carlo simulation. Figure 4.11 shows the JES correction factors and their errors as a function of the jet energy and the  $\eta_{det}$  position of the jet. Figure 4.12 shows the same histograms for Monte Carlo. Hadronic jets with  $E < 15$  GeV are calibrated with the JES for jets with  $E = 15$  GeV.

### 4.6 Missing Transverse Energy ( $\cancel{E}_T$ )

The missing transverse energy ( $\cancel{E}_T$ ) measures the imbalance of the deposited energy in the calorimeter system. The imbalance stems from physics objects like

e.g. neutrinos, which do not deposit their energy in the detector. The missing transverse energy corresponds to the negative sum of the calibrated energy depositions in the detector. It is calculated from the raw missing transverse energy and additional corrections for the calorimeter response of physics objects. The finite energy resolution of the calorimeter system leads to a certain  $\cancel{E}_T$  resolution, which is worsened by additional detector effects like noise in the readout electronics. The amount of missing transverse energy in an event is an import signature for various physics processes, and its precise knowledge is vital for both analyses that are presented later.

The raw missing transverse energy ( $METB$ ) is calculated using all calorimeter cells within the electromagnetic and fine hadronic layers of the calorimeter that have a non-zero energy. Cells from the coarse hadronic layer are excluded, except for coarse hadronic cells which belong to a good jet (see Section 4.5). This avoids mismeasured missing transverse energy from noise in the coarse hadronic layer. The projections of  $METB$  on the  $x$  and  $y$  axis are given by:

$$METB_{x,y} = - \left( \sum_{i \in \{E^{cell}, \cancel{E}_T > 0\}} E_{x,y}^i + \sum_{i \in \{good\ jets\ and\ E^{CH} > 0\}} E_{x,y}^i \right) \quad (4.9)$$

$$METB = \sqrt{METB_x^2 + METB_y^2}. \quad (4.10)$$

The raw missing transverse energy has to be corrected for the calorimeter response of the physics objects. For electron candidates, the difference of the fully calibrated energy of the electron and the sum of the corresponding calorimeter cells is propagated into  $\cancel{E}_T$ . For jet candidates, the jet energy scale calibration is propagated into the calculation of the missing transverse energy. There is currently no dedicated energy calibration for tau candidates available, however, Monte Carlo studies and first results from analyses that use hadronic tau decays indicate that the energy corrections are small [60]. Muons are minimum ionizing particles which deposit only a small amount of energy in the calorimeter. Their presence can thus also fake missing transverse energy in the detector. Their energy deposition is corrected by the difference to the full muon transverse momentum as measured in the muon system and in the tracker. Insufficient calibration of the energy measurement of the physics objects can deteriorate the resolution of the missing transverse energy.

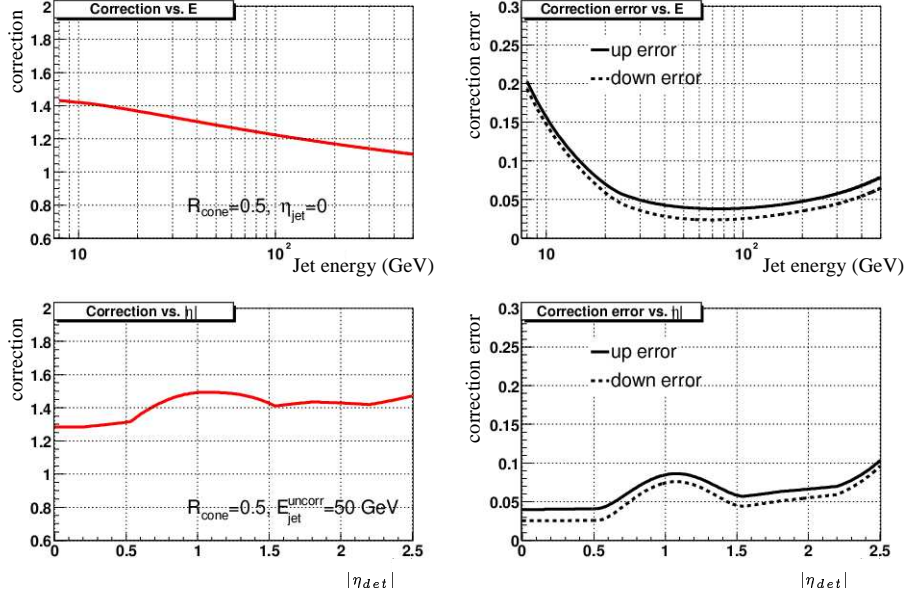


Figure 4.11: Jet energy scale calibration factors and the corresponding errors for data as a function of the uncalibrated jet energy for  $\eta = 0$  (top) and as a function of  $\eta_{det}$  for  $E_{jet} = 50 \text{ GeV}$  (bottom) (from Ref. [64]).

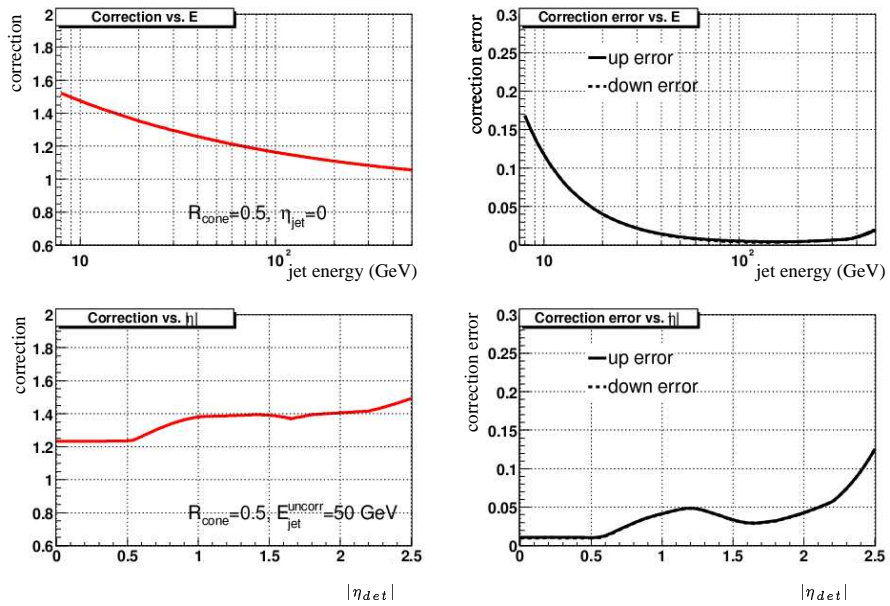


Figure 4.12: Jet energy scale calibration factors and the corresponding errors for Monte Carlo as a function of the uncalibrated jet energy for  $\eta = 0$  (top) and as a function of  $\eta_{det}$  for  $E_{jet} = 50 \text{ GeV}$  (bottom) (from Ref. [64]).

# 5 Data Sample and Monte Carlo Simulation

The first part of this chapter describes the data sample that is used for both analyses, the trigger requirements and the applied data quality criteria. The quality criteria are needed to ensure that all detector components necessary for the reconstruction of the final state objects have been working well.

The second part describes the Standard Model Monte Carlo samples that are used. Due to an incomplete implementation of the detector in the full detector simulation and a missing trigger simulation, the Monte Carlo samples do not reproduce the data correctly. Hence efficiency corrections are derived for data comparisons and acceptance estimations.

## 5.1 Data Sample

The data sample used in this thesis has been collected from August 2002 to June 2004 by the DØ detector. During this period, roughly 1 billion events have been recorded.

The DØ experiment provides *skims* of the Run II data in order to reduce the processing effort for the individual analyses. A skim is a preselection of data events containing specific physics objects with quality requirements. This thesis uses the EM1TRK skim, which requires one electron with  $|ID| = 10, 11$  (see Section 4.3) and  $E_T$  in excess of 8 GeV and a track with  $p_T > 5$  GeV matched to the electron within  $\Delta\phi < 0.1$  to be present in the event. The EM1TRK skim consists of approximately 55 million events.

### 5.1.1 Data Quality Criteria

Both analyses rely on good identification and a precise measurement of the kinematic quantities of an electron, a hadronic tau, tracks and additional jets. Furthermore, the missing transverse energy is of importance and needs to be accurately measured. To ensure that all detector components, which are needed for the reconstruction of these objects, have been working well, certain quality requirements are imposed. These quality requirements are either evaluated for a whole *run*, corresponding to usually several hours of data taking, or for a *luminosity block*, corresponding to one minute of data taking. The following quality requirements are imposed:

- **Calorimeter quality selection:** Data units where the direct run control or the distribution of characteristic quantities (e.g. large average  $E_T$ ) indicate calorimeter problems are discarded [65, 66, 67].
- **Tracking quality selection:** Runs with known problems in either the SMT or in the CFT are discarded [67].
- **Luminosity quality selection:** Luminosity blocks with problems in the luminosity DAQ or HV settings, with online losses, incomplete events, L3 losses, unreadable tapes and problems with the reference triggers (see Section 5.2) are discarded from the data sample [69].

### 5.1.2 Trigger Selection

The rate of  $p\bar{p}$  collisions at the Tevatron is significantly higher than the rate at which events can be read out and stored for offline analysis. In order to select only interesting physics events and filter them out of the large background of inelastic proton-antiproton reactions (see discussion in Chapter 3), various dedicated triggers have been developed. The data sample for this thesis has been collected during two different trigger epochs. The first trigger epoch (August 2002-June 2003) is covered by trigger list v5-v11 and contains the run numbers 151817-178721. The second trigger epoch (July 2003-August 2004) is covered by trigger list v12 and contains the run numbers 178722-194566. Both trigger epochs are treated separately due to major changes and improvements for trigger list v12.

Based on the characteristic detector signature of an electron (see Section 4.3), electrons can be identified very clearly at the trigger level. Hence the various single electron triggers are used to select the data. These triggers are combined with a logical OR as they can trigger a given data event simultaneously. Table 5.1 gives an overview of the single electron triggers that are used in this thesis. A detailed description of the trigger names used at the different trigger levels is presented in Table 5.2. The trigger efficiency is discussed in Section 5.5.1.

## 5.2 Integrated luminosity

The integrated luminosity of the data sample is calculated using the single electron trigger with the highest  $p_T$  threshold. For the first trigger epoch, covering trigger list v5-v11, the integrated luminosity is calculated using EM\_MX. For the second trigger epoch, covering trigger list v12, E1\_SH30 is used to calculate the integrated luminosity. Table 5.3 shows the integrated luminosity for different trigger versions and data taking periods.

Trigger Name	Level 1	Level 2	Level 3
Trigger List v5-v11			
EM_HI	CEM(1,10)	EM(1,12)	L20
EM_HLSH	CEM(1,10)	EM(1,12)	SH20
EM_HI_SH_TR	CEM(1,10)	EM(1,12)	TK12*SH12
EM_MX	CEM(1,15)	none	L30
EM_MX_SH	CEM(1,15)	none	SH20
EM_MX_SH_TR	CEM(1,15)	none	TK12*SH12
Trigger List v12			
Ex_SH30	E1-E4	none	SH30
Ex_SHT20	E1-E4	none	SHT20
Ex_T13L15	E1-E4, E6	none	T13L15
Ex_SHT15_TK13	E1, E2, E4-E6	none	SHT15*TK13
Ex_T7SHT8_2TK5	E1-E8	none	T7SHT8*2TK5

Table 5.1: Single electron triggers used in both analyses. The symbol \* denotes a logical AND. The description of the trigger names is given in Table 5.2.

The integrated *delivered luminosity* [68] is calculated using the rate of inelastic collisions measured with the luminosity monitor (see Section 2.3.5). The integrated *reconstructed luminosity* [69] corresponds to the fraction of recorded events that is reconstructed and that pass the data quality requirements presented in Section 5.1.1.

The estimated systematic error on the integrated luminosity is 6.5 % [70]. Main contributions to this error stem from the measurement of the inelastic proton-antiproton cross-section followed by the understanding of the kinematic distributions for diffractive processes [71].

The resulting integrated luminosity for the data set used in both analyses is:

$$\int \mathcal{L} dt = 327.3 \pm 21.3 \text{ pb}^{-1}. \quad (5.1)$$

### 5.3 Standard Model Monte Carlo Samples

The search for the associated production of the lightest chargino and the second lightest neutralino (see Chapter 6) and the search for neutral MSSM Higgs bosons (see Chapter 7) are both performed in a final state consisting of an electron, a hadronic tau and missing transverse energy. The third lepton in the trilepton analysis is identified by an isolated track. There are only a few Standard Model processes which can produce the same final state signature, meaning that the resulting final state consists of a real electron, a real hadronic tau decay and true missing transverse energy. However, there are a variety of backgrounds which can produce a similar detector signature due to lepton

## 5 Data Sample and Monte Carlo Simulation

---

	Description
Level 1	
CEM(N,x)	N electromagnetic tower(s) with $E_T > x$ GeV
TTK(N,x)	N tracks with $p_T > x$ GeV
TIS(N,x)	N isolated tracks with $p_T > x$ GeV
E1	CEM(1,10)
E2	CEM(2,6)
E3	CEM(1,9)*CEM(2,3)
E4	CEM(1,9)*TTK(1,10)
E5	CEM(1,6)*CEM(2,3)*TTK(1,10)
E6	CEM(1,6)*TIS(1,10)
E7	CEM(1,6)*CEM(2,3)*TTK(1,5)*TTK(2,3)
E8	CEM(1,10)*TTK(2,5)*TIS(1,5)
Level 2	
EM(1,12)	One EM candidate with $E_T > 12$ GeV
Level 3	
L20	One electron with $ \eta  < 3.0$ and $E_T > 20$ GeV passing loose EM cluster requirements (EM fraction > 0.9).
L30	One electron with $ \eta  < 3.0$ and $E_T > 30$ GeV passing loose requirements.
SH20	One electron with $ \eta  < 3.0$ and $E_T > 20$ GeV passing loose requirements including shower shape cuts.
TK12*SH12	One electron with $ \eta  < 3.0$ and $E_T > 12$ GeV passing loose requirements including shower shape cuts. Event must contain one track with $p_T > 12$ GeV.
SH30	One electron with $ \eta  < 3.6$ and $E_T > 30$ GeV passing loose shower shape requirements.
SHT20	One electron with $ \eta  < 3.6$ and $E_T > 20$ GeV passing tight shower shape requirements.
T13L15	One electron with $ \eta  < 3.6$ and $E_T > 15$ GeV passing loose requirements with a matched track with $p_T > 13$ GeV.
SHT15*TK13	One electron with $ \eta  < 3.6$ and $E_T > 15$ GeV passing tight shower shape requirements. Event must contain one track with $p_T > 13$ GeV.
T7SHT8*2TK5	One electron with $ \eta  < 3.6$ and $E_T > 8$ GeV passing tight shower shape requirements with a matched track with $p_T > 7$ GeV. Event must contain two tracks with $p_T > 5$ GeV.

Table 5.2: Description of the trigger names that are used at the different trigger levels. The symbol \* denotes a logical AND.

Trigger Version	Reference Trigger	Delivered Luminosity	Reconstructed Luminosity (data quality applied)
v5-v11	EM_MX	179.0 pb <sup>-1</sup>	121.3 pb <sup>-1</sup>
v12	E1_SH30	247.8 pb <sup>-1</sup>	206.0 pb <sup>-1</sup>
Sum		426.8 pb <sup>-1</sup>	327.3 pb <sup>-1</sup>

Table 5.3: Integrated delivered and reconstructed luminosity for the data of the two trigger epochs used in this thesis. The data quality criteria presented in Section 5.1.1 are applied.

misidentification and/or  $\cancel{E}_T$  mismeasurement. All *background processes* are summarized in Table 5.4. They are simulated using Monte Carlo methods described in Section 3.6. The leading order cross sections are scaled with a K-factor to take higher order QCD corrections into account (see Section 3.5). The background from QCD multijet production (QCD background) is derived from data, the exact procedure is described in Section 5.4.

The reconstructed electron usually stems from a real electron or a misidentified jet, while the reconstructed tau can stem from either a real tau decay or from a misidentified electron, muon or jet. The events can contain true missing transverse energy arising from neutrino(s) in the final state, or the energy imbalance can be a consequence of an energy mismeasurement. Since the various Standard Model background sources are of different importance for the trilepton and the Higgs analysis, a further discussion follows in Chapters 6 resp. 7.

## 5.4 Background from QCD Jet Production

The Standard Model background from QCD jet production corresponds to events where jets are misidentified as an electron and a hadronically decaying tau. The contributions of QCD multijet processes are determined from data by selecting a sample that is dominated by QCD events. This *QCD sample* will be used in both analyses to determine the QCD background at various stages of the selection.

The QCD sample is determined by selecting events where the electron and the tau candidate have the same charge (so-called *like-sign* events). Since a typical jet is composed of numerous hadronization products, both like-sign and unlike-sign events occur in QCD multijet processes. The like-sign sample is expected to be dominated by QCD multijet events.

A variety of the Standard Model processes listed in Table 5.4 can also result in a like-sign  $e + \tau_h$  final state. Their contribution to the QCD sample is estimated by selecting like-sign  $e + \tau_h$  events in Monte Carlo. This contribution is subtracted from the QCD sample. The probability to measure the wrong electron charge in  $Z/\gamma^* \rightarrow ee$  event is significantly lower in Monte Carlo than in data. To correct for this effect, a *charge misidentification factor* of 4.5 is

## 5 Data Sample and Monte Carlo Simulation

---

Process	Mass Range [GeV]	K-factor	$\sigma \times BR$ [pb]	# Events
$Z/\gamma^* \rightarrow ee$	$15 < M_{ee} < 60$	NNLO	$434 \pm 15$	300k
$Z/\gamma^* \rightarrow ee$	$60 < M_{ee} < 130$	NNLO	$254 \pm 8$	300k
$Z/\gamma^* \rightarrow ee$	$130 < M_{ee} < 250$	NNLO	$2.0 \pm 0.6$	261k
$Z/\gamma^* \rightarrow ee$	$250 < M_{ee} < 500$	NNLO	$0.167 \pm 0.006$	50k
$Z/\gamma^* \rightarrow ee$	$M_{ee} > 500$	NNLO	$0.00070 \pm 0.0003$	25k
$Z/\gamma^* \rightarrow \tau\tau$	$15 < M_{\tau\tau} < 60$	NNLO	$434 \pm 15$	300k
$Z/\gamma^* \rightarrow \tau\tau$	$60 < M_{\tau\tau} < 130$	NNLO	$254 \pm 8$	400k
$Z/\gamma^* \rightarrow \tau\tau$	$130 < M_{\tau\tau} < 250$	NNLO	$2.0 \pm 0.6$	104k
$Z/\gamma^* \rightarrow \tau\tau$	$250 < M_{\tau\tau} < 500$	NNLO	$0.167 \pm 0.006$	48.5k
$Z/\gamma^* \rightarrow \tau\tau$	$M_{\tau\tau} > 500$	NNLO	$0.0070 \pm 0.0003$	23k
$W(\rightarrow e)$ incl.		NNLO	$2600 \pm 93$	1.80M
$W(\rightarrow \mu)$ incl.		NNLO	$2600 \pm 93$	2.83M
$W(\rightarrow \tau)$ incl.		NNLO	$2600 \pm 93$	1.74M
$WW(\rightarrow 2 \text{ leptons})$		NLO	$1.67 \pm 0.07$	170k
$WZ$ incl.		NLO	$3.58 \pm 0.25$	53k
$ZZ$ incl.		NLO	$1.42 \pm 0.08$	53.5k
$t\bar{t} \rightarrow b\bar{b}ll\nu\nu$		NLO	$0.67 \pm 0.04$	101k
$t\bar{t} \rightarrow b\bar{b}jjl\nu$		NLO	$2.68 \pm 0.13$	150k
$\Upsilon(1s)$			$35 \pm 10$	30k

Table 5.4: Cross section times branching ratio ( $\sigma \times BR$ ) and number of generated events for the different background Monte Carlo samples. The error on the cross section is given by the PDF uncertainty (see Ref. [72]). The leading-order cross section is scaled with a K-factor (see Section 3.5). For the  $Z/\gamma^*$  and  $W$  inclusive samples  $K_{NNLO}$  from Ref. [73] is used. Cross sections for the di-boson samples are calculated in [74], while the cross sections for the  $t\bar{t}$  samples are taken from [75].

derived in a data/Monte Carlo comparison of the invariant mass distribution of the electron and the tau at preselection stage. The correction factor is applied to the like-sign  $Z/\gamma^* \rightarrow ee$  events before they are subtracted from the QCD sample.

In order to estimate the QCD background in both analyzes correctly, the QCD sample is normalized to data. This normalization is done at an early selection stage in a region of phase space where QCD multijet events dominate, the backgrounds from other Standard Model processes are small and where the signal contribution can be neglected.

In the search for associated neutralino/chargino production, the normalization of the QCD sample to the data is performed in the  $M(e, \tau_h) > 130$  GeV region of the invariant electron and tau mass at preselection stage. In the search for neutral MSSM Higgs bosons, the  $NN < 0.3$  region of the tau neural network output at preselection state is used. The latter method can not be used for trilepton analysis, since a tau neural network output that exceeds 0.3 is required in the preselection to keep the amount of data manageable. For both methods a scale factor for each tau type is derived, and the uncertainty on these scale factors is taken into account as a systematic error. Within the errors, both methods

result in the same QCD scale factors for each tau type, which are presented in Table 5.5. Figure 5.1 shows the invariant  $e + \tau_h$  mass distribution at preselection level, Figure 5.2 shows the neural network distributions for all three tau types at preselection level. The QCD scale factors are applied, demonstrating a good modeling of the QCD background.

Tau Type	QCD Scale Factor
1	$2.09 \pm 0.09$
2	$2.32 \pm 0.05$
3	$1.96 \pm 0.02$

Table 5.5: QCD scale factors with their respective errors.

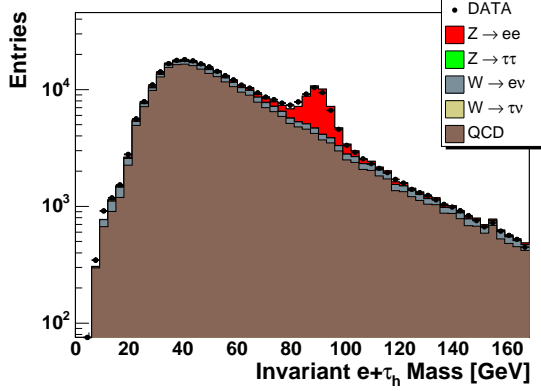


Figure 5.1: QCD background normalization using the invariant  $e + \tau_h$  mass distribution.

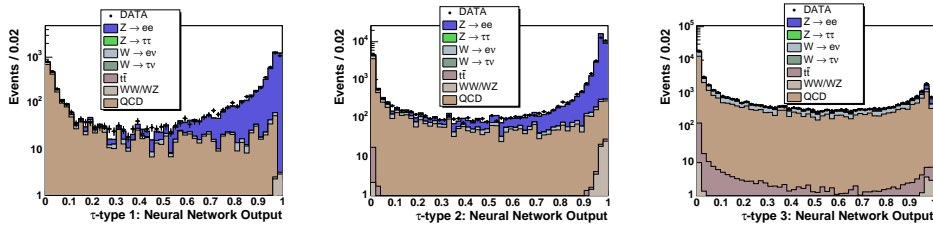


Figure 5.2: QCD background normalization using the tau neural network distributions for tau type 1 (left), tau type 2 (middle) and tau type 3 (right). All distributions are shown at preselection level.

## 5.5 Monte Carlo Efficiency and Resolution Corrections

The various signal and background Monte Carlo samples are used to estimate the number of Standard Model background events at each selection stage and

to determine signal efficiencies. In addition, they are used to optimize the event selection criteria. Hence it is required to cross-check that the simulated events reproduce the data events. If necessary, corrections have to be applied.

The Monte Carlo samples do not reproduce the data correctly due to the fact that the triggers are not simulated in Monte Carlo and due to an incomplete implementation of the detector in GEANT [49]. These effects lead to corrections of the electron identification efficiency and the resolution of the missing transverse energy. Further corrections have to be determined for the  $p_T$  resolution of the tracker and the calorimeter.

The corrections which are derived in the following sections affect mainly the electron candidate. Hence they play an important role in the correct modeling of signal and background samples like the  $Z/\gamma^* \rightarrow ee$  and  $W \rightarrow e\nu$  backgrounds, which are both relevant for the optimization of the selection criteria. The uncertainties of all corrections are included in the systematic error on the final results.

### 5.5.1 Trigger Efficiency

The efficiencies of the single electron triggers used in both analyses have to be measured in data and then be folded into both signal and background Monte Carlo. This is done separately for data taken with trigger version v5-v11 and for data taken with trigger version v12.

The trigger efficiency is measured for each selected trigger in a di-electron selection using the tag-and-probe method. The di-electron selection requires two EM candidate objects ( $|ID| = 10, 11$ ,  $\text{EMfrac} > 0.9$ ,  $\text{iso} < 0.15$ ) with  $p_T > 8 \text{ GeV}$ . The tag electron is required to have a likelihood value that exceeds 0.8 and to pass a single electron trigger, either EM\_HI or EM\_HI\_SH in the case of trigger list v11 respectively E1\_SH30 or E1\_SHT20 for trigger list v12. The probe electron has to fulfill the electron identification criteria that are applied in each analysis:  $\text{HMx8} < 20$  and track match with  $E/p$  in the case of the trilepton analysis, respectively likelihood  $> 0.8$  in the case of the search for neutral MSSM Higgs bosons. For each trigger (see Table 5.1) it is tested whether the probe electron has passed the corresponding requirements at each trigger level. The trigger efficiency corresponds to the ratio of the number of probe electrons passing the trigger requirements and the number of all probe electrons. It is a function of the electron transverse momentum. For the tag-and-probe method, both electrons are considered as possible tags to avoid any bias. Due to the tight di-electron selection cuts, the QCD contribution is negligible and is accounted for by a systematic error. In the final analysis, the trigger version to correct for is chosen randomly for each Monte Carlo event according to the luminosity share. The measured trigger efficiencies are presented below.

As discussed in Section 4.4, no attempt is made at reconstruction stage to separate electrons from taus. Therefore real electrons will be reconstructed with

a very high efficiency as tau type 2 candidates (resp. tau type 1 candidates in the inter-cryostat region), and the tau candidate can fire the single electron trigger and contribute to the total trigger efficiency of the event. A further discussion follows in Chapter 6 and 7.

### Trigger List v11

The trigger list v11 single electron triggers selected for this thesis are listed in Table 5.1. The triggers EM\_HI, EM\_HI\_SH, EM\_MX and EM\_MX\_SH are purely based on the energy measurement in the calorimeter system, and they are combined into a single trigger efficiency measurement. The result is presented in Figure 5.3. The trigger efficiency is fitted using a Gaussian error function with the halfpoint H, the slope S and the plateau P:

$$\epsilon^{trigger} = 0.5 \times P \times (1 + \text{Errorfct}\left(\frac{p_T - H}{\sqrt{p_T} \times S}\right)) \quad (5.2)$$

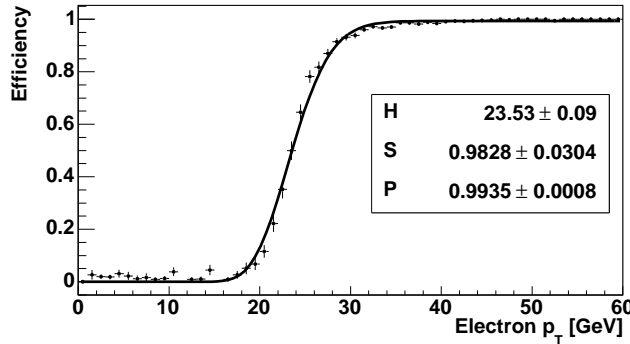


Figure 5.3: Trigger efficiency for the combined EM\_HI, EM\_HI\_SH, EM\_MX and EM\_MX\_SH triggers in trigger list v11: the Level 3  $E_T$  threshold of 20 GeV is clearly visible.

The kinematic range for electron triggering is extended to lower transverse momenta by adding tracking information. Since the L1CTT (see Section 2.3.7) was not commissioned for this run period, tracking information within the trigger system was not available until Level 3. Both EM\_HI\_SH\_TR and EM\_MX\_SH\_TR require one track with  $p_T > 12$  GeV at Level 3. This leads to an  $\eta$  dependence of the trigger efficiency since the CFT acceptance region extends only up to  $|\eta_{det}| = 1.6$ . Given that there is no matching performed at Level 3 between the calorimeter cluster and the track, the track can either stem from the electron or the tau candidate. It is therefore necessary to study the trigger efficiencies for the calorimeter requirement and the track requirement of the trigger separately. Both efficiencies are shown in Figure 5.4. The trigger efficiency for EM\_HI(MX)\_SH\_TR is a combination of the calorimeter and track trigger efficiency. Times when EM\_HI\_SH\_TR or EM\_MX\_SH\_TR were turned off or prescaled lead to an inefficiency, which is folded into the trigger

## 5 Data Sample and Monte Carlo Simulation

---

efficiency. Hence the low plateau efficiency of approximately 0.5 for the track trigger efficiency. The trigger efficiencies are fitted using Eqn. 5.2.

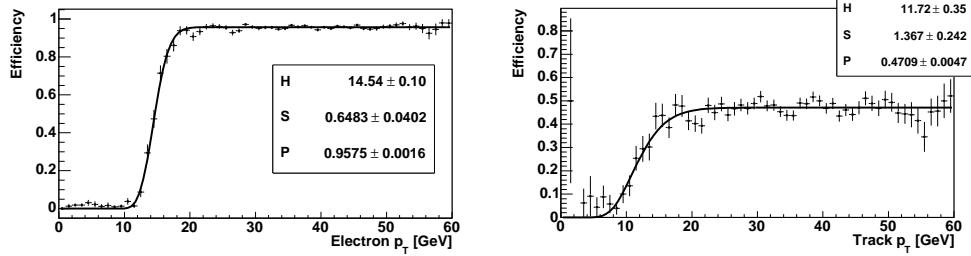


Figure 5.4: Trigger efficiency for EM\_HI(MX)\_SH.TR: the left plot shows the trigger efficiency for the calorimeter requirement with a Level 3  $E_T$  threshold of 12 GeV, the right plot shows the track trigger efficiency with a  $p_T$  threshold of 12 GeV. EM\_HI(MX)\_SH.TR extends the kinematic range of the single electron triggers shown in Figure 5.3 at lower electron transverse momenta.

### Trigger List v12

The trigger list v12 single electron triggers selected for this thesis are summarized in Table 5.1. Each trigger is simulated separately, taking into account a possible  $\eta$  dependence stemming from a track requirement at Level 1 or Level 3. The resulting trigger efficiencies are fitted with either a Gaussian error function (see description for trigger list v11) or using the sum of a Gaussian error function (with the half point H, the slope S and the plateau P) and a polynomial of 2nd order:

$$\epsilon^{trigger} = 0.5 \times P \times (1 + \text{Errorfct} \left( \frac{p_T - H}{\sqrt{p_T} \times S} \right)) \quad (5.3)$$

$$+ p_0 + p_1 \times p_T + p_2 \times p_T^2 \quad (5.4)$$

Due to the large amount of available single electron triggers in v12, only a subset of the eligible triggers are chosen to be visualized here. The combined trigger efficiency of the most important single electron triggers for this thesis, restricted to  $|\eta_{det}| < 1.6$ , is shown in Figure 5.5. Due to the two tracks which are required to satisfy E8\_T7SHT8\_2TK5, the efficiency of the resulting trigger combination is shown as a two-dimensional function of electron  $p_T$  and tau  $p_T$ . Fixing the transverse momentum of the tau to 25 GeV, the single electron trigger efficiency for trigger list v12 can be plotted as a function of the electron  $p_T$ . This displays the contributions of each trigger individually.

#### 5.5.2 Electron Efficiency and Resolution Corrections

Both analyses use electrons over the whole  $\eta_{det}$ -range without constraints on the azimuthal angle  $\phi$ . This includes less sensitive detector regions which consist of the  $\phi$ -cracks at the borders of the calorimeter tower in the central calorimeter

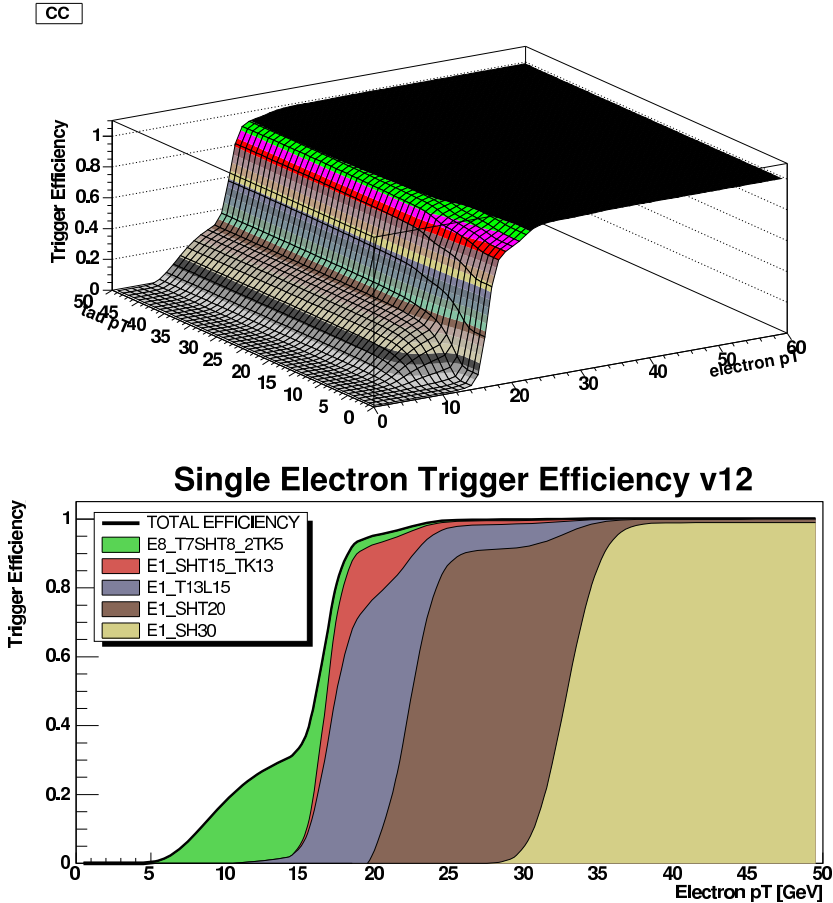


Figure 5.5: The upper plot shows the combination of the most important v12 single trigger efficiencies as a function of tau  $p_T$  and electron  $p_T$ . The lower plot shows a slice plane at tau  $p_T = 25$  GeV. The various colors represent the contribution of the most important single electron triggers.

(see Section 2.3.3), referred to as *non-fiducial* regions. Due to the poor modeling of the energy deposition at the borders of calorimeter towers, electrons that are located in these regions are studied separately.

### EM Candidate Efficiency

Efficiencies for the identification of EM candidates (see Section 4.3) are measured for data and Monte Carlo in  $Z/\gamma^* \rightarrow ee$  events using a tag-and-probe method [77, 78]. The EM candidate efficiency comprises the calorimeter clustering and the requirements on the electromagnetic fraction and the isolation. Events are required to have one electron (tag) that passes all the EM candidate selection criteria ( $|ID| = 10, 11$ ,  $\text{EMfrac} > 0.9$ ,  $\text{iso} < 0.15$ ), is matched to a track and is identified as the trigger object. A second isolated track (probe) is required in each event, and the invariant mass of the electron and the track is required to be in a window of  $\pm 20$  GeV around the  $Z$  boson mass. This sam-

ple is used to search for electromagnetic clusters that can be matched to the extrapolated track within  $\Delta\mathcal{R} < 0.1$ . The EM candidate efficiency is given by the ratio of the number of events where the track is successfully matched to an electromagnetic cluster and the total number of events in the sample. The QCD background is estimated by performing an exponential fit to the sidebands of the  $Z$  mass peak and is subtracted. The resulting EM candidate efficiencies are shown in Table 5.6. Since the efficiencies for Monte Carlo and data agree within the errors, no correction factor is applied for the EM candidate identification.

	$ \eta_{det}  < 1.05$	$1.5 <  \eta_{det}  < 2.3$
EM Candidate Efficiency (Data)	$0.988 \pm 0.003$	$0.995 \pm 0.011$
EM Candidate Efficiency (Monte Carlo)	$0.991 \pm 0.001$	$0.991 \pm 0.001$
Monte Carlo Correction Factor	$0.997 \pm 0.003$	$1.004 \pm 0.011$

Table 5.6: EM candidate efficiencies in data and Monte Carlo and the resulting Monte Carlo correction factor as measured in  $Z \rightarrow ee$  events. The efficiencies for data are taken from [77], the efficiencies for Monte Carlo are taken from [78].

### Likelihood Efficiency

The electron likelihood efficiency is measured in a similar way as the EM candidate efficiency, using  $Z/\gamma^* \rightarrow ee$  events in data and Monte Carlo and a tag-and-probe method. Starting from events with at least two EM candidates ( $|\text{ID}| = 10, 11$ ,  $\text{EMfrac} > 0.9$ ,  $\text{iso} < 0.15$ ) with  $p_T > 15$  GeV and  $|\eta| < 3.0$ , the tag electron is required to have a likelihood value that exceeds 0.8 and to pass a single electron trigger. The invariant mass of the two electrons has to be in a window of  $\pm 30$  GeV around the  $Z$  mass. The QCD background contribution is estimated by performing a fit to the sidebands of the  $Z$  peak. This background contribution is subtracted for the efficiency calculation. The measurements are performed in different  $\eta_{det}$  bins for fiducial CC electrons, non-fiducial CC electrons and EC electrons. The resulting ratio in data and Monte Carlo is shown in Figure 5.6. The  $\eta$ -dependent efficiency correction is applied to the Monte Carlo electron candidate if the likelihood cut is performed.

### Efficiency for Track Match with E/p Requirement

The efficiency for the track match with E/p requirement (see Section 4.3) is measured in a similar way as the EM candidate and likelihood efficiency. Starting from events with at least two EM candidates ( $|\text{ID}| = 10, 11$ ,  $\text{EMfrac} > 0.9$ ,  $\text{iso} < 0.15$ ) with  $\text{HMx8} < 20$ ,  $p_T > 25$  GeV and  $|\eta| < 2.5$ , the tag electron is required to be located in the CC region, to have a track match (with E/p requirement) and to pass a single electron trigger. The invariant mass of the two electrons has to be in a window of  $\pm 30$  GeV around the  $Z$  mass. The QCD background contribution is estimated by performing a fit to the sidebands of the  $Z$  peak and is subtracted. The resulting efficiencies for both data and Monte Carlo are shown as a function of  $\eta_{det}$  in Figure 5.7. The resulting Monte Carlo

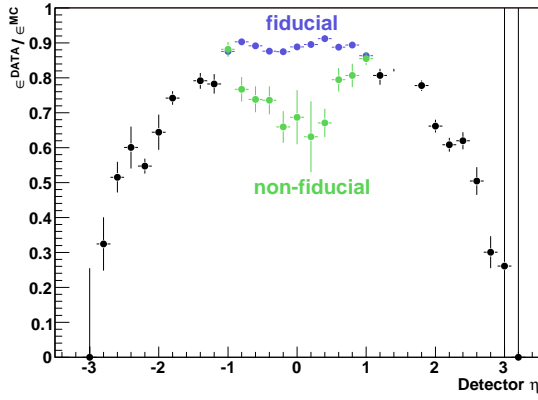


Figure 5.6: Electron efficiency correction for likelihood  $> 0.8$  as a function of  $\eta_{det}$ . The efficiency correction in the central calorimeter is shown separately for fiducial and non-fiducial regions.

correction factor is shown in Figure 5.8. The  $\eta$ -dependent factor is applied to the Monte Carlo electron candidate if the track match with E/p requirement is applied.

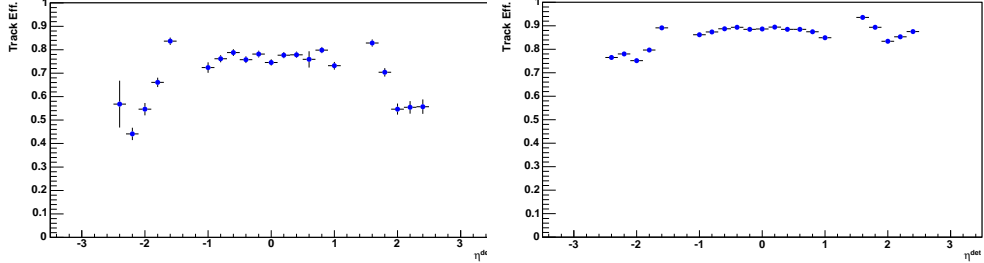


Figure 5.7: Efficiency for the track match with E/p requirement as a function of  $\eta_{det}$  in data (left) and Monte Carlo (right).

### Electron Smearing

The calorimeter energy resolution for electrons is not perfectly modeled in the detector simulation. This is mainly due to an incomplete description of the material in front of the calorimeter and to an insufficient modeling of the electronic noise. Hence the reconstructed electron energies in Monte Carlo have to be smeared. The smearing is optimized by comparing the  $p_T$  and invariant mass distributions for  $Z \rightarrow ee$  candidates in data and Monte Carlo. The procedure is performed separately for fiducial electrons in CC, non-fiducial electrons in CC, electrons in the ICR and electrons in EC. The electron energies are smeared with a Gaussian of rms  $= \sigma_{el}$  and scaled with  $corr_{el}$  according to:

$$E_{new} = E_{old} * corr_{el} * (1. + gauss(\sigma_{el})). \quad (5.5)$$

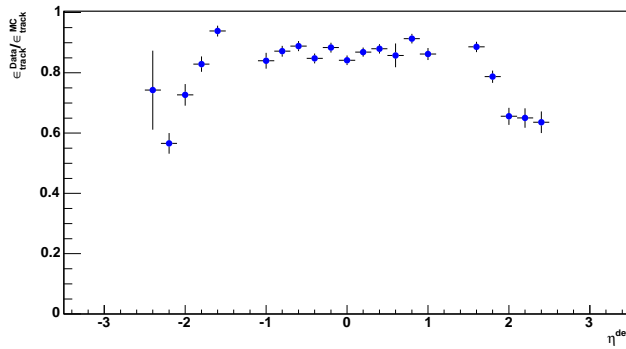


Figure 5.8: Monte Carlo efficiency correction for the electron with track match with  $E/p$  requirement as a function of  $\eta_{det}$ .

The smearing and scaling parameters for the four detector regions are listed in Table 5.7. All electron energy corrections are propagated into the calculation of the missing transverse energy. Figure 5.9 shows the distribution of the di-electron mass in  $Z \rightarrow ee$  events in data and Monte Carlo for different detector regions. Smearing and efficiency corrections are applied to the Monte Carlo electrons.

Region	$\sigma_{el}$	corr <sub>el</sub>
CC fiducial	$0.040 \pm 0.004$	$1.006 \pm 0.001$
CC non-fiducial	$0.080 \pm 0.004$	$0.950 \pm 0.002$
ICR	$0.055 \pm 0.010$	$0.984 \pm 0.001$
EC	$0.035 \pm 0.006$	$0.990 \pm 0.001$

Table 5.7: Smearing parameters for electrons as defined in Eqn. 5.5 (from Ref. [78]).

### 5.5.3 Tau Efficiency and Resolution Corrections

The Monte Carlo tau candidate is corrected for the different track reconstruction efficiency in data and Monte Carlo events. The track reconstruction efficiency is measured in a sample consisting of isolated muon events. These muons are reconstructed using information from the muon and calorimeter system only. In this sample, the track reconstruction efficiency is measured by noting the probability of there being a central track pointing toward the muon. The measurement is performed in two different run periods [83], and the following Monte Carlo efficiency correction factors are derived:

- Run number  $< 175757$ :  $\epsilon = 0.981 \pm 0.027$
- Run number  $\geq 175757$ :  $\epsilon = 0.993 \pm 0.026$

The electromagnetic fraction of the tau energy is smeared with the same prescription that is used for the electron smearing. This is necessary in order to

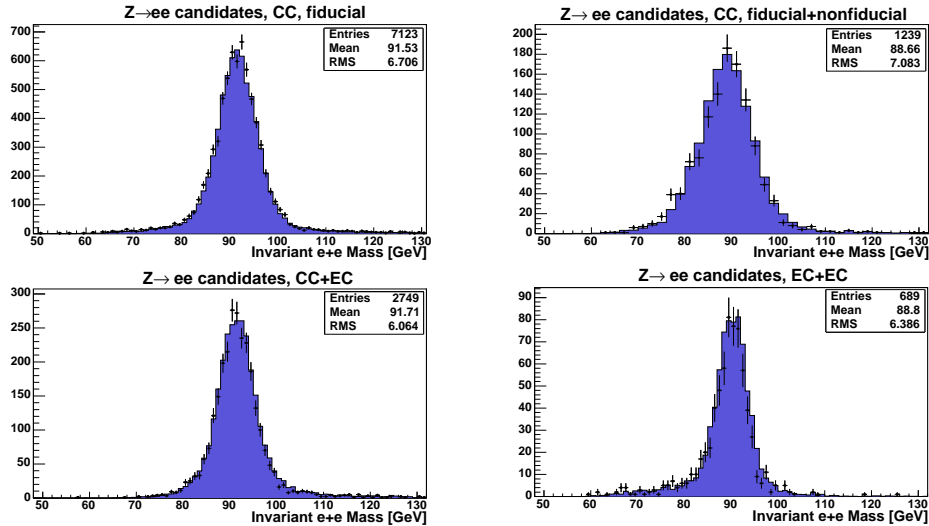


Figure 5.9: Distribution of the invariant di-electron mass in data and Monte Carlo for both electrons in fiducial detector regions (a), for one electron near a  $\phi$ -crack (b) and one (c) or both electrons (d) with  $|\eta_{det}| > 1.5$ . Smearing and efficiency corrections have been applied to the Monte Carlo electrons.

correctly describe the large amount of tau fakes stemming from electrons. In addition, the transverse momentum of all tracks associated to the tau candidate have to smeared since the  $1/p_T$  resolution of the tracker is not modeled correctly in the detector simulation. The track smearing is described in Chapter 5.5.5.

All described tau efficiency and resolution corrections are cross-checked in a  $Z/\gamma^* \rightarrow \tau\tau$  cross section measurement, which is described in Ref. [97].

#### 5.5.4 $p_T(Z)$ Reweighting

The  $p_T$  distribution of the  $Z$  boson is not properly described in Monte Carlo events generated with PYTHIA 6.202. To correct for this, a tuning of the PYTHIA samples via input parameters based on the differential  $Z$  boson production cross section  $\frac{d\sigma}{dp_T}$  as measured in  $Z/\gamma^* \rightarrow \mu\mu$  events in Run I and Run II data has been performed [84]. Figure 5.10 shows the ratios of the number of events in the tuned and default Monte Carlo in four different mass windows, which are fitted using a modified Fermi function. The correction factors which result from these fits are used to reweight the  $Z/\gamma^* \rightarrow ll$  Monte Carlo that is used in this thesis.

#### 5.5.5 Track Smearing

Due to the fact that the Monte Carlo uses an idealized geometry of the tracking system, the  $1/p_T$  resolution of the tracker is not modeled correctly in the detector simulation. Hence the track  $p_T$  needs to be smeared. The Monte Carlo

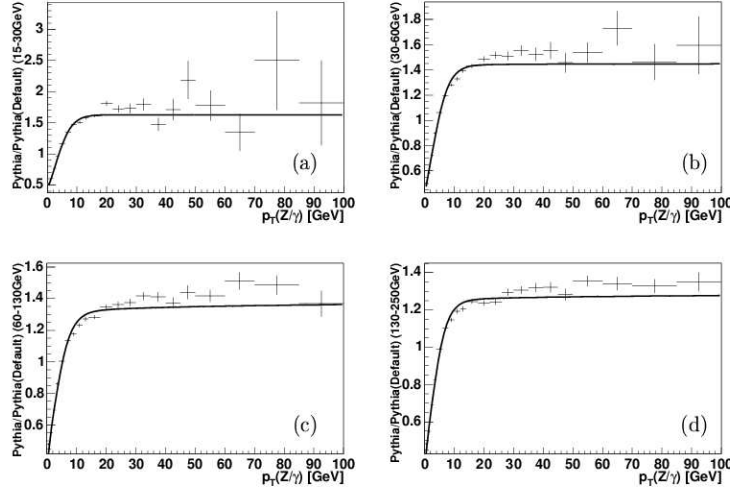


Figure 5.10: Ratio between tuned and default PYTHIA 6.202 Monte Carlo as a function of the transverse momentum of the  $Z$  boson  $p_T(Z)$ . The following four mass ranges were considered: (a)  $15 \text{ GeV} < M(Z/\gamma^*) < 30 \text{ GeV}$ , (b)  $30 \text{ GeV} < M(Z/\gamma^*) < 60 \text{ GeV}$ , (c)  $60 \text{ GeV} < M(Z/\gamma^*) < 130 \text{ GeV}$  and (d)  $130 \text{ GeV} < M(Z/\gamma^*) < 250 \text{ GeV}$  (from Ref. [84]).

is tuned to describe the data by smearing the inverse of the track transverse momentum using the following function:

$$\frac{1}{p_T} \rightarrow \frac{1}{p_T} + (A + B/p_T) * Gaussian(0, 1) \quad (5.6)$$

with  $A=0.0013$  and  $B=0.017$  for tracks with SMT hits and with  $A=0.0023$  and  $B=0.028$  for tracks without SMT hits. These parameters are derived by comparing the width of the invariant mass distribution in  $Z \rightarrow \mu\mu$  and  $J/\psi \rightarrow \mu\mu$  events in data and Monte Carlo [85].

### 5.5.6 $\cancel{E}_T$ Smearing

The correct modeling of the missing transverse energy distribution in background events is necessary for the optimization of both analyses, since it is an important quantity in the signal selection.

The raw missing transverse energy (see Section 4.6) is corrected for the calorimeter response of the physics objects. In addition, the smearing of the electron and tau candidate (see above) is propagated into the  $\cancel{E}_T$  calculation. Problems in the calorimeter simulation do not only affect the energy of the clustered objects and lead to the resolution corrections mentioned above, but also affect the unclustered energy. Hence the missing transverse energy distribution is not modeled properly in Monte Carlo. To correct for this effect, the x- and y-component of the missing transverse energy in Monte Carlo have to be smeared. This smearing is done using a Gaussian with  $\sigma = 2.55 + 0.00895 * \text{SUET}$  [86],

which is proportional to the scalar sum of the unclustered transverse energy (SUET) in the event. The missing transverse energy and its azimuthal direction are recalculated from the smeared x- and y-components.

*5 Data Sample and Monte Carlo Simulation*

---

# 6 Search for Associated Chargino/Neutralino Production in $e + \tau_h$ Final States

One of the most promising channels to search for supersymmetry in R-parity conserving models at the Tevatron is the associated production of the second lightest neutralino and the lightest chargino decaying into final states with three charged leptons and missing transverse energy. This channel is also referred to as the *trilepton channel*. The following chapter discusses the phenomenology of this channel and describes the signal selection, which is optimized for a final state consisting of an electron, a hadronic tau decay, an additional lepton and missing transverse energy. This final state is particularly important for high  $\tan\beta$  scenarios, where the branching ratio into taus is enhanced due to stau mixing. A dedicated event selection has been tuned on Monte Carlo in order to efficiently separate the signal from Standard Model backgrounds. The obtained results of this analysis are presented and discussed at the end of the chapter.

## 6.1 Trilepton Signature at the Tevatron

### 6.1.1 Production of Supersymmetric Particles

At hadron colliders like the Tevatron, SUSY particles can be produced by either strong or electroweak interactions. Colored particles (squarks, gluinos) are mainly produced in strong interactions, while electroweak interactions result in charginos, neutralinos and sleptons. The cross sections for the production of supersymmetric particles are comparable to the cross sections for the production of the respective Standard Model partners (at same  $Q^2$ ), since the couplings of SUSY particles are identical to the couplings of their Standard Model partners. Assuming R-parity conservation, supersymmetric particles are produced in pairs and the lightest supersymmetric particle (LSP) is stable.

The dominant source of SUSY particles at hadron colliders is expected to be the strong production of squarks and gluinos, assuming that these particles are sufficiently light [87]. This is followed by the electroweak production of charginos and neutralinos. Indirect searches for squarks and gluinos at LEP II in GUT-constrained supersymmetry models resulted in lower mass limits of the order of 300-400 GeV [88]. At this mass scale, however, the cross section for the strong production of SUSY particles at the Tevatron is low.

### Production of Charginos and Neutralinos

At leading order, charginos and neutralinos are produced in electroweak s- and t-channel reactions of a quark and an antiquark [89]. Figure 6.1 shows the respective Feynman diagrams. The relative contributions of the two amplitudes depends on the chargino and neutralino field contents and on the squark masses. The vector boson in the s-channel couples to the gaugino and higgsino components of the charginos and neutralinos. The squarks in the t-channel exchange, which are partners of light quarks, couple mainly to the gaugino components. For large squark masses, the t-channel contributions are suppressed, leading to an enhanced cross section since there is a destructive interference between the amplitudes.

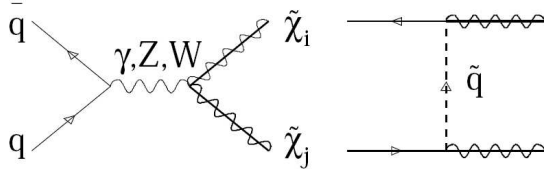


Figure 6.1: Leading order diagrams for the production of chargino/neutralino pairs in quark-antiquark collisions (from Ref. [89]).

At the Tevatron, the processes of interest are the pair production of the lightest chargino ( $\tilde{\chi}_1^\pm \tilde{\chi}_1^\pm$ ), the associated production of chargino/neutralino ( $\tilde{\chi}_1^\pm \tilde{\chi}_2^0$ ) and the pair production of the next-to-lightest neutralino ( $\tilde{\chi}_2^0 \tilde{\chi}_2^0$ ). All other combinations in the gaugino region have either a very low cross section or lead to final states which cannot be detected or separated from the background. The NLO cross sections as a function of the gaugino mass for these three processes are shown in Figure 6.2. While the NNLO corrections are expected to be small, the NLO contributions increase the cross sections [89]. In the mass range beyond the lower bounds of LEP II, between 100 GeV and 150 GeV, the K-factor for chargino/neutralino production is in the range  $1.26 > K_{\text{NLO}} > 1.23$ . The NLO production cross sections range from 0.1 to 1 pb.

#### 6.1.2 Decay of Supersymmetric Particles

Assuming R-parity conservation, charginos and neutralinos decay directly or via cascades into the LSP and Standard Model particles. Their decays, which are mediated by gauge bosons or sfermions, will be discussed in the following.

The chargino decay modes are shown in Figure 6.3. The chargino can decay via a virtual  $W$  boson into two fermions and a lighter neutralino. 2-body decays into a lighter neutralino and a real  $W$  become dominant if the mass difference between the chargino and the neutralino is large enough. If the  $W$  decays leptonically, the final state consists of the light neutralino, a charged lepton and the corresponding neutrino. If the decay via  $W$  boson is suppressed

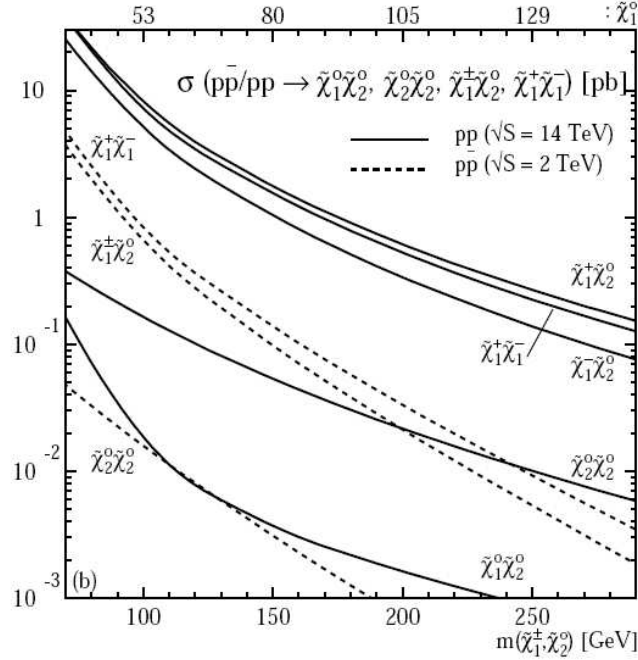


Figure 6.2: NLO cross sections for chargino/neutralino pair production as a function of the gaugino masses (from Ref. [89]). The cross sections are shown in the mSUGRA scenario with the parameters:  $m_{1/2} = 150$  GeV,  $m_0 = 100$  GeV,  $A_0 = 300$  GeV,  $\text{sgn}(\mu) = +1$  and  $\tan \beta = 4$ . This leads to the masses  $m_{\tilde{\chi}_1^\pm} = 101$  GeV,  $m_{\tilde{\chi}_2^0} = 104$  GeV and  $m_{\tilde{\chi}_1^0} = 56$  GeV. The dashed lines show the predictions for the Tevatron center-of-mass energy, the continuous lines are the predictions for the LHC center-of-mass energy.

or if the sfermions are light enough, 3-body decays mediated by a sfermion become important. The chargino decays into a sfermion and the Standard Model weak isospin partner. Since the sfermion decays further into its partner fermion and a lighter neutralino, the final state is the same as expected from  $W$  boson mediated decays. However, the resulting final state products have different kinematics. If the sfermion mass is low enough, 2-body decays into a real sfermion and a fermion become dominant.

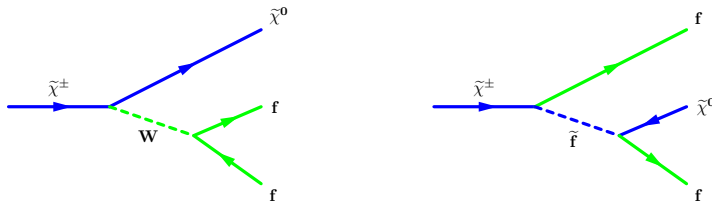


Figure 6.3: Decay modes of the chargino via a  $W$  boson (left) and via a sfermion (right).

The neutralino decay modes are shown in Figure 6.4. In large regions of the SUSY parameter space the 3-body decay via a virtual  $Z$  boson into a fermion pair and a lighter neutralino dominates. 2-body decays into a lighter neutralino and a real  $Z$  are possible if the mass difference between the neutralinos is large enough. If the  $Z$  boson decays into charged leptons, the final state consists of the light neutralino and a charged lepton pair. As already discussed for the chargino decay, sfermion mediated 3-body decays can also become important for the neutralino decay. In contrast to the chargino, the neutralino couples to a sfermion and its Standard Model partner. 2-body decays into a real sfermion and a fermion become dominant if the the sfermion mass is light enough.

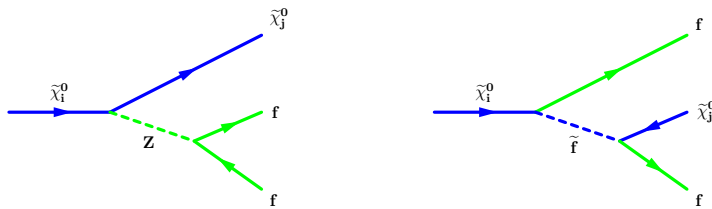


Figure 6.4: Decay modes of the neutralino via a  $Z$  boson (left) and via a sfermion (right) for  $i > j$ .

### Stau Mixing Effects

The leptonic final states are in general not equally composed of the three lepton generations due to a potential difference in the slepton masses. The large Standard Model tau mass can lead to different masses and field contents for the two stau particles  $\tilde{\tau}_1$  and  $\tilde{\tau}_2$  (lighter and heavier stau) in comparison to the other two slepton generations. This results in different branching ratios for final states with taus and final states with electron or muons.

The off-diagonal elements in the stau mass matrix, which are proportional to the Standard Model tau mass and  $A_\tau - \mu \tan \beta$  (see Section 1.2.5), introduce a mixing between the two stau chirality states. As a result, the lightest stau can become significantly lighter than the lightest selectron or smuon and therefore increasing the branching ratio into taus. In addition it acquires a left-handed component which couples to the  $SU(2)_L$  gauginos. Assuming that  $A_\tau$  and  $\mu$  are at the order of the electroweak scale, the stau mixing is mostly a function of  $\tan \beta$ . This dependence is shown in Figure 6.5, where the gaugino and slepton masses and  $\sigma \times BR$  into three lepton final states is shown. From the dependence on  $\tan \beta$  follows that final states with tau leptons dominate for large  $\tan \beta$ . The scan is performed for low values of  $m_0$ , leading to a low sfermion mass and 2-body decays of  $\tilde{\chi}_2^0$  into a light slepton and its Standard Model partner.

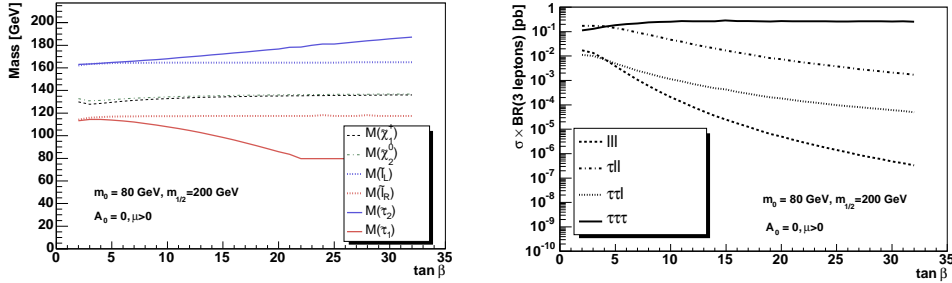


Figure 6.5: Masses of SUSY particles (left) and total cross section of the associated production of the lightest chargino and the second lightest neutralino into various trilepton final states as a function of  $\tan \beta$  for  $\mu > 0$ ,  $m_{1/2} = 200$  GeV,  $m_0 = 100$  GeV and  $A_0 = 0$ .

### 6.1.3 Signal Topology

The associated production of chargino/neutralino with the subsequent decay into charged leptons leads to final states with three charged leptons and missing transverse energy. Leptonic final states can be separated more easily from the large background of hadronic Standard Model background processes and are therefore of particular interest. Examples of the s- and t-channel leading order Feynman diagrams for this process are shown in Figure 6.6.

The available phase space for the three final state leptons (electrons, muons or taus) depends strongly on the mass differences of the involved particles.

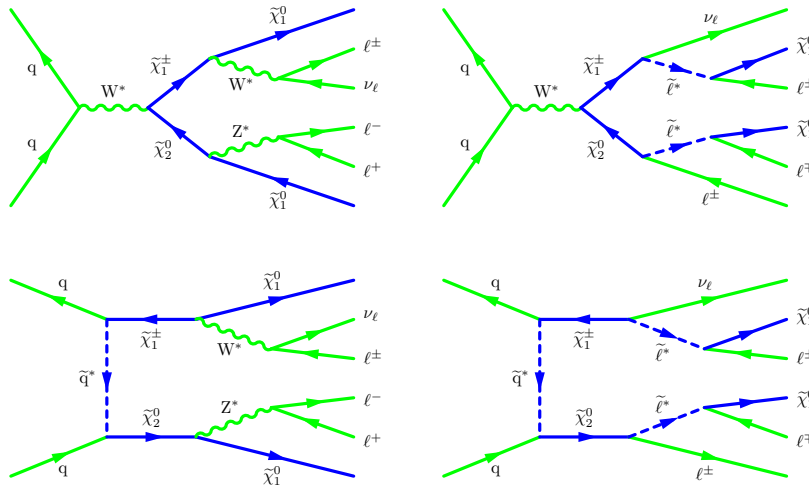


Figure 6.6: Examples of Feynman diagrams for the associated chargino/neutralino production via the s-channel (upper row) and t-channel (lower row) and the subsequent decay in trilepton final states. Diagrams with mixed  $W/Z$ - $\ell$  decays are not shown.

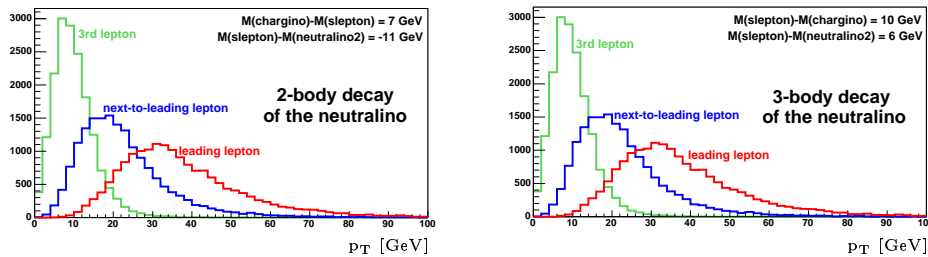


Figure 6.7: Parton level  $p_T$  distributions of leptons resulting from the associated production of charginos and neutralinos for different mass relations. The SUSY reference points C1 (left) and D4 (right) are shown (see Section 6.2).

Figure 6.7 shows the  $p_T$  distribution of the three leptons in two scenarios. If the slepton mass is larger than the gaugino masses, the 3-body decays are dominant. If the sleptons are considerably lighter than the gauginos, 2-body decays into real sleptons are dominant. Both scenarios lead to final states objects with transverse momenta which are usually large enough to be reconstructed with high efficiency. Problems arise in the transition region, when the mass difference between chargino and/or neutralino and its direct decay products is very small. In this region the available phase space for the lepton is rather small, which results in a small transverse momentum of the lepton.

Due to the neutrino which is produced in the hadronic tau decay, the  $p_T$  spectrum of the reconstructed decay products is always softer than for the tau itself. Hence hadronically decaying taus have to be reconstructed and identified with high efficiency down to very small values of  $p_T$ . This is of particular importance in the case where both chargino and neutralino decay into taus, and the electron is stemming from a leptonic tau decay. Due to two neutrinos in the leptonic tau decay, the resulting transverse momentum of the electron is significantly smaller than of the original tau. Hence the electron identification has to be highly efficient down to very small values of  $p_T$ . The same applies to the muon identification.

#### 6.1.4 Standard Model Background

Although most Standard Model processes can be effectively suppressed by requiring three charged leptons and missing transverse energy, a variety of these processes can produce a similar detector signature due to lepton misidentification or  $\cancel{E}_T$  mismeasurement. Especially the tau candidate suffers from large background contributions, where e.g. an electron or a QCD jet is misidentified as a tau. These so-called *tau fakes* make the  $e + \tau_h + \ell$  final state challenging. A brief overview of the most important backgrounds is presented here, the selection strategy to suppress these backgrounds is discussed in Section 6.4. Cross sections for the background processes are listed in Table 5.4.

- QCD Jet Production

The QCD jet production is the largest background source due to its very

high cross section, although no isolated leptons are produced in this process. Jets can be misidentified as leptons, especially as tau candidates, and a mismeasurement of the jet energy can lead to artificial missing transverse energy.

- $W \rightarrow \ell\nu$

Another large background source due to its large cross section is the  $W + \text{jet} \rightarrow \ell\nu + \text{jet}$  process, especially the  $W$  production with a subsequent decay into an electron. A jet from  $W + \text{jet}$  production can be misidentified as the tau, and the third lepton can be faked by an additional jet or photon.

- $Z/\gamma^* \rightarrow \ell\ell$

The  $Z/\gamma^* \rightarrow \ell\ell$  process creates two opposite sign leptons in the final state. The  $Z/\gamma^* \rightarrow ee$  process is an important background source because real electrons are not only reconstructed as electron candidates, but also pass all tau selection criteria and end up as tau candidates. Significant missing transverse energy can arise from mismeasurement. The event is selected if an additional jet or photon is misreconstructed as a third lepton. The  $Z/\gamma^* \rightarrow \tau\tau$  final state, with subsequent hadronic decay of one tau and leptonic decay into an electron of the second tau, is selected if an additional jet or photon is misreconstructed as a third lepton.

- Di-boson:  $WW$ ,  $WZ$ ,  $ZZ$

The most important irreducible background consists of the associated production of a  $W$  and a  $Z$  boson with subsequent leptonic decays of both gauge bosons. The resulting final state is identical to the trilepton final state, with the missing transverse energy stemming from the  $W \rightarrow \ell\nu$  decay. However, the invariant mass of two opposite sign leptons of the same generation is expected to be in the range of the  $Z$  mass.

Another irreducible background can result from  $ZZ$  production, when one  $Z$  decays into an electron pair and the second  $Z$  decays into a tau pair. Other  $Z$  decay modes can lead to final states with a real electron and a tau fake stemming from either an electron or a jet. These events are selected if the third lepton is either a real lepton or a misidentified jet and if the missing transverse energy is the result of mismeasured energy or stemming from  $Z \rightarrow \nu\nu$ .

The production of two  $W$  bosons can lead to final states with two leptons of opposite sign and real missing transverse energy. A jet or a photon from  $W + \text{jet}$  or  $W + \gamma$  can be misreconstructed as a third lepton.

- $t\bar{t}$

The production of a  $t\bar{t}$  pair with subsequent semileptonic decay of both top quarks leads to two leptons, two hard  $b$  jets and missing transverse energy in the final state. The tau candidate can either be a real tau or a fake stemming from one of the leptons or jets. The event is selected if one of the remaining objects is misidentified as a third lepton.

## 6.2 Signal Monte Carlo

The different SUSY reference points which are considered for optimization of the event selection are outlined in Table 6.1. The NLO corrections for the cross section are taken from Ref. [89] and range from  $1.23 < K_{\text{NLO}} < 1.26$  for the gaugino masses analyzed in this analysis.

With the current data set, the sensitivity<sup>1</sup> for supersymmetry is limited to models with a low value of  $\tan \beta$ . This leads to a small mixing in the stau sector, and therefore to a minimal suppression of decays into electron or muon. The signal Monte Carlo samples are also characterized by low chargino and neutralino masses, which leads to a large  $\tilde{\chi}_1^\pm \tilde{\chi}_2^0$  cross section (see Figure 6.2), and low slepton masses, which leads to a large leptonic branching ratio of the chargino and the next-to-lightest neutralino. Common features of the GUT-constrained models at the SUSY mass scale of interest are the wino-like lightest chargino and second-lightest neutralino and the following specific mass relations:  $m_{\tilde{\chi}_1^\pm} \approx m_{\tilde{\chi}_2^0}$  and  $m_{\tilde{\chi}_2^0} \approx 2 \cdot m_{\tilde{\chi}_1^0}$ . The Monte Carlo samples are also used in trilepton searches covering the final states  $e + e + \ell$  [78],  $e + \mu + \ell$  [92],  $\mu + \mu + \ell$  [93], likesign  $\mu + \mu$  [94] and  $\mu + \tau_h + \ell$  [95].

The signal acceptance of this analysis has also been studied for a SUSY parameter space with high values of  $\tan \beta$ . In this case chargino and neutralino decay

---

<sup>1</sup>The statistical methods used in this thesis are presented in detail in the established text books [90, 91].

	$m_0$ [GeV]	$m_{1/2}$ [GeV]	$A_0$ [GeV]	$\tan \beta$	$\text{sgn}(\mu)$	# Events
C1	64	175	0	3	+	21500
D1	68	180	0	3	+	25500
D4	92	180	0	3	+	21500
E1	72	185	0	3	+	31000

	$m_{\tilde{\chi}_2^0}$ [GeV]	$m_{\tilde{\chi}^\pm}$ [GeV]	$m_{\tilde{\chi}_1^0}$ [GeV]	$m_\ell$ [GeV]	$m_{\tilde{\tau}}$ [GeV]	$m_{\tilde{\nu}}$ [GeV]
C1	110	106	60	99	98	122
D1	114	110	62	103	101	128
D4	114	110	62	120	119	142
E1	118	114	65	107	105	133

	$\text{BR}(\tilde{\chi}_2^0)$		$\text{BR}(\tilde{\chi}^\pm)$		$\text{BR}(\ell)$	$\sigma \times \text{BR} \times K_{\text{NLO}}$
	(e/ $\mu$ )	( $\tau$ )	(e/ $\mu$ )	( $\tau$ )		[pb]
C1	0.29	0.42	0.04	0.82	0.86	0.692
D1	0.29	0.42	0.04	0.82	0.85	0.579
D4	0.18	0.21	0.15	0.19	0.28	0.180
E1	0.29	0.42	0.04	0.81	0.85	0.489

Table 6.1: Properties of SUSY reference points which are considered in this analysis.

mainly into taus (see Figure 6.5), and at least one tau is required to decay leptonically into an electron in order to be triggered by the single electron trigger. Due to two neutrinos coming out of the leptonic tau decay, the transverse momentum of the electron is too small to be triggered with reasonable efficiency with the current single electron triggers. Additional problems arise from the fact that the tau reconstruction/identification efficiency is low for low- $p_T$ . A more detailed discussion follows in Section 6.7.

### 6.3 Reference Signal: $Z/\gamma^* \rightarrow \tau\tau \rightarrow e + \tau_h$

As a first step towards the trilepton analysis in the  $e + \tau$  final state, a basic comparison of the  $Z/\gamma^* \rightarrow \tau\tau \rightarrow e + \tau_h$  signal in data and Monte Carlo is performed. The purpose of this cross check is to show the ability to select the  $e + \tau_h$  final state and to verify the applied Monte Carlo correction factors and the trigger simulation. DØ has performed a cross section measurement of the process  $p\bar{p} \rightarrow Z \rightarrow \tau\tau \rightarrow \mu + \tau_h$  [97], however the  $Z \rightarrow \tau\tau \rightarrow e + \tau_h$  signal has not yet been established.

#### 6.3.1 Event Selection

The selection strategy for the reference signal is equivalent to the initial steps of the trilepton search, making it an ideal testbed for the latter. Both analyses use the same data set, and the object identification cuts on the electron and the tau are identical. A summary of the selection procedure is given in Table 6.2. The number of events selected in data and expected from Standard Model processes are presented in Table 6.3.

(1) Preselection	Electron: $ ID  = 10, 11$ , $\text{EMfrac} > 0.9$ , $\text{iso} < 0.15$ , $\text{HMx8} < 20$ track match with E/p, $p_T > 8 \text{ GeV}$ Tau: $p_T > 8 \text{ GeV}$ , $\tau$ -type 1, 2, 3, $ \eta_{det}  < 1.1$ or $1.6 <  \eta_{det}  < 2.5$ $\Delta\mathcal{R}(e, \tau) > 0.4$ $\Delta z_0(e, \tau) < 2 \text{ cm}$ $\Delta z_0(e/\tau, \text{primary vertex}) < 1 \text{ cm}$
(2) Anti-Electron	$35 \text{ GeV} < M(e, \tau) < 75 \text{ GeV}$ $E_T > 5 \text{ GeV}$ for $\tau$ -type 1, 2; $E_T > 10 \text{ GeV}$ for $\tau$ -type 3 $E_T^{HAD}/p_T^{\tau, \text{trk}} > 0.3$
(3) Anti-W	$\tau$ -type 1: $M_T(e, E_T) < 20 \text{ GeV}$ ; $\tau$ -type 2, 3: $M_T(e, E_T) < 15 \text{ GeV}$
(4) Anti-QCD	$NN > 0.9$ , unlike-sign $\tau$ -type 1, 2: $\Delta\phi(e, \tau) > 2.75$ ; $\tau$ -type 3: $\Delta\phi(e, \tau) > 2.9$

Table 6.2: Summary of the selection criteria for the  $Z/\gamma^* \rightarrow \tau\tau \rightarrow e + \tau_h$  signal.

#### (1) Preselection

The events have to be triggered by one of the single electron triggers (see Section 5.1.2). As pointed out Section 5.5.1, the tau candidate can fire the

single electron trigger due to the large amount of tau fakes from electrons. Hence the total trigger efficiency of the event is a combination of the trigger efficiency of the electron and the trigger efficiency of the tau. The tau trigger efficiency is calculated by matching the tau to an EM candidate object (with spatial track match) in a  $\Delta R < 0.4$  cone. The trigger efficiency of the matched EM candidate object is taken as the trigger efficiency of the tau, and combined with the electron trigger efficiency to give the total trigger efficiency of the event.

The leading electron candidate passing the following identification cuts is selected: standard electron identification (see EM candidate description in Chapter 4.3),  $H_{\text{Mx8}} < 20$ , track match with  $E/p$  requirement and  $p_T > 8$  GeV. A tau candidate of type 1, 2 or 3 with  $p_T > 8$  GeV, which is well separated from the electron candidate ( $\Delta R > 0.4$ ), is required. Both particles have to stem from the same vertex (distance of the vertex z positions  $\Delta z_0 < 2$  cm), and this vertex is required to be identical with the primary vertex ( $\Delta z_0 < 1$  cm). To avoid phase space regions with unfavorable signal-to-background ratios, both the electron and tau candidate must be detected in  $|\eta_{\text{det}}| < 2.5$ . In addition, the tau candidate is required to be outside the inter-cryostat region.

Figure 6.8 shows the invariant  $e + \tau_h$  mass, the neural network output,  $E_T$  and the tau type distribution at this preselection stage, before further selection

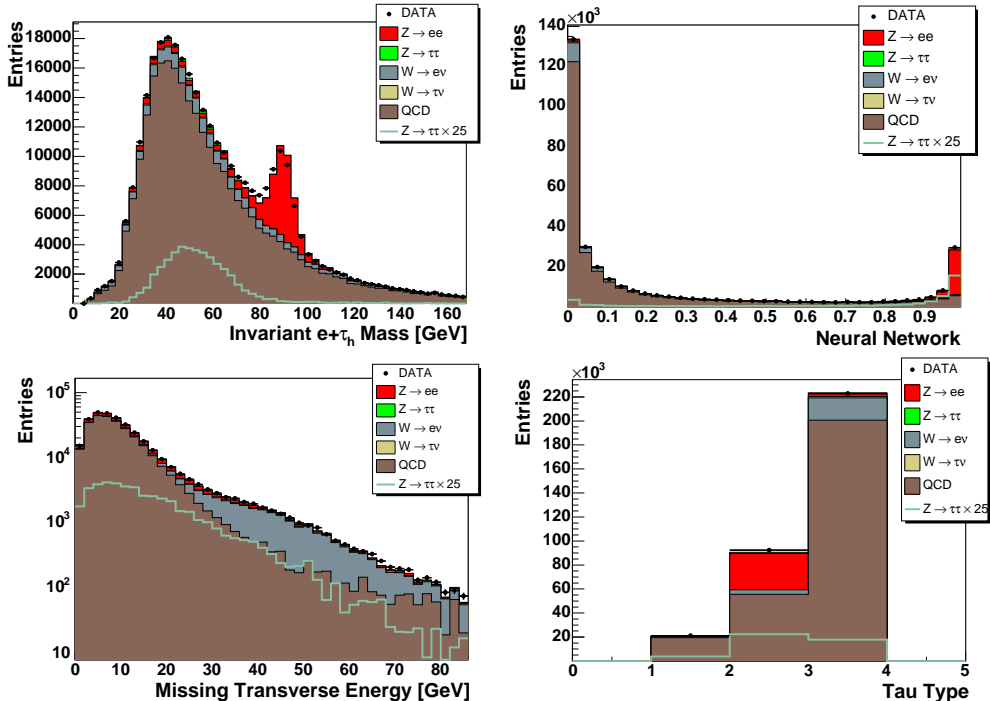


Figure 6.8: Various distributions at preselection stage (1): invariant  $e + \tau_h$  mass (upper left), neural network output (upper right), missing transverse energy (lower left), tau type (lower right). In all distributions, the  $Z/\gamma^* \rightarrow \tau\tau$  signal is scaled by a factor of 25 in order to see the expected shape. All three tau types are combined.

criteria are applied. The QCD multijet background is estimated from data and normalized at preselection using the invariant  $e + \tau_h$  mass distribution (see description in Section 5.4). The  $Z/\gamma^* \rightarrow \tau\tau$  signal is scaled by a factor of 25 in order to see the expected shape in the distributions. The neutrinos in both leptonic and hadronic tau decay lead to significant missing transverse energy. Hence the  $Z \rightarrow \tau\tau \rightarrow e + \tau_h$  mass peak is not located at 90 GeV, but shifted towards low values in the invariant mass plot.

The main background contributions at the preselection stage are QCD di-jets, where both electron and tau are faked by a jet,  $Z/\gamma^* \rightarrow ee$ , where the second electron is reconstructed as a tau candidate, and  $W \rightarrow e\nu$ , where the tau is faked by an additional jet. These background contributions are orders of magnitude larger than the reference signal. The selection strategy to suppress these backgrounds is discussed in the following.

## (2) Anti-Electron

A major background source for the  $e + \tau_h$  final state is the  $Z/\gamma^* \rightarrow ee$  process, where one of the two electrons fakes the tau. As discussed in Section 4.4, it is expected that electrons are reconstructed with high efficiency as tau candidates. Hence the  $Z \rightarrow ee$  mass peak in Figure 6.8. These tau fakes can be reduced by cutting on the invariant  $e + \tau_h$  mass and by requiring a significant amount of hadronic energy to be present for the tau. This is done by comparing the track  $p_T$  of the tau candidate with its energy deposition in the hadronic calorimeter. Assuming that an electron has faked the tau, the hadronic energy is the result of calorimeter noise. Hence the ratio  $E_T^{HAD}/p_T^{trk}$  is very small. For a real hadronic tau decay, this ratio of transverse hadronic energy and track  $p_T$  is more balanced. This is shown for Monte Carlo events in Figure 6.9. Requiring the ratio to exceed 0.3 reduces the tau fakes from electrons significantly. The electron contamination is studied in more detail in Section 7.3. Further rejection is achieved by requiring a minimal amount of missing transverse energy to be present in the event, since  $Z/\gamma^* \rightarrow ee$  events are expected to be balanced in the transverse plane.

## (3) Anti-W

The  $W$  background is reduced by cutting on the *transverse mass*  $M_T$  of the electron and the missing transverse energy, defined as:

$$M_T = \sqrt{2 \cdot \cancel{E}_T \cdot p_T^e \cdot (1 - \cos \Delta\phi)} \quad (6.1)$$

where  $\Delta\phi$  is the azimuthal angle between  $\cancel{E}_T$  and the electron. For  $Z \rightarrow \tau\tau$  events, the missing transverse energy is dominated by the neutrinos from the leptonic tau decay:  $\tau \rightarrow e\nu_e\nu_\tau$ . Hence the missing transverse energy vector points into the direction of the leptonic tau decay, leading to small values of  $M_T$ . In contrast to this, leptonic  $W$  decays have the  $\cancel{E}_T$  vector pointing in

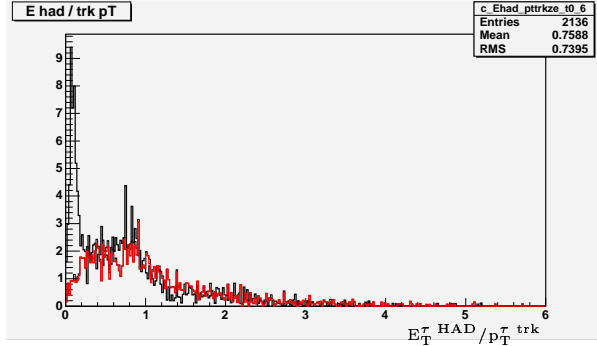


Figure 6.9: Ratio of the transverse hadronic tau energy and the associated tau track(s) ( $E_{T}^{\tau, HAD}/p_{T}^{\tau, trk}$ ) for hadronic tau decays (red line) and for tau fakes from electrons (black line). In contrast to real hadronic tau decays, tau fakes stemming from electrons show a large imbalance and peak at very small values.

the opposite direction to the lepton, leading to large values of  $M_T$ . Figure 6.10 shows the transverse mass distribution at preselection stage (1) and before the cut on the transverse mass is applied

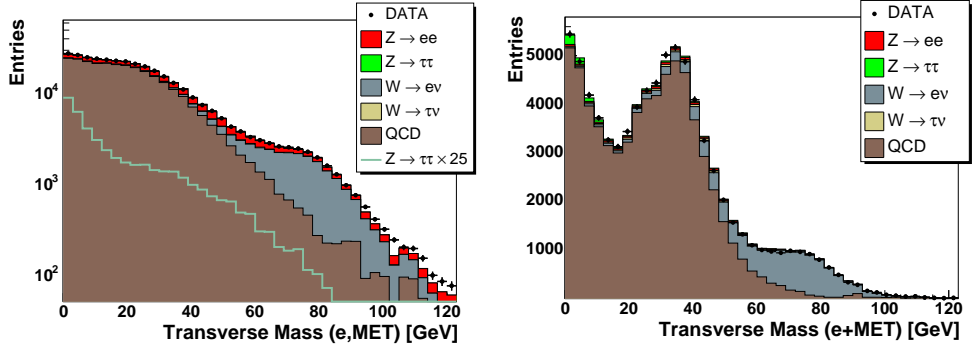


Figure 6.10: Distribution of the transverse mass of the electron and missing transverse energy at preselection stage (1) (left) and before the anti-W selection criteria (3) are applied (right). All three tau types are combined.

#### (4) Anti-QCD

After the anti-W selection criteria are applied, the dominant background contribution stems from QCD jet production (see Table 6.3). The QCD contribution can be significantly reduced by cutting on the neural network output of the tau candidate, by using the back-to-back topology of the  $Z \rightarrow \tau\tau$  signal, and by requiring that the electron and the tau have opposite charge. Figure 6.11 shows the azimuthal angle between the electron and tau and the neural network output before the corresponding cuts are applied.

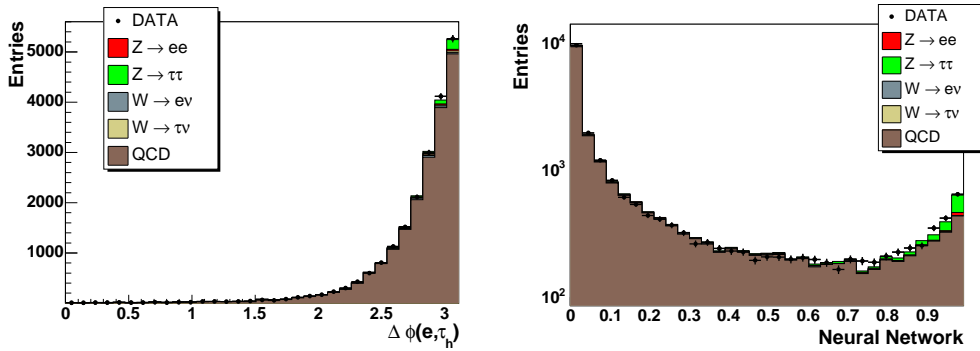


Figure 6.11: Distribution of the azimuthal angle between the electron and tau (left) and the neural network output (right) before the anti-QCD selection criteria are applied. All three tau types are combined.

### 6.3.2 Results

The number of events selected in data and expected from Standard Model processes is shown in Table 6.3. After all selection criteria are applied, the selected data sample is dominated by the  $Z/\gamma^* \rightarrow \tau\tau \rightarrow e + \tau_h$  signal. The systematic error is estimated to be 7.4 % without and 9.8 % with the error on the luminosity measurement of 6.5 % taken into account. Main contributions arise from the QCD normalization (5.5 %), the tau identification (2.8 %) and the jet energy scale (1.8 %).

The distribution of the invariant  $e + \tau_h$  mass, tau type, electron  $p_T$  and tau  $p_T$  after application of all cuts is shown in Figure 6.12. The fully corrected Monte Carlo (see Section 5.5 for the efficiency corrections) describes the data for all relevant quantities, giving confidence that the corrections for Monte Carlo with respect to data are correctly determined. Within the systematic and sta-

Cut	Data	Sum BGND	QCD
(1) Preselection	331130	$329427 \pm 763 \pm 32284$	$271266 \pm 755$
(2) Anti-Electron	81096	$81402 \pm 368 \pm 7977$	$68227 \pm 361$
(3) Anti-W	22579	$22517 \pm 214 \pm 2206$	$21594 \pm 213$
(4) Anti-QCD	374	$365.0 \pm 15.2 \pm 35.8$	$97.9 \pm 14.3$
Cut	$Z/\gamma^* \rightarrow \tau\tau$	$Z/\gamma^* \rightarrow ee$	$W \rightarrow e\nu$
(1) Preselection	$1745 \pm 20$	$32461 \pm 57$	$22606 \pm 93$
(2) Anti-Electron	$790 \pm 9$	$703 \pm 18$	$11021 \pm 65$
(3) Anti-W	$476 \pm 6$	$138 \pm 5$	$190 \pm 11$
(4) Anti-QCD	$242.7 \pm 4.6$	$24.4 \pm 2.6$	$< 0.5$
Cut	$W \rightarrow \tau\nu$		
(1) Preselection	$1349 \pm 23$		
(2) Anti-Electron	$661 \pm 16$		
(3) Anti-W	$119 \pm 7$		
(4) Anti-QCD	$< 0.5$		

Table 6.3: Number of events observed in data and expected for Standard Model processes at different stages of the  $Z/\gamma^* \rightarrow \tau\tau \rightarrow e + \tau_h$  selection. All three tau types are combined. The errors for the numbers of the individual backgrounds are statistical. For the sum of all backgrounds, both statistical and systematic errors are given.

tistical errors the result agrees with the  $Z \rightarrow \tau\tau$  Standard Model cross section of 245 pb (see Table 5.4).

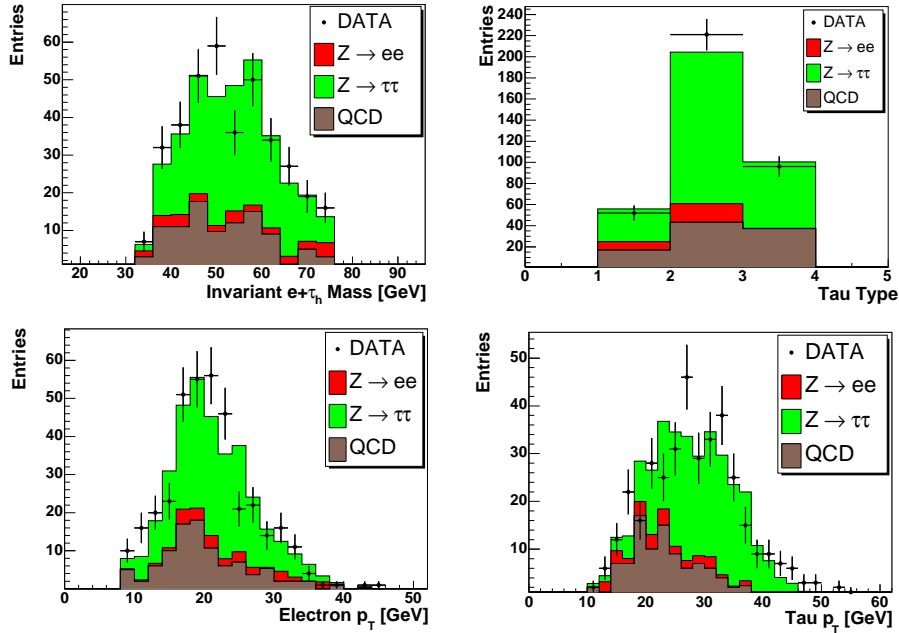


Figure 6.12: Distributions of important variables of the  $Z/\gamma^* \rightarrow \tau\tau$  selection after application of all cuts. The upper row shows the invariant  $e + \tau_h$  mass distribution (left) and the tau type distribution. The lower row shows the  $p_T$  distribution of the electron (left) and the tau (right). All three tau types are combined.

## 6.4 Trilepton Event Selection and Data/Monte Carlo Comparison

The selection uses the trilepton selection criteria which have been developed for the  $e + e + \ell$  final state. A detailed description of the individual cuts and their optimization is described in Ref. [78]. For the  $e + \tau_h + \ell$  final state, the second electron is replaced by a hadronic tau. The individual cut values are optimized for the  $e + \tau_h + \ell$  final state.

Table 6.4 briefly summarizes the selection procedure. All cut values were chosen to achieve a maximal sensitivity for the analysis. The number of events selected in data and expected from Standard Model processes are presented in Table 6.6.

The signal event topology contains a third lepton, which is exploited by requiring an isolated high-quality track or by requiring an additional tau candidate with a high neural network output in the event. If both objects are present, the second tau candidate is used. The considerable amount of missing energy in the event stemming from the LSP and the neutrinos is used to discriminate the signal from di-jet and  $Z$  backgrounds.

(1) Preselection	Electron: $ ID  = 10, 11$ , $\text{EMfrac} > 0.9$ , $\text{iso} < 0.15$ , $\text{HMx8} < 20$ track match with E/p, $p_T > 8 \text{ GeV}$ Tau: $p_T > 8 \text{ GeV}$ , type 1 or 2, $ \eta_{det}  < 2.5$ $\Delta\mathcal{R}(e, \tau) > 0.4$ $\Delta z_0(e, \tau) < 2 \text{ cm}$ $\Delta z_0(e/\tau, \text{primary vertex}) < 1 \text{ cm}$ Anti-QCD: electron track isolation, tau NN>0.95
(2) Z Veto	$10 \text{ GeV} < M(e, \tau_h) < 60 \text{ GeV}$ $\Delta\phi(e, \tau) < 2.9$
(3) Significant MET	$t\bar{t}$ veto: $H_T < 60 \text{ GeV}$ Scaled MET> $8.0 \sqrt{\text{GeV}}$ $\text{Min}(M_T(e, \cancel{E}_T), M_T(\tau, \cancel{E}_T)) > 10 \text{ GeV}$ $\cancel{E}_T > 25 \text{ GeV}$
(4) 3 <sup>rd</sup> Track or 2 <sup>nd</sup> tau	track: $p_T > 5 \text{ GeV}$ , track + calorimeter isolation 2 <sup>nd</sup> tau: all three tau types, $p_T > 8 \text{ GeV}$ , NN > 0.95, $\Delta\phi(\tau, \cancel{E}_T) > 0.3$ , $\Delta\phi(e, \tau) < 2.9$
(5) Boson and Di-boson Veto	$\Delta\phi(\text{track}, \cancel{E}_T) > 0.3$ $M(\text{tau track}, \text{track}) < 70 \text{ GeV}$ $W$ veto: $p_T^{\text{track}} > 9 \text{ GeV}$ if $50 \text{ GeV} < M_T(e, \cancel{E}_T) < 90 \text{ GeV}$
(6) $p_T^{trk}$ and $\cancel{E}_T$	$p_T^{trk} \times \cancel{E}_T > 350 \text{ GeV}^2$

Table 6.4: Summary of the applied selection cuts in order to discriminate between signal and background.

The QCD multijet background is estimated using like-sign  $e + \tau_h$  events (see Section 5.4). Since the signal sample also contains like-sign events, rejection factors are derived for selection stages (4) and (5) the final cuts in the event selection to estimate the expected QCD contribution. These rejection factors are derived using a loose  $e + \tau_h$  selection, which differs from the presented event selection only by changing the electron and tau identification criteria: the electron track is not required to be isolated, the cut on the electron shower shape variable is loosened ( $\text{HMx8}<100$ ) and the tau neural network output is required to exceed only 0.3. The remaining QCD events in this loose preselection exceed the expected signal events by a factor of 60 after requiring a third track. Therefore the signal contribution to the like-sign event sample can be neglected and rejection factors are derived. These rejection factor are applied to scale the QCD jet contribution in the trilepton selection.

### (1) Preselection

The object identification criteria of the electron and tau candidate are identical to the requirements that are used to extract the  $Z \rightarrow \tau\tau$  reference signal. There are however the following differences:

- Due to the large QCD background in tau type 3 (see e.g. the tau type distribution in Figure 6.8), only tau type 1 and 2 are retained for the

analysis.

- The tau candidate is allowed to be in the inter-cryostat region ( $1.1 < |\eta_{det}| < 1.6$ ) in order to regain some of the efficiency loss of the  $e + e + \ell$  final state [78]. This detector region is not equipped with an electromagnetic calorimeter, hence an electron deposits all its energy in the hadronic calorimeter.

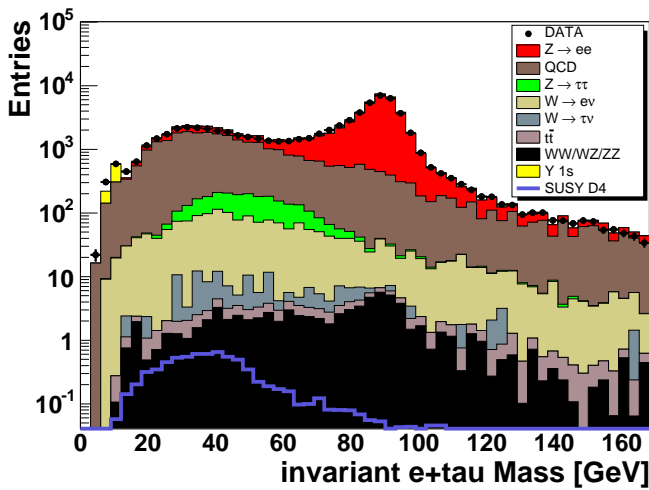


Figure 6.13: Distribution of the invariant  $e + \tau_h$  mass in data (points with error bars), background simulation (histograms, complemented with the QCD expectation) and signal expectation for SUSY point D4 (empty histogram). Tau type 1 and 2 are combined for this plot.

Figure 6.13 shows the invariant  $e + \tau_h$  mass distribution in data, background and signal point D4 at this stage. A good agreement between data and Monte Carlo is observed. The dominant background contribution stems from  $Z/\gamma^* \rightarrow ee$  events, where the second electron fakes the tau. Additional important background sources include QCD jet production,  $Z/\gamma^* \rightarrow \tau\tau$  events,  $W \rightarrow e\nu$  and Di-Boson events (mainly  $WZ$  production). To significantly reduce background from QCD multijet production, anti-QCD selection criteria are already performed at preselection stage.

#### *Anti-QCD: Neural Network Output and Electron Track Isolation*

A large amount of the background consists of QCD multijet events, where both the electron and the tau are faked by a jet. This background can be significantly reduced by cutting on the tau neural network output and by requiring a tight cut on the electron track isolation.

Figure 6.14 shows the neural network distribution of the tau candidate. A large fraction of the QCD background is rejected by requiring the neural network output to be larger than 0.95.

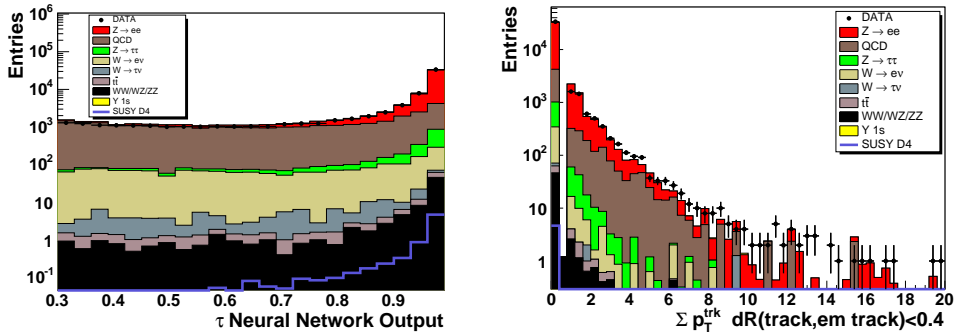


Figure 6.14: (left) Distribution of the neural network output before the corresponding cut is applied. Tau type 1 and 2 are combined for this plot.

(right) Distribution of  $\sum p_T^{trk}$  in the isolation cone  $\Delta R(trk, EM trk) < 0.4$  after the NN cut and before the corresponding cut is applied. Tau type 1 and 2 are combined for this plot.

If a QCD jet is misidentified as an electron, additional (low- $p_T$ ) tracks from charged particles which form the jet are expected. An isolation cone around the electron track of  $\Delta R < 0.4$  is defined, and the scalar sum of the transverse momentum of additional tracks in this cone can be used to distinguish a real (isolated) electron from a jet fake. The distribution of this quantity in data, background and Monte Carlo is shown in Figure 6.14. The sum is required to be smaller than 1 GeV.

## (2) Z Veto

The  $Z/\gamma^* \rightarrow ee$  background can be significantly reduced by cutting on the invariant  $e + \tau_h$  mass and by cutting on the azimuthal angle between the electron and the tau.

The invariant  $e + \tau_h$  mass distribution in Figure 6.13 shows that vast majority of the di-electron background are  $Z \rightarrow ee$  events, resulting in a mass peak at 90 GeV. Since the invariant mass distribution of the SUSY signal peaks at lower values,  $Z \rightarrow ee$  events are rejected by requiring the invariant electron and tau mass to be in the range  $10 \text{ GeV} < M(e, \tau_h) < 60 \text{ GeV}$ .

Electron and tau from chargino and neutralino decays have no preferred azimuthal angle  $\Delta\phi(e, \tau_h)$ , while  $Z/\gamma^* \rightarrow \ell\ell$  events are mainly back-to-back in the transverse plane. Figure 6.15 shows the  $\Delta\phi$  distribution in data, background and Monte Carlo. The selection criteria described in (1) and the cut on invariant  $e + \tau_h$  mass are applied. Data and background expectation are in good agreement after the  $p_T(Z)$  reweighting (see Section 5.5.4). The azimuthal angle between the electrons is required to be less than 2.9.

The anti-QCD cuts and the Z veto cuts reduce the background by a factor of 11 while losing 23 % of the SUSY signal.

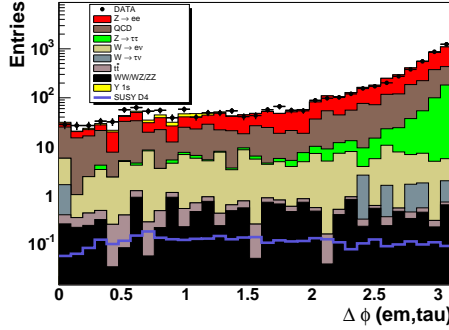


Figure 6.15: Distribution of  $\Delta\phi$  between the electron and the tau candidate. The cuts described in (1) and the invariant  $e + \tau_h$  mass cut are applied. Tau type 1 and 2 are combined for this plot.

### (3) Significant Missing Transverse Energy

#### *Missing Transverse Energy ( $\cancel{E}_T$ )*

The two LSPs and the neutrinos in the signal topology lead to a considerable amount of missing transverse energy, while  $Z/\gamma^* \rightarrow ee$  and QCD di-jet events are characterized by small values of missing transverse energy. Figure 6.16 shows the  $\cancel{E}_T$  distribution in data and for the background expectation at selection stage (2). Data and Monte Carlo are in reasonable agreement. All events with  $\cancel{E}_T \leq 25$  GeV are discarded.

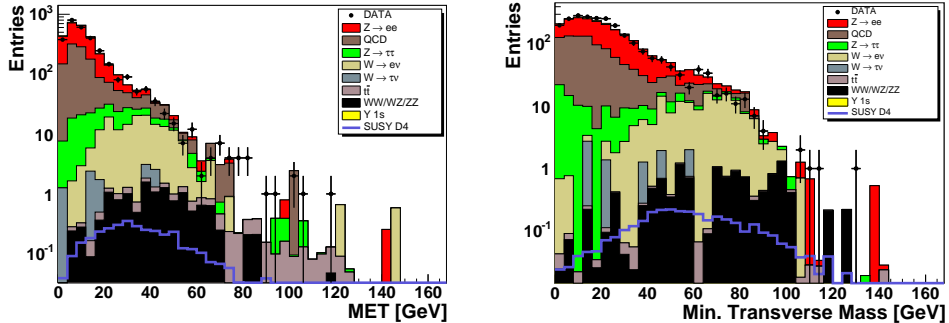


Figure 6.16: Missing transverse energy distribution (left) and minimum of  $M_T(e, \cancel{E}_T)$  and  $M_T(\tau_h, \cancel{E}_T)$  (right) at selection stage (2). Tau type 1 and 2 are combined for this plot.

#### *Minimum Transverse Mass ( $M_T$ )*

Large reconstructed missing transverse energy in background events without true  $\cancel{E}_T$  is often due to poorly measured electron or tau energy. As a consequence, the azimuthal angle between the missing transverse energy vector and the electron or the tau is small. This results in small values for the minimal transverse mass (see Eqn. 6.1) of either the electron and  $\cancel{E}_T$  or of the tau

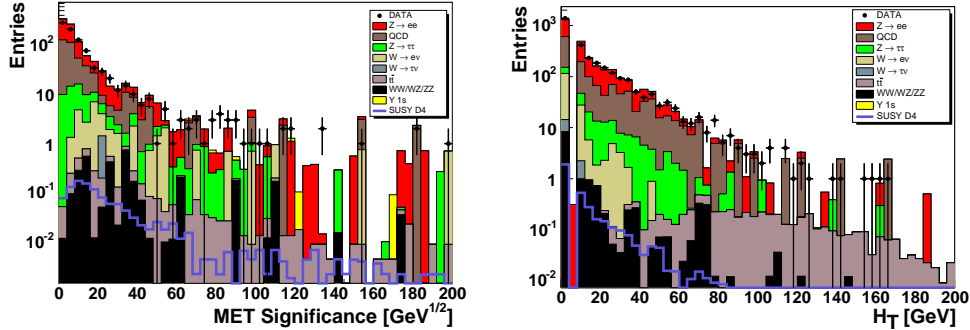


Figure 6.17: Distribution of the  $\cancel{E}_T$  significance (left) and of the sum of the jet transverse momenta  $H_T$  (right) at selection stage (2). Tau type 1 and 2 are combined for this plot.

and  $\cancel{E}_T$ . The signal, in contrast, is characterized by larger values of the transverse mass. Figure 6.16 shows the minimum of the electron and tau transverse mass before the corresponding cut is applied. Events with a minimal transverse mass below 10 GeV are discarded.

#### *Significance of $\cancel{E}_T$ and $H_T$*

Large values of the missing transverse energy in  $Z + jets$  and QCD multijet events stem mostly from fluctuations of the reconstructed jet energies. An  $\cancel{E}_T$  significance [78] is calculated, defined as:

$$\text{MET Significance} = \frac{\cancel{E}_T}{\sqrt{\sum_{\text{Jets}} \sigma_{E_T(\text{jet})||\cancel{E}_T}^2}}. \quad (6.2)$$

Figure 6.17 shows the distribution of this quantity at selection stage (2). Background events from  $Z + jet$  and QCD jet production are characterized by small values of the missing transverse energy significance. To further reject these events, the  $\cancel{E}_T$  significance is required to be in excess of  $8.0 \sqrt{\text{GeV}}$ .

As discussed in Section 6.1.4,  $t\bar{t}$  events become an important background source in later stages of the selection due to the considerable amount of true missing transverse energy. In contrast to the signal, these events are characterized by the presence of at least two hard jets, stemming from the top decay into  $b$  quarks. As a consequence, the  $t\bar{t}$  contribution can be reduced by a cut on the scalar sum of the  $p_T$  of the good jets in the event, called  $H_T$ . The distribution of the quantity is shown in Figure 6.17 after the  $Z$  veto. The  $t\bar{t}$  background shows a broad distribution with a mean value around 100 GeV. Data and background expectation are in reasonable agreement in the selected  $H_T$  range. A large part of the  $t\bar{t}$  background is rejected by requiring  $H_T < 60$  GeV, while still keeping a high efficiency for SUSY signal events.

The combined cuts on the missing transverse energy, the MET significance and  $H_T$  reduce the background by a factor of 13, while losing 34 % of the SUSY signal.

#### (4) Selection of a Third Track or a Second Tau Candidate

The most important backgrounds remaining after selection stage (3) are  $W \rightarrow e\nu$  and QCD multijet events (see Table 6.6).  $W$  events are characterized by genuine missing transverse energy, hence they become important once the other backgrounds are reduced by cutting on  $\cancel{E}_T$ . The QCD jet production remains important throughout the analysis due to its large cross section. Both the  $W$  and QCD background events, and to a minor extent also the remaining  $Z/\gamma^*$  events, can be significantly reduced by exploiting the fact that there is a third isolated charged lepton in the SUSY final state.

One approach is to require a third identified lepton in the event, which is well separated from both the electron and tau and which stems from the same vertex. Since the third lepton has only a small transverse momentum (see Figure 6.7), the efficiency of this method suffers from a decreasing identification efficiency at low values of  $p_T$ .

An alternate approach, which leads to a higher signal-to-background ratio, consists in requiring an isolated high-quality track. This track needs to be separated from both the electron and tau and stem from the same vertex. While this method works well if the third lepton is an electron or a muon, the efficiency for hadronic tau decays suffers from a higher hadronic activity.

This analysis makes use of both methods by requiring either a second reconstructed tau with a high neural network output (all three tau types are used) or an additional isolated high-quality track. If both a tau and a track are present and meet the corresponding requirements, the second tau is selected.

##### *Selection of a Third Track*

The third track has to be separated from the both the electron and tau candidate ( $\Delta\mathcal{R}(e/\tau_h, track) > 0.2$ ), and it must stem from the same vertex ( $|\Delta z_0| < 2$  cm). The signal is characterized by an isolated high- $p_T$  track, while the background has either low- $p_T$  tracks or consists of non-isolated tracks. To ensure good transverse momentum measurement and to retain only isolated tracks, the following quality criteria are applied:

- $\geq 17$  hits (at least 1 CFT hit) or  $\geq 14$  CFT hits;
- Track  $\chi^2/Ndf < 3.0$ ;
- Track isolation: the scalar  $p_T$  sum of all tracks in a hollow cone of  $0.1 < |\Delta\mathcal{R}| < 0.4$  around the track is required to be smaller than 1 GeV. The tracks that are used for this quantity are required to originate from the same vertex;
- Calorimeter isolation: the scalar  $E_T$  sum of in the electromagnetic and the fine hadronic cells in a hollow cone of  $0.2 < \Delta\mathcal{R} < 0.4$  around the extrapolation of the third track into the calorimeter is required to be less than 3 GeV and less than 60 % of  $\sqrt{p_T(track)}$ .

Figure 6.18 shows the distribution of the track transverse momentum in data and background expectation after selection stage (2) and before the cut on the transverse momentum of the track is applied. This analysis requires a third track with  $p_T > 5$  GeV. The Monte Carlo efficiency corrections derived for the tracking (see Chapter 5.5.5) are applied.

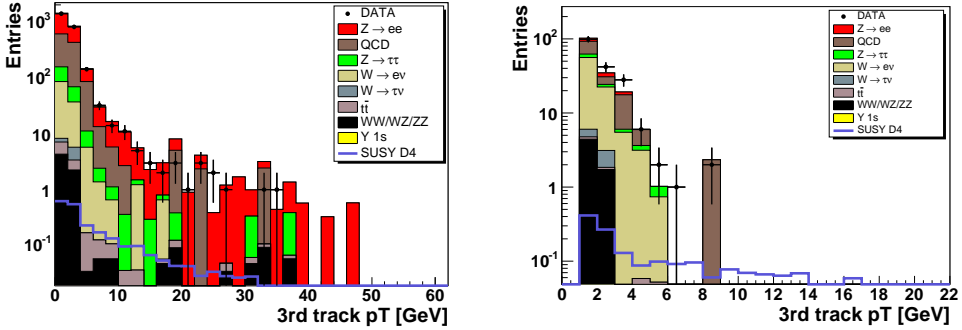


Figure 6.18: Distribution of the transverse momentum of the third track at selection stage (2) (left) and before the  $p_T$  cut on third track (right). Tau type 1 and 2 are combined for this plot.

### Selection of a Second Tau

The second tau has to be separated from both the electron and the leading hadronic tau candidate ( $\Delta\mathcal{R}(e/\tau_h, \text{track}) > 0.2$ ), and it is required to originate from the same vertex ( $|\Delta z_0| < 2.0$  cm). Its transverse momentum has to be larger than 8 GeV, and the neural network output must exceed 0.95. All three tau types are allowed. Figure 6.19 shows the transverse momentum and the neural network distribution of the second tau at selection stage (2), and before a cut on the second tau is applied. Requiring  $\Delta\phi$  between the leading electron and the second tau to be smaller than 2.9 removes  $Z/\gamma^* \rightarrow ee$  events where the second electron fakes the second tau. Events with poorly measured tau energy are removed by requiring the azimuthal angle  $\Delta\phi$  between the  $\cancel{E}_T$  vector and the second tau to be larger than 0.3.

The reconstructed final state consists of three fully identified leptons: one electron and two taus with a high neural network output. Due to the low background of less than 0.15 events (mostly from  $WZ$  events), no further cuts are applied to these events. As stated above, the signal efficiency suffers from the small identification efficiency and contributes to 15 % of the overall signal efficiency. The overlap between the second tau and third track requirement is taken into account in this number.

### (5) Boson and Di-boson Veto

The  $WZ$  process is one of the main backgrounds at the end of the selection, despite of its small production cross section. Leptonic decays of the  $W$  and

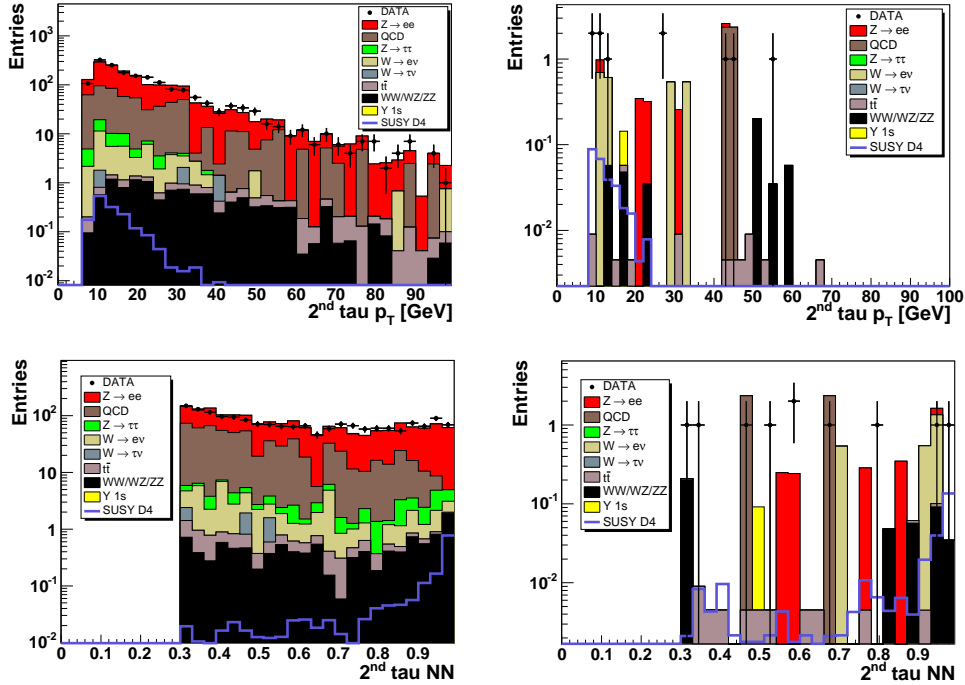


Figure 6.19: The upper row shows the transverse momentum distribution of the second tau at selection stage (2) (left) and before the cut on the second tau is applied (right). The lower row shows the neural network output distribution for the second tau at the same stages. The neural network cut at 0.3 is of technical nature to keep data volume small. the Tau type 1 and 2 are combined for this plot.

the  $Z$  bosons result in the same final state topology as in the search for neutralino/chargino production: three leptons and missing transverse energy. Requiring that the invariant mass of the tau track and the third track is smaller than 70 GeV rejects  $WZ$  events where the  $Z$  boson decays into an electron or muon pair, where the electron/muon is misidentified as the tau. Events where the  $Z$  decays into a tau pair (with subsequent hadronic and/or leptonic tau decay) are irreducible background since the  $Z$  boson mass cannot be reconstructed due to the escaping neutrinos in the tau decay.

The  $W \rightarrow e\nu$  background sums up to 0.6 events at this selection stage. It consists of a reconstructed electron, a jet faking the tau and an additional low- $p_T$  track. These events are effectively reduced by raising the  $p_T$  threshold of the third track to 9 GeV if the transverse mass of the electron and  $\cancel{E}_T$  is between 50 and 90 GeV (see Ref. [95]). This results in a background rejection factor of 2.6 for the  $W \rightarrow e\nu$  background.

### (6) Combined Cut on $p_T^{trk}$ and $\cancel{E}_T$

A further reduction of the background events is necessary and achieved by cutting on the value of  $p_T^{trk} \times \cancel{E}_T$ . This cut exploits two important characteristics of the signal final state: the presence of a third lepton with relatively high transverse momentum and a substantial amount of missing transverse energy. The final cut value has been determined by varying the cut value in the range between 250 and 400  $\text{GeV}^2$  in steps of 50  $\text{GeV}^2$ , and the position is chosen such that it gives the best expected 95% confidence limit on the signal cross section in the absence of a SUSY signal using the LEP CLs method [96]. All events with  $p_T^{trk} \times \cancel{E}_T \leq 350 \text{ GeV}^2$  are discarded. Figure 6.20 shows the distribution of data and expected background after selection stage (2) and before the cut is applied.

The last cut reduces the expected background to  $0.582^{+0.112}_{-0.105}(\text{stat})$ , while no event is selected in data. A detailed discussion of the obtained results follows in Section 6.6, after a study of the systematic uncertainties.

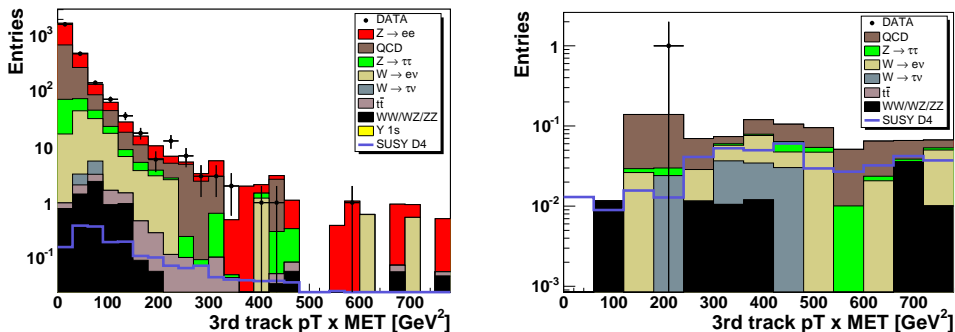


Figure 6.20: Distribution of  $p_T^{trk} \times \cancel{E}_T$  after selection stage (2) (left) and before the corresponding cut is applied (right). Tau type 1 and 2 are combined for this plot.

## 6.5 Systematic Uncertainties

Various sources of systematic uncertainties have been studied to investigate their influence on signal efficiencies and background expectations. The most important contribution stems from the detector modeling, which includes the electron/tau reconstruction efficiencies, the electron smearing and the calibration of the jet energy scale. Other contributions arise from the modeling of the trigger efficiencies, the modeling of the physics process, the calculation of the expected QCD background and from the measurement of the integrated luminosity.

- QCD Scale Factor

The contribution from the description of the QCD multijet background,

in particular the tau type dependent reweighting of the QCD sample (see Table 5.5 in Section 5.4), is estimated by varying the corresponding scale factors within the error of the global normalization.

- PDF/Scale Error on Cross Section

The PDF-related errors on the Standard Model background cross sections, which are presented in Table 5.4, are calculated according to Ref. [72]. The PDF uncertainty on the SUSY signal cross section increases with the chargino and neutralino masses and has been conservatively estimated as 3.5 %.

- Jet Energy Scale

The calibration of the jets (jet energy scale) is an important source of systematic uncertainty due to the fact that it is propagated into the missing transverse energy. Its contribution is calculated by varying the jet energy scale corrections for data and Monte Carlo within their errors.

- $\cancel{E}_T$  Smearing

The smearing of the missing transverse energy in Monte Carlo increases the number of events that are expected to pass the  $\cancel{E}_T$  requirement in the event selection. This uncertainty is taken into account conservatively by calculating the difference in the number of expected events for background and signal with smeared and unsmeared Monte Carlo.

- Electron Reconstruction/Track Match Efficiency

Another important contribution to the systematic error stems from the modeling of the electron efficiency, in particular the reconstruction efficiency (which comprises the identification efficiency) and the track match efficiency. Both contributions are calculated by varying the Monte Carlo efficiency corrections within their errors, as listed in Table 5.6 and shown in Figure 5.8.

- Electron Smearing

The electron smearing in Monte Carlo has an impact on the number of the selected events, mainly via propagation of the modification of the transverse momenta of electron and tau into the missing transverse energy calculation. The contribution to the systematic error is estimated by comparing the results with and without smearing, which leads to a conservative estimation for this error.

- Trigger Efficiency

An incorrect modeling of the trigger efficiency leads to a wrong estimate of the Standard Model background and to an incorrect signal efficiency. The effect of the trigger efficiency is calculated by varying the parameters of the resulting fits to the trigger acceptance within the  $1\sigma$  error of the fit.

- Tau Track Efficiency

The contribution of the tau track efficiency (see Section 5.5.3) to the

systematic error is estimated by varying the correction factors within its errors (see Section 5.5.3).

The individual contributions are summarized in Table 6.5 for Standard Model processes and for SUSY processes after the last selection cut. The total systematic error is calculated as the square root of the quadratic sum of the individual errors, assuming that they are independent.

The systematic error for the background estimate after all cuts is, as expected, largely dominated by the contribution from the jet energy scale. Further dominant sources for the background sample arise from the modeling of the physics processes, the tau track efficiency, the trigger efficiency and the  $\cancel{E}_T$  smearing. In combination with the error of the luminosity measurement of 6.5 % (see Ref. [70]), the total systematic error for the background is 19.4 %. The main contribution to the systematic error of the signal efficiency stems from the modeling of the physics process, the tau track efficiency and the trigger efficiency. The systematic error on the signal expectation adds up to 8.2 %.

The size of the systematic error for both signal and background is to a large part due to an incomplete understanding of the detector. This error is expected to be reduced in the future.

Source	Background	Signal
QCD Scale Factor	7 %	–
Jet Energy Scale	15.4 %	0.1 %
PDF/Scale Error on Cross Section	5.4 %	3.5 %
$\cancel{E}_T$ Smearing	1.6 %	1.1 %
Electron Reconstruction Efficiency	0.6 %	0.4 %
Electron Track match Efficiency	0.8 %	0.5 %
Electron Smearing	1.5 %	0.4 %
Trigger Efficiency	2.5 %	1.8 %
Tau track Efficiency	2.8 %	2.8 %
Quadratic Sum	18.3 %	5.0 %
Integrated Luminosity	6.5 %	6.5 %
Quadratic Sum Total	19.4 %	8.2 %

Table 6.5: Systematic uncertainties on the number of events expected from Standard Model processes and from SUSY processes after the last selection cut (relative errors are quoted).

## 6.6 Results

The number of candidate events observed and background events expected after application of the successive selection cuts are listed in Table 6.6. The comparison of data and Monte Carlo shows a good agreement at all stages of the selection. After the final selection criteria, the total background expectation is

Cut	Data	Sum BGND	
(1) Preselection	33466	$32572.5 \pm 105.9 \pm 6319.0$	
(2) $Z$ veto	2977	$2952.4 \pm 54.1 \pm 572.8$	
(3) Significant MET	215	$220.6 \pm 19.0 \pm 42.8$	
(4) 3 <sup>rd</sup> Track OR 2 <sup>nd</sup> tau	3	$3.271^{+0.800}_{-0.800} \pm 0.635$	
(5) (Di-)Boson Rejection	1	$0.977^{+0.225}_{-0.189} \pm 0.190$	
(6) $p_T^{\text{trk}} \times \cancel{E}_T$	0	$0.582^{+0.112}_{-0.105} \pm 0.113$	
Cut	QCD	$Z/\gamma^* \rightarrow ee$	$Z/\gamma^* \rightarrow \tau\tau$
(1) Preselection	$3092.9 \pm 75.7$	$28289.2 \pm 72.7$	$668.5 \pm 6.7$
(2) $Z$ veto	$1037.9 \pm 51.4$	$1564.8 \pm 13.9$	$136.3 \pm 3.9$
(3) Significant MET	$86.6 \pm 17.1$	$15.7 \pm 1.7$	$8.2 \pm 0.9$
(4) 3 <sup>rd</sup> Track OR 2 <sup>nd</sup> tau	$0.908 \pm 0.712$	$0.588 \pm 0.294$	$0.772 \pm 0.188$
(5) (Di-)Boson Rejection	$0.445 \pm 0.174$	$0.0^{+0.120}_{-0.0}$	$0.059 \pm 0.017$
(6) $p_T^{\text{trk}} \times \cancel{E}_T$	$0.218 \pm 0.086$	$0.0^{+0.039}_{-0.0}$	$0.050 \pm 0.015$
Cut	$W \rightarrow e\nu$	$W \rightarrow \tau\nu$	$WW/WZ/ZZ$
(1) Preselection	$272.7 \pm 12.8$	$8.5 \pm 1.9$	$48.6 \pm 1.3$
(2) $Z$ veto	$144.6 \pm 9.1$	$7.3 \pm 1.7$	$12.7 \pm 0.9$
(3) Significant MET	$98.5 \pm 7.8$	$2.5 \pm 1.0$	$9.6 \pm 0.9$
(4) 3 <sup>rd</sup> Track OR 2 <sup>nd</sup> tau	$0.600 \pm 0.080$	$0.103 \pm 0.042$	$0.287 \pm 0.059$
(5) (Di-)Boson Rejection	$0.231 \pm 0.046$	$0.103 \pm 0.042$	$0.126 \pm 0.034$
(6) $p_T^{\text{trk}} \times \cancel{E}_T$	$0.154 \pm 0.036$	$0.031 \pm 0.031$	$0.116 \pm 0.032$
Cut	$t\bar{t}$	$\Upsilon(1s)$	
(1) Preselection	$16.3 \pm 0.3$	$192.4 \pm 4.1$	
(2) $Z$ veto	$5.3 \pm 0.2$	$49.9 \pm 2.1$	
(3) Significant MET	$0.7 \pm 0.1$	$0.3 \pm 0.2$	
(4) 3 <sup>rd</sup> Track OR 2 <sup>nd</sup> tau	$0.013 \pm 0.008$	$0.0^{+0.009}_{-0.0}$	
(5) (Di-)Boson Rejection	$0.013 \pm 0.008$	$0.0^{+0.002}_{-0.0}$	
(6) $p_T^{\text{trk}} \times \cancel{E}_T$	$0.013 \pm 0.008$	$0.0^{+0.002}_{-0.0}$	

Table 6.6: Number of candidate events observed and background events expected at different stages of the selection. The errors for the numbers of the individual backgrounds are statistical. For the sum of all backgrounds, both statistical and systematic errors are given.

$0.582^{+0.112}_{-0.105}(\text{stat}) \pm 0.113(\text{sys})$  events, while no event is observed in the data. The remaining background stems mostly from QCD,  $W \rightarrow e\nu$  and di-boson events. The dominant contribution in the di-boson sample is caused by  $WZ$  events.

Cut	C1	D1
$m_{\tilde{\chi}_1^\pm}$ [GeV]	106	110
(1) Preselection	$11.20 \pm 0.29 \pm 0.92$	$9.58 \pm 0.21 \pm 0.79$
(2) $Z$ veto	$9.23 \pm 0.25 \pm 0.76$	$7.57 \pm 0.18 \pm 0.62$
(3) Significant MET	$5.90 \pm 0.20 \pm 0.48$	$4.80 \pm 0.15 \pm 0.39$
(4) 3 <sup>rd</sup> Track OR 2 <sup>nd</sup> tau	$1.986 \pm 0.115 \pm 0.160$	$1.747 \pm 0.111 \pm 0.143$
(5) (Di-)Boson Rejection	$1.271 \pm 0.093 \pm 0.104$	$1.077 \pm 0.071 \pm 0.088$
(6) $p_T^{\text{trk}} \times \cancel{E}_T$	$1.116 \pm 0.087 \pm 0.092$	$0.969 \pm 0.068 \pm 0.079$
Cut	D4	E1
$m_{\tilde{\chi}_1^\pm}$ [GeV]	110	114
(1) Preselection	$4.67 \pm 0.09 \pm 0.38$	$8.73 \pm 0.17 \pm 0.72$
(2) $Z$ veto	$3.59 \pm 0.08 \pm 0.29$	$6.90 \pm 0.15 \pm 0.57$
(3) Significant MET	$2.38 \pm 0.07 \pm 0.20$	$4.46 \pm 0.12 \pm 0.37$
(4) 3 <sup>rd</sup> Track OR 2 <sup>nd</sup> tau	$0.973 \pm 0.044 \pm 0.080$	$1.382 \pm 0.069 \pm 0.113$
(5) (Di-)Boson Rejection	$0.691 \pm 0.037 \pm 0.057$	$1.059 \pm 0.059 \pm 0.087$
(6) $p_T^{\text{trk}} \times \cancel{E}_T$	$0.634 \pm 0.035 \pm 0.052$	$0.968 \pm 0.057 \pm 0.079$

Table 6.7: Number of signal events expected at different stages of the selection with statistical and systematic errors.

	C1	D1	D4	E1
$\epsilon(e + \tau_h + \ell)$ [%]	$0.45 \pm 0.04 \pm 0.03$	$0.49 \pm 0.03 \pm 0.04$	$1.03 \pm 0.06 \pm 0.08$	$0.52 \pm 0.03 \pm 0.04$

Table 6.8: Selection efficiencies for the four SUSY reference points after application of all selection criteria with statistical error. The branching ratio into  $e + \tau_h + \ell$  is included.

Table 6.7 gives an overview of the expected number of SUSY signal events at all stages of the selection. The number of expected signal events is in the range from 0.6 to 1.1 for the chosen reference points. The selection efficiencies for these signal points are presented in Table 6.8. The largest efficiency is achieved for reference point D4, despite of its unfavorable branching ratio into leptons (see Table 6.1). In the case of SUSY point D4, the neutralino and the chargino decay mainly via virtual sfermions and gauge bosons (3-body decays), resulting in a large transverse momtum of the electron. Hence the electron is the leading lepton, yielding to a high trigger effciency.

Since no evidence for the associated chargino/neutralino production in  $e + \tau_h + \ell$  final state is observed, upper limits on the product of the production cross section and the leptonic branching ratio,  $\sigma(\tilde{\chi}_2^0 \tilde{\chi}_1^\pm) \times \text{BR}(3\ell)$ , are extracted. As discussed in Section 6.2, the studied parameter space is characterized by low values of  $\tan\beta$ . To probe the supersymmetric parameter space beyond the existing LEP II limits, a combination of various trilepton analyses is necessary. The combined result is presented in Section 6.6.2.

### 6.6.1 Flavor Composition of the Signal Final State

In order to combine the obtained results with the results from other trilepton searches and to study the combined sensitivity in the SUSY parameter space, it is necessary to understand the flavor composition of the signal final state. Overlap between the  $e + \tau_h + \ell$  final state and other final states is expected, and has to be taken into account when combining all results.

As discussed in Section 4.4, an electron (muon) from a leptonic tau decay cannot be distinguished from a direct decay into an electron (muon). Hence it is of no interest in the following if the reconstructed electron or muon originates from a leptonic tau decay or a direct decay.

Since real electrons are reconstructed as hadronic tau decays with a very high efficiency (see discussion in Section 4.4.2), it is expected that the selected signal final states consist to some extent of two electrons (stemming from the next-to-lightest neutralino decay) and an additional lepton (from the chargino decay). In the  $e + \tau_h + \ell$  analysis, one of the two electrons is reconstructed as the electron, while the second electron is reconstructed as the hadronically decaying tau. The additional lepton – which can either be an electron, a muon or a tau – is identified as the third track. Hence there is a significant overlap with the search for associated chargino/neutralino production in the  $e + e + \ell$  final state. In order to recover efficiency losses of the  $e + e + \ell$  analysis, there is no attempt made to separate electrons from hadronic tau decays. The main efficiency loss occurs for events where one electron is located in the inter-cryostat region ( $1.1 \leq \eta_{det} \leq 1.6$ ). This detector region is not equipped with an electromagnetic calorimeter, hence the electron reconstruction fails. However, these electrons are reconstructed as taus of type 1, since their detector signal (one isolated track pointing to a narrow calorimeter cluster with only a small amount of electromagnetic energy) matches the tau type 1 reconstruction criteria (see Section 4.4.2). The overlap with the  $e + e + \ell$  final state is studied for each SUSY reference point separately. It amounts to up to 40 % for reference point D4 and up to 30 % for the remaining SUSY points.

The efficiency for selecting signal final states that consist of one or more real muons is small. The rate at which a muon fakes an electron (using the applied electron identification criteria) is insignificant. The fake rate for taus from muons is in the order of 20 % for tau type 1 and 10 % for tau type 2. The probability that a real muon fakes a tau of type 3 is tiny due to the requirement that at least two tracks have to point to the calorimeter cluster. Large contributions to the  $e + \tau_h + \ell$  analysis are therefore only expected in the signal final state with two muons and an electron ( $\mu + \mu + e$ ) and with two electrons and a muon ( $e + e + \mu$ ). The first case, where one muon fakes the hadronic tau decay and the second muon leads to the third track, amounts to 5 % overlap. The latter case, where the muon primarily leads to the third track, is already covered in the overlap with the  $e + e + \ell$  analysis.

### 6.6.2 Combination with Additional Trilepton Analyses

A combination of six analyses which search for the associated production of the lightest chargino and the second-lightest neutralino in final states with three leptons and missing transverse energy is performed to increase the sensitivity. The combination consists of analyses that cover the following final states:

- two electrons and a third lepton ( $e + e + \ell$ ) [78];
- an electron, a muon and a third lepton ( $e + \mu + \ell$ ) [92];
- two muons and a third lepton ( $\mu + \mu + \ell$ ) [93];
- two like-sign muons (LS  $\mu + \mu$ ) [94];
- a muon, a hadronically decaying tau and a third lepton ( $\mu + \tau_h + \ell$ ) [95];
- an electron, a hadronically decaying tau and a third lepton ( $e + \tau_h + \ell$ ).

A set of reference parameter points has been simulated for chargino masses in the region near and beyond the LEP II chargino mass limit of 103 GeV. These SUSY points are characterized by an equal branching ratio of chargino and neutralino into leptons. Table 6.9 presents an overview of these reference points and lists the most important properties. The obtained efficiencies for each analysis are shown in Table 6.10. The number of signal events expected for the six analysis channels for each SUSY point is given in Table 6.11. To avoid double-counting, a signal selected by more than one analysis channel is assigned to one channel and removed from the other channels in a way which maximizes the combined sensitivity.

Point	$m_0$ [GeV]	$m_{1/2}$ [GeV]	$\text{sgn}(\mu)$	$m_{\tilde{\chi}_2^0}$ [GeV]	$m_{\tilde{\chi}^\pm}$ [GeV]	$m_{\tilde{\ell}_R}$ [GeV]	$m_{\tilde{\chi}_1^0}$ [GeV]	$\text{BR}(\ell)$	$\sigma \times \text{BR}(3\ell)$ [pb]
A5	88	165	–	102	103	114	55	0.35	0.536
A6	200	126	+	102	103	208	52	0.35	0.400
B6	200	132	–	106	107	209	54	0.34	0.331
C6	200	138	–	110	111	210	57	0.33	0.264
D6	200	142	–	114	114	210	58	0.32	0.231
E6	200	148	–	118	119	211	61	0.30	0.179
F6	200	166	–	132	132	212	69	0.23	0.102

Table 6.9: Properties of SUSY reference points used in the combination. All points have  $\tan\beta=3$  and  $A_0 = 0$ .

The number of events observed in data and the number of background events expected from Monte Carlo for each analysis at the end of the selection is shown in Table 6.12. Combining all six analyses, the expected background sums up to  $3.85 \pm 0.57(\text{stat}) \pm 0.48(\text{sys})$  events, while 4 events remain in data. Since no evidence for supersymmetry is observed, an upper limit on the total

Point	$\epsilon(e + e + \ell)$ [%]	$\epsilon(e + \mu + \ell)$ [%]	$\epsilon(\mu + \mu + \ell)$ [%]
A5	1.77 $\pm$ 0.08 $\pm$ 0.14	1.21 $\pm$ 0.04 $\pm$ 0.10	0.83 $\pm$ 0.02 $\pm$ 0.11
A6	2.18 $\pm$ 0.08 $\pm$ 0.18	1.57 $\pm$ 0.03 $\pm$ 0.12	0.91 $\pm$ 0.02 $\pm$ 0.12
B6	2.37 $\pm$ 0.08 $\pm$ 0.19	1.75 $\pm$ 0.04 $\pm$ 0.14	0.87 $\pm$ 0.02 $\pm$ 0.11
C6	2.46 $\pm$ 0.09 $\pm$ 0.20	1.70 $\pm$ 0.05 $\pm$ 0.13	0.91 $\pm$ 0.03 $\pm$ 0.12
D6	2.79 $\pm$ 0.10 $\pm$ 0.23	1.92 $\pm$ 0.05 $\pm$ 0.15	0.90 $\pm$ 0.05 $\pm$ 0.11
E6	2.71 $\pm$ 0.09 $\pm$ 0.22	1.85 $\pm$ 0.06 $\pm$ 0.15	0.87 $\pm$ 0.02 $\pm$ 0.11
F6	2.97 $\pm$ 0.10 $\pm$ 0.24	2.11 $\pm$ 0.11 $\pm$ 0.17	0.76 $\pm$ 0.02 $\pm$ 0.10
Point	$\epsilon(\text{LS } \mu + \mu)$ [%]	$\epsilon(\mu + \tau_h + \ell)$ [%]	$\epsilon(e + \tau_h + \ell)$ [%]
A5	0.58 $\pm$ 0.11 $\pm$ 0.09	0.60 $\pm$ 0.03 $\pm$ 0.05	0.35 $\pm$ 0.01 $\pm$ 0.03
A6	0.62 $\pm$ 0.14 $\pm$ 0.10	0.85 $\pm$ 0.02 $\pm$ 0.07	0.47 $\pm$ 0.01 $\pm$ 0.04
B6	0.68 $\pm$ 0.11 $\pm$ 0.11	0.90 $\pm$ 0.02 $\pm$ 0.07	0.45 $\pm$ 0.01 $\pm$ 0.03
C6	0.74 $\pm$ 0.14 $\pm$ 0.12	0.99 $\pm$ 0.03 $\pm$ 0.08	0.57 $\pm$ 0.01 $\pm$ 0.04
D6	0.83 $\pm$ 0.15 $\pm$ 0.13	0.99 $\pm$ 0.03 $\pm$ 0.08	0.51 $\pm$ 0.01 $\pm$ 0.04
E6	0.86 $\pm$ 0.18 $\pm$ 0.13	0.99 $\pm$ 0.03 $\pm$ 0.08	0.48 $\pm$ 0.01 $\pm$ 0.04
F6	0.87 $\pm$ 0.17 $\pm$ 0.14	1.33 $\pm$ 0.08 $\pm$ 0.11	0.59 $\pm$ 0.01 $\pm$ 0.04

Table 6.10: Selection efficiencies for the SUSY reference points used in the combination (see Table 6.9) for all six trilepton analysis channels, given with statistic and systematic error. Overlaps between the different channels are taken into account and are subtracted.

Point	$e + e + \ell$	$e + \mu + \ell$	$\mu + \mu + \ell$
A5	3.19 $\pm$ 0.14 $\pm$ 0.26	2.17 $\pm$ 0.07 $\pm$ 0.17	1.41 $\pm$ 0.04 $\pm$ 0.18
A6	2.94 $\pm$ 0.11 $\pm$ 0.24	2.11 $\pm$ 0.04 $\pm$ 0.17	1.16 $\pm$ 0.03 $\pm$ 0.15
B6	2.62 $\pm$ 0.09 $\pm$ 0.21	1.92 $\pm$ 0.04 $\pm$ 0.15	0.91 $\pm$ 0.02 $\pm$ 0.12
C6	2.15 $\pm$ 0.08 $\pm$ 0.17	1.48 $\pm$ 0.04 $\pm$ 0.12	0.75 $\pm$ 0.02 $\pm$ 0.10
D6	2.15 $\pm$ 0.07 $\pm$ 0.17	1.47 $\pm$ 0.04 $\pm$ 0.12	0.65 $\pm$ 0.03 $\pm$ 0.08
E6	1.63 $\pm$ 0.06 $\pm$ 0.13	1.11 $\pm$ 0.04 $\pm$ 0.09	0.49 $\pm$ 0.01 $\pm$ 0.06
F6	0.97 $\pm$ 0.03 $\pm$ 0.08	0.68 $\pm$ 0.04 $\pm$ 0.05	0.23 $\pm$ 0.01 $\pm$ 0.03
Point	LS $\mu + \mu$	$\mu + \tau_h + \ell$	$e + \tau_h + \ell$
A5	1.03 $\pm$ 0.19 $\pm$ 0.16	1.02 $\pm$ 0.04 $\pm$ 0.08	0.65 $\pm$ 0.02 $\pm$ 0.05
A6	0.82 $\pm$ 0.19 $\pm$ 0.13	1.08 $\pm$ 0.03 $\pm$ 0.09	0.65 $\pm$ 0.01 $\pm$ 0.05
B6	0.73 $\pm$ 0.12 $\pm$ 0.11	0.93 $\pm$ 0.02 $\pm$ 0.08	0.51 $\pm$ 0.01 $\pm$ 0.04
C6	0.63 $\pm$ 0.12 $\pm$ 0.10	0.82 $\pm$ 0.02 $\pm$ 0.07	0.51 $\pm$ 0.01 $\pm$ 0.04
D6	0.62 $\pm$ 0.12 $\pm$ 0.10	0.72 $\pm$ 0.02 $\pm$ 0.06	0.41 $\pm$ 0.01 $\pm$ 0.03
E6	0.51 $\pm$ 0.11 $\pm$ 0.08	0.56 $\pm$ 0.02 $\pm$ 0.04	0.30 $\pm$ 0.01 $\pm$ 0.02
F6	0.28 $\pm$ 0.05 $\pm$ 0.04	0.41 $\pm$ 0.02 $\pm$ 0.03	0.20 $\pm$ 0.00 $\pm$ 0.02

Table 6.11: Number of expected signal events at the end of the selection for the SUSY reference points used in the combination (see Table 6.9). All six trilepton analysis channels are shown with statistic and systematic error. Overlaps between the different channels are subtracted as described in the text.

cross section times branching ratio into three leptons using the likelihood ratio method (LEP CLs method [96]) is extracted. Systematic and statistical errors are taken into account in the combination including their correlations. The

flavor composition of the selected  $e + \tau_h + \ell$  final state and the overlap with the other trilepton analyses is discussed in Section 6.6.1. The overlap between backgrounds is negligible.

Analysis	Data	Total Background
$e + e + \ell$	0	$0.21 \pm 0.11 \pm 0.05$
$e + \mu + \ell$	0	$0.31 \pm 0.13 \pm 0.03$
$\mu + \mu + \ell$	2	$1.75 \pm 0.37 \pm 0.44$
LS $\mu + \mu$	1	$0.64 \pm 0.36 \pm 0.13$
$e + \tau_h + \ell$	0	$0.58 \pm 0.11 \pm 0.11$
$\mu + \tau_h + \ell$	1	$0.36 \pm 0.12 \pm 0.06$
SUM	4	$3.85 \pm 0.57 \pm 0.48$

Table 6.12: Number of candidate events observed and background events expected in the six trilepton analysis channels. The errors for the numbers are statistical and systematic.

### Extraction and Interpretation of the Cross Section Limits

The upper limits on the production cross section times branching ratio into three leptons are derived using the selection efficiencies for the SUSY signal presented in Table 6.10 as a function of the chargino mass.

The combined results are compared with predictions from the MSSM in order to restrict the allowed SUSY parameter space. Due to the large number of unknown parameters in the general MSSM, resulting from the parametrization of the supersymmetry breaking (see Section 1.2), the derived cross section limits are compared with selected benchmark models. The derived constraints on the chargino mass are specific for the chosen benchmark scenarios, but they can be applied to any MSSM model with comparable mass relations and branching ratios.

The upper limit on the cross section of chargino/neutralino production times branching ratio into three leptons in the 3-body region are compared with the predictions for chargino mass scans from the following benchmark scenarios:

- *3l-max scenario*: The leptonic branching ratio is maximally enhanced in this scenario, since the sleptons are mass degenerated with the second-lightest neutralino and the latter decays dominantly via sfermion mediated 3-body topologies. Due to  $m_{\tilde{\chi}_1^\pm} \approx m_{\tilde{\chi}_2^0}$ , the sfermion mediated 3-body decay is also the dominating chargino decay mode. Scalar mass unification is assumed in calculating the cross section.
- *heavy-squarks scenario*: The squarks are assumed to be very heavy (TeV scale), which suppresses the destructive interference from t-channel contribution to the production cross section, leading to a maximally enhanced cross section (see Section 6.1.3). This model is a variation of the 3l-max

scenario, where the unification of slepton and squark masses is dropped. It provides an upper bound on the trilepton cross section for 3-body topologies without stau mixing.

- *large  $m_0$  scenario:* Assuming scalar mass unification and raising  $m_0$  to the TeV scale, this model results in large slepton and squark masses. Charginos and Neutralinos decay via gauge boson mediated 3-body decays. The impact of the stau mixing on the branching ratios is negligible, since the slepton mass difference is small compared to the slepton mass and since decay via  $W/Z$  dominate.

Figure 6.21 compares the results of the chargino mass scan in the 3-body domain for the combined analysis with the model predictions for negligible stau mixing (low  $\tan\beta$  regime). The obtained upper cross section limit for the trilepton analyses without taus can be improved by 10 % when adding the two dedicated tau analyses  $e + \tau_h + \ell$  and  $\mu + \tau_h + \ell$ . Lower limits on the chargino mass of  $m_{\tilde{\chi}_1^\pm} > 114$  GeV in the 3l-max scenario and  $m_{\tilde{\chi}_1^\pm} > 125$  GeV in the heavy-squarks scenario are derived by combining the trilepton analyses without taus. These mass limits can be improved by adding the two dedicated tau analyses, resulting in a combined limit on the chargino mass of

$$m_{\tilde{\chi}_1^\pm} > 116 \text{ GeV} \quad (6.3)$$

for the 3l-max scenario and

$$m_{\tilde{\chi}_1^\pm} > 128 \text{ GeV} \quad (6.4)$$

for the heavy-squarks scenario.

The combination of all trilepton analyses is sensitive to SUSY models with chargino masses beyond the limits from SUSY searches at LEP II and Tevatron Run I.

### 6.6.3 Further Prospects

The sensitivity of all six trilepton analyses is mainly limited by data statistics, hence the mass coverage of these analyses is expected to increase with the integrated luminosity. Using only the electron and muon final states and combining both Tevatron experiments DØ and CDF, a study in Ref. [78] shows that chargino masses up to 200 GeV can be excluded in the 3l-max scenario with the full Run II data set of  $\mathcal{L} = 8 \text{ fb}^{-1}$ . Improvements in understanding and simulating the detector are expected to further increase the sensitivity of the SUSY searches.

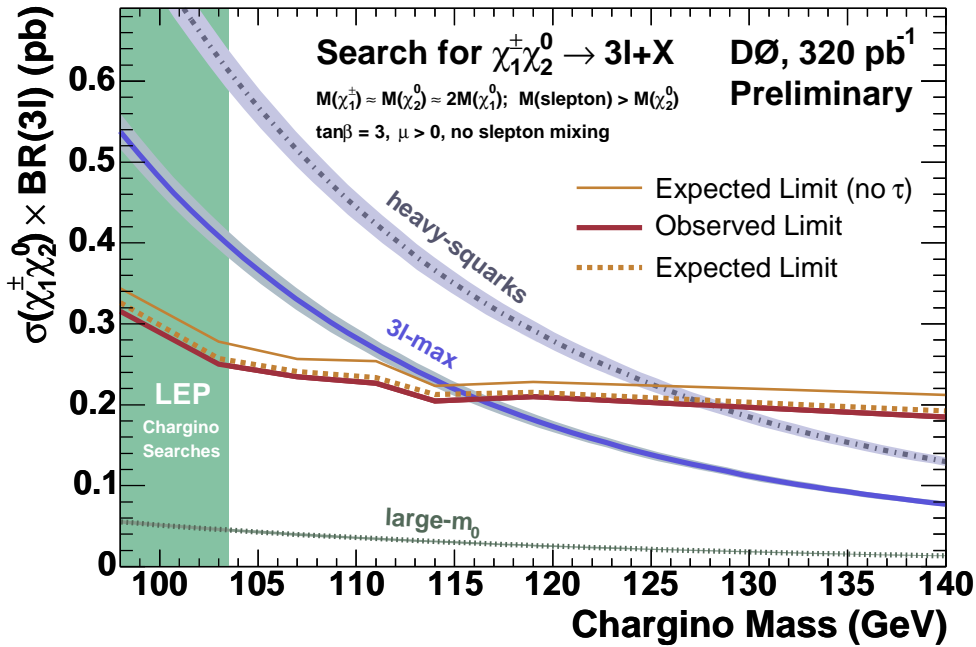


Figure 6.21: Limits on the total cross section times branching ratio into three leptons for associated chargino and neutralino production with leptonic final states. Three model lines are plotted as a reference: The top line corresponds to the signal cross section times leptonic branching fraction predicted for models with heavy squark masses and low slepton masses. The middle line corresponds to the signal expectation for low slepton masses in mSUGRA. The bottom line describes the signal expectation for large  $m_0$  with the chargino and the neutralino decaying via virtual gauge bosons. The PDF and scale uncertainties are shown as shaded bands. The expected limit is shown for the trilepton final state without the two tau analyses and with the tau analyses. The observed limit is calculated using all trilepton final states. Chargino masses below 103 GeV are excluded by direct searches at LEP.

## 6.7 Outlook: Sensitivity for the SUSY Parameter Space with Large Values of $\tan \beta$

The ultimate goal of the trilepton searches in tau final states is to search for supersymmetry in a parameter space which is characterized by high values of  $\tan \beta$ . Due to stau mixing effects (see Section 6.1.2), the lightest chargino and the second-lightest neutralino decay dominantly into final states with tau leptons in the considered mSUGRA model. In these parameter regions, the selections that are optimized on final states with electrons and muons have a low efficiency. These domains can only be covered with dedicated tau analyses as developed in this thesis.

A feasibility study is performed in order to estimate the signal efficiency for high  $\tan \beta$  scenarios with the current trilepton analyses. For this study, a set of reference parameter points has been simulated with a chargino mass of 104 GeV (motivated by the LEP limit of 104 GeV [26]) and a neutralino mass of 108 GeV. The low chargino and neutralino masses lead to a large  $\tilde{\chi}_1^\pm \tilde{\chi}_2^0$  cross section (see Figure 6.2). The relevant gaugino and slepton masses for the simulated SUSY points are outlined in Table 6.13. By varying the selectron/smuon and stau mass, different branching ratios of the second-lightest neutralino into tau final states are simulated. The branching ratio of the lightest chargino into charged leptons is kept constant for all SUSY points, and corresponds to approximately 30 % for each lepton flavor. Table 6.14 gives an overview of the different branching ratios of chargino and next-to-lightest neutralino into lepton final states.

Point	$m_{\tilde{\chi}_1^\pm}$ [GeV]	$m_{\tilde{\chi}_2^0}$ [GeV]	$m_{\tilde{\ell}_R}$ [GeV]	$m_{\tilde{\ell}_L}$ [GeV]	$m_{\tilde{\tau}}$ [GeV]	$\text{BR}(3\ell)^* K_{\text{NLO}}$ [pb]
T1	104	108	1000	1100	109	0.214
T2			140	172	109	0.238
T3			130	164	109	0.244
T4			120	156	109	0.257
T5			115	152	109	0.280
T6			112	150	109	0.296
T7			109	148	109	0.327
T8			109	148	112	0.308
T9			109	148	120	0.297
T10			109	148	1000	0.281

Table 6.13: Properties of SUSY reference points that are used to study the parameter space with large values of  $\tan \beta$ . The chargino and next-to-lightest neutralino mass are kept constant for all points.

Figure 6.22 shows the selection efficiency of all trilepton analyses for the various reference points. The branching ratio of the next-to-lightest neutralino into tau final states decreases from left (T1) to right (T10), while the branching ratio into electron/muon increases. Hence, the expected final state for T1 consist of electron/muon from the chargino decay and a tau pair from the next-to-

Point	$\text{BR}(\tilde{\chi}_2^0 \rightarrow e/\mu)$ [%]	$\text{BR}(\tilde{\chi}_2^0 \rightarrow \tau)$ [%]	$\text{BR}(\tilde{\chi}_1^\pm \rightarrow e/\mu)$ [%]	$\text{BR}(\tilde{\chi}_1^\pm \rightarrow \tau)$ [%]
T1	0.005	0.570	0.180	0.253
T2	0.080	0.491	0.242	0.234
T3	0.127	0.446	0.260	0.229
T4	0.213	0.375	0.286	0.221
T5	0.286	0.323	0.303	0.215
T6	0.351	0.283	0.315	0.212
T7	0.455	0.227	0.329	0.207
T8	0.512	0.159	0.336	0.192
T9	0.591	0.084	0.348	0.164
T10	0.706	0.001	0.380	0.085

Table 6.14: Branching ratio into leptons for the SUSY reference points considered in this study. The gaugino/slepton masses are shown in Table 6.13.

lightest neutralino decay. For SUSY point T10, the expected final state consist of electron/muon from the chargino decay and an electron/muon pair from the next-to-lightest neutralino decay.

The trilepton analyses without taus show an increasing selection efficiency from T1 to T10. The small efficiency for T1 is expected, since the electron/muon fake rate from taus is tiny. The efficiency for SUSY point T10 is in the order of 1 %. This is comparable to the selection efficiencies quoted in Table 6.10, which are achieved for SUSY parameter points with low  $\tan \beta$  and hence without stau mixing.

The trilepton analyses with taus ( $e + \tau_h + \ell$  and  $\mu + \tau_h + \ell$ ) are expected to have a selection efficiency for T1 which is comparable to T10. However, the selection efficiency shows the same behavior as for analyses without taus. Although it has to be noted that the relative importance of the tau analyses for T1 is higher than for T10, the decrease for the dedicated tau analyses is not expected and needs explanation. For the studied SUSY parameter space, two problem areas are identified: the single electron trigger efficiency and the tau reconstruction efficiency.

### Single Electron Trigger

The left plot in Figure 6.23 shows the parton level transverse momentum of the electron, stemming from the chargino decay, and the visible decay products of the two hadronically decaying taus, which stem from the neutralino decay. The slepton mass for SUSY point T3 – which is used as a reference – is  $m_{\tilde{\ell}} = 130$  GeV, hence 3-body decays are dominant. The electron transverse momentum spectrum is rather soft and has a mean value of  $p_T = 14$  GeV, which makes it difficult to trigger on these events using the single electron triggers. The efficiency of the single electron triggers (see e.g. Figure 5.5) is fully efficient for  $p_T > 18$  GeV and decreases drastically for low- $p_T$  objects, which results in

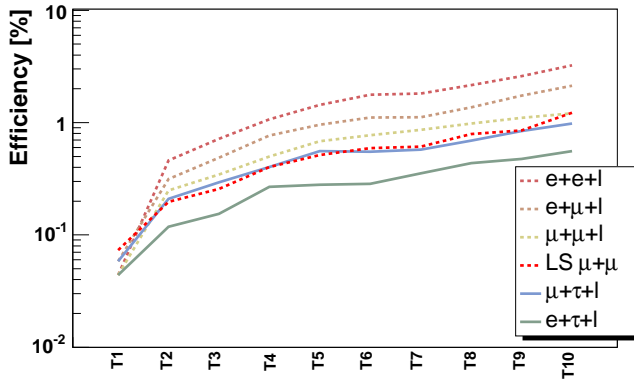


Figure 6.22: Efficiency of the different trilepton analyses for the various SUSY reference points. The branching ratio  $\tilde{\chi}_2^0 \rightarrow \tau\tau\tilde{\chi}_1^0$  decreases from SUSY point T1 (left) to T10 (right).

a large trigger inefficiency for the signal events in the  $e + \tau_h + \ell$  analysis. The  $\mu + \tau_h + \ell$  analysis [95] profits from the lower  $p_T$  thresholds of the single muon triggers, leading to a higher trigger efficiency in comparison to the  $e + \tau_h + \ell$  analysis and hence to a higher selection efficiency.

#### Tau Reconstruction Efficiency

Figure 6.23 (right) shows the reconstruction efficiency for tau candidates as a function of the visible tau transverse momentum. The plot indicates that the tau reconstruction efficiency for low- $p_T$  objects is strongly diminished, resulting in a small efficiency for taus with  $p_T < 7$  GeV. This leads to an additional inefficiency for analyses searching for trilepton final states with hadronic tau decay. Due to the escaping neutrino in the hadronic tau decay, the  $p_T$  spectrum for the two hadronically decaying taus is softer than for the electrons or muons

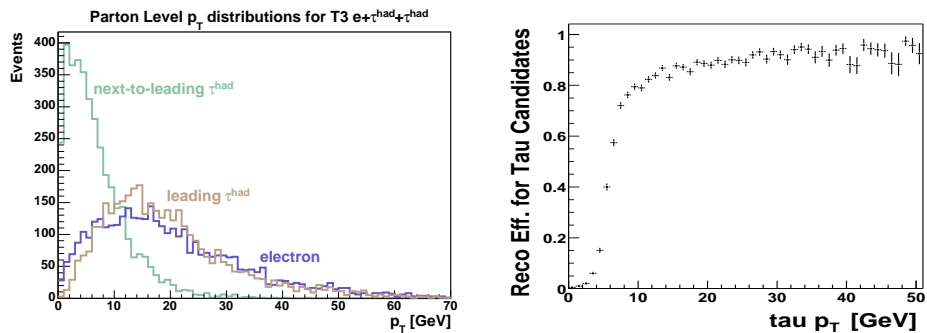


Figure 6.23: *left:* Parton level  $p_T$  distribution of the electron and the two hadronically decaying taus for SUSY point T3.  
*right:* Reconstruction efficiency for tau candidates as a function of the transverse momentum.

if the second-lightest neutralino decays into an electron or muon pair.

Both problems, the small trigger efficiency for low- $p_T$  objects and the insufficient reconstruction efficiency for low- $p_T$  taus, are currently addressed in order to gain sensitivity for the SUSY parameter space at high values of  $\tan \beta$ .



## 7 Search for MSSM Higgs Bosons in $e + \tau_h$ Final States

A discovery of supersymmetry is not only possible by searching directly for supersymmetric particles, but also by searching for the five physical Higgs boson states. While the search for associated chargino/neutralino production in  $e + \tau_h$  final states (see description in Chapter 6) is currently limited to low values of the mSUGRA parameter  $\tan \beta$ , the focus of the search for neutral MSSM Higgs bosons are large values of  $\tan \beta$  – hence both analyses can be regarded as complementary.

The following chapter gives an overview of neutral MSSM Higgs boson production and decay at the Tevatron. A search for the production of a neutral Higgs and subsequent decay into a tau pair is described. Over a large region of the supersymmetric parameter space, the rates for this process are significantly larger than in the Standard Model case for a Higgs boson of the same mass. The signal selection is optimized for a final state consisting of an electron, a hadronically decaying tau and missing transverse energy. The result of this search is combined with results from analyses that cover the  $\mu + \tau_h$  and  $e + \mu$  final states. DØ has performed a search for neutral MSSM Higgs bosons decaying in  $b\bar{b}$  final states, where the Higgs is produced in association with a pair of  $b$  quarks. The results of the  $b\bar{b}$  final state are combined with the results from the  $\tau\tau$  final state and presented at the end of this Chapter.

### 7.1 MSSM Higgs Boson Signature at the Tevatron

As discussed in Section 1.2.6, both hypercharge  $Y = -1$  and  $Y = +1$  Higgs doublets are required to avoid anomalies in the supersymmetric extension of the Standard Model and to generate mass for both up-type and down-type fermions. The resulting Higgs sector after electroweak symmetry breaking consists of five physical Higgs bosons. In the absence of explicit CP-violation in the soft symmetry-breaking terms, these are the light and heavy CP-even neutral Higgs bosons,  $h$  and  $H$ , the CP-odd neutral Higgs boson,  $A$ , and the two charged Higgs bosons  $H^\pm$ . At tree level, the following ordering of masses is valid:

$$M_h < (M_Z, M_A) < M_H \text{ and } M_{W^\pm} < M_{H^\pm}.$$

This ordering is substantially modified by radiative corrections [98], the largest contribution arising from incomplete cancellation between top and stop loops.

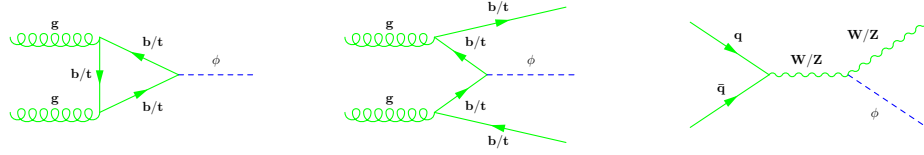


Figure 7.1: Feynman diagrams for the neutral MSSM Higgs boson production processes of interest at the Tevatron: gluon fusion (*left*), associated production with heavy quarks (*middle*), associated production with gauge bosons (*right*).

The corrections affect mainly the neutral Higgs boson masses and decay branching ratios.

At leading order, the MSSM Higgs sector is fully specified by two parameters, which are generally chosen to be  $M_A$ , the mass of the CP-odd Higgs boson, and  $\tan \beta$ , the ratio of the vacuum expectation values of the two Higgs doublets (see Section 1.2.6). In the region of large  $\tan \beta$ , the  $A$  boson is nearly degenerated in mass with either the  $h$  or the  $H$  boson and their production cross sections can be added. In the following, the neutral MSSM Higgs bosons will be generally denoted as  $\phi$ .

### 7.1.1 Neutral Higgs Boson Production

Neutral supersymmetric Higgs boson production at hadron colliders occurs in various channels. At the Tevatron, the following processes are of interest (see Figure 7.1):

- $gg \rightarrow \phi$  [ $\phi = h, H, A$ ]: The *gluon fusion* process is mediated by heavy top and bottom quark triangle loops and the corresponding supersymmetric partners. Production cross sections for the light scalar  $h$  and the pseudoscalar  $A$  Higgs bosons easily exceed 10 pb at large values of  $\tan \beta$  and for  $M_\phi < 180$  GeV. At small  $\tan \beta$ , the production cross sections range from 0.1 pb to 1 pb for  $M_\phi < 180$  GeV.
- $gg \rightarrow \phi t\bar{t}, \phi b\bar{b}$  [ $\phi = h, H, A$ ]: In the Standard Model, the *associated Higgs production with heavy quarks* has a production cross section of less than 0.01 pb (for  $M_h > 110$  GeV [99]) and suffers from small event rates. In the MSSM, however, radiation off bottom quarks becomes important for large  $\tan \beta$  with cross sections exceeding 10 pb for  $h$  and  $A$  (with  $M_\phi < 180$  GeV).
- $q\bar{q} \rightarrow V^* \rightarrow V\phi$  [ $V = W, Z$ ] [ $\phi = h, H$ ]: In comparison to the gluon fusion and the associated production with  $b$  quarks, the *associated production with weak gauge bosons* has a smaller cross section. Over most of the parameter space, one of the two CP-even Higgs bosons has very suppressed couplings to  $VV$ , while the other one couples to  $VV$  with Standard Model

strength. For the latter, this production process can be important. The light CP-even scalar Higgs boson  $h$  has Standard Model-like couplings to vector bosons in the decoupling regime ( $M_A \rightarrow \infty$ ). The heavy CP-even scalar Higgs boson  $H$  has Standard Model-like couplings to vector bosons for large  $\tan \beta$  and low  $M_A$ . In either case, the corresponding scalar  $\phi$  has a mass of less than 130 GeV.

The production cross section for neutral MSSM Higgs bosons is given in Figure 7.2 for the  $m_h^{max}$  scenario and for  $\tan \beta$  values of 5 and 40. Figure 7.3 shows the same plots for the no-mixing scenario. A description of both the  $m_h^{max}$  and the no-mixing scenario, which are considered as benchmark scenarios, is presented in Section 1.2.6. At the Tevatron, the dominant production mechanisms for the neutral supersymmetric Higgs bosons at high  $\tan \beta$  are the gluon fusion and the associated production with  $b$  quarks.

In contrast to the Standard Model, the MSSM Higgs boson production cross section is strongly enhanced for large values of  $\tan \beta$ . This is the result of enhanced couplings of the Higgs bosons to down-type fermions (see discussion in Section 1.2.6 and Table 1.7). At leading order, the production cross section is proportional to  $\tan^2 \beta$ . Figure 7.4 shows the cross section times branching ratio for the process  $p\bar{p} \rightarrow \phi \rightarrow \tau\tau$  as a function of  $M_\phi$  for different values of  $\tan \beta$  in the two benchmark scenarios that are considered in this analysis.

### 7.1.2 Neutral Higgs Boson Decay

The branching ratios of the neutral MSSM Higgs bosons have to be considered as a function of their mass as well as  $\tan \beta$  and the SUSY parameters. Figure 7.5 shows the branching ratios of  $h$ ,  $H$  and  $A$  for two different  $\tan \beta$  values as a function of their mass. The following list presents a brief discussion of the neutral Higgs boson decays:

- $\phi \rightarrow f\bar{f}$ : The decay modes  $h, H, A \rightarrow b\bar{b}, \tau^+\tau^-$  are the dominant decay modes for large  $\tan \beta$ . The branching ratio into  $b\bar{b}$  is in the order of 90 %, while the branching ratio for  $\tau\tau$  reaches 8 – 10 %. For small values of  $\tan \beta$ , they are only important for neutral Higgs masses smaller than 200 GeV.
- $\phi \rightarrow WW, ZZ$ : In the MSSM, the decays of  $h$  and  $H$  into  $WW$  and  $ZZ$  are generally suppressed by kinematics and Higgs couplings. Their branching ratios are sizeable only for small and moderate values of  $\tan \beta$  or in the decoupling regime  $M_A \rightarrow \infty$ , where the light CP-even Higgs  $h$  effectively behaves like a Standard Model Higgs boson while all others MSSM Higgs bosons are heavy.
- $\phi \rightarrow gg, \gamma\gamma$ : The gluonic and photonic decays of the Higgs bosons  $h, H, A$  have only relatively small branching ratios and are only of interest in a very limited region of the supersymmetric parameter space.

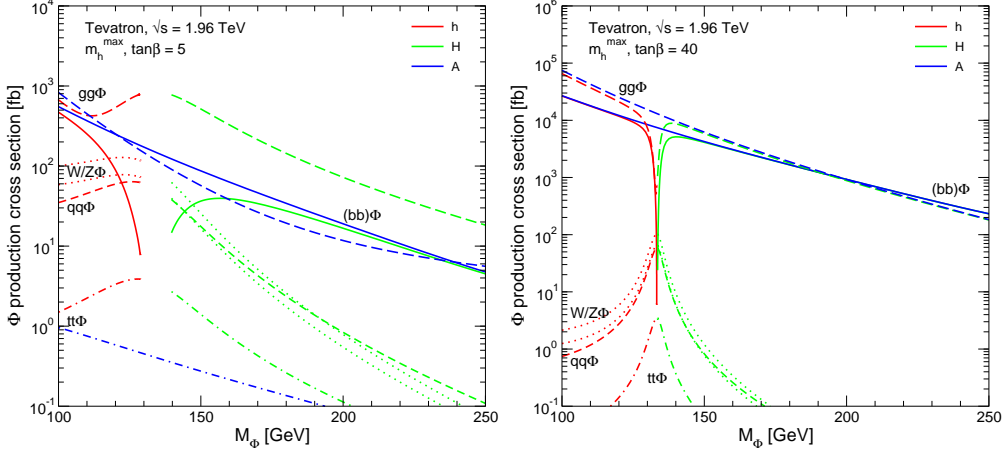


Figure 7.2: Cross section for neutral MSSM Higgs boson production as a function of their masses in the  $m_h^{max}$  scenario for  $\tan\beta = 5$  (left) and  $\tan\beta = 40$  (right). The histograms are taken from Ref. [100].

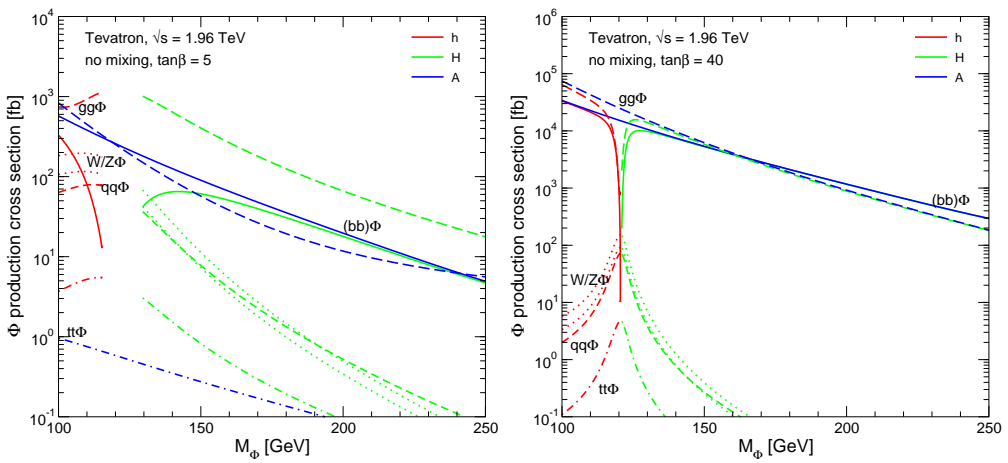


Figure 7.3: Cross section for neutral MSSM Higgs boson production as a function of their masses in the no-mixing scenario for  $\tan\beta = 5$  (left) and  $\tan\beta = 40$  (right). The histograms are taken from Ref. [100].

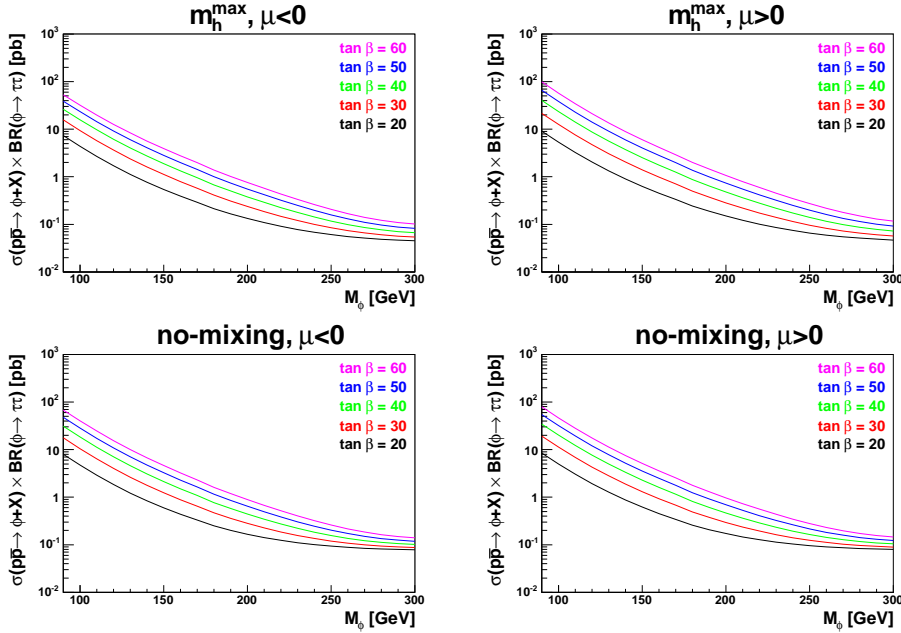


Figure 7.4: Cross section times branching ratio for the process  $p\bar{p} \rightarrow \phi + X \rightarrow \tau\tau + X$  as a function of  $M_\phi$  for different values of  $\tan\beta$ . The first row shows the dependence for the  $m_h^{max}$  scenario with  $\mu < 0$  and  $\mu > 0$ , the second row shows the same for the no-mixing scenario.

- $H \rightarrow hh$ : For small  $\tan\beta$  and  $M_H < 200$  GeV, the decay mode  $H \rightarrow hh$  is significant in the MSSM only for a very small range of  $H$  masses. It is dominant for small values of  $\tan\beta$  and a Higgs mass range of  $200$  GeV  $< M_H < 2M_t$ .
- $H \rightarrow ZA$ ;  $A \rightarrow Zh$ : The decay modes  $H \rightarrow ZA$  and  $A \rightarrow Zh$  are only important for small  $\tan\beta$  below the  $t\bar{t}$  threshold. The decay  $A \rightarrow Zh$  is only relevant for  $M_A > 200$  GeV and  $\tan\beta$  near its experimental lower limit.
- $\phi \rightarrow supersymmetric particles$ : The decays into charginos, neutralinos and third-generation squarks and sleptons can become important if they are kinematically allowed. For Higgs masses below 130 GeV, the range of SUSY parameter space in which decays into supersymmetric particles are dominant is rather small, if the current bounds on SUSY masses are taken into account. The branching ratio of  $h \rightarrow \tilde{\chi}^0 \tilde{\chi}^0$  (“invisible decay”) could become sizable for large values of  $M_h$  near its upper theoretical limit, assuming the decay is kinematically possible.

In this analysis it is assumed that supersymmetric particles are sufficiently heavy, hence they do not play an important role in the phenomenology of MSSM Higgs boson decays.

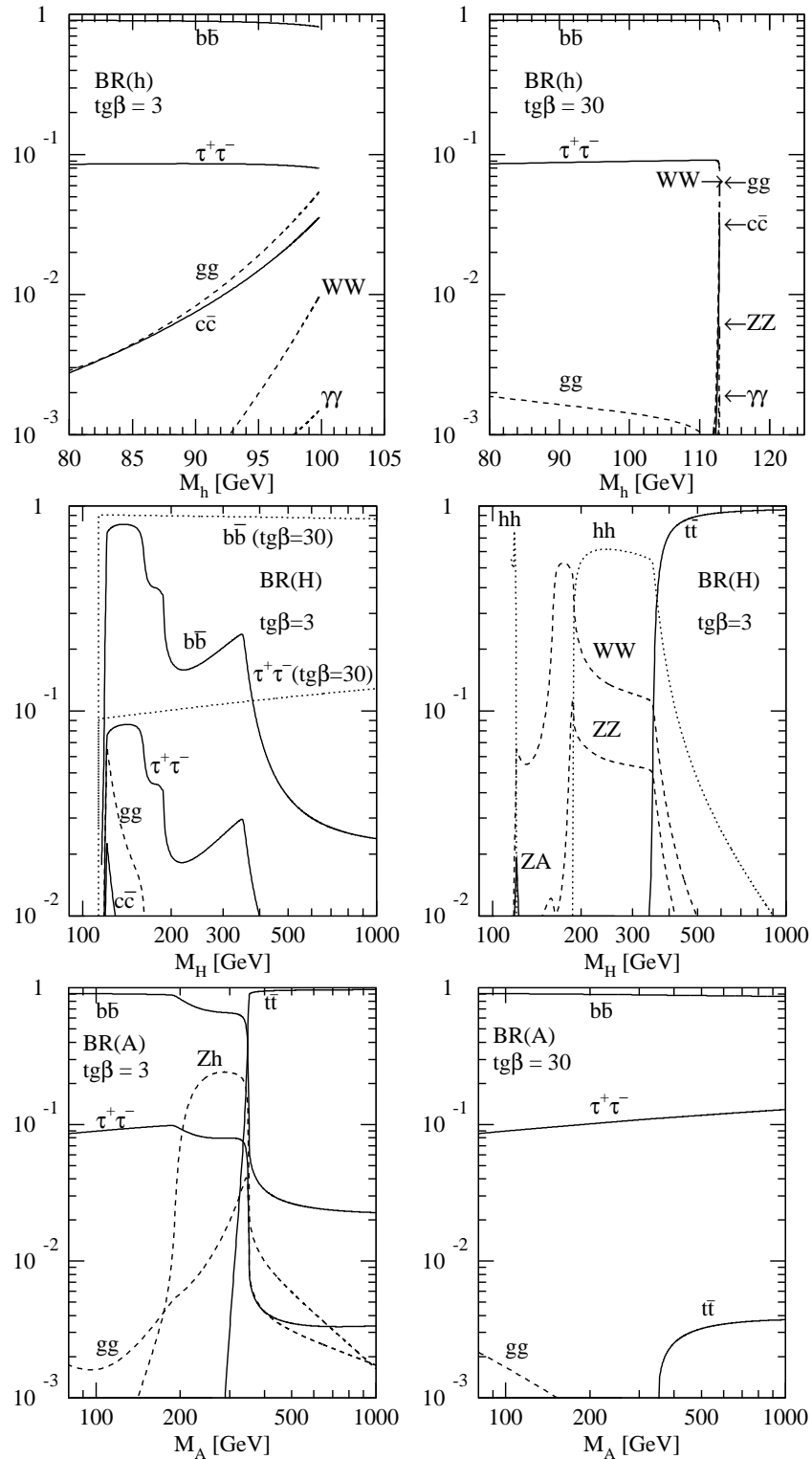


Figure 7.5: Branching ratios of neutral MSSM Higgs bosons as a function of their masses for  $\tan\beta = 3$  and  $\tan\beta = 30$  assuming a SUSY mass scale of 1 TeV and no mixing (from Ref. [101]).

### 7.1.3 Higgs Width

The total decay width of neutral MSSM Higgs bosons is studied as a function of  $\tan \beta$  using FEYNHIGGS [102] in version 2.3. Figure 7.6 shows the result for the  $m_h^{max}$  scenario with  $\mu < 0$ , which gives the largest values for the total decay width. The plot indicates that, for a given neutral Higgs boson mass  $M_\phi$ , the total decay width shows a large increase with  $\tan \beta$ . The broadening of the total decay width, which is the result of an increasing  $\phi \rightarrow b\bar{b}$  and  $\phi \rightarrow \tau\tau$  coupling, impacts directly the limit calculation by changing the shape of the reconstructed mass distribution and can lead to a decreasing signal efficiency. Its impact on the results of this analysis is studied in Section 7.5.1.

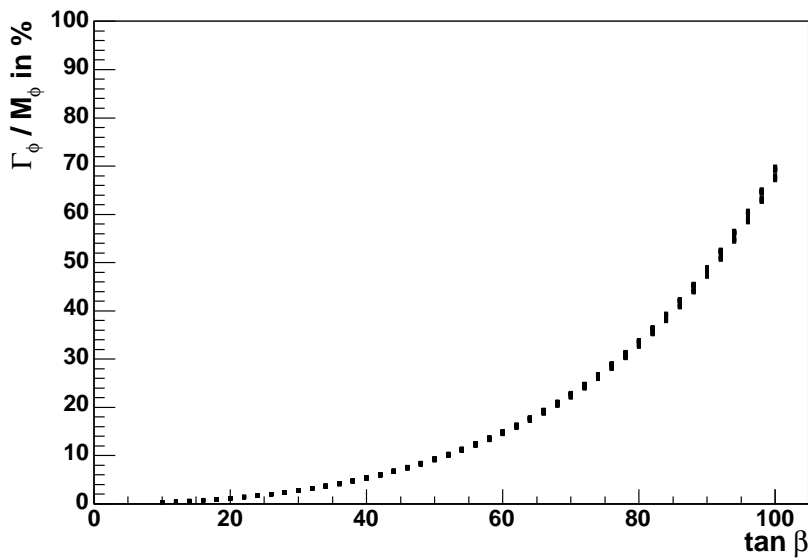


Figure 7.6: Higgs width as a function of  $\tan \beta$ . The spread for a given  $\tan \beta$  is the result of the different neutral Higgs boson masses ( $90 \text{ GeV} < M_\phi < 300 \text{ GeV}$ ).

### 7.1.4 Signal Topology

The Feynman diagrams for the neutral MSSM Higgs boson production via gluon-gluon fusion and via associated production with  $b$  quarks, followed by a subsequent decay into a tau pair, are given in Figure 7.7. As discussed above, the rates for these processes are strongly enhanced in the MSSM over a large region of the parameter space. Although the branching ratio into a tau pair is significantly smaller compared to the branching ratio into a pair of  $b$  quarks ( $\phi \rightarrow b\bar{b}$ ), the  $b\bar{b}$  final state suffers from large di-jet backgrounds and is normally only searched for in processes where the Higgs boson is produced in association with heavy quarks.

The further decay of the tau pair into either leptons or hadrons leads to six possible final states for the  $\phi \rightarrow \tau\tau$  process, which are presented in Table 7.1

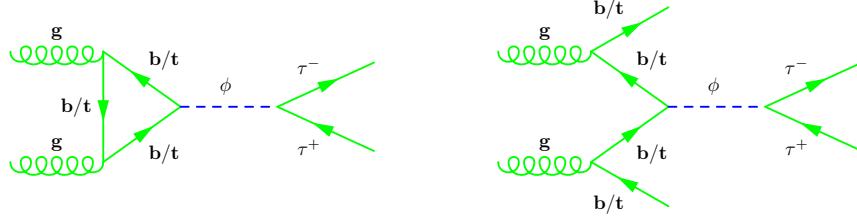


Figure 7.7: Production of a neutral MSSM Higgs boson with subsequent decay into two tau leptons:  $p\bar{p} \rightarrow \phi + X \rightarrow \tau\tau + X$ .

Decay Mode	Fraction
$\tau^+\tau^- \rightarrow e^+\nu_e\bar{\nu}_\tau + e^-\bar{\nu}_e\nu_\tau$	3 %
$\tau^+\tau^- \rightarrow \mu^+\nu_\mu\bar{\nu}_\tau + \mu^-\bar{\nu}_\mu\nu_\tau$	3 %
$\tau^+\tau^- \rightarrow e^+\nu_e\bar{\nu}_\tau + \mu^-\bar{\nu}_\mu\nu_\tau$	6 %
$\tau^+\tau^- \rightarrow e^+\nu_e\bar{\nu}_\tau + \tau_h^-\nu_\tau$	23 %
$\tau^+\tau^- \rightarrow \mu^+\nu_\mu\bar{\nu}_\tau + \tau_h^-\nu_\tau$	23 %
$\tau^+\tau^- \rightarrow \tau_h^+\bar{\nu}_\tau + \tau_h^-\nu_\tau$	41 %

Table 7.1: Illustration of the possible  $\phi \rightarrow \tau\tau$  final states.

together with the corresponding branching fractions. The di-lepton final states  $ee$  and  $\mu\mu$  are not observable due to the small branching ratios and the overwhelming  $Z/\gamma^*$  backgrounds. The dominating di-jet background makes the fully hadronic final state quite challenging. Despite the small branching fraction for the  $e\mu$  final state, the clean detector signature consisting of an opposite sign back-to-back electron-muon pair and missing transverse energy can be used to reject a large part of the Standard Model background. The  $e + \tau_h$  and  $\mu + \tau_h$  final states are both considered the most promising channels to search for neutral MSSM Higgs bosons decaying into a tau pair. They have a relatively large branching ratio and suffer only from moderate Standard Model backgrounds.

The search for the neutral MSSM Higgs boson production with subsequent decay into a tau pair is performed in the three most promising channels  $e + \tau_h$ ,  $\mu + \tau_h$  and  $e + \mu$ . The focus of this analysis is the  $e + \tau_h$  final state. This signal is characterized by an isolated electron resulting from a leptonic tau decay, a hadronic tau decay and missing transverse energy.

### 7.1.5 Standard Model Background

There is a variety of Standard Model processes which can produce a detector signature consistent with an electron and a hadronically decaying tau. The final state of these processes can consist of a real electron and a real hadronic tau decay, or it can be the result of lepton misidentification or  $\cancel{E}_T$  mismeasurement. The  $e + \tau_h$  signature resembles the trilepton final state, except for

the third lepton which is not present here. Hence the Standard Model backgrounds that are already discussed in the trilepton analysis (see Section 6.1.4) play an important role in this selection. The relevance of the different Standard Model background types however changes. Cross sections for the background processes are listed in Table 5.4.

- $Z/\gamma^* \rightarrow \ell\ell$

The most important background contributions arise from  $Z/\gamma^* \rightarrow \ell\ell$  processes. The final state with two electrons contributes significantly in the  $e + \tau_h$  selection due to the high rate of electrons faking a hadronic tau decay. The two electrons have opposite sign, and missing transverse energy can occur due to  $\cancel{E}_T$  mismeasurement. One of the challenges of the event selection is to reduce this background to an acceptable level.

The di-tau final state, with subsequent hadronic decay of one tau and leptonic decay into an electron of the second tau, is the most important irreducible background source. The final state is identical to the expected signal final state, and the invariant mass distribution represents the only discriminant. The missing transverse energy can be included in the calculation of the invariant mass to get a better discrimination.

- QCD Jet Production

The QCD jet production is a large background source due to its very high cross section. A jet can be misidentified as an electron, and especially as a hadronic tau decay. Large missing transverse energy can be faked by a mismeasurement of the jet energy.

- $W \rightarrow \ell\nu$

The  $W \rightarrow \ell\nu$  process is another large background source due to its large cross section. Especially  $W \rightarrow e\nu$  decays lead to a final state with a real electron and significant missing transverse energy. An additional jet from QCD radiation in those events can be misidentified as the tau.

- Di-boson:  $WW$ ,  $WZ$ ,  $ZZ$

Background contributions from di-boson processes ( $WW$ ,  $WZ$ ,  $ZZ$ ) can result in  $e + \tau_h$  final states with significant missing transverse energy. However, these processes have only small cross sections times branching ratios and have been found to be negligible.

- $t\bar{t}$

The production of  $t\bar{t}$  pairs is only of minor importance due to its small cross section.

## 7.2 Signal Monte Carlo

The signal Monte Carlo samples are produced using the PYTHIA [40] event generator in version 6.202 using CTEQ5L parton distribution functions. The Monte

Carlo covers the mass range from 90 GeV to 300 GeV. The threshold of 90 GeV represents the upper limit of the LEP experiments for all  $\tan\beta$  values up to 50 (larger values were not studied) [18]. Due to the small production cross section at the Tevatron, there is currently no sensitivity for Higgs masses beyond 300 GeV. The production cross sections, widths and branching ratios of the neutral MSSM Higgs bosons in the different reference scenarios have been calculated using the program FEYNHIGGS [102], which incorporates the complete set of one-loop corrections and all known two-loop corrections. The contributions from SUSY particles in the loop of the gluon fusion process are taken into account. The different MSSM Higgs mass points which have been simulated are outlined in Table 7.2. Both the production via gluon-gluon fusion and via associated production with  $b$  quarks are taken into account. The cross sections are given for  $\tan\beta = 30$  in the  $m_h^{max}$  scenario with positive  $\mu$ :  $m_{SUSY} = 1000$  GeV,  $\mu = +200$  GeV,  $M_2 = 200$  GeV,  $X_t = 2000$  GeV,  $m_{\tilde{g}} = 800$  GeV. The top quark mass is set to the world average of 172.7 GeV [103].

Point	$M_\phi$ [GeV]	$\sigma \times BR$ [pb]	# Events
A0	90	21.50	47k
A1	100	12.56	47k
A2	110	7.57	48k
A3	120	4.73	48k
A4	130	3.05	49k
A5	140	2.03	47k
A6	150	1.20	106k
A7	160	0.98	47k
A8	170	0.70	48k
A9	180	0.50	48k
A10	190	0.37	47k
A11	200	0.28	56k
A12	250	0.096	59k
A13	270	0.073	49k
A14	300	0.057	59k

Table 7.2:  $\sigma \times BR$  and number of generated events for the process  $\phi \rightarrow \tau\tau$ . The cross section for each point has been calculated using FEYNHIGGS 2.3 [102] and is given for  $\tan\beta = 30$  in the  $m_h^{max}$  scenario with positive  $\mu$ :  $m_{SUSY} = 1000$  GeV,  $\mu = +200$  GeV,  $M_2 = 200$  GeV,  $X_t = 2000$  GeV,  $m_{\tilde{g}} = 800$  GeV. The top quark mass is set to the world average of 172.7 GeV [103].

### 7.3 Event Selection and Data/Monte Carlo Comparison

The event selection is based on the single electron triggers described in Section 5.1.2. Since the tau candidate can fire the single electron trigger, the same strategy as described in Section 6.3 is applied. The QCD multijet background is estimated from data and normalized at preselection stage using the neural network distribution (see Section 5.4). In contrast to the trilepton analysis,

the electron identification is based on the multivariate likelihood variable (see Section 4.3.1) instead of a cut on the shower profile (HMx8) and requiring a track match with E/p. All three tau types are retained for this analysis to get maximal sensitivity.

The signal is characterized by an electron, a hadronically decaying tau, missing transverse energy and little jet activity. For large Higgs boson masses, it would stand out as an enhancement above the background from Standard Model processes in the invariant electron and tau mass, while all backgrounds tend to be at lower invariant masses. In order to increase the separation between signal and background, the missing transverse energy is included in the calculation of the invariant mass, which will be referred to as *visible mass*  $M_{vis}$ . The visible mass is calculated using the four-vectors of the electron, the tau and  $\cancel{E}_T$ . The  $z$  component of  $\cancel{E}_T$  is set to zero, and the energy equals the magnitude of  $\cancel{E}_T$ :

$$M_{vis} = \sqrt{(p_e + p_{\tau_h} + \cancel{E}_T)^2} \quad (7.1)$$

The event selection is optimized to achieve the best expected limit, using the high-mass region defined as  $M_{vis} > 120$  GeV. The calculation of the limit uses the full visible mass spectrum. For the optimization of the event selection, a Higgs mass of  $M_\phi = 150$  GeV is chosen.

Table 7.3 briefly summarizes the applied selection procedure, which is discussed in the following. The number of events selected in data and expected from Standard Model background processes are presented in Table 7.5 for tau type 1, in Table 7.6 for tau type 2 and in Table 7.7 for tau type 3.

(1) Preselection	$p_T^e > 14$ GeV, EM ID with likelihood $> 0.8$ $p_T^{\tau_h} > 20$ GeV $\Delta\mathcal{R}(e, \tau_h) > 0.4$ $\Delta z(e, \tau_h) < 1$ cm $\Delta z(e/\tau_h, primary\ vertex) < 1$ cm
(2) Anti-Electron	$\tau$ -type 1: remove ICR $\tau$ -type 2: $E_T^{\tau HAD}/p_T^{\tau rk} > 0.4$ , remove ICR $\tau$ -type 3: $E_T^{\tau HAD}/p_T^{\tau rk} > 0.2$ , remove ICR
(3) Tau Identification	$\tau$ -type 1: NN $> 0.90$ $\tau$ -type 2: NN $> 0.90$ $\tau$ -type 3: NN $> 0.95$
(4) Anti-W	$M_W < 20$ GeV
(5) Opposite sign	

Table 7.3: Summary of the selection criteria applied to discriminate between signal and background.

### (1) Preselection

The preselection requires an electron with  $p_T > 14$  GeV and a tau candidate with  $p_T > 20$  GeV, which are both well separated ( $\Delta\mathcal{R} > 0.4$ ). The transverse

momentum threshold for the electron is lowered to account for the additional neutrino in the leptonic tau decay. The leading electron passing the following identification cuts is selected: standard electron identification (see EM candidate description in Chapter 4.3) and a likelihood value which exceeds 0.8. All three tau types are considered for this analysis, and the tau candidate with the highest transverse momentum is chosen. Both particles are required to originate from the same vertex (distance of vertex  $z$  positions  $\Delta z_0 < 1$  cm), and this vertex is required to be identical with the primary vertex ( $\Delta z_0 < 1$  cm). The electron and tau candidate must be detected in  $|\eta_{det}| < 2.5$  to avoid topologies with unfavorable signal-to-background ratios.

Figure 7.8 shows the transverse momentum distributions for the electron and the tau candidate as well as their invariant mass, the missing transverse energy and the neural network output at this selection stage for all three tau types separately. A good agreement between data and Monte Carlo is observed in tau type 2 and 3. There is a small disagreement in the transverse momentum distribution for tau type 1 at high- $p_T$ , which also affects the invariant mass and  $\cancel{E}_T$  distribution for this tau type. The discrepancy is the result of an incorrect tau resolution correction for electrons that fake taus of type 1. Since tau fakes from electrons are successfully removed by the anti-electron cut described below, the slight discrepancy at preselection level is understood and not of relevance for the further selection. A signal sample is also shown in all selection plots, corresponding to  $M_\phi = 150$  GeV and normalized with a cross section at  $\tan \beta = 40$ .

The dominant background contribution at preselection stage results from  $Z/\gamma^* \rightarrow ee$  events, where the second electron is reconstructed as the tau candidate. This background has been extensively studied, and dedicated selection criteria have been developed to remove the  $Z/\gamma^* \rightarrow ee$  events. A detailed discussion follows below. Additional important background sources include QCD and  $W \rightarrow e\nu$ , where the tau is faked by a jet. Di-boson and  $t\bar{t}$  backgrounds are only of minor importance. The irreducible  $Z/\gamma^* \rightarrow \tau\tau$  background is hardly visible at preselection stage, but will become more pronounced at the latter stages of the selection.

## (2) Anti-Electron

A major background source for the  $e + \tau_h$  final state is the  $Z/\gamma^* \rightarrow ee$  process, where one of the two final state electrons fakes the tau candidate. All three tau types are affected by this *electron contamination*, however, to various degrees.

The detector response for an electron (an isolated track matched to a narrow calorimeter cluster), resembles the detector response for a 1-prong hadronic tau decay. Since no attempt is made at reconstruction level to separate electron from taus, the vast majority of electrons are reconstructed as tau type 2 candidates. If no electromagnetic subclusters are found, the electrons are reconstructed as tau type 1 candidates. A small fraction will be reconstructed as tau type 3, when more than one track is associated to the calorimeter cluster.

### 7.3 Event Selection and Data/Monte Carlo Comparison

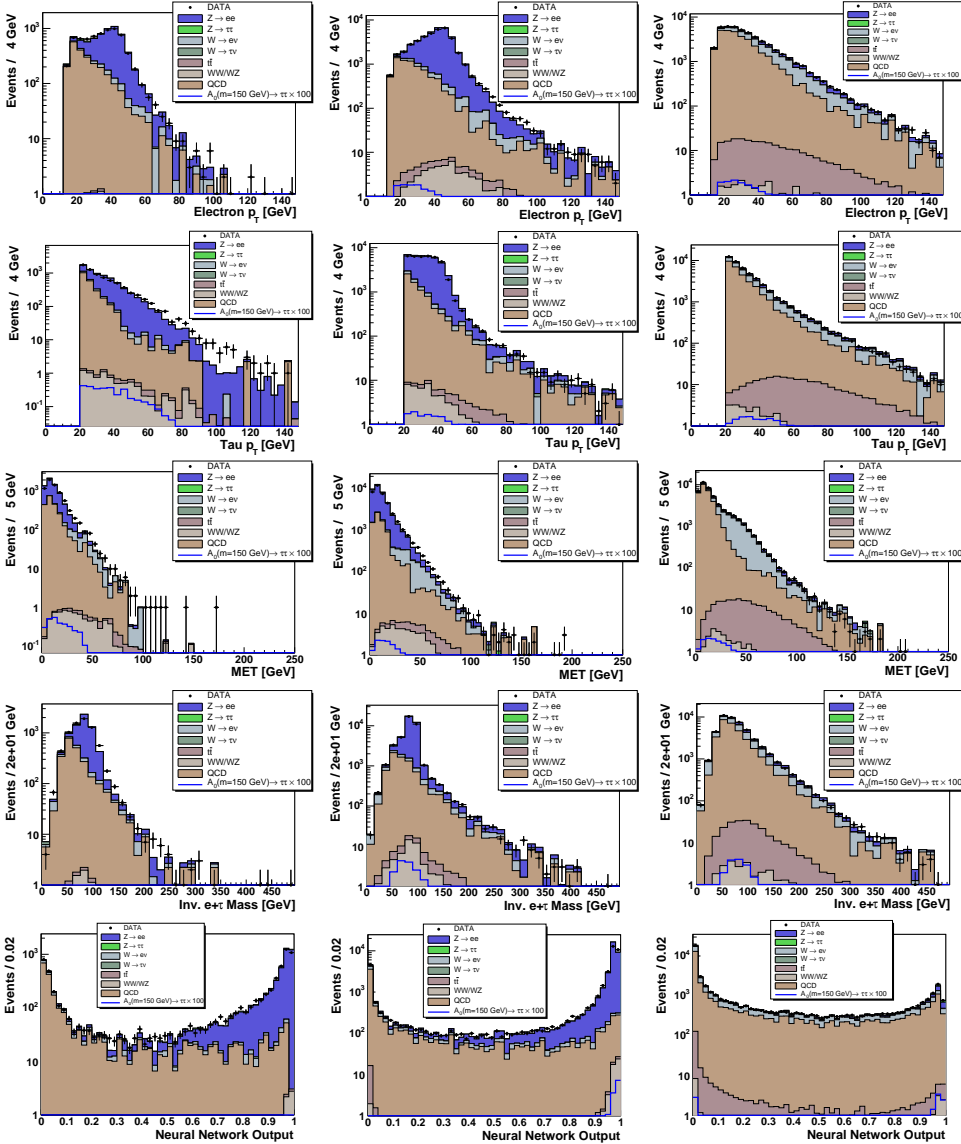


Figure 7.8: Various distributions for each tau type (left: type 1, middle: type 2, right: type 3) at preselection stage (1). Each column shows  $p_T^e$ ,  $p_T^\tau$ ,  $\cancel{E}_T$ , the invariant  $e + \tau_h$  mass and the neural network output.

In the following, the selection criteria applied to reduce the  $Z/\gamma^* \rightarrow ee$  background are described.

### Tau Type 1 Fakes

Figure 7.9 shows the invariant  $e + \tau_h$  mass and the tau  $\eta_{det}$  distribution for tau type 1 at preselection stage (1). The detector eta distribution shows that electrons which are identified as type 1 taus are located in the inter-cryostat region ( $1.1 < |\eta_{det}| < 1.6$ ). This detector region is not equipped with an electromagnetic calorimeter, hence the electron deposits all its energy in the hadronic calorimeter. These tau fakes can be eliminated by applying a topological cut which removes this region. To increase the signal efficiency, the topological cut is done as a function of the  $z$  position of the primary vertex. The  $z$  dependence takes into account that the electrons hit the edges of the calorimeters under different angles. The cut is also applied to tau type 2 and 3 tau candidates.

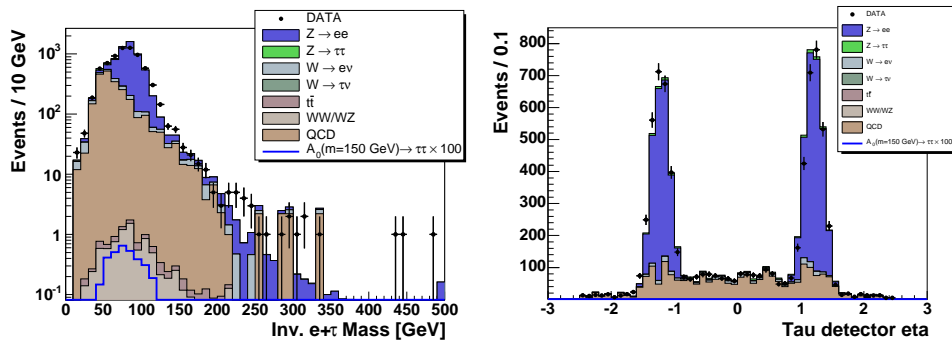


Figure 7.9: Electron contamination for tau type 1: distribution of the invariant  $e + \tau_h$  mass (left) and tau detector eta ( $\eta_{det}$ ) (right).

### $\tau$ -type 2 fakes

The majority of electrons are identified as type 2. This tau type requires that at least one electromagnetic subcluster with a transverse energy of  $E_T > 0.8$  GeV is associated. These tau fakes can be significantly reduced by cutting on ratio of the transverse hadronic energy of the tau candidate and the transverse momentum of the associated tracks:  $E_T^{HAD}/p_T^{trk}$ . This ratio is plotted in Figure 7.10 at preselection stage (1). Tau fakes from electrons show a large imbalance and peak at very small values, since most of the electron energy is deposited in the electromagnetic calorimeter. Only events where this ratio exceeds 0.4 are retained for the analysis. To further reduce the electron contamination for this tau type in the central detector region, only events are retained where the tau candidate is not located close to a  $\phi$ -crack (see Section 2.3.3). Figure 7.11 shows the  $\phi$  position in data and background, after the cut on the ratio of the transverse hadronic tau energy and the transverse momentum of the associated tracks has been performed. The insensitive detector regions

at the cell boundaries lead to a higher tau fake rate from electrons. By retaining only events where the tau candidate is not located close to a  $\phi$ -crack ( $0.02 < \phi$  position  $< 0.18$ ), the electron contamination can be reduced further.

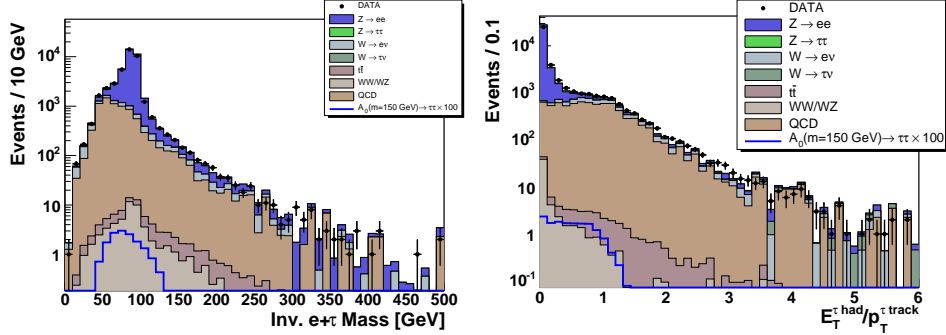


Figure 7.10: Electron contamination in tau type 2: distribution of the invariant  $e + \tau_h$  mass (left) and the ratio of the transverse hadronic tau energy and the associated tau tracks ( $E_T^{\tau HAD}/p_T^{\tau trk}$ ) (right). The distributions are shown at preselection stage (1).

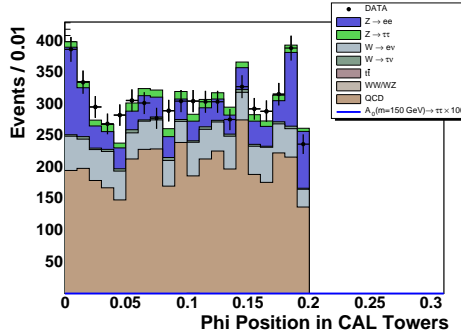


Figure 7.11: Electron contamination in tau type 2: distribution of the tau  $\phi$  position in the central calorimeter towers. For this plot,  $E_T^{\tau HAD}/p_T^{\tau trk} > 0.4$  has been required.

### $\tau$ -type 3 fakes

$Z/\gamma^* \rightarrow ee$  events are also reconstructed in tau type 3, although to a much lesser extent than in tau type 1 and 2. The tau candidate is either faked by an electron or – to a much greater extent – by a jet from  $Z + jet$  production. In the first case, when a real electron fakes the tau, an additional track from the underlying event or a fake track has been associated with the tau candidate in addition to the electron track. These events can be removed with the same strategy that is described in the case of tau type 2 fakes: by applying a cut on the ratio of the transverse hadronic energy and the transverse momentum of the tau tracks ( $E_T^{\tau HAD}/p_T^{\tau trk}$ ). Requiring this ratio to exceed 0.2 removes most of these fakes. Type 3 taus faked by a QCD jet are removed by tightening the cut on the neural network requirement (see below).

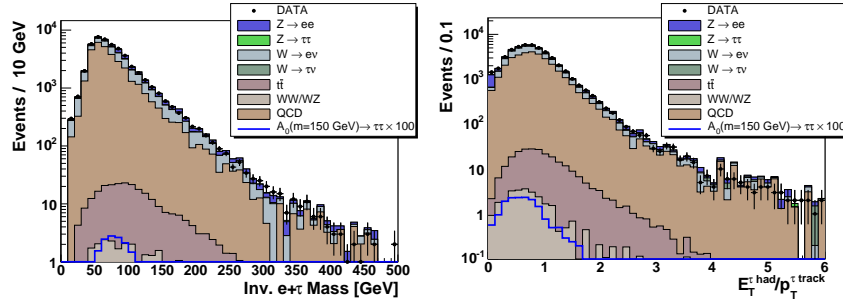


Figure 7.12: Electron contamination in tau type 3: distribution of the invariant  $e + \tau_h$  mass (left) and the ratio of the transverse hadronic tau energy and the associated tau tracks ( $E_T^{\tau \text{ had}}/p_T^{\tau \text{ track}}$ ) (right) at preselection stage (1).

Figure 7.13 shows the transverse momentum distributions for the electron and tau candidate, their invariant mass, the missing transverse energy of the event and the tau neural network output distribution. The plots are presented separately for all three tau types after application of the anti-electron cuts (2). A good agreement between data and Monte Carlo is observed for all three tau types, the discrepancy in tau type 1 is not visible any more. After selection stage (2), the remaining background is dominated by QCD jet production. This background can be reduced by applying a cut on the tau neural network output.

### (3) Tau Identification

To significantly reduce the QCD background, while retaining a large fraction of the signal, a cut on the neural network output of the tau is applied. The value has to exceed 0.9 for tau type 1 and 2, and 0.95 for tau type 3. The neural network cut for tau type 3 is tighter due to a significantly larger background from multi-jet events.

Figure 7.14 shows the transverse momentum distributions for the electron and tau candidate, their invariant mass and the missing transverse energy of the event for each tau type after the tau identification (3) is applied. A reasonable agreement between data and Monte Carlo is observed for all three tau types. The remaining background is dominated by QCD jet production and  $W$  events.

### (4) W Veto

The main selection criteria is a veto on  $W$  bosons to reject  $W \rightarrow \ell\nu$  events. These events can be misidentified as high-mass  $e + \tau_h$  pairs if they are produced in association with an energetic jet which fakes the hadronic tau decay. Since the tau  $p_T$  is required to exceed 20 GeV, the  $W$  recoils against a high- $E_T$  jet and is therefore strongly boosted. Characteristic for these events is a small angle between the missing transverse energy vector and the electron. The mass

### 7.3 Event Selection and Data/Monte Carlo Comparison

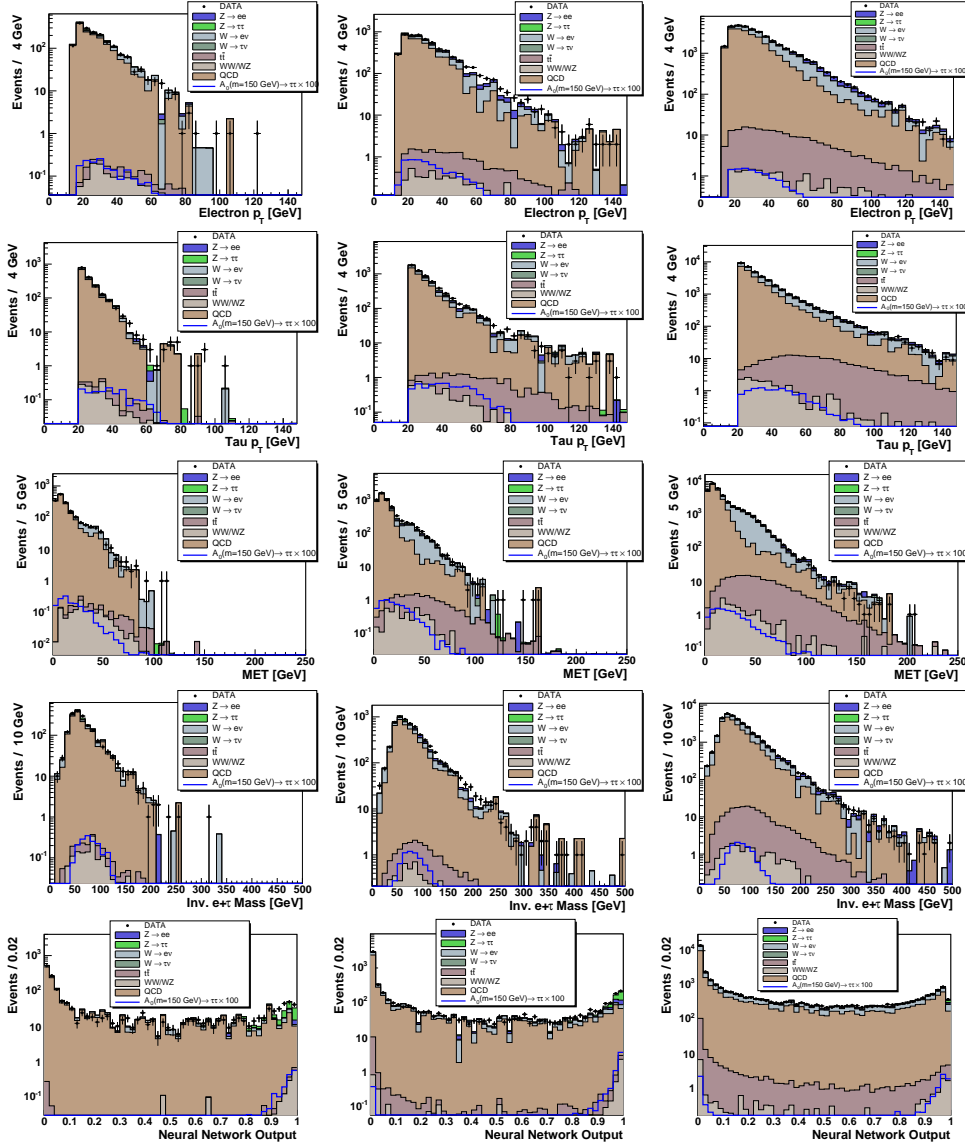


Figure 7.13: Various distributions for each tau type (left: type 1, middle: type 2, right: type 3) after anti-electron cuts (2). Each column shows  $p_T^e$ ,  $p_T^\tau$ ,  $\cancel{E}_T$ , the invariant  $e + \tau_h$  mass and the neural network output.

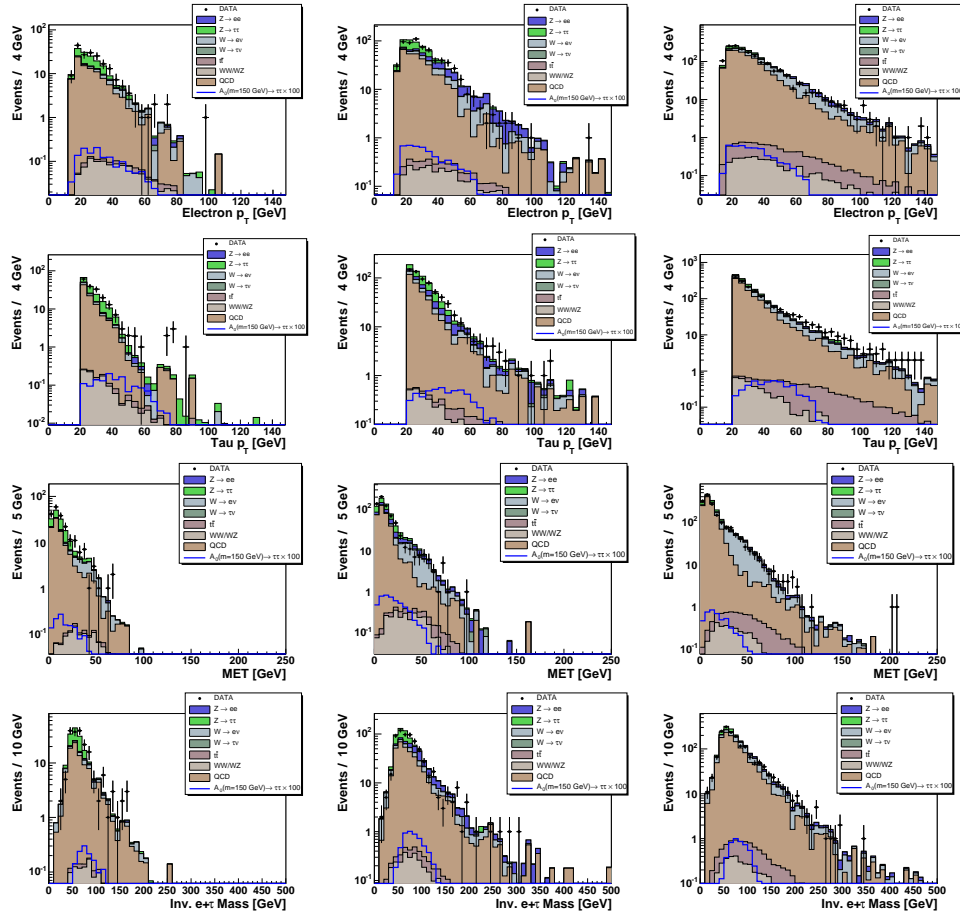


Figure 7.14: Various distributions for each tau type (left: type 1, middle: type 2, right: type 3) after tau identification cuts (3). Each column shows  $p_T^e$ ,  $p_T^\tau$ ,  $\cancel{E}_T$  and the invariant  $e + \tau_h$  mass.

of the  $W$  boson can be reconstructed in the following approximation:

$$M_W = \sqrt{2 \cdot E^\nu \cdot E^e \cdot (1 - \cos(\Delta\phi))} \quad (7.2)$$

with

$$E^\nu = \cancel{E}_T \times \frac{E^e}{p_T^e}, \quad (7.3)$$

$$\Delta\phi = \angle(p_T^e, \cancel{E}_T). \quad (7.4)$$

The distribution of the  $M_W$  for all three tau types is shown in Figure 7.15. The majority of the signal events are located at low values of  $M_W$  due to the small opening angle between the missing transverse energy vector and the electron. The missing transverse energy is resulting from the neutrino. In order to remove backgrounds from  $W + jet$  processes,  $M_W$  is required to be less than 20 GeV. Several values of this cut were considered and compared by optimizing for the best expected limit.

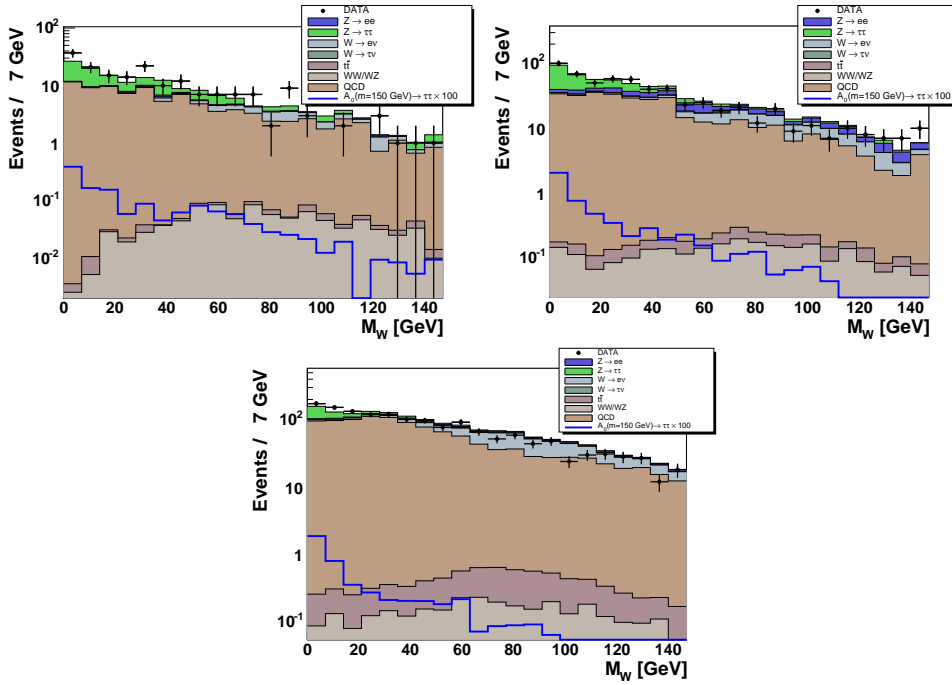


Figure 7.15: Distributions of the  $W$  mass for tau type 1 (upper left), tau type 2 (upper right) and tau type 3 (bottom) before the corresponding cut is applied.

### (5) Opposite Sign Event Selection

The signal consists of an electron and a hadronic tau with opposite charge. Hence all like-sign events in data and Monte Carlo are discarded. Since the QCD background is estimated from a like-sign  $e + \tau_h$  QCD sample, it is scaled with a factor of 0.5.

After the last cut, the expected Standard Model background sums up to  $43.90 \pm 1.64(\text{stat})$  events for tau type 1,  $150.80 \pm 3.08(\text{stat})$  events for tau type 2 and  $232.57 \pm 3.43(\text{stat})$  events for tau type 3. The number of observed events in data is 57 for tau type 1, 171 for tau type 2 and 256 for tau type 3. Taking only the statistical error into account, the Standard Model prediction is approximately 10 % lower than the number of observed events for each tau type. A detailed discussion of the obtained results follows in Section 7.5, after a study of the systematic uncertainties.

## 7.4 Systematic Uncertainties

Various sources of systematic uncertainties are identified and studied to investigate their influence on signal efficiencies and background expectations. As in the trilepton analysis, import contributions result from the QCD modeling, the measurement of the integrated luminosity, the modeling of the physics process

and the modeling of the detector (e.g. efficiency corrections, smearing). However, the importance of the individual contributions differ significantly from the trilepton analysis.

- **QCD Normalization**

The most dominant contribution to the systematic error stems from the description of the QCD jet background. It is estimated by varying the QCD scale factors, which are derived independently for each tau type (see Section 5.4), within their statistical errors and found to be 9.1 %. The large contribution to the systematic error is the result of the significant QCD jet background contribution in the final selected sample.

- **Jet Energy Scale**

The calibration of the jets (jet energy scale) contributes to the systematic error since the jet corrections are propagated into the missing transverse energy. The effect is calculated by varying the jet energy scale corrections for data and Monte Carlo within their errors. This results in a 1.8 % contribution to the systematic error on the background and in a 3.8 % systematic error on the signal efficiency.

- **$\cancel{E}_T$  Smearing**

The smearing of the missing transverse energy in Monte Carlo impacts the number of events that are expected to pass the cut on the reconstructed  $W$  mass (see Section 7.3). This uncertainty is conservatively taken into account by calculating the difference in the number of expected events for background and signal with smeared and unsmeared Monte Carlo, resulting in a 1.2 % contribution to the systematic error on the background and in a 0.6 % systematic error on the signal efficiency.

- **Electron Reconstruction/Identification Efficiency**

The modeling of the electron reconstruction and identification efficiency are calculated by varying the Monte Carlo efficiency corrections within their errors, as listed in Table 5.6 and shown in Figure 5.6. This results in a systematic error of 0.6 % for the background and of 1.2 % for the signal efficiency.

- **Electron Smearing**

The electron smearing in Monte Carlo can result in a different number of selected events after the transverse momentum selection. The modifications are also propagated into the missing transverse energy, affecting the  $W$  mass reconstruction. Its impact on the systematic error is estimated conservatively by comparing the results with and without smearing. The electron smearing gives rise to a contribution of 0.1 % in both background and signal sample.

- **Trigger Simulation**

An incorrect modeling of the trigger efficiency has an impact on the expected number of Standard Model background events and the signal ef-

Source	Background	Signal
QCD normalization	9.1 %	–
Jet Energy Scale	1.8 %	3.8 %
MET smearing	1.2 %	0.6 %
EM reconstruction and identification	0.6 %	1.2 %
EM smearing	0.1 %	0.1 %
Trigger simulation	2.5 %	1.8 %
Tau identification	3.6 %	3.6 %
Tau track efficiency	2.7 %	2.7 %
$Z/\gamma^*$ cross section	3.3 %	–
$p_T(Z)$ reweighting	0.7 %	–
Quadratic sum	11.2 %	6.3 %
Integrated luminosity	6.5 %	6.5 %
Quadratic sum total	13.0 %	9.1 %

Table 7.4: Systematic uncertainties on the number of events expected from Standard Model processes and for the signal process after the last selection criteria (relative errors are quoted).

ficiency. The effect of the trigger efficiency is calculated by varying the parameters of the individual fits (see Section 5.5.1) within their  $1\sigma$  error.

- Tau Identification/Track Efficiency

Systematic errors stemming from the tau identification and the tau track efficiency contribute with 3.6 % resp. 2.7 % to both the systematic error on the background and the signal efficiency. A detailed study of systematic errors stemming from the tau neural network, which is referred to as tau identification, has been performed in Ref. [97]. The impact of the tau track efficiency is estimated by varying the correction factors within its errors (see Section 5.5.3).

- PDF/Scale Error on Cross Section and  $p_T(Z)$  Reweighting

The PDF-related errors on the Standard Model background cross sections (see Table 5.4), especially on the dominant  $Z/\gamma^*$  background, lead to a 3.3 % systematic error on the background. The error on the  $p_T(Z)$  reweighting (see Section 5.5.4) is estimated by varying the fit weights within their errors, resulting in a contribution of 0.7 % to the systematic error on the background.

All contributions are summarized in Table 7.4 for Standard Model processes and a MSSM Higgs signal after the last selection cut. The systematic error on the signal has been studied using a Higgs boson mass of 150 GeV. The total systematic error is calculated as the square root of the quadratic sum of the individual errors, assuming that they are independent.

After application of all selection criteria, the systematic error on the background sample is 11.2 %. Dominant sources of this error arise from the QCD background modeling, the tau reconstruction and identification and the  $Z/\gamma^*$

cross section. In combination with the error on the luminosity measurement of 6.5 % (see Ref. [70]), the total systematic error on the background is 13.0 %. The systematic error on the signal expectation adds up to 6.3 % without and 9.1 % with the error on the luminosity measurement taken into account. Main contributions stem from the jet energy scale and the tau reconstruction and identification.

## 7.5 Results

### 7.5.1 The $e + \tau_h$ Result

A detailed comparison between the number of events observed and background events expected after each cut stage is shown in Table 7.5 for tau type 1, in Table 7.6 for tau type 2 and in Table 7.7 for tau type 3. Each table lists the contributions from the different background sources. Taking both statistical and systematic error into account, the numbers of expected events for each tau type are in agreement with the numbers of observed events. However, there is a slight disagreement in the last stages of the selection affecting all three tau types: the background expectation underestimates the number of observed data events.

After the final cut, the combined background expectation for all three tau types is  $427.3 \pm 4.9(\text{stat}) \pm 55.5(\text{sys})$  events, while 484 events are observed in data. The excess seen in data is within  $1\sigma$  of the background expectation, hence no clear evidence for the production of neutral MSSM Higgs bosons in  $e + \tau_h$  final states is observed. At the end of the selection, the dominant background contributions stem from  $Z/\gamma^* \rightarrow \tau\tau$  and QCD jet production, while further backgrounds from  $Z/\gamma^* \rightarrow ee$ ,  $W \rightarrow \ell\nu$ , di-boson and  $t\bar{t}$  are negligible.

The signal efficiency, given by the ratio of the number of events after each selection stage and the total number of  $\phi \rightarrow \tau\tau$  events, is presented in Table 7.8 for a neutral MSSM Higgs boson of mass  $M_\phi = 150$  GeV. At the end of the selection, the signal efficiency is  $(0.12 \pm 0.01)$  % for tau type 1,  $(0.52 \pm 0.05)$  % for tau type 2 and  $(0.44 \pm 0.04)$  % for tau type 3 – including the branching ratio into  $e + \tau_h$  final states.

Figure 7.16 shows the distribution of the visible mass  $M_{vis}$  for each tau type after all selection criteria are applied. As discussed in Section 7.3, a neutral MSSM Higgs boson signal is expected to stand out as an enhancement over the Standard Model prediction at large values of  $M_{vis}$ . The excess in data events is not confined to a definite range in the visible mass spectrum, supporting the conclusion that no evidence for neutral MSSM Higgs boson production decaying into  $e + \tau_h$  final states is observed. The visible mass plots show that a large part of the QCD background is located at low values ( $M_{vis} \leq 100$  GeV), where an excess stemming from neutral MSSM Higgs bosons decaying into a tau pair is not expected. The cross section limit calculation is using the complete  $M_{vis}$  spectrum, hence the information about the shape is included in the limit

Tau Type 1			
Cut	Data	Sum BGND	
(1) Preselection	7200	$7273.06 \pm 94.32 \pm 945.50$	
(2) Anti-Electron	1765	$1777.97 \pm 68.20 \pm 231.14$	
(3) Tau ID	191	$167.97 \pm 4.59 \pm 21.84$	
(4) W Veto	71	$58.76 \pm 2.43 \pm 7.64$	
(5) Opposite Sign	57	$43.90 \pm 1.64 \pm 5.71$	
Cut	QCD	$Z/\gamma^* \rightarrow \tau\tau$	$Z/\gamma^* \rightarrow ee$
(1) Preselection	$2104.00 \pm 90.04$	$131.30 \pm 2.68$	$4541.00 \pm 21.37$
(2) Anti-Electron	$1400.00 \pm 66.76$	$74.72 \pm 2.12$	$21.11 \pm 2.26$
(3) Tau ID	$87.56 \pm 4.12$	$52.00 \pm 1.63$	$3.22 \pm 0.35$
(4) W Veto	$28.89 \pm 2.06$	$28.72 \pm 1.26$	$0.31 \pm 0.10$
(5) Opposite Sign	$14.45 \pm 1.03$	$28.71 \pm 1.26$	$0.20 \pm 0.08$
Cut	$W \rightarrow \tau\nu$	$WW/WZ$	$t\bar{t}$
(1) Preselection	$15.70 \pm 2.52$	$8.42 \pm 0.19$	$1.94 \pm 0.11$
(2) Anti-Electron	$8.73 \pm 1.86$	$1.44 \pm 0.07$	$0.77 \pm 0.08$
(3) Tau ID	$1.17 \pm 0.25$	$1.15 \pm 0.05$	$0.18 \pm 0.02$
(4) W Veto	$0.11 \pm 0.08$	$0.04 \pm 0.01$	$0.01 \pm 0.01$
(5) Opposite Sign	$0.11 \pm 0.08$	$0.04 \pm 0.01$	$0.01 \pm 0.01$

Table 7.5: Number of events observed in data and expected for background at different stages of the selection for tau type 1. The errors for the numbers of the individual backgrounds are statistical. For the sum of all backgrounds, both statistical and systematic errors are given.

Tau Type 2			
Cut	Data	Sum BGND	
(1) Preselection	40345	$41825.78 \pm 191.47 \pm 5437.35$	
(2) Anti-Electron	5963	$5684.00 \pm 127.68 \pm 738.92$	
(3) Tau ID	647	$655.33 \pm 10.58 \pm 85.19$	
(4) W Veto	217	$204.33 \pm 5.16 \pm 26.56$	
(5) Opposite Sign	171	$150.80 \pm 3.08 \pm 19.60$	
Cut	QCD	$Z/\gamma^* \rightarrow \tau\tau$	$Z/\gamma^* \rightarrow ee$
(1) Preselection	$7443.00 \pm 181.00$	$459.90 \pm 4.48$	$32130.00 \pm 56.31$
(2) Anti-Electron	$4196.00 \pm 125.80$	$195.40 \pm 2.89$	$238.20 \pm 6.09$
(3) Tau ID	$333.20 \pm 9.95$	$151.70 \pm 2.41$	$77.33 \pm 1.98$
(4) W Veto	$92.57 \pm 4.72$	$94.32 \pm 1.86$	$12.08 \pm 0.84$
(5) Opposite Sign	$46.29 \pm 2.36$	$93.74 \pm 1.86$	$7.23 \pm 0.59$
Cut	$W \rightarrow \tau\nu$	$WW/WZ$	$t\bar{t}$
(1) Preselection	$102.40 \pm 6.30$	$54.18 \pm 0.51$	$29.30 \pm 0.47$
(2) Anti-Electron	$62.25 \pm 5.10$	$5.01 \pm 0.15$	$15.14 \pm 0.38$
(3) Tau ID	$6.61 \pm 0.52$	$3.07 \pm 0.09$	$1.37 \pm 0.03$
(4) W Veto	$1.30 \pm 0.23$	$0.32 \pm 0.05$	$0.12 \pm 0.01$
(5) Opposite Sign	$0.90 \pm 0.20$	$0.26 \pm 0.04$	$0.07 \pm 0.01$

Table 7.6: Number of events observed in data and expected for background at different stages of the selection for tau type 2. For a description of the errors see Table 7.5.

Tau Type 3				
Cut	Data	Sum BGND		
(1) Preselection	47343	47396.30	$\pm 321.97$	$\pm 6161.52$
(2) Anti-Electron	35529	35882.27	$\pm 281.49$	$\pm 4664.70$
(3) Tau ID	1635	1764.47	$\pm 16.84$	$\pm 229.38$
(4) W Veto	447	392.54	$\pm 5.98$	$\pm 51.03$
(5) Opposite Sign	256	232.57	$\pm 3.43$	$\pm 30.23$
Cut	QCD	$Z/\gamma^* \rightarrow \tau\tau$	$Z/\gamma^* \rightarrow ee$	$W \rightarrow e\nu$
(1) Preselection	32130.00	$\pm 314.20$	552.60	$\pm 6.02$
(2) Anti-Electron	24540.00	$\pm 274.60$	402.30	$\pm 5.14$
(3) Tau ID	1216.00	$\pm 16.50$	135.90	$\pm 2.48$
(4) W Veto	277.50	$\pm 5.59$	90.72	$\pm 2.06$
(5) Opposite Sign	138.75	$\pm 2.80$	80.26	$\pm 1.93$
Cut	$W \rightarrow \tau\nu$	$WW/WZ$	$t\bar{t}$	
(1) Preselection	815.80	$\pm 17.91$	26.90	$\pm 0.47$
(2) Anti-Electron	637.10	$\pm 15.85$	20.17	$\pm 0.43$
(3) Tau ID	19.26	$\pm 0.48$	3.79	$\pm 0.08$
(4) W Veto	4.38	$\pm 0.23$	0.30	$\pm 0.03$
(5) Opposite Sign	2.57	$\pm 0.18$	0.24	$\pm 0.02$
			$0.27 \pm 0.01$	

Table 7.7: Number of events observed in data and expected for background at different stages of the selection for tau type 3. For a description of the errors see Table 7.5.

Efficiency ( $M_\phi = 150$ GeV) [%]			
Cut	Tau Type 1	Tau Type 2	Tau Type 3
(1) Preselection	$0.54 \pm 0.02 \pm 0.05$	$2.56 \pm 0.04 \pm 0.23$	$2.79 \pm 0.05 \pm 0.25$
(2) Anti-Electron	$0.29 \pm 0.01 \pm 0.03$	$1.11 \pm 0.03 \pm 0.10$	$2.04 \pm 0.04 \pm 0.19$
(3) Tau ID	$0.23 \pm 0.01 \pm 0.02$	$0.89 \pm 0.03 \pm 0.08$	$0.81 \pm 0.02 \pm 0.07$
(4) W Veto	$0.12 \pm 0.01 \pm 0.01$	$0.53 \pm 0.02 \pm 0.05$	$0.49 \pm 0.02 \pm 0.04$
(5) Opposite Sign	$0.12 \pm 0.01 \pm 0.01$	$0.52 \pm 0.02 \pm 0.05$	$0.44 \pm 0.01 \pm 0.04$

Table 7.8: Selection efficiency for a neutral MSSM Higgs boson of mass  $M_\phi = 150$  GeV at different stages of the selection for all three tau types, given with statistic and systematic error. The efficiency is normalized to  $\phi \rightarrow \tau\tau \rightarrow \text{all}$ , hence the branching ratio into  $e + \tau_h$  final states is included.

calculation. Bins with a small signal over background ratio – as the bins in the low- $M_{vis}$  region – are not affecting the limit. The  $Z/\gamma^* \rightarrow \tau\tau$  process leads to the same final state as  $\phi \rightarrow \tau\tau$  and is therefore an irreducible background.

An upper limit on the product of the cross section of neutral MSSM Higgs boson and branching ratio into a tau pair is extracted using the visible mass distribution ( $M_{vis}$ ). The calculated limit for the  $e + \tau_h$  analysis is shown in Figure 7.17. To increase the sensitivity, the obtained result is combined with searches in two other  $\phi \rightarrow \tau\tau$  final states:  $\mu + \tau_h$  and  $e + \mu$ . The resulting limit is transformed into an exclusion plot in the  $(M_A, \tan \beta)$ -plane. Section 7.5.2 presents the combined results. The cross section limit and the excluded SUSY parameter space are further improved by combining the  $\phi \rightarrow \tau\tau$  search with the results obtained by the DØ search for  $\phi b(\bar{b}) \rightarrow b\bar{b}b(\bar{b})$ . The combination of the results and the extracted limits are also described in Section 7.5.2.

### Higgs Width

The impact on the drastically increasing Higgs width with increasing  $\tan \beta$  (see Section 7.1.3) is studied by comparing the signal efficiencies and expected cross section limits for two different Higgs boson masses ( $M_\phi = 130$  GeV and  $M_\phi = 200$  GeV) at  $\tan \beta$  values of 30 and 100. Due to the broadening of the total decay width with increasing  $\tan \beta$ , a fraction of the signal events at  $\tan \beta = 100$  is shifted towards large values in the  $M_{vis}$  spectrum. These signal events dominate in the limit calculation since the background from Standard Model processes is small in the high- $M_{vis}$  region. This results in an improvement of the expected limit for  $\tan \beta = 100$  in comparison to  $\tan \beta = 30$ , hence the impact of the Higgs boson width on this analysis has been conservatively neglected.

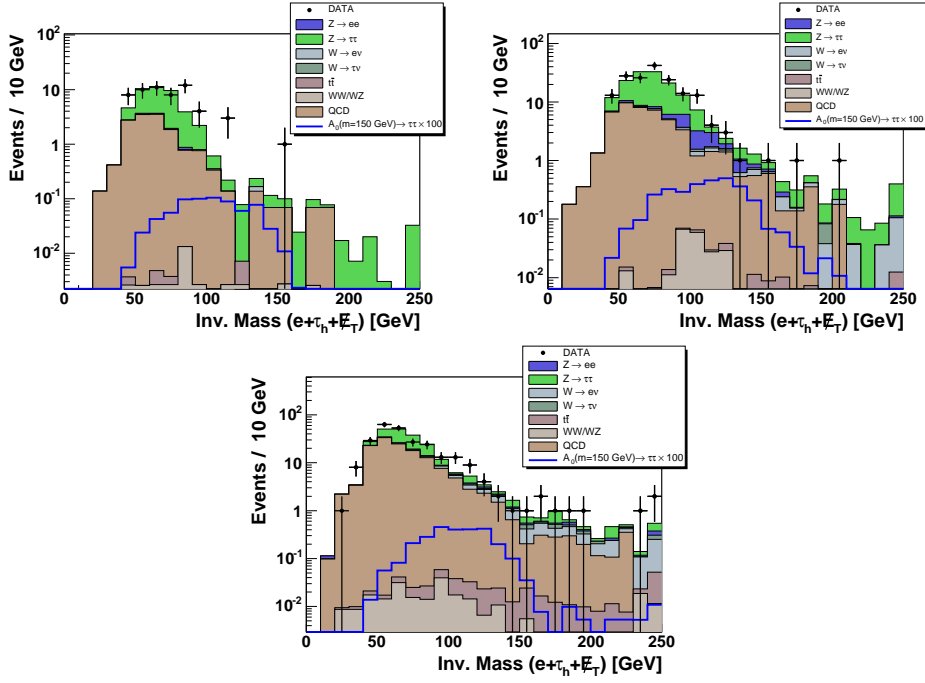


Figure 7.16: Distributions of the visible mass  $M_{vis}$  for tau type 1 (upper left), tau type 2 (upper right) and tau type 3 (bottom) after all selection criteria are applied. The highest bin contains the overflow.

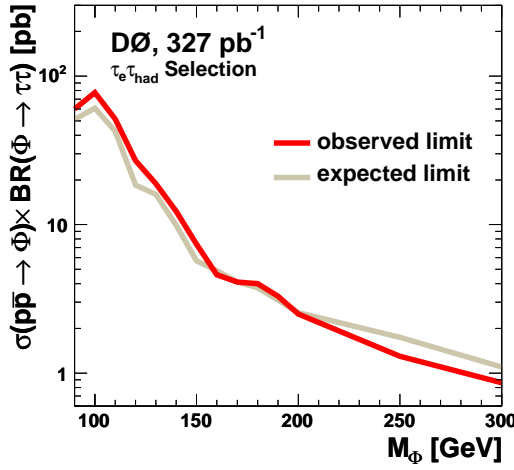


Figure 7.17: Observed and expected 95 % CL limit on the cross section times branching ratio for the process  $p\bar{p} \rightarrow \phi \rightarrow \tau\tau$  as a function of the neutral Higgs boson mass  $M_\phi$  for the  $e + \tau_h$  analysis.

### 7.5.2 Combination with Additional MSSM Higgs Analyses

A combination of three analyses which search for the production of neutral MSSM Higgs bosons with subsequent decay into a tau pair is performed to increase the sensitivity. The combination consists of the  $e + \tau_h$ , the  $\mu + \tau_h$  [104] and the  $e + \mu$  [104] final state, which are the most promising final states of the tau pair in terms of branching ratios and expected Standard Model backgrounds (see Section 7.1.4).

In a further step, the obtained results of the search for neutral MSSM Higgs bosons decaying into a tau pair ( $\phi \rightarrow \tau\tau$ ) are combined with the DØ results for the associated production of neutral MSSM Higgs boson with bottom quarks and subsequent decay of the Higgs into  $b\bar{b}$  ( $\phi b(\bar{b}) \rightarrow b\bar{b}b(\bar{b})$ ).

The results of both combinations are discussed in the following.

#### Combination with Additional $\phi \rightarrow \tau\tau$ Analyses

The  $e + \tau_h$  event selection is presented in detail in Section 7.3. The selection criteria for the  $\mu + \tau_h$  channel are identical with the ones used in the  $e + \tau_h$  selection, with the anti-electron cuts being replaced by anti-muon cuts. The  $e + \mu$  channel uses slightly different selection criteria, which account for the two isolated leptons and the enhanced number of neutrinos in the final state. Details for both analyses are given in Ref. [104].

The number of events observed in data and the number of background events expected from Monte Carlo for each analysis at the end of the selection is shown in Table 7.9. In addition, the signal efficiency for a neutral Higgs boson mass of  $M_\phi = 150$  GeV after application of all selection criteria is listed in the table for each channel. Observed data and expected background events are in good agreement for all three analyses. No evidence for the production of neutral MSSM Higgs bosons decaying into a tau pair is found, allowing to set a limit on the production cross section times branching ratio.

Figure 7.18 shows the signal efficiency of each analysis and the combined sum of all three analyses as a function of the neutral Higgs boson mass  $M_\phi$ . Since the tau branching ratios are included, the signal efficiency for the  $e + \mu$  analysis is low. Compared to the  $\mu + \tau_h$  analysis, the large electron contamination from  $Z/\gamma^* \rightarrow ee$  events in the  $e + \tau_h$  analysis and the resulting anti-electron cuts (see discussion in Section 7.3) lead to a smaller signal efficiency.

The results of all analyses are combined to extract a limit on the total cross section for neutral MSSM Higgs Boson production decaying into a tau pair. The limit is calculated using the complete visible mass spectrum  $M_{vis}$  and the likelihood ratio method (LEP CLs method, see Ref. [96]). The visible mass distributions for the combined  $e + \tau_h$  and  $\mu + \tau_h$  channels and for the  $e + \mu$  channel are shown in Figure 7.19, after all selection criteria are applied. Systematic and statistical errors, which are discussed for the  $e + \tau_h$  analysis in Section 7.4 and for the other two analyses in Ref. [104], are taken into account

Analysis	$e\tau_h$	$\mu\tau_h$	$e\mu$
Data	484	575	41
Total background	$427.3 \pm 55.7$	$576.3 \pm 61.5$	$43.5 \pm 5.3$
QCD	$199.5 \pm 26.0$	$62.2 \pm 6.6$	$2.1 \pm 0.4$
$Z/\gamma^* \rightarrow \tau\tau$	$202.7 \pm 26.3$	$491.7 \pm 52.6$	$39.4 \pm 5.0$
$Z/\gamma^* \rightarrow ee, \mu\mu$	$10.2 \pm 1.4$	$4.6 \pm 1.1$	$0.63 \pm 0.12$
$W \rightarrow e\nu, \mu\nu, \tau\nu$	$14.0 \pm 1.9$	$13.5 \pm 1.6$	$0.30 \pm 0.20$
Di-boson	$0.54 \pm 0.09$	$3.05 \pm 0.33$	$0.99 \pm 0.14$
$t\bar{t}$	$0.35 \pm 0.05$	$1.22 \pm 0.14$	$0.06 \pm 0.02$
Efficiency ( $M_\phi = 150$ GeV) [%]	$1.08 \pm 0.10$	$1.95 \pm 0.18$	$0.26 \pm 0.03$

Table 7.9: Number of events observed in data and expected for background and the efficiency for a signal with  $M_\phi = 150$  GeV for the three combined analysis channels. Statistical and systematic uncertainties are added in quadrature.

in the combination including their correlations. Due to the different S/B ratios for the three tau types, each tau type is added to the limit calculation as an independent channel. The best expected limit is achieved by splitting the  $M_W$  distribution for each channel into two subsamples, one with  $M_W < 6$  GeV and one with  $6 \text{ GeV} < M_W < 20$  GeV. Each subsample enters the limit calculation as a separate channel due to significant differences in the signal-to-background ratio (see Figure 7.20). The additional separation in  $M_W$  leads to an improvement of  $\sim 20\%$  in the expected limit.

Figure 7.21 shows the resulting observed and expected 95 % CL limits on the cross section times branching ratio for the process  $p\bar{p} \rightarrow \phi \rightarrow \tau\tau$  as a function of the neutral Higgs mass  $M_\phi$ . For comparison, the observed and expected limit of the recent CDF Run II result for  $\phi \rightarrow \tau\tau$  is also shown (see Ref. [19]). The CDF result uses data corresponding to an integrated luminosity of  $\mathcal{L} = 310 \text{ pb}^{-1}$ , and combines the search results from the  $e + \tau_h$  and  $\mu + \tau_h$  final states. Comparing the expected limits derived by the two experiments, the DØ analysis results in a better limit for neutral MSSM Higgs bosons with masses greater than 120 GeV, while CDF has a slightly better limit for  $M_\phi < 120$  GeV.

The resulting cross section limit can be interpreted as an exclusion in the  $(M_A, \tan \beta)$  plane. This is shown in Figure 7.22 for both the  $m_h^{max}$  and the no-mixing scenario, each with  $\mu < 0$  and  $\mu > 0$ . The detailed parameters for the two SUSY benchmark scenarios are given in Table 1.8. For illustration purposes, the limit is shown up to  $\tan \beta = 100$ , ignoring the effects from potentially large higher-order corrections in the very-high  $\tan \beta$  regime.

In the  $m_h^{max}$  scenario, the LEP II experiments exclude values of  $M_h$  and  $M_A$  less than 92.9 GeV and 93.4 GeV at 95 % confidence level (see Ref. [18]). In the same model, small values of  $\tan \beta$  up to  $\tan \beta = 3$  can be excluded over the whole considered mass range ( $M_\phi < 200$  GeV). The changes of the sign of the Higgs mass parameter  $\mu$  barely affect the exclusion limits. Since the LEP experiments studied only  $\tan \beta$  values up to 50, the extrapolated exclusion region for larger values is shown in a lighter color. The Tevatron  $\phi \rightarrow \tau\tau$

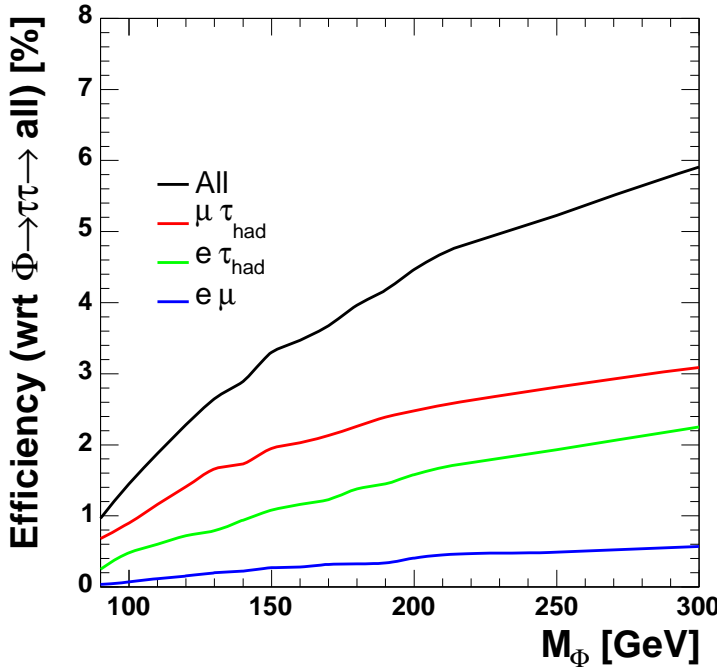


Figure 7.18: Signal efficiency as a function of  $M_\phi$  for the process  $p\bar{p} \rightarrow \phi \rightarrow \tau\tau$  for each analysis channel and the sum of all channels. The tau branching ratios are included in the signal efficiencies.

analyses exclude a significant portion of the parameter space, depending on the CP-odd Higgs mass and the sign of the Higgs mass parameter. DØ excludes  $\tan\beta$  values down to 60 for small values of  $M_A$ . Effects from potentially large higher-order corrections in the very high  $\tan\beta$  regime are ignored.

In the no-mixing scenario, the LEP II experiments exclude values of  $M_\phi$  less than 94.8 GeV and 92.7 GeV at 95 % confidence level for  $\mu < 0$  and  $\mu > 0$ . Small values of  $\tan\beta$  up to  $\tan\beta = 6$  can be excluded over the whole considered mass range for  $\mu > 0$ . For  $\mu < 0$ , the mass region around 115 GeV is excluded for all values of  $\tan\beta$ . For larger Higgs masses,  $\tan\beta$  values of at least  $\tan\beta = 14$  can be excluded for most values of  $M_A$ . As in the  $m_h^{max}$  scenario, the exclusion region for  $\tan\beta > 50$  values is shown in a lighter color since this parameter space was not studied at LEP. The DØ  $\phi \rightarrow \tau\tau$  analyses exclude  $\tan\beta$  values down to 65 for small values of  $M_A$ . As in the  $m_h^{max}$  scenario, radiative corrections – which can be sizeable for large  $\tan\beta$  – are ignored.

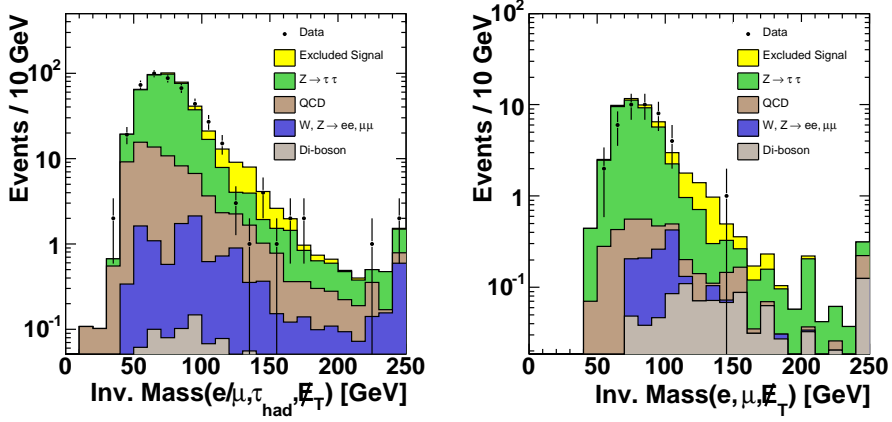


Figure 7.19: The combined distribution of the visible mass  $M_{vis}$  at the end of the selection for the two final states involving hadronic tau decays (left) and for the  $e + \mu$  final state (right). The highest bin contains the overflow.

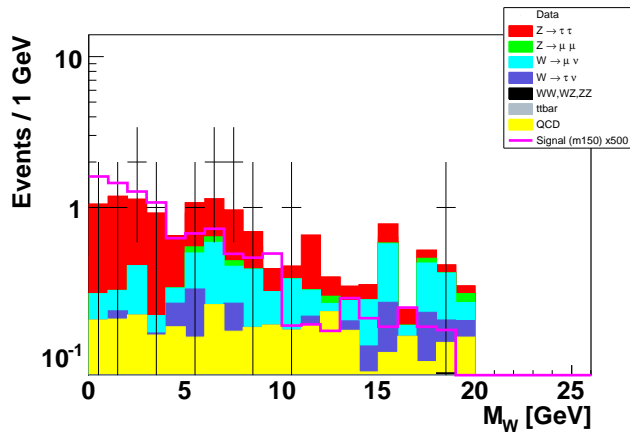


Figure 7.20:  $M_W$  in the  $\mu + \tau_h$  analysis after application of all selection criteria in the high-mass region  $M_{vis} > 120$  GeV. The best expected limit is achieved by splitting the  $M_W$  distribution into two subsamples due to different signal-to-background ratios:  $M_W < 6$  GeV,  $6$  GeV  $< M_W < 20$  GeV. The plot is taken from Ref. [104].

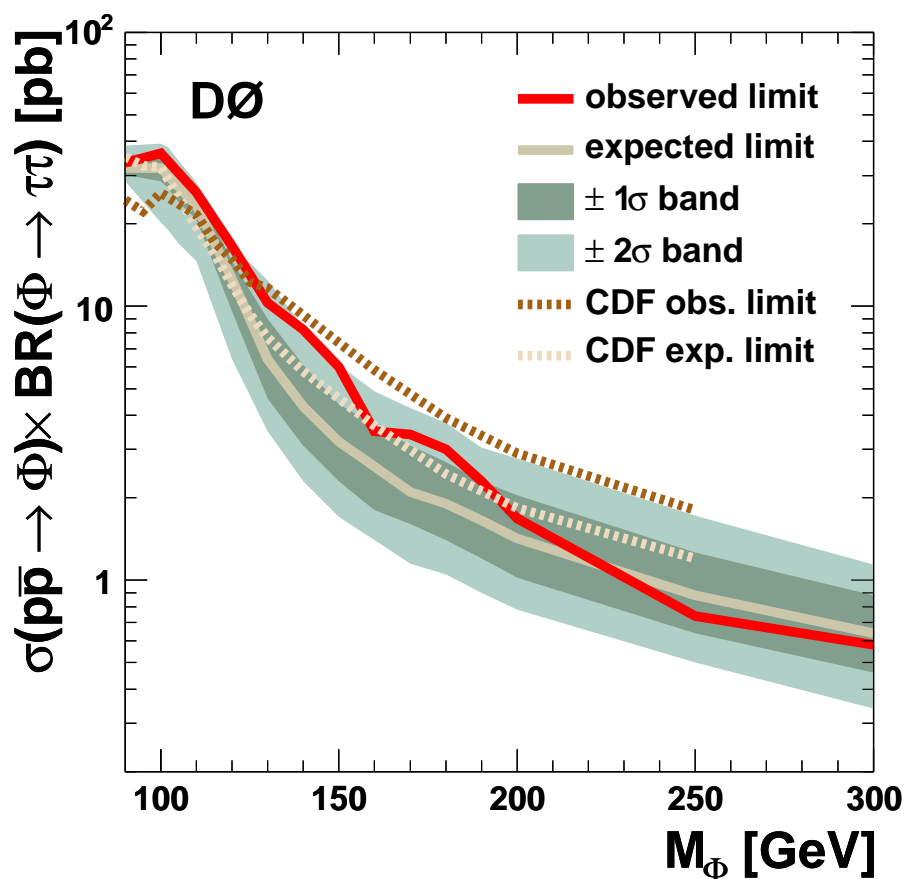


Figure 7.21: The observed and expected 95 % CL limits on the cross section times branching ratio for the process  $p\bar{p} \rightarrow \phi \rightarrow \tau\tau$  as a function of the neutral Higgs boson mass  $M_\phi$  in linear scale (top) and logarithmic scale (bottom). The CDF observed and expected limit for the same channel, taken from the recent publication (see Ref. [19]) based on data corresponding to  $\mathcal{L} = 310 \text{ pb}^{-1}$ , is shown for comparison.

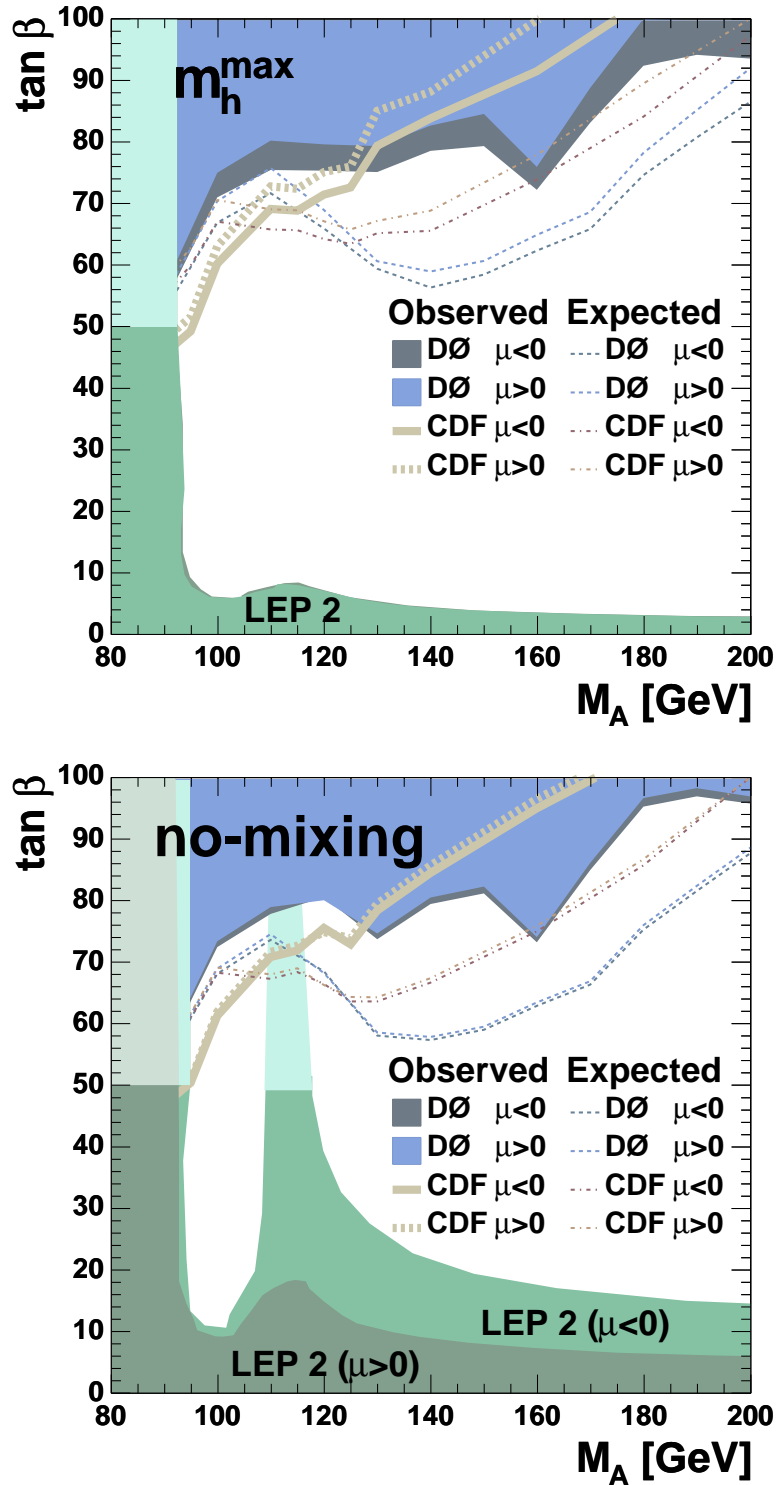


Figure 7.22: Excluded regions in the  $(M_A, \tan \beta)$ -plane for the  $m_h^{\max}$  scenario (top) and the no-mixing scenario (bottom). The  $e + \tau_h$ ,  $\mu + \tau_h$  and  $e + \mu$  analysis have been combined.

### Combination with the $\phi b(\bar{b}) \rightarrow b\bar{b}b(\bar{b})$ Analysis

Using Run II data corresponding to an integrated luminosity of  $260 \text{ pb}^{-1}$ , DØ has performed a search for the associated production of neutral MSSM Higgs bosons with bottom quarks and subsequent decay of the Higgs into  $b\bar{b}$ . The search strategy relies on the identification of at least three  $b$  jets in the event, and a signal would lead to an excess in the invariant  $b\bar{b}$  mass distribution. Figure 7.23 (left) shows the invariant mass spectrum of the two leading  $b$  jets at the end of the selection. No evidence for production of neutral Higgs bosons in association with  $b$ -jets is observed, and limits on the production cross section are derived (Figure 7.23 (right)). Details about this analysis can be found in Ref. [105]. The result is published in Ref. [20], and it is re-interpreted using the updated definitions of the two MSSM reference scenarios used in this thesis.

The results of the  $\phi \rightarrow \tau\tau$  search in the various final states mentioned above are combined with the result of  $\phi b(\bar{b}) \rightarrow b\bar{b}b(\bar{b})$  in order to further increase the sensitivity and to exclude a larger region in the  $(M_A, \tan \beta)$ -plane. The combination is performed by adding the invariant  $b\bar{b}$  mass distribution as an additional channel to the limit calculation. Figure 7.24 shows the excluded regions in the  $m_h^{max}$  and the no-mixing scenario for the combination.

In the  $m_h^{max}$  scenario, the excluded region for  $\mu < 0$  is significantly larger compared to the  $\phi \rightarrow \tau\tau$  results alone. There are, however, only small changes in the excluded region for  $\mu > 0$ . This is due to a small  $\phi b(\bar{b})$  cross section in this SUSY scenario, resulting in a small contribution to the combined limit.

In the no-mixing scenario, the  $\phi b(\bar{b})$  contributes equally to both  $\mu < 0$  and  $\mu > 0$  scenarios. The excluded region in the  $(M_A, \tan \beta)$ -plane is comparable to the CDF result for small masses of  $A$  ( $m_A < 120 \text{ GeV}$ ), while it significantly improves on the CDF result for large masses ( $m_A > 120 \text{ GeV}$ ).

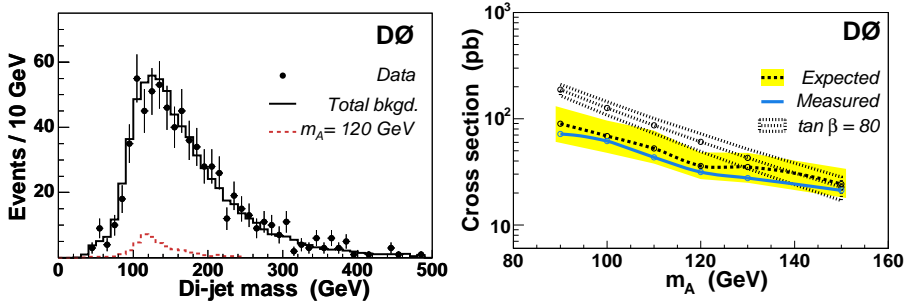


Figure 7.23: *left:* Invariant mass spectrum of two leading  $b$  jets in events with at least three  $b$  jets in the  $\phi b(\bar{b}) \rightarrow b\bar{b}b(\bar{b})$  analysis. The signal corresponds to a  $120 \text{ GeV}$  Higgs boson that can be excluded at  $95\% \text{ CL}$ .

*right:* Expected and observed  $95\% \text{ CL}$  upper limits on the signal cross section as a function of  $M_A$ . The band indicates the  $\pm 1\sigma$  range on the expected limit. Also shown is the cross section for the signal at  $\tan \beta = 80$  in the no-mixing scenario, with the theoretical uncertainty indicated by the overlaid band.

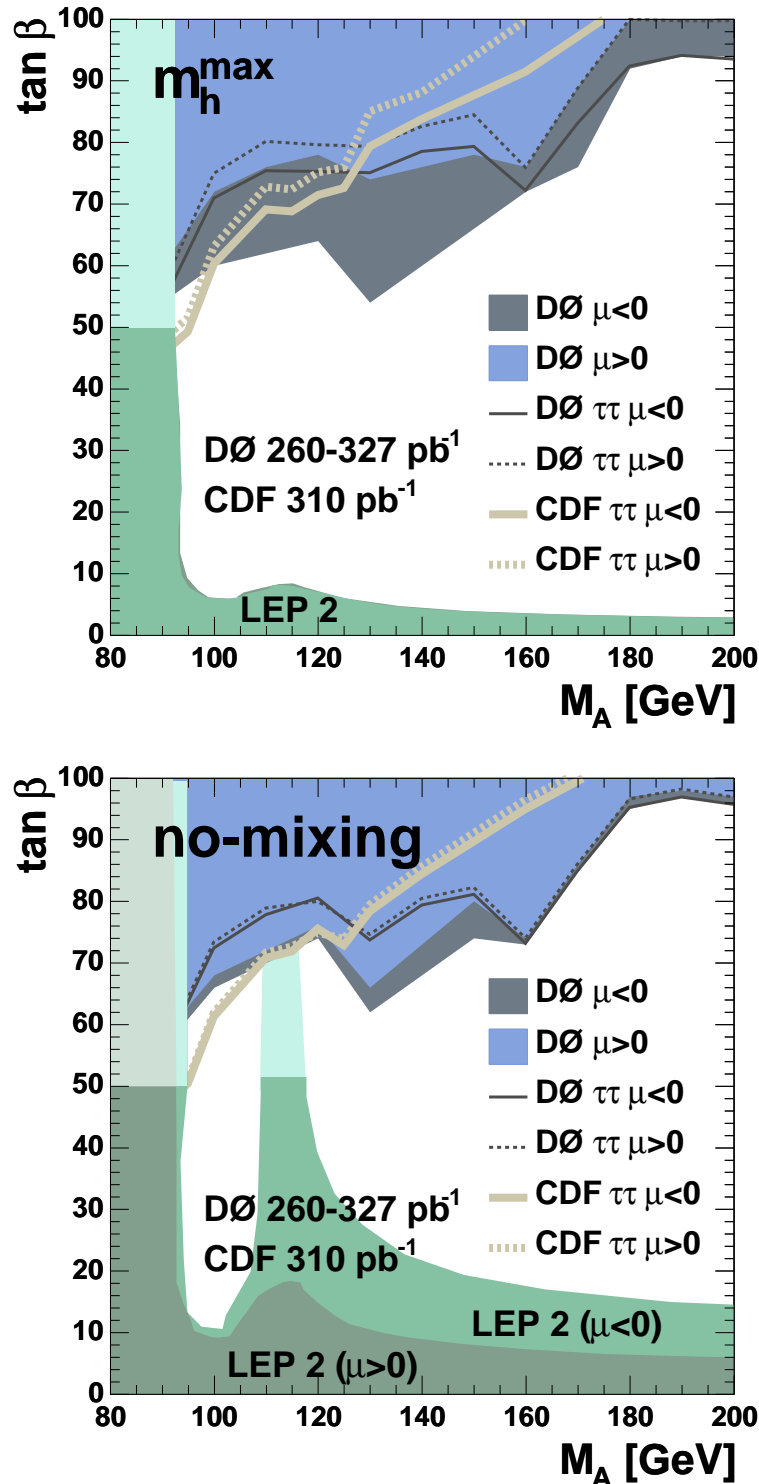


Figure 7.24: Excluded regions in the  $(M_A, \tan \beta)$ -plane for the  $m_h^{\max}$  scenario (top) and the no-mixing scenario (bottom). The  $\phi \rightarrow \tau\tau$  analyses (with the final states:  $e + \tau_h$ ,  $\mu + \tau_h$ ,  $e + \mu$ ) are combined with the result from  $\phi b(\bar{b}) \rightarrow b\bar{b}b(\bar{b})$ .

## 7.6 Outlook

The sensitivity of the search for neutral MSSM Higgs bosons decaying to tau pairs is mainly limited by the available data statistics. The cross section limit improves with the integrated luminosity in Run II, and consequently the excluded region in the  $(M_A, \tan \beta)$ -plane expands. Improvements in understanding and simulating of the detector are expected to increase the sensitivity further. By the end of Run II in 2008/09, the Tevatron is expected to have delivered an integrated luminosity of  $8 \text{ pb}^{-1}$  per experiment.

Studies have been performed in Ref. [106] to estimate the exclusion potential of the  $\phi \rightarrow \tau\tau$  searches with increasing luminosity. Figure 7.25 shows the expected 95 % CL exclusion for a neutral MSSM Higgs boson search in the  $(M_A, \tan \beta)$ -plane for different integrated luminosities. Results from CDF and DØ are combined, assuming similar performance. For  $\mathcal{L} = 8 \text{ fb}^{-1}$ , the searches are expected to be sensitive for large  $\tan \beta$  ranges down to  $\tan \beta \approx 20$ . Compared to the current  $\phi \rightarrow \tau\tau$  analyses, the study assumes an improvement of the order of 30 % in signal efficiency. This improvement results from adding the fully hadronic decay final state  $\tau_h \tau_h$  and a better understanding of the detectors and the tau energy scale.

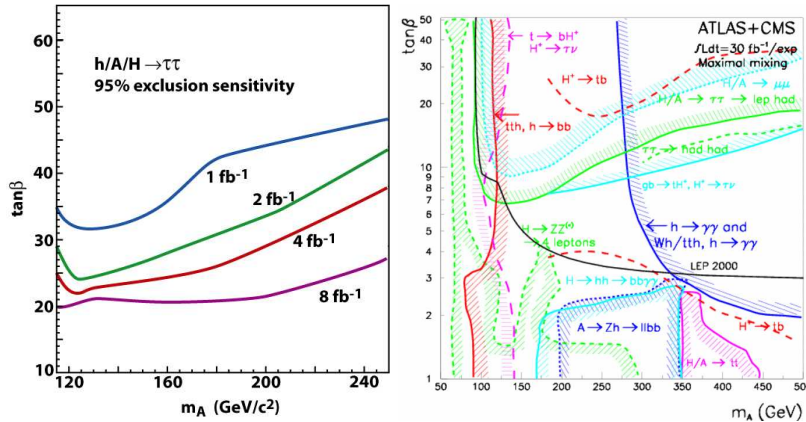


Figure 7.25: *left:* Expectations for the exclusion potential at 95 % CL for a combined DØ-CDF search for neutral MSSM Higgs bosons decaying to tau pairs in the  $(M_A, \tan \beta)$ -plane (from Ref. [106]).  
*right:* Combined sensitivity of the ATLAS and CMS experiments for the discovery of MSSM Higgs bosons in the maximal mixing scenario for an integrated luminosity of  $30 \text{ fb}^{-1}$ . The  $5\sigma$  discovery curves are shown in the  $(M_A, \tan \beta)$ -plane for individual channels (from Ref. [101]).

Even with the full data set expected for Run II, the Tevatron experiments will not be able to cover the full  $(M_A, \tan \beta)$ -plane. With the start-up of the Large Hadron Collider in 2007/08, the two LHC experiments ATLAS and CMS will continue the search for neutral MSSM Higgs bosons. Figure 7.25 shows the combined ATLAS-CMS discovery potential in the  $(M_A, \tan \beta)$ -plane. With an integrated luminosity of  $30 \text{ fb}^{-1}$ , corresponding to three years of data taking at low luminosity, the whole plane is expected to be covered.



## 8 Summary and Conclusion

A search for new physics beyond the Standard Model as predicted by supersymmetric models has been performed in final states with an electron, a hadronically decaying tau and missing transverse energy. The search has been performed in two analyses, which cover a complementary supersymmetric parameter space: the first analysis searches for the direct production of supersymmetric particles and probes small values of  $\tan\beta$ , while the second one searches for neutral Higgs bosons in an extended Higgs sector, focussing on the high  $\tan\beta$  parameter space. The dataset analyzed has been collected with the DØ detector at the Tevatron  $p\bar{p}$  collider (Fermilab) at a center-of-mass energy of  $\sqrt{s} = 1.96$  TeV from April 2002 to July 2004 and corresponds to an integrated luminosity of  $327 \text{ pb}^{-1}$ .

A final state consisting of an electron and a hadronic tau decay is challenging in a hadron collider environment due to large background contributions from QCD jet production and  $Z/\gamma^* \rightarrow ee$  processes. Selection criteria have been developed to suppress these large backgrounds and to establish the  $Z/\gamma^* \rightarrow \tau\tau \rightarrow e + \tau_h$  signal as a reference.

A promising source for supersymmetric particles at the Tevatron is the associated production of the lightest chargino  $\tilde{\chi}_1^\pm$  and the second-lightest neutralino  $\tilde{\chi}_2^0$ . The leptonic decay of these particles,  $\tilde{\chi}_2^0 \rightarrow \tilde{\chi}_1^0 \ell \ell$  and  $\tilde{\chi}_1^\pm \rightarrow \tilde{\chi}_1^0 \ell \nu$ , leads to a detector signature with three charged leptons and large missing transverse energy. A search for this process has been performed in final states with an electron, a hadronically decaying tau decay and a third lepton.

No evidence for the production of supersymmetric particles has been found. The result of this analysis has been combined with various leptonic final states ( $e + e + \ell$ ,  $\mu + \mu + \ell$ ,  $e + \mu + \ell$ , like-sign  $\mu + \mu$ ,  $\mu + \tau_h + \ell$ ), and an upper limit on the product of cross section times branching ratio,  $\sigma(\tilde{\chi}_2^0 \tilde{\chi}_1^\pm) \times \text{BR}(3\ell)$ , has been set as a function of the chargino mass. Although only small values of  $\tan\beta$  are accessible with the current dataset, the inclusion of the two dedicated tau analyses ( $e + \tau_h + \ell$  and  $\mu + \tau_h + \ell$ ) improves the lower limit on the cross section. In a supersymmetric scenario with heavy sleptons and enhanced leptonic branching fractions for charginos and neutralinos, a chargino lower mass limit of 116 GeV is derived at 95 % CL. Chargino masses up to 128 GeV are excluded in related scenarios with heavy squarks. These results constrain the SUSY parameter space beyond the existing LEP II and Tevatron Run I limits.

The Minimal Supersymmetric Standard Model (MSSM) requires two complex Higgs doublets, leading to an enhanced Standard Model Higgs sector with three neutral and a pair of charged Higgs bosons. At large values of  $\tan\beta$ , the coupling of the neutral Higgs bosons to down type quarks and leptons is strongly

enhanced, leading to sizeable production cross sections. The decay into a tau pair can lead to a final state with an electron, a hadronically decaying tau and considerable missing transverse energy.

A signal selection for the  $e + \tau_h$  final state has been developed, and the results were combined with analyses that cover the  $\mu + \tau_h$  and  $e + \mu$  final states. No excess compared to the expectations from Standard Model processes has been found, and limits on the production cross section times branching ratio have been set. The results have also been combined with those obtained from the DØ search for the associated production of neutral Higgs bosons with  $b$  quarks and subsequent decay of the Higgs boson into  $b\bar{b}$ . The combined result represents the most stringent limit on the production of neutral MSSM Higgs bosons at hadron colliders at present. In the  $m_h^{max}$  scenario with  $\mu < 0$ , a significant part of the parameter space down to  $\tan \beta = 56$  can be excluded for  $M_A = 130$  GeV. In the no-mixing scenario,  $\tan \beta$  values down to 62 can be excluded for  $M_A = 130$  GeV and  $\mu < 0$ . The excluded regions decrease with increasing  $M_A$ . The obtained results are complimentary to the LEP II results, which are limited to  $M_A < 95$  GeV for all values of  $\tan \beta$  due to kinematic reasons or to small values of  $\tan \beta$  for larger  $M_A$ .

The sensitivity of the search for associated chargino/neutralino production in final states with three leptons and the search for neutral MSSM Higgs bosons in final states with two taus is mainly limited by data statistics. Improved understanding and simulation of the detector combined with a larger data sample are expected to significantly increase the sensitivity of the SUSY searches. However, even with the full data set expected for Run II, the Tevatron experiments will only be sensitive to limited chargino masses and will not be able to cover the full  $(M_A, \tan \beta)$ -plane (see Ref. [106]). Next generation experiments at the LHC (see Ref. [107] and [108]) will continue the search beyond the Tevatron limits.

# List of Tables

1.1	Overview of the Standard Model fermions and their masses . . . . .	2
1.2	Standard Model gauge bosons and their properties . . . . .	2
1.3	Weak isospin, hypercharge, electric charge of the fermions . . . . .	4
1.4	Couplings of the Standard Model Higgs bosons to fermions and massive gauge bosons . . . . .	7
1.5	Overview of the SUSY particles . . . . .	11
1.6	Superfields in the MSSM . . . . .	12
1.7	MSSM correction factors to Higgs boson couplings with respect to the Standard Model couplings to fermions and massive gauge bosons . . . . .	18
1.8	Values of the SUSY parameters for the no-mixing and $m_h$ -max benchmark scenarios . . . . .	19
4.1	Tau decay channel and branching ratios . . . . .	56
4.2	Input variables for the three neural networks . . . . .	62
5.1	Single electron triggers used in both analyses . . . . .	73
5.2	Description of the trigger names that are used at the different trigger levels . . . . .	74
5.3	Integrated delivered and reconstructed luminosity . . . . .	75
5.4	$\sigma \times BR$ and number of generated events for the different background Monte Carlo samples. . . . .	76
5.5	QCD scale factors . . . . .	77
5.6	EM Candidate efficiencies in data and Monte Carlo . . . . .	82
5.7	Smearing parameters for electrons . . . . .	84
6.1	SUSY analysis: properties of SUSY reference points which are considered in this analysis . . . . .	96
6.2	SUSY analysis: summary of the selection criteria for the $Z/\gamma^* \rightarrow \tau\tau \rightarrow e + \tau_h$ signal . . . . .	97
6.3	$Z/\gamma^* \rightarrow \tau\tau$ : number of events observed in data and expected for Standard Model processes at different stages of the selection $Z/\gamma^* \rightarrow \tau\tau \rightarrow e + \tau_h$ . . . . .	101
6.4	SUSY analysis: summary of the applied selection cuts . . . . .	103
6.5	SUSY analysis: systematic uncertainties . . . . .	113
6.6	SUSY analysis: number of candidate events observed and background events expected at different stages of the selection . . . . .	114

6.7	SUSY analysis: number of signal events expected at different stages of the selection . . . . .	115
6.8	SUSY analysis: selection efficiencies for the SUSY reference points after application of all selection criteria . . . . .	115
6.9	SUSY analysis: properties of SUSY reference points used in the combination . . . . .	117
6.10	SUSY analysis: selection efficiencies for the SUSY reference points used in the combination . . . . .	118
6.11	SUSY analysis: number of expected signal events at the end of the selection for the SUSY reference points used in the combination	118
6.12	SUSY analysis: combined number of candidate events observed and background events expected in the six trilepton analysis channels . . . . .	119
6.13	SUSY analysis: properties of SUSY reference points that are used to study the parameter space with high $\tan\beta$ . . . . .	122
6.14	SUSY analysis: branching ratio into leptons for the SUSY reference points used to study the parameter space with high $\tan\beta$ .	123
7.1	Higgs analysis: overview of the possible $\phi \rightarrow \tau\tau$ final states . . .	134
7.2	Higgs analysis: $\sigma \times BR$ and number of generated events for the process $\phi \rightarrow \tau\tau$ . . . . .	136
7.3	Higgs analysis: summary of the selection criteria . . . . .	137
7.4	Higgs analysis: systematic uncertainties . . . . .	147
7.5	Higgs analysis: number of events observed in data and expected for background at different stages of the selection for tau type 1 .	149
7.6	Higgs analysis: number of events observed in data and expected for background at different stages of the selection for tau type 2 .	149
7.7	Higgs analysis: number of events observed in data and expected for background at different stages of the selection for tau type 3 .	150
7.8	Higgs analysis: selection efficiency for a neutral MSSM Higgs boson of mass $M_\phi = 150$ GeV at different stages of the selection	150
7.9	Higgs analysis: number of events observed in data and expected for background for all three analysis channels . . . . .	154

# List of Figures

1.1	Higgs potential in the case of a single complex scalar field $\phi$ . . . . .	6
1.2	Radiative corrections to the squared Higgs boson mass from fermions and bosons . . . . .	8
1.3	Scale dependence of the couplings in the SM and in a MSSM scenario . . . . .	9
1.4	Running of the soft-supersymmetry breaking parameters with $Q$ . . . . .	15
1.5	LEP combined lower limits in a constraint MSSM on $m_{\tilde{t}}$ and on $m_{\tilde{\chi}_1^+}$ . . . . .	20
2.1	Schematic view of the Fermilab accelerator chain . . . . .	25
2.2	Diagram of the upgraded D $\emptyset$ detector . . . . .	27
2.3	The central tracking system . . . . .	28
2.4	Schematic 3D view of the silicon microstrip detector (SMT) . . . . .	29
2.5	Isometric view of the central and two end calorimeters . . . . .	30
2.6	Schematic view of a portion of the D $\emptyset$ calorimeter . . . . .	31
2.7	Schematic side view of the muon system . . . . .	33
2.8	Schematic drawing showing the location of the luminosity monitor detectors . . . . .	34
2.9	Overview of the D $\emptyset$ trigger and data acquisition system . . . . .	35
2.10	Block diagram of the D $\emptyset$ trigger system . . . . .	37
3.1	Parton distribution function of the proton as calculated for $Q^2 = 10^4$ GeV using CTEQ6 [39] . . . . .	43
3.2	Cross sections and number of expected events for selected processes at the Tevatron . . . . .	44
4.1	Distribution of various input quantities for the electron likelihood .	55
4.2	Distribution of the resulting electron likelihood . . . . .	55
4.3	Tau type misclassification . . . . .	59
4.4	Neural network input variables for tau type 1 . . . . .	63
4.5	Neural network output variable for tau type 1 . . . . .	63
4.6	Neural network input variables for tau type 2 . . . . .	64
4.7	Neural network output variable for tau type 2 . . . . .	64
4.8	Neural network input variables for tau type 3 . . . . .	65
4.9	Neural network output variable for tau type 3 . . . . .	65
4.10	Background rejection versus tau efficiency for all three tau types	66
4.11	Jet energy scale calibration factors for data . . . . .	70
4.12	Jet energy scale calibration factors for Monte Carlo . . . . .	70

5.1	QCD background normalization using the invariant $e + \tau_h$ mass distribution . . . . .	77
5.2	QCD background normalization using the neural network distributions . . . . .	77
5.3	Trigger list v11: single electron trigger efficiency for the combination of EM_HI, EM_HL_SH, EM_MX and EM_MX_SH . . . . .	79
5.4	Trigger list v11: single electron trigger efficiency for EM_HI_SH_TR and EM_MX_SH_TR . . . . .	80
5.5	Combined turn-on curve for trigger list v12 . . . . .	81
5.6	Electron efficiency correction for likelihood $> 0.8$ . . . . .	83
5.7	Efficiency for the track match with E/p requirement . . . . .	83
5.8	Efficiency correction for track match with E/p requirement . . . . .	84
5.9	Distribution of the invariant di-electron mass in data and Monte Carlo . . . . .	85
5.10	Ratio between tuned and default PYTHIA Monte Carlo as a function of $p_T(Z)$ . . . . .	86
6.1	SUSY analysis: leading order diagrams for the production of chargino/neutralino pairs in quark-antiquark collisions . . . . .	90
6.2	SUSY analysis: NLO cross sections for chargino/neutralino pair production as a function of the gaugino masses . . . . .	91
6.3	SUSY analysis: Feynman diagrams for the chargino decay . . . . .	91
6.4	SUSY analysis: Feynman diagrams for the neutralino decay . . . . .	92
6.5	SUSY analysis: masses of SUSY particles and $\sigma \times \text{BR}(3 \text{ leptons})$ of the associated chargino/neutralino production as a function of $\tan \beta$ . . . . .	93
6.6	SUSY analysis: Feynman diagrams for the associated chargino/neutralino production via the s- and t-channel followed by the subsequent decay in trilepton final states . . . . .	93
6.7	SUSY analysis: parton level $p_T$ distributions of leptons from associated chargino/neutralino production . . . . .	94
6.8	$Z/\gamma^* \rightarrow \tau\tau$ : various distributions at preselection stage . . . . .	98
6.9	$Z/\gamma^* \rightarrow \tau\tau$ : ratio of the transverse hadronic tau energy and the associated tau track(s) . . . . .	100
6.10	$Z/\gamma^* \rightarrow \tau\tau$ : transverse mass distributions at preselection stage and before the anti-W criteria selection is applied . . . . .	100
6.11	$Z/\gamma^* \rightarrow \tau\tau$ : distribution of $\Delta\phi(e, \tau_h)$ and neural network output . . . . .	101
6.12	SUSY analysis: distribution of important variables of the $Z/\gamma^* \rightarrow \tau\tau$ selection after application of all cuts . . . . .	102
6.13	SUSY analysis: invariant $e + \tau_h$ mass distribution . . . . .	104
6.14	SUSY analysis: distribution and the neural network output and the electron track isolation . . . . .	105
6.15	SUSY analysis: distribution of $\Delta\phi(e, \tau)$ . . . . .	106
6.16	SUSY analysis: distribution of $\cancel{E}_T$ and of the minimum of $M_T(e, \cancel{E}_T)$ and $M_T(\tau_h, \cancel{E}_T)$ . . . . .	106
6.17	SUSY analysis: distribution of the $\cancel{E}_T$ significance and $H_T$ . . . . .	107
6.18	SUSY analysis: $p_T$ distribution of the third track . . . . .	109

6.19 SUSY analysis: $p_T$ and neural network output distribution of the second tau . . . . .	110
6.20 SUSY analysis: distribution of $p_T^{trk} \times \not{E}_T$ . . . . .	111
6.21 SUSY analysis: combined limits on $\sigma(\tilde{\chi}_1^\pm \tilde{\chi}_2^0) \times BR(3\ lep)$ with leptonic final states . . . . .	121
6.22 SUSY analysis: efficiency of the different trilepton analyses for the reference points . . . . .	124
6.23 SUSY analysis: parton level $p_T$ distribution for SUSY point T3 and reconstruction efficiency for tau candidates . . . . .	124
7.1 Higgs analysis: Feynman diagrams for the neutral MSSM Higgs boson production processes of interest at the Tevatron . . . . .	128
7.2 Higgs analysis: cross section for neutral MSSM Higgs production as a function of their masses for $\tan \beta = 5$ and $\tan \beta = 40$ . . . . .	130
7.3 Higgs analysis: cross section for neutral MSSM Higgs production as a function of their masses for $\tan \beta = 5$ and $\tan \beta = 40$ . . . . .	130
7.4 Higgs analysis: cross section for $p\bar{p} \rightarrow \phi \rightarrow \tau\tau$ as a function of $M_\phi$ for different $\tan \beta$ . . . . .	131
7.5 Higgs analysis: branching ratios of neutral MSSM Higgs bosons as a function of their masses for $\tan \beta = 3$ and $\tan \beta = 30$ . . . . .	132
7.6 Higgs analysis: Higgs width as a function of $\tan \beta$ . . . . .	133
7.7 Higgs analysis: production of a neutral MSSM Higgs boson with subsequent decay into two $\tau$ leptons . . . . .	134
7.8 Higgs analysis: various distributions for each tau type at preselection stage . . . . .	139
7.9 Higgs analysis: electron contamination for tau type 1 . . . . .	140
7.10 Higgs analysis: electron contamination for tau type 2 . . . . .	141
7.11 Higgs analysis: electron contamination for tau type 2 in $\phi$ -cracks	141
7.12 Higgs analysis: electron contamination for tau type 3 . . . . .	142
7.13 Higgs analysis: various distributions for each tau type after anti-electron cuts . . . . .	143
7.14 Higgs analysis: various distributions for each tau type after tau identification . . . . .	144
7.15 Higgs analysis: $W$ mass distributions before corresponding cut .	145
7.16 Higgs analysis: distributions of the visible mass for all tau types after all selection criteria are applied . . . . .	152
7.17 Higgs analysis: observed and expected 95 % CL limits on the cross section times branching ratio for the $e + \tau_h$ analysis . . . . .	152
7.18 Higgs analysis: signal efficiency as a function of $M_\phi$ . . . . .	155
7.19 Higgs analysis: combined distribution of $M_{vis}$ for all three final states . . . . .	156
7.20 Higgs analysis: $M_W$ in the $\mu + \tau_h$ analysis after application of all selection criteria in the high-mass region $M_{vis} > 120$ GeV . . . . .	156
7.21 Higgs analysis: observed and expected 95 % CL limits on the cross section times branching ratio . . . . .	157
7.22 Higgs analysis: excluded regions in the $(M_A, \tan \beta)$ -plane for the $m_h^{max}$ and the no-mixing scenario . . . . .	158

7.23 Higgs analysis: invariant mass of the two leading jets and expected and observed cross section limit for the $\phi b(\bar{b}) \rightarrow b\bar{b}b(\bar{b})$ analysis . . . . .	159
7.24 Higgs analysis: excluded regions in the $(M_A, \tan \beta)$ -plane for the $m_h^{max}$ and the no-mixing scenario after combination of $\phi \rightarrow \tau\tau$ with $\phi b(\bar{b}) \rightarrow b\bar{b}b(\bar{b})$ . . . . .	160
7.25 Higgs analysis: exclusion potential for a combined DØ-CDF search for neutral MSSM Higgs bosons decaying to tau pairs for different integrated luminosities and combined sensitivity of the ATLAS and CMS experiments for the discovery of MSSM Higgs bosons in the $m_h^{max}$ scenario. . . . .	161

## Bibliography

- [1] S. L. Glashow, Nucl. Phys. **22** (1961) 579;  
S. Weinberg, Phys. Rev. Lett. **19** (1967) 1264;  
A. Salam, *Elementary Particle Theory*, ed. N. Svartholm (Almqvist and Wiksell, Stockholm, 1968), 367;  
P.W. Higgs, Phys. Rev. Lett. **13** (1964) 508-509.
- [2] D.J. Gross and F. Wilczek, Phys. Rev. **D8** (1973) 3633;  
H.D. Politzer, Phys. Rep. **14** (1974) 129.
- [3] S. Eidelmann *et al.*, [Particle Data Group] Phys. Lett. **B592**, 283-288 (2004).
- [4] N. Cabibbo, *Unitary Symmetry and Leptonic Decays*, Phys. Rev. Lett. **10** (1963) 531-532;  
M. Kobayashi, K. Maskawa, *CP Violation in the Renormalizable Theory of Weak Interaction*, Prog. Theor. Phys. **49** (1973) 652-657.
- [5] Y. Fukuda *et al.*, Phys. Rev. Lett. **81** (1998) 1562-1567.
- [6] LEP Higgs Working Group, “*Search for Standard Model Higgs Bosons at LEP*”, LHWG Note 2001-03, CERN-EP/2001-055.
- [7] R.N. Mohapatra, “*Unification and Supersymmetry*”, Springer Verlag, New York, Berlin, Heidelberg (2003).
- [8] S.P. Martin, “*A Supersymmetry Primer*”, hep-ph/9709356.
- [9] M. Drees, “*An Introduction to Supersymmetry*”, APCTP-5 KEK-TH-501 (1996), hep-ph/9611409.
- [10] Y.A. Golfand and E.P. Likhtman, JETP Lett. **13** (1971) 452;  
D. Volkov and V.P. Akulov, JETP Lett. **16** (1972) 438;  
H.P. Nilles, Phys. Rep. **110** (1984) 1;  
H.E. Haber and G.L. Kane, Phys. Rep. **117** (1985) 75.
- [11] E. Cremmer *et al.*, Phys. Lett. **B116** (1982) 231;  
A.H. Chamseddine, R. Arnowitt and P. Nath, Phys. Rev. Lett. **29** (1982) 970;  
J. Bagger and E. Witten, Phys. Lett. **B118** (1982) 103.
- [12] S. Abel *et al.*, “*Report of SUGRA Working Group for Run II of the Tevatron*”, hep-ph/0003154.

## Bibliography

---

- [13] G.F. Giudice, R. Rattazzi, “*Theories with Gauge-Mediated Supersymmetry Breaking*”, hep-ph/9801271.
- [14] C. Csaki, “*The Minimal Supersymmetric Standard Model (MSSM)*”, hep-ph/9606414.
- [15] A. D. Sakharov, JETP Lett. **5** (1967) 24;  
A. Pilaftsis, Phys. Rev. **D58** (1998) 096010, hep-ph/9803279.
- [16] M. Carena, S. Heinemeyer, C.E.M. Wagner, G. Weiglein, “*Minimal Supersymmetric Standard Model Higgs rates and backgrounds in ATLAS*”, ATLAS Internal Note ATL-PHYS-96-074, Eur. Phys. J. **C26** (2003) 601-607.
- [17] M. Carena, S. Heinemeyer, C.E.M. Wagner, G. Weiglein, “*Suggestions for benchmark scenarios for MSSM Higgs boson searches at hadron colliders*”, Eur. Phys. J. **C26** (2003) 601-607.
- [18] LEP Higgs Working Group, “*Search for Neutral MSSM Higgs Bosons at LEP*”, LHWG Note 2005-01.  
<http://lephiggs.web.cern.ch/LEPHIGGS/www/Welcome.html>
- [19] A. Abulencia *et al.*, “*Search for neutral MSSM Higgs bosons decaying to  $\tau$  pairs in  $p\bar{p}$  collisions at  $\sqrt{s} = 1.96$  TeV*”, hep-ex/0509015.
- [20] V. M. Abazov *et al.*, “*Search for neutral supersymmetric Higgs bosons in multijet events at  $\sqrt{s} = 1.96$  TeV*”, Phys. Rev. Lett. **95** (2005) 151801; hep-ex/0504018.
- [21] Heister *et al.* – ALEPH Collaboration, “*Absolute Lower Limits on the Masses of Selectrons and Sneutrinos in the MSSM*”, Phys. Lett. **B544** (2002) 73-88.
- [22] B. Abbott *et al.*, “*Search for Trilepton Signatures from Associated Gaugino Pair Production*”, Phys. Rev. Lett. **80** (1998) 8.
- [23] F. Abe *et al.*, “*Search for Chargino-Neutralino Associated Production at the Fermilab Tevatron Collider*”, Phys. Rev. Lett. **80** (1998) 5275.
- [24] G.W. Bennet *et al.*, Phys. Rev. Lett **92** (2004) 161802.
- [25] LEPSUSYWG, ALEPH, DELPHI, L3 and OPAL experiments, Note LEPSUSYWG/04-01.1 (2004),  
<http://lepsusy.web.cern.ch/lepsusy/Welcome.html>
- [26] LEPSUSYWG, ALEPH, DELPHI, L3 and OPAL experiments, Note LEPSUSYWG/01-03.1 (2001),  
<http://lepsusy.web.cern.ch/lepsusy/Welcome.html>

- [27] Fermilab Beams Division, <http://www-bd.fnal.gov/>
- [28] <http://www.fnal.gov/>
- [29] <http://lhc-new-homepage.web.cern.ch/lhc-new-homepage>
- [30] <http://public.web.cern.ch/Public/Welcome.html>
- [31] <http://www-cdf.fnal.gov>
- [32] <http://www-d0.fnal.gov>
- [33] <http://www-zeus.desy.de>
- [34] <http://www-h1.desy.de>
- [35] <http://www.desy.de>
- [36] S. Abachi *et al.*, Nucl. Instr. and Meth. **A338** (1994) 185.
- [37] V.M. Abazov *et al.*, “*The Upgraded DØ Detector*”, hep-ph/0507191.
- [38] <http://www-d0.fnal.gov/D0Code/source/d0reco>
- [39] CTEQ group “*New Generation of Parton Distributions with Uncertainties from Global QCD Analysis (CTEQ6)*”, hep-ph/0201195.
- [40] T. Sjostrand *et al.*, Comp. Phys. Commun. **135** (2001) 238.
- [41] S. Jadach *et al.*, “*The  $\tau$  decay library TAUOLA, update with exact  $O(\alpha)$  QED corrections in  $\tau \rightarrow \mu(\text{el})\nu\bar{\nu}$  decay modes*”, CERN-TH. 6195/91.
- [42] P. Golonka, B. Kersevan, T. Pierzchala, E. Richter-Was, M. Worek, “The tauola-photos-F environment for the TAUOLA and PHOTOS packages, release II”, hep-ph/0312240.
- [43] G. Altarelli, G. Parisi, Nucl. Phys. **B126** (1977) 298.
- [44] S. Eidelmann *et al.*, [Particle Data Group] Phys. Lett. **B592** (2004) 283-288.
- [45] T. Sjostrand *et al.*, Comp. Phys. Commun. **135** (2001) 238.
- [46] B. Andersson *et al.*, Phys. Rep. **97** (1983);  
B. Andersson, “*The Lund Model*”, Cambridge University Press (1998).
- [47] Y. Fisyak, J. Womersley, “*DØGSTAR, DØ GEANT simulation of the Total Apparatus Response*”, DØ Note 3191.
- [48] <http://www-d0.fnal.gov/computing/MonteCarlo/simulation/d0sim.html>
- [49] Application Software Group, CERN Computing and Networks Division, “*GEANT, Detector Description and Simulation Tool*”, CERN Program Library Long Writeup W5013.

## Bibliography

---

- [50] G. Borisov,  
[http://www-d0.fnal.gov/global\\_tracking/talks/20030228/talk-adm-030228.ps](http://www-d0.fnal.gov/global_tracking/talks/20030228/talk-adm-030228.ps)
- [51] A. Khanov, “HTF: Histogramming Method for Finding Tracks”, DØ Note 3778.
- [52] S. Kermiche, A. Mendès, M.-C. Cousinou, A. Cothenet, “Energy Scale studies and calibration of the DØ electromagnetic calorimeter using  $Z^0$  and  $J/\psi \rightarrow e^+e^-$  Run II events”, DØ Note 4945.
- [53] S.-J. Park, “ $t\bar{t}$  cross section in the  $e+jets$  channel in Monte Carlo”, Diploma Thesis (2003).
- [54] J. Koszminski, R. Kehoe, H. Weerts, S.-J. Park, A. Quadtt, J. Gardner, S. Jabeen, “Electron Likelihood in p14”, DØ Note 4449.
- [55] A. Abdesselam, “Comparison of H-Matrices for electron identification in DØ Run II”, DØ Note 3745.
- [56] E. Busato, B. Andrieu, “Jet Algorithms in the DØ Run II Software: Description and User’s Guide”, DØ Note 4457.
- [57] D. Chakraborty, F. Charles, S. Duensing, C. Galea, A. Gay, Y. Gerstein, A-C. Le Bihan, C. Noeding, A. Patwa, S. Protopopescu, “Certification of  $\tau$  lepton id (p14)”, DØ Note 4453.
- [58] Jean-Pierre Ernenwein,  
<http://e.home.cern.ch/e/ernen/www/NN/index.html>
- [59] D. Chakraborty, Y. Coadou, S. Duensing, C. Galea, Y. Gerstein, A-C. Le Bihan, C. Noeding, S. Protopopescu, “Reconstruction of  $\tau$  leptons in hadronic final states at DØ Run 2”, DØ Note 4210.
- [60] S. Duensing, “Measurement of the  $Z^0 \rightarrow \tau^-\tau^+$  cross section using the  $\tau_\mu\tau_{had}$  final state at DØ in Run 2”, DØ Note 4255.
- [61] [http://www-d0.fnal.gov/computing/algorithms/calgo/jet\\_met/certification.html](http://www-d0.fnal.gov/computing/algorithms/calgo/jet_met/certification.html)
- [62] [http://www-d0.fnal.gov/phys\\_id/jets/jetid.html](http://www-d0.fnal.gov/phys_id/jets/jetid.html)
- [63] J-L. Agram *et al.*, “Jet Energy Scale at DØ Run II”, DØ Note 4720.
- [64] [http://www-d0.fnal.gov/phys\\_id/jes/d0\\_private/jes.html](http://www-d0.fnal.gov/phys_id/jes/d0_private/jes.html)
- [65] [http://www-clued0.fnal.gov/~pverdier/d0\\_private/MetRunSel](http://www-clued0.fnal.gov/~pverdier/d0_private/MetRunSel)
- [66] P. Verdier, S. Trincaz-Duvois, “Missing ET Status”, presentation at the ADM meeting (2004/10/15),  
<http://www-d0.hef.kun.nl//askArchive.php?base=agenda&categ=a041625&id=a041625s1t0/transparencies>

- [67] [http://www-d0.fnal.gov/computing/data\\_quality/dataqual.html](http://www-d0.fnal.gov/computing/data_quality/dataqual.html)
- [68] M. Begel, D. Edmunds, P. Laurens, R. Partridge, “*DØ Luminosity in Run 2: Delivered*”, DØ Note 3970.
- [69] P. Kumar Mal, M. Begel, M. Verzocchi, H. Schellman “*DØ Luminosity in Run 2: Reconstructed*”, DØ Note 4438.
- [70] T. Edwards, S. Yacoob, T. Andeen, J. Park, B. Casey, M. Begel, R. Partridge, H. Schellman, A. Sznajder, “*The Updated DØ Luminosity Determination – Short Summary*”, DØ Note 4328.
- [71] T. Edwards, S. Yacoob, T. Andeen, M. Begel, B. Casey, R. Partridge, H. Schellman and A. Sznajder “*Determination of the Effective Inelastic p-pbar Cross-Section for the DØ Run II Luminosity Measurement*”, FERMILAB-TM-2278-E.
- [72] V. Buescher, J.-F. Grivaz, T. Nunnemann, M. Wobisch, “*Conclusions of Mini-Workshop on PDF uncertainties and related topics*”, DØ Note 4618.
- [73] R. Hamberg, W. L. van Neerven and T. Matsuura, “*A Complete calculation of the Order  $\alpha_s^2$  Correction to the Drell-Yan K-Factor*”, Nucl. Phys. **B359** (1991) 343 [Erratum-ibid. B 644 (2002) 403].
- [74] DØ New Phenomena MC webpage,  
[http://www-clued0.fnal.gov/~nunne/cross-sections/mcfm\\_cross-sections.html](http://www-clued0.fnal.gov/~nunne/cross-sections/mcfm_cross-sections.html)
- [75] DØ Monte Carlo webpage,  
[http://d0-france.in2p3.fr/WORKING\\_GROUPS/MONTECARLO/Catalog/current](http://d0-france.in2p3.fr/WORKING_GROUPS/MONTECARLO/Catalog/current)
- [76] T. Nunnemann, “*NNLO Cross-Sections for Drell-Yan, Z and W Production using Modern Parton Distribution Functions*”, DØ Note 4476.
- [77] DØ Collaboration, “*Measurement of the Cross Section for W and Z Production to Electron Final States with the DØ Detector at  $\sqrt{s} = 1.96$  TeV*”, DØ Note 4403-CONF (2004);  
D. Chapin *et al.*, “*Measurement of  $Z \rightarrow ee$  and  $W \rightarrow e\nu$  production cross sections with  $|\eta| < 1.05$* ”,  
[http://www-d0.fnal.gov/Run2Physics/d0\\_private/eb/Run2EB\\_003/Run2EB\\_003.html](http://www-d0.fnal.gov/Run2Physics/d0_private/eb/Run2EB_003/Run2EB_003.html)
- [78] U. Blumenschein, “*Suche nach assoziierter Chargino-Neutralino Produktion in Proton-Antiproton Kollisionen bei 1.96 TeV*”, PhD thesis, University of Freiburg (2005).
- [79] <http://www-d0.fnal.gov/computing/algorithms/calgo/calgo.html>
- [80] [http://www-d0.fnal.gov/phys\\_id/emid/d0\\_private/certification/welcome.html](http://www-d0.fnal.gov/phys_id/emid/d0_private/certification/welcome.html),

## Bibliography

---

[http://www-d0.fnal.gov/phys\\_id/emid/d0\\_private/EM\\_Particle\\_Documentation\\_EMID.html](http://www-d0.fnal.gov/phys_id/emid/d0_private/EM_Particle_Documentation_EMID.html)

- [81] <http://www-d0.fnal.gov/Run2Physics/cs/d0correct/d0correct.html>
- [82] J. Kozminski, R. Kehoe, H. Weerts, S. Park, A. Quadt, J. Gardner, Sh. Jabeen, “*Electron Likelihood in p14*”, DØ Note 4449.
- [83] E.W. Varnes, “*Track reconstruction efficiency measurement with single muons*”, DØ Note 4317.
- [84] B. Tiller, T. Nunnemann, “*Measurement of the differential Z0-boson production cross-section as function of transverse momentum*”, DØ Note 4660.
- [85] R. Stroehmer, “*Common MC Smearing*”, presentation available at:  
<http://www-d0.hef.kun.nl//fullAgenda.php?id=a042017>
- [86] A. Kumar, R. Kehoe, K. Ranjan and B.C. Choudhary, “*Oversmearing of Missing Transverse Energy in  $Z \rightarrow ee + X$  Monte Carlo Events*”, DØ Note 4554.
- [87] W. Beenakker, R. Hopker, M. Spira, P.M. Zerwas, “*Squark and Gluino Production at Hadron Colliders*”, Nucl. Phys. **B492** (1997), hep-ph/9610490.
- [88] LEPSUSYWG, ALEPH, DELPHI, L3 and OPAL experiments, Note LEPSUSYWG/04-02.1  
<http://lepsusy.web.cern.ch/lepsusy/Welcome.html>
- [89] W. Beenakker *et. al.*, “*The Production of Charginos/Neutralinos and Sleptons at Hadron Colliders*”, Phys. Rev. Lett. **83** (1999), hep-ph/9906298.
- [90] G. Cowan, “*Statistical Data Analysis*”, Oxford University Press, Oxford, New York, 1998
- [91] R.J. Barlow, “*Statistics, a guide to the use of statistical methods in the physical sciences*”, John Wiley and Sons, New York, 1997
- [92] M. Hohlfeld, “*Search for Associated Chargino and Neutralino Production in  $e + \mu + \ell$  Final States in DØ Data from Run II*”, DØ Note 4543.
- [93] M. Binder, “*Search for the Associated Chargino-Neutralino Production in Final States with Two Muons and Additional Lepton*”, DØ Note 4806.
- [94] A. Yurkewicz, “*Search for mSUGRA SUSY in the Like-Sign Dimuon Channel*”, DØ Note 4408.
- [95] I. Torchiani, “*Search for the Associated Production of Charginos and Neutralinos in the  $\mu + \tau + \ell$  Final State*”, DØ Note 4743.
- [96] T. Junk, Nucl. Instr. and Meth. **A434** (1999) 435.

- [97] V.M. Abazov *et. al.*, “First Measurement of  $\sigma(p\bar{b} \rightarrow Z) \cdot Br(Z \rightarrow \tau\tau)$  at  $\sqrt{s} = 1.96$  TeV”, Phys. Rev. **D71**, 072004 (2005), hep-ex/0412020.
- [98] G. Degrassi, S. Heinemeyer, W. Hollik, P. Slavich, G. Weiglein, Eur. Phys. J. **C28** (2003) 133.
- [99] M. Carena, J. Conway, H. Haber, J. Hobbs, “Report of the Tevatron Higgs Working Group”, hep-ph/0010338.
- [100] <http://maltoni.home.cern.ch/maltoni/TeV4LHC/>
- [101] V. Büscher and K. Jakobs, “Higgs Boson Searches at Hadron Colliders”, hep-ph/0504099.
- [102] S. Heinemeyer, W. Hollik and G. Weiglein, Phys. Rev. **D58** (1998) 091701, Phys. Lett. **B440** (1998) 296, FEYNHIGGS program: <http://www.feynhiggs.de>
- [103] CDF Collaboration, DØ Collaboration, Tevatron Electroweak Working Group, “Combination of CDF and DØ Results on the Top-Quark Mass”, hep-ex/0507091.
- [104] V. Büscher, C. Noeding, M. Titov, I. Torchiani, “Search for Neutral Higgs Bosons Decaying to Tau Pairs”, DØ Note 4952.
- [105] A. Haas, A. Kharchilava, M. Michaut, J. Rani, T. Scanlon, B. Tuchming, “DØ Search for Neutral Higgs Bosons at High  $\tan b$  in Multi-Jet Events Using p14 Data”, DØ Note 4671.
- [106] <http://www-cdf.fnal.gov/physics/projections/>
- [107] ATLAS collaboration, “ATLAS: Detector and Physics Performance Technical Design Report, Vol. II”, CERN-LHCC-99-15 (1999), <http://atlas.web.cern.ch/Atlas/GROUPS/PHYSICS/TDR/access.html>
- [108] S. Villa, “Discovery Potential for SUGRA/SUSY at CMS”, CMS CR-2003/033 — PRS PH-SUSY;  
D. Denegri, “Summary of the CMS Discovery Potential for the MSSM SUSY Higgses”, hep-ph/0112045;  
F.E. Paige, “SUSY signatures at LHC”, [http://www-library.desy.de/proc/proc02-02/Proceedings/pl.1b/paige\\\_pr.pdf](http://www-library.desy.de/preparch/desy/proc/proc02-02/Proceedings/pl.1b/paige\_pr.pdf)

*Bibliography*

---

# Acknowledgements

On this last page I would like to thank everybody who somehow contributed to this thesis and who made the few last years such an enjoyable and unforgettable experience. My apologies to everyone I've left out – my memory has never been the best.

First I would like to thank my supervisor Karl Jakobs for giving me the opportunity to work within the DØ collaboration at Fermilab. Even when progress was staggering, he succeeded in lifting my spirits and in keeping up my interest in physics. His valuable advice and fantastic support are without precedent.

I would like to express my gratitude to Volker Büscher, who successfully guided me through both analyses and who always had useful advice and ideas when I was stuck. This work would have definitely not been possible without his help.

A special thank you goes to the (former) CTT group, who gave me cordial welcome at Fermilab and provided me with lots of support during the first 1.5 years of my stay at Fermilab. It was great fun working on the trigger hardware, and in the end it was even working! In this context, I would like to thank Levan Babukhadia, Jerry Blazey, Fred Borcherding, Stefan Grünendahl, Manuel Martin and Jamieson Olson.

A big thank you goes to all my colleagues and friends here in Freiburg. It has been a pleasure to work with you, and sometimes there was even time to go out and have fun. Very special thanks go to Ulla Blumenschein, Ingo Torchiani and Andrea Dahlhoff. You know why (and if you don't, I'm not going to tell you). Special mentioning deserve Uli Parzefal and Elke Lützner for their support. It was a pleasure to work in the DØ group here in Freiburg, big thanks go to Harald Fox, Henrik Nilsen, Olav Mundal, Björn Penning and Maxim Titov. Of course I should not forget to thank Michael Dührssen and Michael Heldmann for their computer miracles.

Only a few know that I originally started this PhD in Mainz, before moving to Freiburg (after a slight detour via Chicago). I did enjoy my time there, and I would have loved to stay a bit longer. My respect goes to Konrad Kleinknecht, who leads a great particle physics group in Mainz. Of all the great colleagues there are a few names that really stick out: Marc Hohlfeld, David Meder-Marouelli, Silvia Müller, Uli Schäfer and Jürgen Thomas.

There are a few close friends who stayed at my side during the last years, even though I did not reply to the e-mails or phone calls as often I should have done. Failure lies deep in the human heart. A big thank you goes to Alexander

Huf, Mirko Cinchetti and Stefan Christ. Special thanks go to Kirsten and Klaus Münich for their close friendship.

I am deeply grateful to my family, especially to my mother Heidrun and my sister Claudia. Without their help, encouragement and support throughout the last years, I wouldn't be where I am today, and this work would not have been possible at all. Words cannot express how much you mean to me.

Last – but definitely not least – I would like to thank my partner Will for the wonderful last years, and especially for his understanding and patience.